VNIVERSITAT DE VALÈNCIA

The use of polyoxometalates for the design of high-nuclearity magnetic clusters, single-ion magnets and photo-responsive materials

Memoria de Tesis Doctoral presentada por

Yan Duan

para optar al grado de Doctor en Nanociencia y Nanotecnología

Dirigida por **Dr. Eugenio Coronado Miralles** y **Dr. Carlos Giménez-Saiz**

May 2017

Instituto de Ciencia Molecular (ICMol)
Universitat de València

El Dr. **Eugenio Coronado Miralles**, Profesor Catedrático del Departamento de Química Inorgánica de la Universidad de València y el Dr. **Carlos Giménez-Saiz**, Profesor Titular del Departamento de Química Inorgánica de la Universidad de València.

CERTIFICAN:

Que la memoria presentada por Dña. Yan DUAN con título "**The use of polyoxometalates for the design of high-nuclearity magnetic clusters, single-ion magnets and photo-responsive materials**" ha sido realizada bajo su dirección en el Instituto de Ciencia Molecular de la Universidad de Valencia, autorizando mediante este escrito la presentación de la misma para optar al grado de Doctor en Nanociencia y Nanotecnología.

En Paterna, a 02 de mayo de 2017

Dr. **Eugenio Coronado Miralles**

Dr. **Carlos Giménez-Saiz**

A Mi Familia

Dedicated to My Beloved Family

谨以此书献给我挚爱的家人

Acknowledgements

I want to express my entire acknowledgement to all the people that have crossed my life path during all these years. Forgive me for not naming all of you here.

First and foremost, I want to express my deepest gratitude to my advisor, Eugenio Coronado, not only for giving me the opportunity to work in his laboratories but also for all his time, ideas and funding that made my Ph.D. experience productive and stimulating. I appreciate him for his guidance, inspiration, encouragement and support during the development of this work. He is that kind of person you will never forget once you meet him. He is one of the smartest people I know. I hope that I could be as lively, enthusiastic and energetic in research as him.

I would also like to thank my thesis co-director, Carlos Giménez-Saiz, who picked me up from the train station the first day I arrived to Valencia. I deeply thank him for showing me the entire lab staff and introducing me all the lab members, for his instructions on scientific problems as well as other problems in life. He has been teaching me all about self-discipline in laboratory work, in solving the crystal structures and in written scientific articles. I really appreciate his scientific advices and many insightful discussions and suggestions. He was one of my primary resources for getting my scientific questions answered and was fundamental in helping me cranked out this thesis.

I will forever be thankful to my master mentor, Li-Min Zheng, for providing me the opportunity to join the group of CORONADO. She has been helpful in providing advices during all these years. She was and she is one of my best models as a scientist, mentor and teacher. I still remember fondly my time as a student in her lab in Nanjing University. She was the reason why I decided to pursue a career in research. Her enthusiasm and love for teaching and investigating are contagious.

My sincere thanks go also to Juan Modesto Clemente-Juan, for his generous help with all kinds of problems in the magnetic study of all the complexes, for his enthusiasm and his sunshine face always with beautiful smile.

I would like to thank Alex Gaita-Ariño, for his kind and warm hearted, for his supporting and encouragement, for his guidance during my thesis and for being always ready for helping me with my writing and my life.

I want to express my sincere gratitude to John Errington, for his kind and patient guidance in the lab work at Newcastle University and for showing me the Newcastle city under the rain.

I would also thank all my collaborators, especially Stephen Hill in Florida and Fernando Luis in Zaragoza. Thanks to João C. Waerenborg for all the Mössbauer measurements, for his kind help and support.

I would like to thank Carlos Gómez and Samia Benmansour, for their kind support and encouragement, for their patient explaining me any doubt I had.

My grateful also goes to Helena, Lorena, Salvador and Jose Jaime, for helping me in the lab, solving the problems for unstable complexes and sharing information about related experimental details.

A good supporting system is important for surviving and staying in the lab. I would like to express my thanks to Chema and Gloria, for their kindly help and for their hard working. Thanks to Chema for encouraging me to keep going on with my work. I want to express my sincere gratitude to Ángel López, for his humour that makes the life in the lab more relax, for having good ideas of whatever kind of problem in the lab. My thanks also go to Jose Vicente Usagre for helping me with the equipment and for his great technical support and teaching me "*español de la calle*".

Great thanks also go to Ruth, Estrella, Marian, Paco and Manuel, for them to be always kind and patient. Thanks for Paco´s help in guiding me everywhere in Valencia to make different kind of documents the first year when I just arrived. Thanks for his company to many excursions and trips. All journeys have made my life during these years much more colourful. Thanks to Marian as a friend/sister for giving me suggestions and supporting me.

I would like to express my appreciation to Carlos Martí, Guillermo, Julia, Concha, Efrén, María, Gonzalo, Juanpi, Mónica, ... Thanks to Carlos Martí for providing me his kindness, his insight and suggestions, which are precious to me. With all of you, the life of research seems more entertainment.

I acknowledge the old and new companies in my office for all the moment we have shared. Néstor, Patricia, Marc, Verónica, Ramón, Roger and Katia. Thanks to Vero, for all the support and encourage, for her patient and kindness, for all the wonderful moments we have spent. Thanks to Garín for being always a gentle man and being always ready for helping. Thanks to Jorge, Gustavo, "los dos Javi"… I want to express my sincere

gratitude to past and present members of all UIMM group for their support and friendship. Their kindness and help made me feel at home and I cherished being part of UIMM.

My great thanks also go to all my Spanish family: Santiago, Asun, Pilar, Mari, Amparo, Oleg, José Vicente and all the students from Colegio Mayor San Juan de Ribera. Thanks for their company, for providing me a lovely home, for their kindness and help. Many thanks to Santiago, for being so thoughtful with all the details in the college, for encouraging me to keep going on, for showing me the culture and the religion, for all the discussions we had many nights after dinner. Without you, life in Spain would not have been the same.

I am also very grateful to my best friends Marc Coronado and Samuel Mañas, for helping me to get through all the difficult times, for all the emotional support, entertainment and caring. Thanks for all the moments we lived, for their continuously enduring my stubborn and strictness for all the things, for showing me the culture of Spain. Thanks for their company during all these years. Without both of you, life would not have been the same. I only hope to share more years with both you.

Lastly, I would like to extend my deepest gratitude to my family for their love and encouragement. To my parents for their everlasting and unconditional love, who raised me and supported me in all my pursuits, allowing me to realize my own potential. All the support they have provided me over these years was the greatest gift. Thanks to my old sister for her wise guide, for her support and love, for her help with every kind of life problem. Thanks to my young sister for her optimistic suggestions. Thanks to my brother, for taking care of her little sister and teaching her how to fly. Thank you!

Yan Duan

University of Valencia

May 2017

Motivation and Objectives

"If we knew what it was we were doing, it would not be called research, would it?"

---Albert Einstein (1897-1955)

Polyoxometalates (POMs) are a class of inorganic clusters composed of oxygen and d^0 and/or d^1 constituent metal atoms of the groups 5 and 6 (most frequently, Mo, W, V and Nb) with medium to large sizes (typically between 1 - 5 nm) and high anionic charges (usually from −3 to −16) exhibiting remarkable structural, electronic, magnetic and photochromic properties. Since the discovery of the first POM in the mid-nineteenth century, thousands of POM compounds have been reported. However, new structures and properties of POMs are continuously being discovered.

Our research group has been using POMs as minimal models in molecular magnetism to study fundamental phenomena such as anisotropic magnetic exchange and electron transfer.[1] Recently, POMs have also shown to be ideal candidates for experiments in many topics regarding molecular nanoscience, including molecular nanomagnetism and spintronics,[1h, 1j, 2] quantum computing[3] and molecular photochromism[4] due to the following reasons:

(a) POMs are very stable, robust and resistant to oxidation, maintaining their structural integrity in the solid state or in solution, and even when deposited on surfaces.

(b) POMs can act as polydentate O-donor ligands to accommodate one or more magnetic ions at specific sites, leading to magnetic molecules and large magnetic clusters with large variety of topologies.

(c) POMs can easily accept various numbers of electrons, which will usually be delocalized on the constituent W or Mo metals giving rise to mixed valence clusters with interesting magnetic or (photo/electro)-chromic effects.

Therefore, these characteristics open up a multitude of possibilities for the study of the interaction of localized spins in clusters of different magnetic nuclearities encapsulated in POMs. In addition, the third characteristic make POMs a unique class of inorganic materials that can act as electron acceptors in photo-induced electron transfer processes having reversible redox behavior, photoactivity and excellent stability. Finally, the combined effects of electron transfer and magnetic exchange make POM chemistry an exciting playground for theoretical proposals to advance the understanding of

fundamental single-molecule spintronic processes.[5] In this context, this doctoral thesis intends to advance in the development and application of technologies based on molecules.

In the present doctoral thesis, POMs will be employed as building blocks for the incorporation of multinuclear cobalt-containing magnetic complexes, for the construction of lanthanoid-based single ion magnets and functional nanoscale systems and for the design of new systems with photochromic effects. Both, traditional methods and original synthetic strategies will be applied for the preparation of these POM-based functional systems, which will be chemically and physically characterised, and their stabilities in solid state and in solution will be determined.

References

[1] (a) C. J. Gómez-García, E. Coronado, J. J. Borrás-Almenar, M. Aebersold, H. U. Güdel and H. Mutka, *Physica B*, 1992, **180**, 238-240; (b) J. R. Galán-Mascarós, C. J. Gómez-García, J. J. Borrás-Almenar and E. Coronado, *Adv Mater.*, 1994, **6**, 221-223; (c) J. M. Clemente, H. Andrés, M. Aebersold, J. J. Borrás-Almenar, E. Coronado, H. U. Güdel, H. Buttner and G. Kearly, *Inorg. Chem.*, 1997, **36**, 2244-2245; (d) J. M. Clemente-Juan, E. Coronado, A. Gaita-Ariño, C. Giménez-Saiz, G. Chaboussant, H. U. Güdel, R. Burriel and H. Mutka, *Chem. Eur. J.*, 2002, **8**, 5701-5708; (e) J. M. Clemente-Juan, E. Coronado, A. Forment-Aliaga, J. R. Galán-Mascarós, C. Giménez-Saiz and C. J. Gómez-García, *Inorg. Chem.*, 2004, **43**, 2689-2694; (f) J. M. Clemente-Juan, E. Coronado, A. Gaita-Ariño, C. Giménez-Saiz, H. U. Güdel, A. Sieber, R. Bircher and H. Mutka, *Inorg. Chem.*, 2005, **44**, 3389-3395; (g) A. Palii, B. Tsukerblat, S. Klokishner, K. R. Dunbar, J. M. Clemente-Juan and E. Coronado, *Chem. Soc. Rev.*, 2011, **40**, 3130-3156; (h) J. M. Clemente-Juan, E. Coronado and A. Gaita-Ariño, *Chem. Soc. Rev.*, 2012, **41**, 7464-7478; (i) S. Cardona-Serra, J. M. Clemente-Juan, E. Coronado, A. Gaita-Ariño, A. Camón, M. Evangelisti, F. Luis, M. J. Martínez-Pérez and J. Sesé, *J. Am. Chem. Soc.*, 2012, **134**, 14982-14990; (j) J. J. Baldoví, S. Cardona-Serra, J. M. Clemente-Juan, E. Coronado, A. Gaita-Ariño and H. Prima-García, *Chem. Commun.*, 2013, **49**, 8922-8924; (k) S. Cardona-Serra, J. M. Clemente-Juan, E. Coronado, C. Martí-Gastaldo and E. Navarro-Moratalla, *Eur. J. Inorg. Chem.*, 2013, **10-11**, 1903-1909.

[2] A. Giusti, G. Charron, S. Mazerat, J. Compain, P. Mialane, A. Dolbecq, E. Rivière, W. Wernsdorfer, R. N. Bibouni, B. Keita, L. Nadjo, A. Filoramo, J. Bourgoin and T. Mallah, *Angew. Chem. Int. Ed.*, 2009, **48**, 4949-4952.

[3] (a) R. E. P. Winpenny, *Angew. Chem. Int. Ed.*, 2008, **47**, 7992-7994; (b) D. Stepanenko, M. Trif and D. Loss, *Inorg. Chim. Acta*, 2008, **361**, 3740-3745.

[4] (a) T. He and J. Yao, *Prog Mater Sci*., 2006, **51**, 810-879; (b) V. Coué, R. Dessapt, M. Bujoli-Doeuff, M. Evain and S. Jobic, *Inorg. Chem.*, 2007, **46**, 2824-2835; (c) Y. Yang, L. Yue, H. Li, E. Maher, Y. Li, Y. Wang, L. Wu and V. W. Yam, *Small*, 2012, **8**, 3105-3110; (d) H. El Moll, A. Dolbecq, I. M. Mbomekalle, J. Marrot, P. Deniard, R. Dessapt and P. Mialane, *Inorg. Chem.*, 2012, **51**, 2291-2302; (e) K. Hakouk, O. Oms, A. Dolbecq, H. El Moll, J. Marrot, M. Evain, F. Molton, C. Duboc, P. Deniard, S. Jobic, P. Mialane and R. Dessapt, *Inorg. Chem.*, 2013, **52**, 555-557; (f) Q. Zheng, L. Vilà-Nadal, C. Busche, J. S. Mathieson, D. Long and L. Cronin, *Angew. Chem. Int. Ed.*, 2015, **54**, 7895-7899; (g) Y. Gong, Q. Hu, C. Wang, L. Zang and L. Yu, *Langmuir*, 2016, **32**, 421-427; (h) W. Chen, U. Tong, T. Zeng, C. Streb and Y. Song, *J. Mater. Chem. C.*, 2015, **3**, 4388-4393; (i) C. Streb, *Dalton Trans.*, 2012, **41**, 1651-1659; (j) B. Matt, J. Fize, J. Moussa, H. Amouri, A. Pereira, V. Artero, G. Izzet and A. Proust, *Energy Environ. Sci.*, 2013, **6**, 1504-1508; (k) A. Proust, R. Thouvenot and P. Gouzerh, *Chem. Comm.*, 2008, 1837-1852; (l) C. Zhao, C. S. Kambara, Y. Yang, A. L. Kaledin, D. G. Musaev, T. Lian and C. L. Hill, *Inorg. Chem.*, 2013, **52**, 671-678.

[5] J.J. Baldoví, S. Cardona-Serra, A. Gaita-Ariño, E. Coronado. *Chapter Eight - Design of Magnetic Polyoxometalates for Molecular Spintronics and as Spin Qubits.* In: Rudi van Eldik and Leroy Cronin, Editor(s), Advances in Inorganic Chemistry, Academic Press, 2017, **69**, 213-249.

Summary

Towards a better understanding of the present dissertation, a brief summary including the principal aspects of the work developed in each chapter is provided below:

1. **Chapter 1** constitutes a historic overview of POMs, a summary of synthetic strategies and structural description of the relevant POMs of this thesis and a short description of the general properties and the applications of POMs.

2. **Chapter 2** discusses the synthesis and characterisation of several novel multinuclear cobalt-substituted POMs **2.1**-**2.9**. This chapter provides a deep insight into the experimental details of the synthesis and characterisation of cobalt-containing POMs that have been obtained during the course of this doctoral work. This chapter is divided into the following three main parts:

(1) In the first part, the synthesis and full characterisation of four novel tetra-cobalt(II) or hepta-cobalt(II,III)-substituted POMs, having cobalt cores exhibiting cubane or di-cubane topologies, is described. The tetra-cobalt(II)-substituted POM $[Co_4(OH)_3(H_2O)_6(PW_9O_{34})]^{4-}$ (**2.1**) consists of a trilacunary B-α-$[PW_9O_{34}]^{9-}$ unit which accommodates a cubane-like $[Co^{II}_4O_4]$ core. The three hepta-cobalt(II,III)-containing POMs $[Co_7(OH)_6(H_2O)_6(PW_9O_{34})_2]^{9-}$ (**2.2**), $[Co_7(OH)_6(H_2O)_4(PW_9O_{34})_2]_n^{9n-}$ (**2.3**) and $[Co_7(OH)_6(H_2O)_6(P_2W_{15}O_{56})_2]^{15-}$ (**2.4**) encapsulate a dicubane-like $[Co^{II}_6Co^{III}O_8]$ core between two trilacunary B-α-$[PW_9O_{34}]^{9-}$ units (in **2.2** and **2.3**) or two trilacunary α-$[P_2W_{15}O_{56}]^{12-}$ (in **2.4**) units. The chemical structure, stability studies in solution by UV-vis spectroscopy and cyclic voltammetry, and the magnetic properties of the resulting clusters are discussed.

(2) In the second part, a synthetic procedure is presented to construct new magnetic POMs containing one or two subunits of '$[Co_4(OH)_3(H_2O)_{6-n}(PW_9O_{34})]^{3-}$' (n = 3 or 5). The substitution of the water ligands present in these subunits by oxo or hydroxo ligands belonging to other POM fragments, gives rise to the following larger magnetic POM anions: $[Co_7(OH)_6(H_2O)_6(PW_9O_{34})_2]^{9-}$ (**2.2**), $[Co_7(OH)_6(H_2O)_4(PW_9O_{34})_2]_n^{9n-}$ (**2.3**), $[Co_8(OH)_6(H_2O)_6\{W_8O_{28}(OH)_2\}(PW_9O_{34})_2]^{16-}$ (**2.5**), $[Co_{11}(OH)_5(H_2O)_5(W_6O_{24})(PW_9O_{34})_3]^{22-}$ (**2.6**) and $[\{Co_4(OH)_3(H_2O)(PW_9O_{34})\}_2\{K\subset(H_2W_{12}O_{41})_2\}\{Co(H_2O)_4\}_2]^{17-}$ (**2.7**). The

crystal structures, magnetic characterisation and stabilities in aqueous solutions of these POM derivatives are also presented.

(3) In the third part, two structurally intriguing cobalt-substituted POMs are described, formulated as $[Co^{II}_4(H_2O)_2(Co^{III}W_9O_{34})(PW_9O_{34})]^{12-}$ (**2.8**) and $[Co_2\{Co_3(H_2O)(Co(OH)_2W_7O_{26})(PW_9O_{34})\}_2]^{22-}$ (**2.9**). **2.8** contains a pentacobalt cluster $\{Co^{II}_4Co^{III}\}$ and represents the first asymmetric sandwich exhibiting Weakley's topology, while POM **2.9** is made up of two capping B-α-$[PW_9O_{34}]^{9-}$ units and two bridging $[W_7O_{26}]^{10-}$ units that assemble to encapsulate a novel deca-Co(II) cluster core comprising octahedral and tetrahedral Co(II) ions. An original reaction based on the partial reductive hydrolysis of the penta-Co(II/III) cluster **2.8** leads to the formation of a higher nuclearity cluster **2.9**. The chemical nature and physical properties of both compounds are studied by XPS, mass spectrometry, ^{31}P-NMR spectroscopy, UV-vis spectroscopy, cyclic voltammetry and magnetic measurements.

3. Chapter 3 deals with a family of heteropolymolybdates-based lanthanoid single molecular magnets (SMMs), with the general formula $[Ln(\beta\text{-}Mo_8O_{26})_2]^{5-}$ (Ln^{3+} = Tb (**3.1**), Dy (**3.2**), Ho (**3.3**), Er (**3.4**), Tm (**3.5**), and Yb (**3.6**)) that are soluble in organic solvents (such as acetone, acetonitrile, N,N-dimethylformamide). The magnetic properties of this series have been correlated with the nature and structure of the coordination site around the lanthanoid cations. The static and dynamic magnetic measurements of this family of complexes have been well studied. For the Ho (**3.3**) and Er (**3.4**) derivatives, slow relaxations of the magnetizations have been observed. A magneto-structural analysis of this family of compounds has been carried out, which is based on an effective crystal field model and compared with the results reported in analogous lanthanoid single ion magnets (SIMs) based on polyoxotungstates.

4. Chapter 4 describes the synthesis and full characterisation of two new POMs: a photo-responsive molecular polyanion with the formula $\{K\subset[(A\text{-}\alpha\text{-}PW_9O_{34})_2Fe_2(C_2O_4)_2]\}^{15-}$ (**4.1**) in which two Fe(III) ions are simultaneously coordinated by two A-α-$[PW_9O_{34}]^{9-}$ units and two oxalato ligands; and the analogous derivative with formula $\{K\subset[(A\text{-}\alpha\text{-}PW_9O_{34})_2Fe_2(C_3H_2O_4)_2]\}^{5-}$ (**4.2**) containing malonato ligands. When irradiated with UV light, the potassium salt of **4.1**, $K_{15}\{K\subset[(A\text{-}\alpha\text{-}PW_9O_{34})_2Fe_2(C_2O_4)_2]\}\cdot 29H_2O$, exhibits a remarkable photocolouration effect attributable

to the partial reduction of the POM, giving rise to a mixed-valence species. The photo-induced colouration process is confirmed to be intramolecular and involves electron transfer from the oxalato ligands, which partially decompose releasing CO_2, towards the Fe(III) ions and the POM units. The mechanism of this photocolouration process is confirmed by DRS, IR, XPS, Mössbauer spectroscopies, magnetism and elemental analysis.

5. General Conclusions. Although specific conclusions have been included at the end of each chapter, the most relevant overall conclusions are summarized in this part of the thesis.

6. *Resumen*. This section contains a resume of the thesis in Spanish.

Most of the results reported in this thesis have already been published. A list of publications is given below:

[1] **Yan Duan**, Juan M. Clemente-Juan, Carlos Giménez-Saiz and Eugenio Coronado: *Cobalt clusters with cubane-type topologies based on trivacant polyoxometalate ligands.* **Inorganic Chemistry** 2016, 55, 925 – 938; DOI: 10.1021/acs.inorgchem.5b02532.

[2] **Yan Duan**, Juan Modesto Clemente Juan, J L G Fierro, Carlos Giménez-Saiz and Eugenio Coronado: *A decacobalt(II) cluster with triple-sandwich structure obtained by partial reductive hydrolysis of a pentacobalt(II/III), Weakley-type, polyoxometalate*. **Chemical Communications** 2016, 52, 13245 – 13248; DOI: 10.1039/C6CC05485D.

[3] **Yan Duan**, Juan M. Clemente-Juan, Eugenio Coronado, Carlos Giménez-Saiz: *Construction of larger polyoxometalates containing* $'[Co_4(OH)_3(H_2O)_{6-n}(PW_9O_{34})]^{3-}$' *(n = 3 or 5) as a common subunit.* **Crystal Growth & Design**, Submitted.

[4] **Yan Duan**, José J. Baldoví, Carlos Bustos, Salvador Cardona-Serra, Pierre Gouzerh, Richard Villanneau, Geoffrey Gontard, Juan Modesto Clemente Juan, Alejandro Gaita-Ariño, Carlos Giménez-Saiz, Anna Proust, Eugenio Coronado: *Single ion magnets based on lanthanoid polyoxomolybdate complexes*. **Dalton Transactions** 2016, **45**, 16653 – 16660; DOI: 10.1039/C6DT02258H.

[5] **Yan Duan**, João Carlos Waerenborgh, Juan Modesto Clemente Juan, Carlos Giménez-Saiz, Eugenio Coronado: *Light-induced decarboxylation in a photo-responsive iron-containing complex based on polyoxometalate and oxalato ligands*. **Chemical Science** 2017, 8, 305 – 315; DOI: 10.1039/C6SC01919F.

In addition, in the course of this thesis I have been involved in the research dealing with the use of magnetic POMs in the theoretical modelling of SIMs and in quantum computing. This physics-oriented research has given rise to the following publications:

[6] José J Baldoví, Juan M Clemente-Juan, Eugenio Coronado, **Yan Duan**, Alejandro Gaita-Ariño, Carlos Giménez-Saiz: *Construction of a General Library for the Rational Design of Nanomagnets and Spin Qubits Based on Mononuclear f-Block Complexes. The Polyoxometalate Case*. **Inorganic Chemistry** 2014, 53, 9976 − 9980; DOI: 10.1021/ic501867d.

[7] Muhandis Shiddiq, Dorsa Komijani, **Yan Duan**, Alejandro Gaita-Ariño, Eugenio Coronado and Stephen Hill: *Enhancing coherence in molecular spin qubits via atomic clock transitions.* **Nature** 2016, 531, 348 – 351; DOI: 10.1038/nature16984.

[8] José J Baldoví, **Yan Duan**, Roser Morales, Alejandro Gaita-Ariño, Eliseo Ruiz, Eugenio Coronado: *Rational Design of Lanthanoid Single-Ion Magnets: Predictive Power of the Theoretical Models*. **Chemistry-A European Journal** 2016, 22, 13532 – 13539; DOI: 10.1002/chem.201601741.

[9] M. D. Jenkins, **Y. Duan**, B. Diosdado, J. J. García-Ripoll, A. Gaita-Ariño, C. Giménez-Saiz, P. J. Alonso, E. Coronado, F. Luis: *Coherent manipulation of three-qubit states in a molecular single-ion magnet.* **Physical Review B 00**, 004400 (2017); DOI: 10.1103/PhysRevB.00.004400.

Table of Contents

Acknowledgements VII

Motivation and Objectives 1

References 3

Summary 5

Table of Contents 9

List of Compounds 15

Chapter 1. General Introduction 17

1.1. A Historical Overview of POMs 19

1.2. Synthesis of POMs 21

1.3. Structural Description of POMs 23

1.4. General Properties and Applications of POMs 28

1.4.1. POM-based Photo-Responsive Materials 28

1.4.2. POMs as Magnetic Model Systems 29

1.4.2.1. Cobalt clusters encapsulated in POMs 30

1.4.2.2. Lanthanoid-Containing POMs 33

1.4.2.3. Mixed-Valence POMs 34

1.5. References 36

Chapter 2. Cobalt-Containing POMs 43

2.1. Cubane cobalt clusters based on trivacant POM ligands 45

2.1.1. Introduction 45

2.1.2. Results and Discussion 47

2.1.2.1. Synthetic approach 47

2.1.2.2. Crystal Structure of **Q-2.1** 49

2.1.2.3. Crystal Structure of **Q-2.2** 53

2.1.2.4. Crystal structure of **Q-2.3** 55

2.1.2.5. Crystal Structure of **Q-2.4** 56

2.1.2.6. Bond valence sum (BVS) calculations 58

2.1.2.7. Stabilities in aqueous solution 62
2.1.2.8. Magnetic Properties 67
2.1.3. Conclusions 72
2.1.4. Experimental Section 74
2.1.4.1. General Methods and Materials 74
2.1.4.2. Synthesis 75
2.1.4.2.1. Synthesis of **Q-2.1** 75
2.1.4.2.2. Synthesis of **Q-2.2** 78
2.1.4.2.3. Synthesis of **Q-2.3** 80
2.1.4.2.4. Synthesis of **Q-2.4** 82
2.1.4.3. X-ray Crystallography 85
2.1.4.4. Magnetic Measurements 88
2.2. Construction of large magnetic POMs containing '$[Co_4(OH)_3(H_2O)_{6-n}(PW_9O_{34})]^{3-}$' (n = 3 or 5) as a common subunit 89
2.2.1. Introduction 89
2.2.2. Results and Discussion 91
2.2.2.1. Synthetic approach 91
2.2.2.2. Crystal structure of **Q-2.1** 93
2.2.2.3. Crystal Structure of **Q'-2.2** 93
2.2.2.4. Crystal Structure of **Q-2.5** 94
2.2.2.5. Crystal Structure of **Q-2.6** 96
2.2.2.6. Crystal Structure of **Q-2.7** 98
2.2.2.7. Bond valence sum (BVS) calculations 100
2.2.2.8. Stabilities in aqueous solution 100
2.2.2.9. Electrochemical experiments 103
2.2.2.10. Magnetic properties 109
2.2.3. Conclusions 111
2.2.4. Experimental section 113
2.2.4.1. General methods and materials 113
2.2.4.2. Synthesis 114
2.2.4.2.1. Preparation of the starting solution 114
2.2.4.2.2. Synthesis of **Q'-2.2** 114
2.2.4.2.3. Synthesis of **Q-2.5** 116
2.2.4.2.4. Synthesis of **Q-2.6** 116
2.2.4.2.5. Synthesis of **Q-2.7** 117
2.2.4.3. X-ray Crystallography 118

2.2.4.4. Magnetic Measurements ... 120
2.3. A decacobalt(II) cluster with triple-sandwich structure obtained by partial reductive hydrolysis of a pentacobalt(II/III) Weakley-type polyoxometalate ... 121
2.3.1. Introduction ... 121
2.3.2. Results and Discussion ... 122
2.3.2.1. Synthetic approach ... 122
2.3.2.2. Crystal Structure of **Q-2.8** ... 123
2.3.2.3. Crystal Structure of **Q-2.9** ... 126
2.3.2.4. Bond valence sum (BVS) calculations ... 130
2.3.2.5. X-ray photoelectron spectroscopy ... 133
2.3.2.6. Mass spectrometry ... 134
2.3.2.7. ^{31}P NMR spectroscopy ... 136
2.3.2.8. UV-visible spectroscopy ... 137
2.3.2.9. Electrochemistry ... 139
2.3.2.10. Magnetic properties ... 140
2.3.3. Conclusions ... 143
2.3.4. Experimental section ... 144
2.3.4.1. General methods and materials ... 144
2.3.4.2. Synthesis ... 145
2.3.4.2.1. Synthesis of **Q-2.8** ... 145
2.3.4.2.2. Synthesis of **Q-2.9** ... 147
2.3.4.3. X-ray crystallography ... 149
2.3.4.4. X-ray photoelectron spectroscopy ... 150
2.3.4.5. Magnetic Measurements ... 151
2.3.4.6. Mass spectrometry ... 151
2.4. References ... 152

Chapter 3. POM-Based SMMs ... 157
3. SIMs based on lanthanoid polyoxomolybdate complexes ... 159
3.1. Introduction ... 159
3.2. Results and Discussion ... 161
3.2.1. Synthetic approach ... 161
3.2.2. Crystal structures of **3.1**-**3.6** ... 161
3.2.3. Solubility and stability ... 165
3.2.4. Magnetic properties ... 166
3.3. Conclusion ... 172

3.4. Experimental Section 173
3.4.1. General Methods and Materials 173
3.4.2. Synthesis 173
3.4.3. X-ray Crystallography 175
3.4.4. Magnetic measurements 176
3.4.5. Ligand field calculations 177
3.5. References 179

Chapter 4. A Photo-Responsive Fe-POM 180
4. Light-induced decarboxylation in a photo-responsive iron-containing complex based on polyoxometalate and oxalato ligands 183
4.1. Introduction 183
4.2. Results and discussion 186
4.2.1. Synthetic approach 186
4.2.2. Crystal Structures 187
4.2.3. Thermogravimetric analysis 191
4.2.4. UV-vis spectra in aqueous solution 191
4.2.5. Photocolouration effect in solid-state 192
4.2.6. Photocolouration effect in solution 197
4.2.7. Infrared spectroscopy 197
4.2.8. XPS Spectra 199
4.2.9. Mössbauer spectroscopy 200
4.2.10. Magnetic properties 205
4.2.11. Mechanism of the photo-induced colouration 208
4.3. Conclusions 210
4.4. Experimental section 211
4.4.1. General methods and materials 211
4.4.2. Synthesis of **Q-4.1** 212
4.4.3. Synthesis of **Q-4.2** 214
4.4.4. Synthesis of **4.1-^{57}Fe** and **4.2-^{57}Fe** 215
4.4.5. Preparation of irradiated samples of **4.1** 216
4.4.6. X-ray Crystallography 218
4.4.7. Mössbauer spectroscopy 221
4.4.8. Magnetic measurements 221
4.5. References 222

Chapter 5. General Conclusions 225

Chapter 6. Resumen de la Tesis Doctoral 229

Antecedentes científicos, Motivación y Objetivos 229

Resumen en español 231

Metodologia General 233

Capítulo 1. Introducción General 234

Capítulo 2. POMs de alta nuclearidad basados en cobalto 234

Resultados y Discusión 235

PARTE 1: Clústeres de cobalto con topologías tipo cubano basados en ligandos polioxometalato trivacantes 235

PARTE 2: Construcción de POMs extendidos que contienen '$[Co_4(OH)_3(H_2O)_{6-n}(PW_9O_{34})]^{3-}$' (n = 3 ó 5) como una subunidad común 237

PARTE 3: Un clúster de decacobalto(II) con estructura de triple sándwich obtenido mediante la hidrólisis reductora de un POM de pentacobalto (II/III) tipo Weakley 239

Capítulo 3. SMM basados en POMs 240

Resultados y Discusión 241

Capítulo 4. Un POM foto-reactivo que contiene Fe 241

Resultados y Discusión 242

Referencias 244

Appendix. Experimental techniques 247

A.1. X-ray photoelectron spectroscopy (XPS) 249

A.2. Mössbauer spectroscopy 251

A.3. Single-crystal X-ray Diffraction 255

A.4. Inductively Coupled Plasma/Optical Emission Spectrometry (ICP-OES) 259

A.5. Superconducting Quantum Interference Device (SQUID) 261

Curriculum Vitae 263

List of Compounds

$Na_{1.5}Cs_{2.5}[Co_4(OH)_3(H_2O)_6(PW_9O_{34})]\cdot 9H_2O$ **Q-2.1**

$Cs_7Na_2[Co_7(OH)_6(H_2O)_6(PW_9O_{34})_2]\cdot 20H_2O$ **Q-2.2**

$K_{4.2}Na_{2.8}\{Co(H_2O)_6\}[Co_7(OH)_6(H_2O)_6(PW_9O_{34})_2]\cdot 19H_2O$ **Q'-2.2**

$K_{5n}Na_{2n}\{Co(H_2O)_2\}_n[Co_7(OH)_6(H_2O)_4(PW_9O_{34})_2]_n\cdot 20nH_2O$ **Q-2.3**

$Na_{15}[Co_7(OH)_6(H_2O)_6(P_2W_{15}O_{56})_2]\cdot 38H_2O$ **Q-2.4**

$K_2Na_{14}[Co_8(OH)_6(H_2O)_6\{W_8O_{28}(OH)_2\}(PW_9O_{34})_2]\cdot 44H_2O$ **Q-2.5**

$K_{12}Na_4H_3\{Co_{1.5}(H_2O)_{5.5}\}[Co_{11}(OH)_5(H_2O)_5(W_6O_{24})(PW_9O_{34})_3]\cdot 37.5H_2O$ **Q-2.6**

$K_{12}Na\{Co_2(H_2O)_{10}\}[\{Co_4(OH)_3(H_2O)(PW_9O_{34})\}_2\{K\subset(H_2W_{12}O_{41})_2\}\{Co(H_2O)_4\}_2]\cdot 71H_2O$ **Q-2.7**

$K_{10.5}Na_{0.3}\{Co_{0.6}(H_2O)_{3.6}\}[Co^{II}_4(H_2O)_2(Co^{III}W_9O_{34})(PW_9O_{34})]\cdot 19.4H_2O$ **Q-2.8**

$K_6\{Co_9(H_2O)_{42}\}[Co_2\{Co_3(H_2O)(Co(OH)_2W_7O_{26})(PW_9O_{34})\}_2]\cdot 26H_2O$ **Q-2.9**

$[(n\text{-}C_4H_9)_4N]_5[Tb(\beta\text{-}Mo_8O_{26})_2]$ **Q-3.1**

$[(n\text{-}C_4H_9)_4N]_5[Dy(\beta\text{-}Mo_8O_{26})_2]$ **Q-3.2**

$[(n\text{-}C_4H_9)_4N]_5[Ho(\beta\text{-}Mo_8O_{26})_2]$ **Q-3.3**

$[(n\text{-}C_4H_9)_4N]_5[Er(\beta\text{-}Mo_8O_{26})_2]$ **Q-3.4**

$[(n\text{-}C_4H_9)_4N]_5[Tm(\beta\text{-}Mo_8O_{26})_2]$ **Q-3.5**

$[(n\text{-}C_4H_9)_4N]_5[Yb(\beta\text{-}Mo_8O_{26})_2]$ **Q-3.6**

$K_{15}\{K\subset[(A\text{-}\alpha\text{-}PW_9O_{34})_2Fe_2(C_2O_4)_2]\}\cdot 29H_2O$ **Q-4.1**

$K_{15}\{K\subset[(A\text{-}\alpha\text{-}PW_9O_{34})_2Fe_2(C_3H_2O_4)_2]\}\cdot 27H_2O$ **Q-4.2**

Chapter 1. General Introduction

Polyoxometalates (POMs) are a well-known group of anionic metal oxide clusters with a large compositional, structural and electronic variety, which are formed in acidic solution via self-assembly of monomeric oxo-anions by condensation of metalate groups. Recently, POMs have acquired a remarkable scientific and technological relevance due to their applicability in various fields such as magnetism,[1-3] nanotechnology, catalysis,[4] material chemistry,[5-7] photochemistry and medicine.[8] In this chapter, a historic overview of POMs is briefly given at the first part, followed by a summary of synthetic strategies and structural descriptions of the more relevant POMs to this work. The chapter is completed with a short description of the general properties and applications of POMs.

1.1. A Historical Overview of POMs

The discovery of POMs dates back to 1783, when the Spanish chemists and mineralogists known as the D'Elhuyar brothers [Juan José D'Elhuyar (Logroño, 1754) and Fausto D'Elhuyar (Logroño, 1755)], discovered a yellow spicy/bitter tasting salt from the reaction of molybdate with phosphate, which is now known as ammonium 12-molybdophosphate $(NH_4)_3[PMo_{12}O_{40}]$ (see **Fig. 1.1**).[9] A quite similar result was reported by Berzelius in 1826.[10] The first systematic study on POMs was made by Marignac in 1862, who prepared and analysed the α- and β-isomers of 12-tungstosilicic acid (labelled initially as 'tungstosilicic acid' and 'silicotungstic acid').[11] Then, in the following sixty years, hundreds of such a kind of compounds were described and thoroughly investigated. In 1928, based on the rules of ionic crystals, Pauling proposed that the structure of 12-tungstate anions was made of a central $[XO_4]$ tetrahedral unit surrounded by twelve corner shared $[MO_6]$ octahedra.[12] Pauling's proposal pushed ahead POM chemistry remarkably. Soon in 1933, with the help of powder X-ray diffraction, Keggin determined the structure of $H_3[PW_{12}O_{40}]\cdot 5H_2O$ (see **Fig. 1.1**), containing four edge-shared triads $[W_3O_{13}]$ units connected to each other via sharing corner. Thus, such a structure was named after Keggin.[13-14] Afterward, a number of reports about isomorphous complexes appeared. No new polyanion structures appeared until 1948, when Evans reported the structure of $[TeMo_6O_{24}]^{6-}$, which had been suggested by Anderson twelve years earlier as a possibility for the 6:1 heteropolyanions and for the para(hepta)molybdate anion $[Mo_7O_{24}]^{6-}$ (see **Fig. 1.1**).[15-16] The different structure of the latter anion was finally reported by Lindqvist in 1950.[17] Since then, more and more techniques were applied to the study of POMs and many other types of polyanions were discovered and reported in the literature. Two important examples are the fundamental structure of Wells-Dawson ion (see **Fig. 1.1**) in 1953[18] and the Preyssler structure (see **Fig. 1.1**) in 1970.[19]

Later on, in the past two decades, the controlled fabrication of giant "nano-sized" clusters, which bridge the gap between "traditional" molecular entities (< 2 nm) and less precisely defined polymeric entities, have been witnessed a great growth. The most well studied species of giant POMs (see **Fig. 1.1**) are the wheel-shaped {Mo154}[20-22], band {Mo176}[23] and the "hedgehog-like" {Mo368}[24] clusters whose size has helped to define the concept of molecular nano-technology.

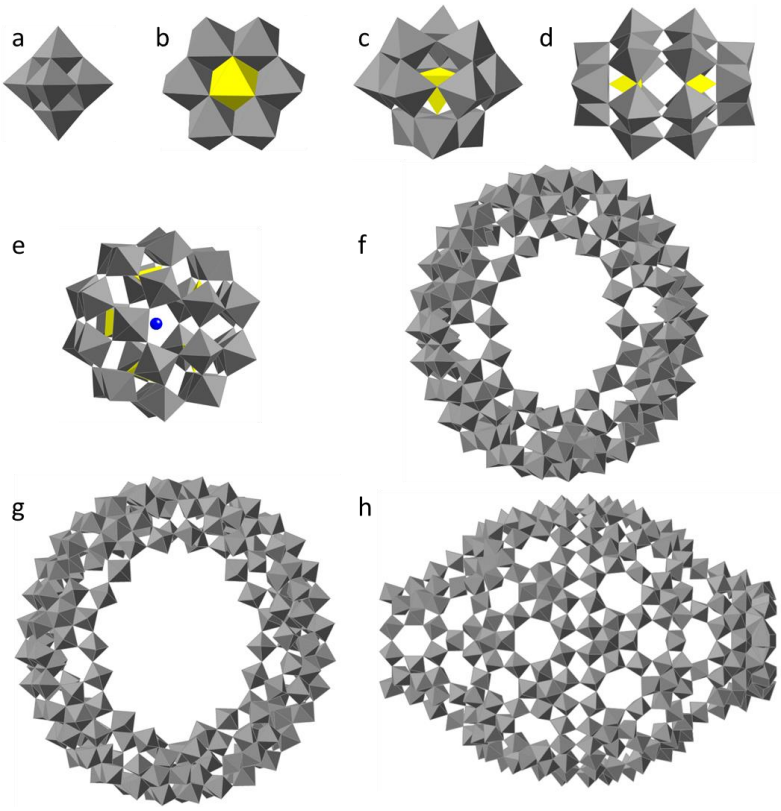

Fig. 1.1.- (a) Lindqvist ($[M_6O_{19}]^{2-}$), (b) Anderson ($[XM_6O_{24}]^{n-}$), (c) Keggin ($[XM_{12}O_{40}]^{n-}$), (d) Dawson ($[X_2M_{18}O_{62}]^{n-}$), (e) Preyssler ($[NaP_5W_{30}O_{110}]^{14-}$), (f) $[Mo_{154}(NO)_{14}O_{448}H_{14}(H_2O)_{70}]^{28-}$ {Mo154}, (g) $[(MoO_3)_{176}(H_2O)_{80}H_{32}]$ {Mo176} and (h) $[H_xMo_{368}O_{1032}(H_2O)_{240}(SO_4)_{48}]_{48}$ {Mo368}.

Countless structures of POMs have been reported in almost half a century, ranging from a domain of a few atoms to nano-size. POM chemistry has undergone a real burst during the last few decades due to the development of modern characterisation techniques such as X-ray single crystal diffraction, nuclear magnetic resonance spectroscopy, mass spectrometry and, also, owing to the promising applications of such types of materials, for example, in catalysis and medicine. According to the web of science, there are more than six hundred scientific publications devoted to POM chemistry in 2016. In the last few years, a large number of reviews have been published addressing different aspects of POM science, including new structures, new synthetic routes, magnetic properties, catalysis, biomedical applications, theoretical calculations, new materials and the design of functional systems.[25-36] More recently, research on POMs is entering in an exciting new phase that is moving from the synthesis and structural characterisation of new cluster systems to the development of functional materials and sophisticated molecular systems.[37-38]

1.2. Synthesis of POMs

In general, the routes to produce POMs usually require a small number of steps (step-by-step approach) or even just one-step (one-pot approach). Depending on the POMs, this can take place either in aqueous or non-aqueous solutions. The reaction conditions are of paramount importance in the synthesis of POMs, in such a way that small variations of pH, ionic strength, concentration of starting materials, type of counterions, presence of other ligands, temperature, pressure and reaction time usually lead to the attainment of different products (see **Fig. 1.2**). Usually, many different POM species coexist in solution and the isolation of a particular species, in its pure form, may require lengthy purification or recrystallization steps.

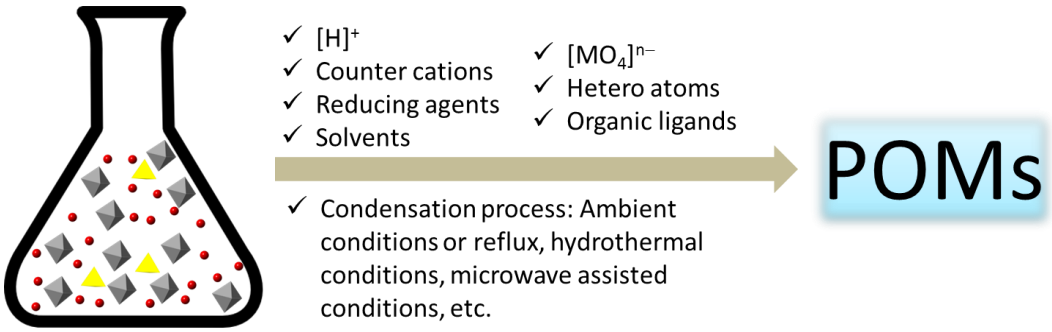

Fig. 1.2.- Parameters that are often adjusted in the synthesis/isolation of new POM clusters. Grey and yellow polyhedra represent constituent metals and heteroatoms, respectively, which self-assemble in acidified solutions to form POMs with different nuclearities.

By far, the most common preparative method involves acidification of aqueous solutions of simple oxoanions of the constituent metals (usually tungsten, molybdenum or vanadium and, less commonly, niobium, chromium or tantalum) and the necessary heteroatoms. During this synthetic procedure, the acidification of the precursor in aqueous solutions will give rise to metal oxide fragments. These fragments act as small building blocks, which are formed by corner-, edge- or face-sharing of polyhedral units, self-assembling to form various polyoxoanions by a condensation process (see **Fig. 1.3**). In many cases, polyoxoanions crystallize as salts from stoichiometrically acidified mixtures of the components at room temperature. However, in some cases, the addition of suitable countercations is important for the crystallization and isolation of the polyoxoanions.

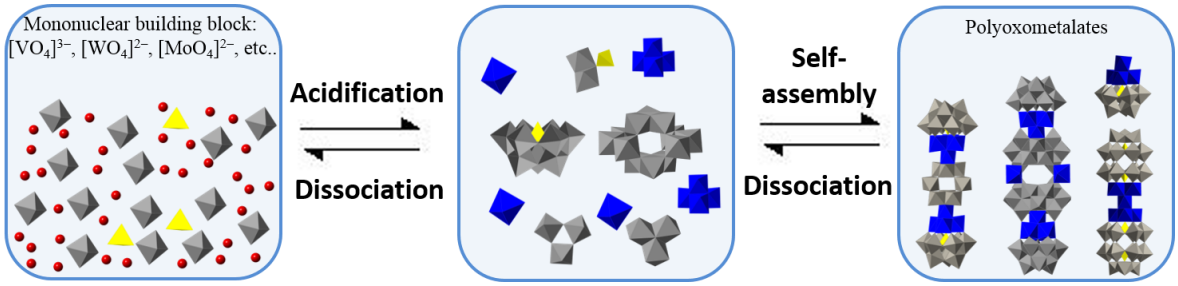

Fig. 1.3.- Scheme highlighting the formation process of POMs from mononuclear building blocks $[MO_4]^{n-}$. The controlled acidification of a solution of $[MO_4]^{n-}$ leads to the formation of discrete structures (POMs).

Compared to the synthesis in aqueous solution, the formation and interconversion of POMs in non-aqueous systems are much less known, although new types of structures and reactivities are accessible in organic solvents. The first systematic preparation of polyoxoanions from organic solutions was carried out by Jahr and Fuchs.[40] Other contributions by Fuchs include the dissolution of metal oxides in organic bases and the precipitation and recrystallization of POM salts from organic solvents.[41] The usual strategy to solubilize POMs in organic solvents consists in the use of organic countercations, particularly quaternary ammonium ions. However, the organic solubility is usually gained at the expense of the crystallinity, as the long chains of tetraalkylammonium cations give rise to substantial disorder in POM crystal structures.[42]

In addition to these traditional synthetic methods, in the last years several new approches and techniques for the preparation of POMs have appeared, such as microwave assisted synthesis, hydrothermal synthesis or the use of 3D-printing and digital technologies to design and manufacture the active reactionware for initiating and monitoring reactions *in situ* as an alternative to the traditional passive-vessel approaches for doing chemistry.[39]

1.3. Structural Description of POMs

POM structures are based on the assembling of [MO_n] ('M' indicates the constituent metal atom and 'n' its coordination number, which can be 4, 5, 6 or 7) polyhedra (commonly octahedra or tetrahedra), connected to each other by one- (corner sharing), two- (edge sharing) or three- (face sharing) oxygen atoms. This section deals with the common POM structures that are related to the content of this work.

POMs can be divided into two different types: isopolyanions and heteropolyanions. The former consists of only one type of addenda atoms and oxygen atoms, while the later contains additional heteroatoms, which can be either from the main group or from the *d*-block. A well-known example of isopolyanion is the so-called hexametalate or Lindqvist anion $[W_6O_{19}]^{2-}$ (see **Fig. 1.4a**), which is made of six edge-shared [WO_6] octahedra, resulting in an overall octahedral assembly. Another relevant example is the octamolybdate anion β-$[Mo_8O_{26}]^{4-}$, which contains eight distorted edge-shared octahedra [MoO_6] (see **Fig. 1.4b**). The most common example of heteropolyanion is the highly symmetrical (T_d) Keggin ion, such as $[PW_{12}O_{40}]^{3-}$ (see **Fig. 1.4c**). This anion is composed of a central, tetrahedral [PO_4] group surrounded by twelve [WO_6] octahedra, which are arranged in four corner shared [W_3O_{13}] triads with each triad being composed of three edge-shared [WO_6] octahedra. Other examples of important heteropolyanions are the Wells-Dawson species $[P_2W_{18}O_{62}]^{6-}$ and the Preyssler anion $[Na(H_2O)P_5W_{30}O_{110}]^{14-}$ (see **Fig. 1.4d**). The former anion contains two [PO_4] hetero groups and a total of 18 addenda atoms. The later is built by five [PW_6] units, which consist of two groups of three corner-shared [WO_6] octahedra (see **Fig. 1.4e**).

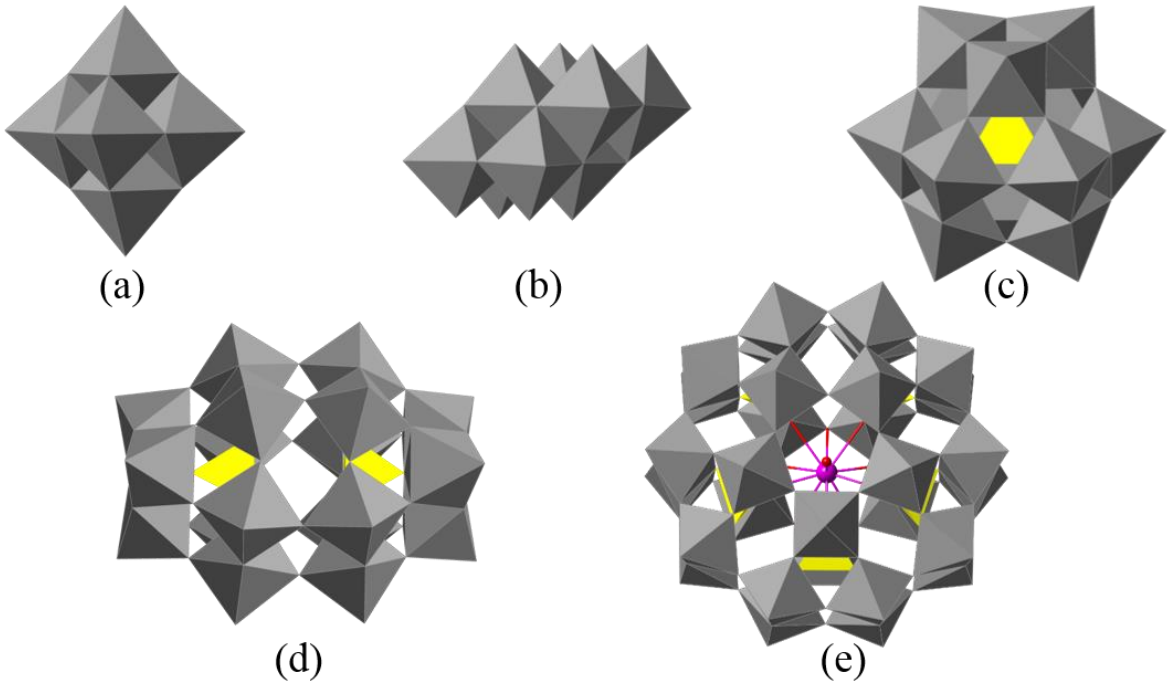

Fig. 1.4.- Polyhedral representations of some isopoly- and heteropolyanions related to this work. (a) Lindqvist anion, (b) octamolybdate anion, (c) Keggin anion, (d) Wells-Dawson anion and (e) Preyssler anion.

Depending on the spatial distribution of the $[MO_x]$ polyhedra, POMs can present multiple isomers. The possible isomerization of the well-known Keggin ion with P(V) as heteroatom is shown below (see **Fig. 1.5**). As mentioned above, the Keggin structure $[PW_{12}O_{40}]^{3-}$ is composed of a tetrahedral heteroatom $[PO_4]$ and each corner of this tetrahedron is associated with a $[W_3O_{13}]$ triad. Baker and Figgis suggested that the Keggin ion can have up to five structural isomers (see **Fig. 1.5**).[43] The parent isomer, with four equivalent triads, is termed as α-Keggin which has an overall T_d symmetry and the other isomers, namely β-, γ-, δ-, and ε-Keggin, are obtained by 60° rotation of one, two, three, and four triads, which have the C_{3v}, C_{2v}, C_{3v} and T_d symmetries, respectively. In general, γ-, δ-, and ε- isomers are less stable than α- and β- isomers. There are two, three and six edge-shared octahedra in γ-, δ- and ε- isomers, individually. The increased coulombic repulsion in the rotated triads and the resultant less favourable $p\pi$-$d\pi$ interactions make all these isomers less stable than the parent α-Keggin isomer.[44-45]

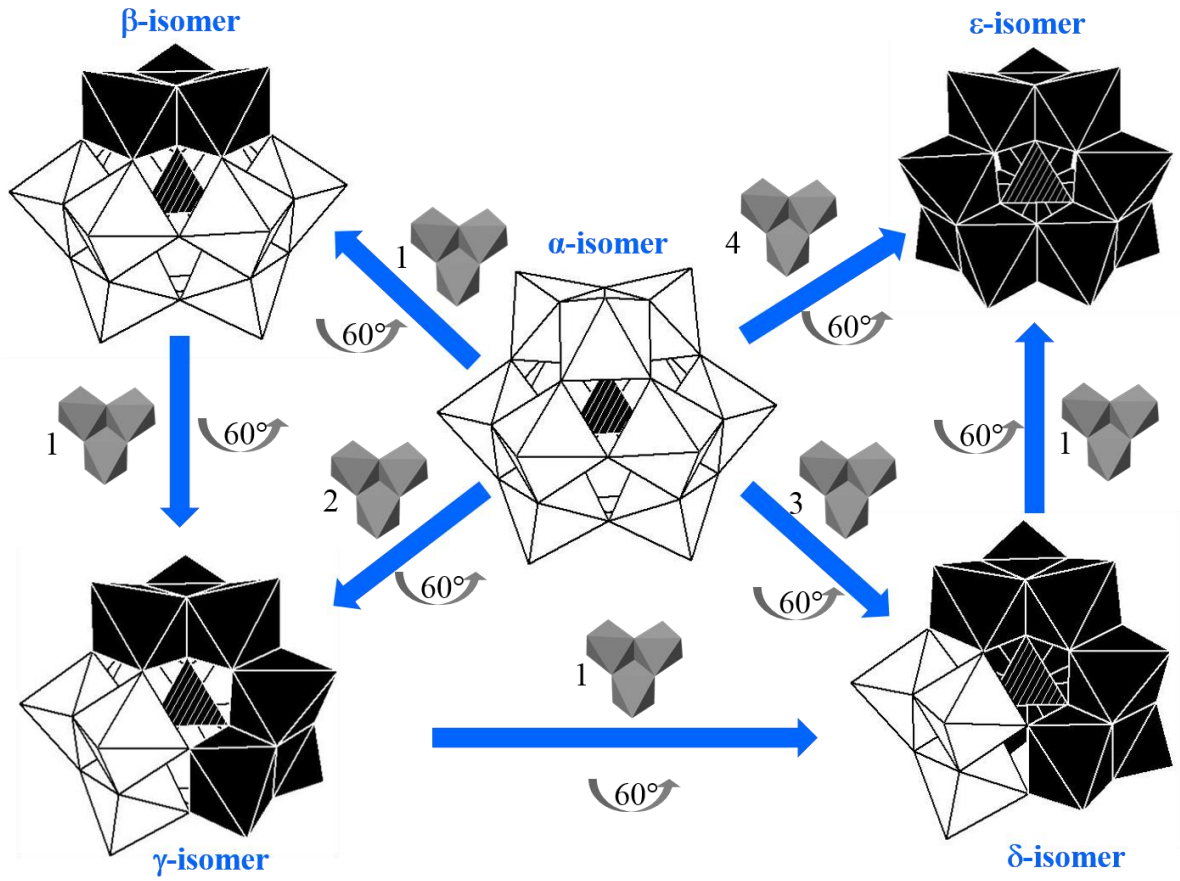

Fig. 1.5.- The five Baker-Figgis isomers of the Keggin polyoxoanion.

Another well studied POM is the Wells-Dawson ion containing P(V) as heteroatom. This POM can be viewed as two trilacunary Keggin units of A-α-$[PW_9O_{34}]^{9-}$ or A-β-$[PW_9O_{34}]^{9-}$ fused together. The α-isomer forms when two A-α units are combined together through all six oxygen atoms of the lacunary sites (see **Fig. 1.6**), whereas the fusion of one A-α and one A-β units generates the β isomer. Finally, linking two A-β produces the γ isomer.[46] In 1970, Baker and Figgis predicted the existence of a total of six possible isomers of the Wells-Dawson ion, named formally as α, β, γ, α*, β*, and γ*.[47] These isomers differ in the relative orientations of the trinuclear $[M_3O_{13}]$ caps and/or the two $[XW_9]$ units. However, only four of these isomers (α, β, γ, and γ*) have actually been experimentally observed.[48-49] Density functional theory calculations have shown that the stability order of these Wells–Dawson isomers is $\alpha > \beta > \gamma > \gamma^* > \beta^* > \alpha^*$.[50]

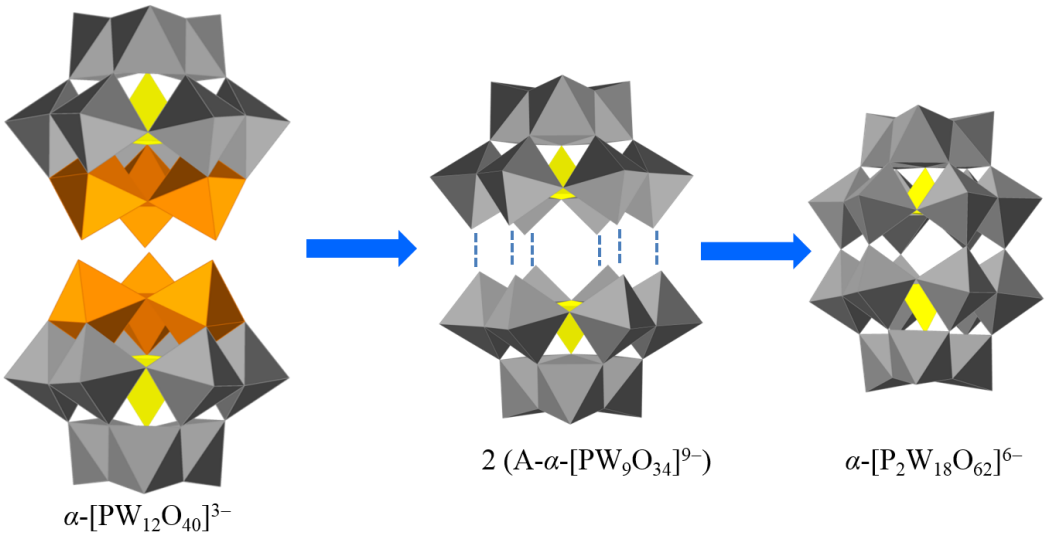

Fig. 1.6.- Building-up process of the *α*-Dawson structure from two A-*α*-Keggin POM units by removal of the orange octahedra. Grey and orange octahedra, [WO_6]; yellow tetrahedra, [PO_4].

Apart from their possible isomerization, POM structures can be chemically modified by the hydrolytic cleavage of the M-O bond under basic conditions to form the so-called lacunary or defect species. These species play very important roles in POM chemistry due to the ability to act as inorganic rigid chelating ligands that can encapsulate transition metal ions of the *d*- or *f*-block. In addition, these species can be assembled among themselves (or with others) to form new species.[51] In the following paragraphs, the lacunary POM structures that have been used in this thesis will be introduced and discussed. These are the lacunary species derived from the Keggin, Wells-Dawson, and Lindqvist ions.

The plenary Keggin ions are stabilized in solution under acidic conditions. By careful basification, the removal of one or more octahedral units can be afforded, forming lacunary species. Regarding trilacunary Keggin species, two isomeric structures, namely A-type and B-type, can be obtained. The former is obtained when corner shared octahedra are removed, and the later when an edge shared triad is eliminated (see **Fig. 1.7**).[52-53]

Regarding the Wells-Dawson ion, only the *α*-isomer produces stable lacunary species. The two monolacunary species α_1-$[P_2W_{17}O_{61}]^{10-}$ and α_2-$[P_2W_{17}O_{61}]^{10-}$ are obtained when one octahedron is lost from the belt or from the cap respectively. Trilacunary $[P_2W_{15}O_{56}]^{12-}$ and hexalacunary $[H_2P_2W_{12}O_{48}]^{12-}$ can also be produced by using bases of different strengths (see **Fig. 1.8**).[54]

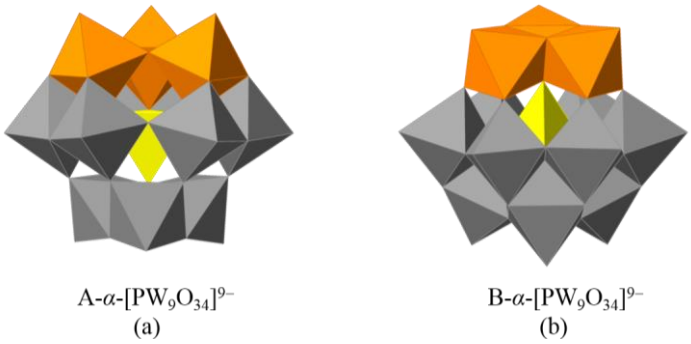

A-α-$[PW_9O_{34}]^{9-}$ (a) B-α-$[PW_9O_{34}]^{9-}$ (b)

Fig. 1.7.- Polyhedral presentations of the A-type (a) and B-type (b) trilacunary species derived from the α-$[PW_{12}O_{40}]^{3-}$ Keggin heteropolyanion (orange triads represent the corner or edge shared octahedra that must be removed to obtain the relevant trilacunary isomer). Grey and orange octahedra, $[WO_6]$; yellow tetrahedra, $[PO_4]$.

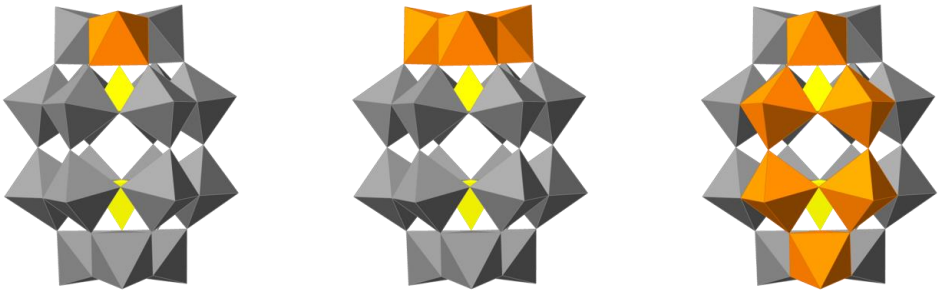

α_1-$[P_2W_{17}O_{61}]^{10-}$ (a) α-$[P_2W_{15}O_{56}]^{12-}$ (b) α-$[H_2P_2W_{12}O_{48}]^{12-}$ (c)

Fig. 1.8.- Polyhedral representations of the accessible lacunary derivatives of the Wells–Dawson polyanions (orange octahedra must be removed to obtain the relevant lacunary isomer). (a) The "mono-lacunary" α_1-$[P_2W_{17}O_{61}]^{10-}$ isomer, (b) the "tri-lacunary" α-$[P_2W_{15}O_{56}]^{12-}$ isomer and (c) the "hexa-lacunary" α-$[H_2P_2W_{12}O_{48}]^{12-}$ isomer. Grey and orange octahedra, $[WO_6]$; yellow tetrahedra, $[PO_4]$.

One more lacunary example relevant to this thesis is the $[W_5O_{18}]^{6-}$ unit, which can be viewed as a monovacant Lindqvist anion. It is derived from the Lindqvist anion $[W_6O_{19}]^{2-}$ by removal of one W=O group (see **Fig. 1.9**).

Fig. 1.9.- Polyhedral representation of the mono-lacunary Lindqvist (orange octahedra must be removed to obtain the relevant lacunary isomer). Grey and orange octahedra, $[WO_6]$.

1.4. General Properties and Applications of POMs

As a subset of metal oxides, POMs are usually air and solvent stable structures with very high molecular weight. They usually have low lattice and solvation energies.[55] The solubility of POMs is mainly determined by the countercations. When the countercation is hydrophilic, for example, H^+, Na^+, K^+, *etc.*, they are usually water soluble; while lipophilic countercations, such as tetraalkylammonium, favour the solubility in non-aqueous media.[56]

Some POMs are able to maintain their structures in solution in a wide pH range, while others are only stable in a narrow pH range. For example, the well-known Keggin POM $[PW_{12}O_{40}]^{3-}$ is stable at pH values lower than 1.5, while the monolacunary species $[PW_{11}O_{39}]^{7-}$ exists in the pH range 2.5-7.0. Further degradation to other lacunary species occurs by increasing the pH, until the free phosphate ion is obtained.[57-58]

POMs are also well-known as "electron reservoirs", due to their high ability to accept electrons without a major change in their structure. They can accept various numbers of electrons leading to mixed-valence systems in which the extra electrons are extensively delocalized over the whole POM framework. In aqueous solution, the additional negative charge is accompanied by protonation and therefore reductions are mostly pH-dependent. Reduced mixed-valence POM species usually show very deep blue colour (a typical example is the two-electron reduced species $[PMo_{12}O_{40}]^{5-}$). For this reason, reduced POMs are called "heteropolyblues".

Taking into account the unmatched range of physical and chemical properties of POMs, large domains of applications can be imagined in various fields, such as catalysis, magnetism, bio- and nanotechnology, medicine and materials science. In the following part, some of the interesting applications that are related to this work will be discussed.

1.4.1. POM-based Photo-Responsive Materials

In the last decades, the study of molecular-based stimuli-responsive materials whose physical or chemical properties can be tuned by applying external stimuli have attracted considerable interest in chemistry due to their potential applications in many fields, such as microelectronics, optics or sensing.[59-61] Among all these materials, photo-responsive materials have been extensively studied due to their capability to reversibly switch with

light between two states having different optical properties. Many examples of photo-magnetic materials,[62] photo-chromic materials[63] and electro-chromic materials[64] have been reported. However, in the following, we are going to focus on the POM-based photochromic systems due to the relation with the present work.

Hybrid organic-inorganic materials based on POMs and organoammonium/sulfonium cations are very promising in the field of photo-responsive materials because they show remarkable and highly tunable photochromism and bleaching rates.[26,65-68] The photochromism mechanism of this type of POM-based materials has been studied in detail, being due to the UV-induced photoreduction of the POM concomitant with electron transfers at the organic-inorganic interface from the organic moiety toward the POM. An interesting approach to obtain such a type of materials can also be achieved by combination of POMs with organic moieties showing photochromic effect, such as spiropyrans (see **Fig. 1.10**), which can reversibly switch between two states with different absorption spectra upon light irradiation.[69]

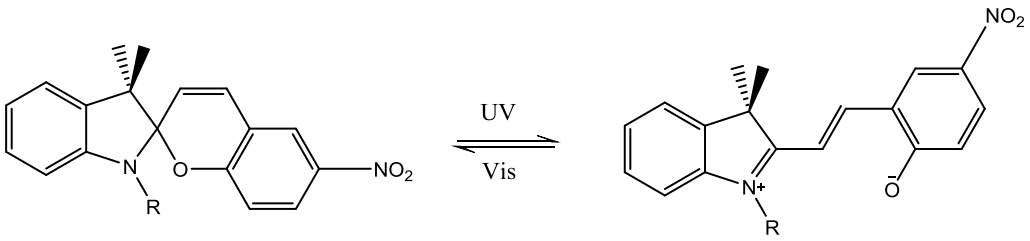

Fig. 1.10.- Schemes of the equilibrium between the two forms of spiropyrans.

1.4.2. POMs as Magnetic Model Systems

In 1998, Coronado *et al.* pointed out that POMs can be used as model objects in molecular magnetism or magnetic components of hybrid molecular materials.[25] The reasons for this derive from the diverse range of structural and electronic properties of POMs. As supporting ligands, they provide well-defined, rigid coordination environments, which can restrain the alignment of spin centers and regulate intramolecular exchange coupling. Thus, they can facilitate target design of magnetic core structures. POM ligands have also been found to induce strong axial magnetic anisotropy, illustrated by a Mn(II)–POM complex.[70] An additional advantage of POMs as ligands in molecular magnetism stems from their diamagnetic structures which can encapsulate paramagnetic metal ions that become well separated from each other leading to an ideal magnetic insulation. This feature was first exploited to check the validity of the exchange

Hamiltonians in magnetic clusters of increasing nuclearities,[28,33] to study the interplay between magnetic exchange and electron transfer in mixed-valence POMs[71-77] and, more recently, to obtain POM-based single-molecule magnets (SMMs) based either on 3*d* or 4*f* metal ions.[2,33,78-101] Due to all the properties mentioned above, POMs have great potential for the discovery and design of new molecular magnetic materials.[33]

In this context, Coronado's group has been interested for a long time in the following three families of magnetic POMs:

1) POMs encapsulating magnetic clusters (with variable nuclearities and high symmetries) of transition metal ions connected through oxo bridges, enabling the magnetic exchange interactions between the metal (mainly cobalt) ions.[102]
2) POMs encapsulating lanthanoid ions, which together with the first family, provide examples of single-molecule magnets.
3) Mixed-valence POMs, which host a number of electrons throughout the whole POM framework usually by hopping.

In the following sections, we will give a brief description of the current state of the art in these subtopics.

1.4.2.1. Cobalt clusters encapsulated in POMs

The series of cobalt-containing POMs is one of the most extended and studied systems in POM chemistry since Baker reported the first examples in 1956.[103] **Table 1.1** contains a literature survey of the cobalt clusters incorporated in polyoxotungstates and **Fig. 1.11** shows their polyhedral representations. It can be seen that, from two to sixteen, almost all cobalt nuclearities have been achieved. All these clusters represent an excellent opportunity to conduct detailed studies on the magnetic exchange interactions in Co(II) clusters. When octahedrally coordinated by the weak ligand field created by POMs, this d^7 ion shows a high spin S = 3/2 with an unquenched orbital momentum. However, the first order spin-orbit coupling, together with the octahedral distortion, result in an extensive splitting of the ${}^4T_{2g}$ ground term leading to an effective ground spin doublet (S = 1/2), which exhibits a large anisotropy.[104] In the past, Coronado´s group studied in detail the anisotropic nature of the exchange interactions in Co(II) clusters with different topologies and nuclearities encapsulated in POMs. The most significant results were: i) the first direct evidence for Co(II)–Co(II) exchange anisotropy in the ferromagnetically-coupled POM $[Co_4(H_2O)_2(PW_9O_{34})_2]^{10-}$, which encapsulates the tetra-nuclear rhomb-like

Table 1.1.- List of polyoxotungstates incorporating cobalt clusters.

Polyhedral representation [a]	Polyanion	Co^{n+} [b]	Reference
a	$[Co^{II}(H_2O)(Co^{II}W_{11}O_{39})]^{8-}$ $[Co^{II}(H_2O)(Co^{III}W_{11}O_{39})]^{7-}$	2	103
b	$[Na_2Co^{II}_2(PW_9O_{34})_2]^{12-}$	2	111
	$[(NaOH_2)_2Co^{II}_2(P_2W_{15}O_{56})_2]^{18-}$		112
	$[\{Co^{III}(en)(OH)_2Co^{III}(en)\}\{PW_{10}O_{37}Co^{III}(en)\}_2]^{8-}$		113
	$[\{Co^{II}W_5O_{18}H\}_2]^{6-}$		114
	$[(P_4W_6O_{34})_2Co^{II}_2Na_2(H_2O)_2]^{18-}$		115
	$[Co^{II}_2(P_2W_{15}O_{56})_2]^{20-}$		116
	$[\{Co^{II}(H_2O)_2(OH)\}_2\{Zn(H_2O)\}_2\{HSiW_{10}O_{36}\}_2]^{8-}$		117
c	$[(NaOH_2)Co^{II}_3(H_2O)(P_2W_{15}O_{56})_2]^{17-}$	3	108, 112
	$[\{Co^{II}_3(SiW_9O_{33}(OH))(SiW_8O_{29}(OH)_2)\}_2]^{22-}$		118
	$[Co^{II}_6(H_2O)_2(PW_9O_{34})_2(PW_6O_{26})]^{17-}$		119, 120
	$[\{(SiW_9O_{33}(OH))(SiW_8O_{29}(OH)_2)Co^{II}_3(H_2O)\}_2Co^{II}(H_2O)_2]^{20-}$		121
	$[(SiW_{10}O_{36})(SiW_8O_{30}(OH))Co^{II}_4(OH)(H_2O)_7]^{10-}$		121
	$[(Co^{II}(H_2O)Co^{II}_2VW_9O_{34})_2(VW_6O_{26})]^{17-}$		122
d	$[Co^{II}_3W(H_2O)_2(GeW_9O_{34})_2]^{8-}$	3	123
	$[WCo^{II}_3(D_2O)_2(ZnW_9O_{34})_2]^{12-}$		107
e	$[Co^{II}_4(H_2O)_2(PW_9O_{34})_2]^{10-}$	4	106, 124-130
	$[Co^{II}_4(H_2O)_2(SiW_9O_{34})_2]^{12-}$		131-133
	$[Co^{II}_4(H_2O)_2(GeW_9O_{34})_2]^{12-}$		123, 132, 134
	$[Co^{II}_4(Hen)_2(SiW_9O_{34})_2]^{10-}$		135
	$[Co^{II}_4(Hen)_2(GeW_9O_{34})_2]^{10-}$		136
	$[Co^{II}_4(Hdap)_2(HGeW_9O_{34})_2]^{8-}$		137
	$[Co^{II}_4(Hdap)_2(PW_9O_{34})_2]^{8-}$		138
	$[Co^{II}_4(H_2O)_2(P_2W_{15}O_{56})_2]^{16-}$		125
	$[Co^{II}_4(H_2O)_2(As_2W_{15}O_{56})_2]^{16-}$		139, 140
	$[\{Co^{II}(H_2O)\}_2(OH)_2\{Co^{II}(H_2O)_2\}_2(H_2SiW_{10}O_{36})_2]^{6-}$		141
	$[Co^{II}_4(H_2O)_2(VW_9O_{34})_2]^{10-}$		142
f	$[\{SiCo^{II}_2W_{10}O_{36}(OH)_2(H_2O)\}_2]^{12-}$	4	143
g	$[(SiW_9O_{34})Co^{II}_4(OH)L_2(CH_3COO)_3]^{8-}$ (L = OH^-, N_3^-)	4	121
h	$[(SiW_9O_{34})Co^{II}_4(OH)_2(H_2O)_3(\beta\text{-alanine})_2]^{4-}$	4	144
i[c]	$[\{Co^{II}_4(OH)(H_2O)_3\}(Si_2W_{19}O_{70})]^{11-}$	4	145
j	$[Co^{II}_3W(L)_2(Co^{II}W_9O_{34})_2]^{12-}$ (L = H_2O, D_2O)	5	146, 147
k	$[Co^{II}_2Co^{III}_4(OH)_5(H_2O)_2(CH_3CO_2)(Si_2W_{18}O_{66})]^{6-}$	6	148
l	$[Co^{II}_6(OH)_3(H_2O)_9(L)(PW_9O_{34})]$ (L = 4,4'-bis(1,2,4-triazol-ylmethyl)biphenyl)	6	149
m	$[\{(PW_9O_{34})Co^{II}_3(OH)(H_2O)_2(Ale)\}_2Co^{II}]^{14-}$ (H_5Ale = alendronic acid)	7	88
n	$[Co^{II}_7(H_2O)_2(OH)_2P_2W_{25}O_{94}]^{16-}$	7	110
o	$[(SiW_9O_{34})_2Co^{II}_8(OH)_6(H_2O)_2(CO_3)_3]^{16-}$	8	121
p	$[Co^{II}_9(OH)_3(H_2O)_6(HPO_4)_2(PW_9O_{34})_3]^{16-}$	9	109, 130, 150,
	$[Co^{II}_9(OH)_3(H_2O)_6(HPO_4)_2(P_2W_{15}O_{56})_3]^{25-}$		151, 93
q	$[Co^{II}_9Cl_2(OH)_3(H_2O)_9(SiW_8O_{31})_3]^{17-}$	9	152
r	$[Co_{14}P_{10}W_{60}O_{232}(OH)_9(H_2O)_6]^{35-}$	14	93
s	$[\{Co^{II}_4(OH)_3PO_4\}_4(PW_9O_{34})_4]^{28-}$	16	153, 154
	$[\{Co^{II}_4(OH)_3PO_4\}_4(SiW_9O_{34})_4]^{32-}$		154
	$[\{Co^{II}_4(OH)_3PO_4\}_4(GeW_9O_{34})_4]^{32-}$		154
	$[\{Co^{II}_4(OH)_3PO_4\}_4(AsW_9O_{34})_4]^{28-}$		154
t	$[Co^{II}_4(OH)_3(H_2O)_6(PW_9O_{34})]^{4-}$	4	155
u	$[Co^{II}_6Co^{III}(OH)_6(H_2O)_6(PW_9O_{34})_2]^{9-}$	7	
	$[Co^{II}_6Co^{III}(OH)_6(H_2O)_4(PW_9O_{34})_2]_n^{9n-}$		155
	$[Co^{II}_6Co^{III}(OH)_6(H_2O)_6(P_2W_{15}O_{56})_2]^{15-}$		156
	$[\{Co^{II}_7As^{III}_6O_9(OH)_6\}(A\text{-}\alpha\text{-}SiW_9O_{34})_2]^{12-}$		

[a.] Refers to the representations shown in **Fig. 1.11**.

[b.] The number of Co^{n+} ions incorporated in the POM structure.

[c.] It contains a tetranuclear cobalt cluster disordered with two different arrangements (see **Fig. 1.11i**).

en = ethylenediamine; dap = 1,2-diaminopropane

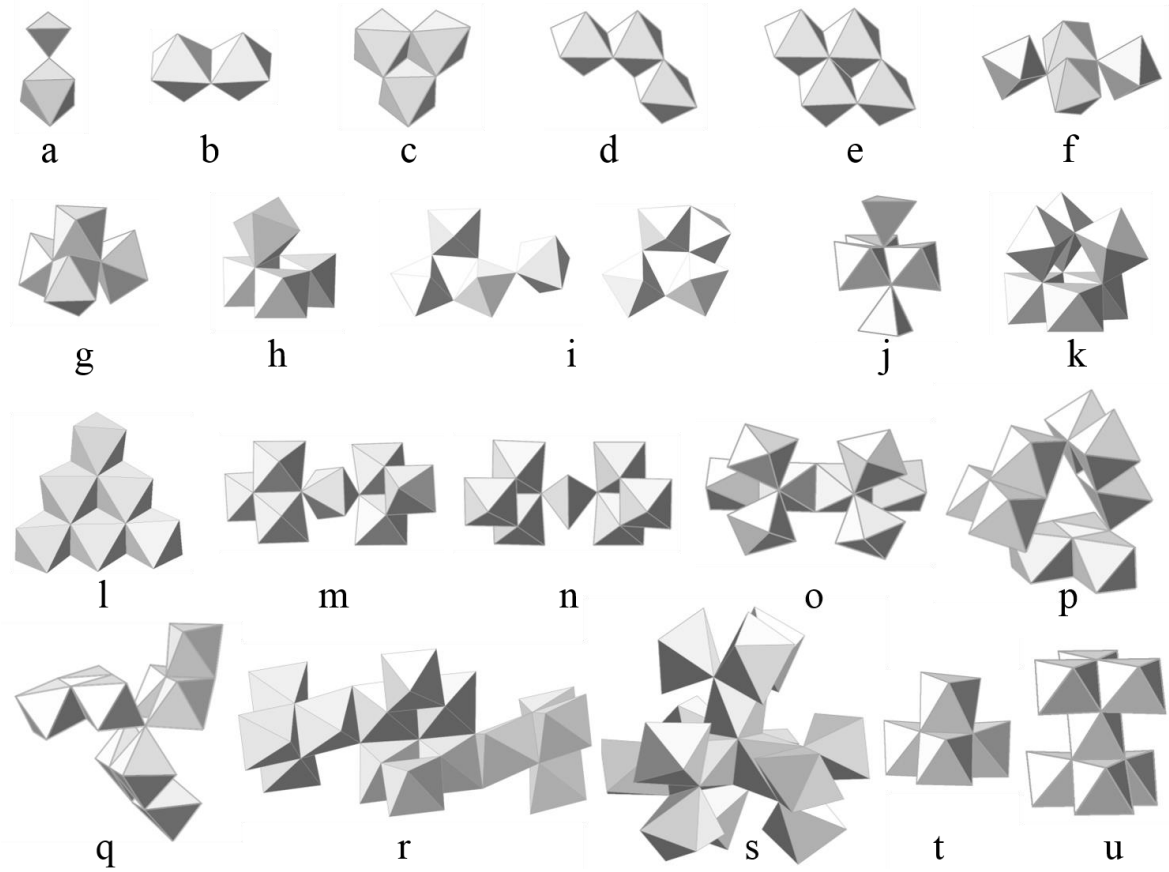

Fig. 1.11.- (a-u) Polyhedral representations of the previously reported cobalt clusters incorporated in polyoxotungstates. (t, u) Cubane and dicubane topologies reported in this thesis. The POM formulas and nuclearities of these clusters can be found in **Table 1.1**.

Co(II) cluster depicted in **Fig. 1.11e**, using Inelastic Neutron Scattering (INS),[105-106] and ii) the effect of the relative orientation of the exchange anisotropy axes in two closely related trinuclear Co(II) clusters (**Fig. 1.11c** and **Fig. 1.11d**) encapsulated in $[(NaOH_2)Co_3(H_2O)(P_2W_{15}O_{56})_2]^{17-}$ and $[Co_3W(H_2O)(ZnW_9O_{34})_2]^{12-}$ respectively.[107-108] In addition, Coronado *et. al* also reported higher nuclearity clusters formed by 7 or 9 Co(II) centers showing the coexistence of ferromagnetic and antiferromagnetic interactions as a consequence of the topologies depicted in **Fig. 1.11n** and **Fig. 1.11p**.[109-110]

According to the research survey in **Table 1.1**, during the last decade a large number of cobalt-containing POMs have been reported. Despite the vast number of cobalt-containing clusters now known and the new structures continuously being discovered, several challenges remain such as the control of the self-assembly process for the formation of structurally different clusters and the understanding of the magnetic interactions within the clusters.

1.4.2.2. Lanthanoid-Containing POMs

Among the multitude of POM structural motifs, the lanthanoid-containing POMs have been attracting increasing attention because they offer particularly interesting features, such as photoluminescence, catalytic, electrochemical and magnetic properties.[157-166] Lanthanoid-containing POMs have been less investigated than those containing 3*d*-transition metal ions. This is mainly due to the larger sizes of the lanthanoid ions compared to 3*d* metal ions, not being fully incorporated into the lacunary site(s) of vacant POM precursors. On the other hand, due to their higher coordination numbers, lanthanoid ions can be used as linkers between one or more lacunary POM units.

The area of lanthanoid-containing POMs is dominated by tungsten-based POMs, as a large number of vacant (lacunary) polyoxotungstate precursors are known (as opposed to vanadium or molybdenum based POM precursors). The first family of lanthanoid-containing isopolyanions was reported in 1971 by Peacock and Weakley: the decatungstate, sandwich-type polyanion with the general formula $[Ln(W_5O_{18})_2]^{9-}$ (Ln^{3+} = La, Ce, Pr, Nd, Sm, Ho, Yb and Y, and for Ce^{4+}).[168] This family of polyanions was obtained by reaction of the lanthanoid ions with Na_2WO_4 in hot aqueous (pH 6.5−7.5) solution.[169] The structure of the $[Ln(W_5O_{18})_2]^{9-}$ polyanions (D_{4d}) consists of two monolacunary, Lindqvist based fragments $[W_5O_{18}]^{6-}$ encapsulating a central metal ion exhibiting a square antiprismatic coordination (see **Fig. 1.12c**).

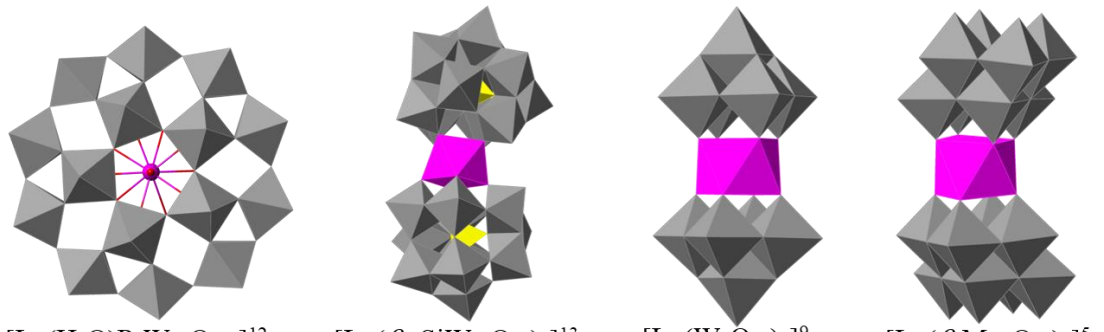

Fig. 1.12.- Polyhedral and ball-and-stick representations of POM-based SMMs. (a) $[Ln(H_2O)P_5W_{30}O_{110}]^{12-}$ polyanion, (b) $[Ln(\beta_2\text{-}SiW_{11}O_{39})_2]^{13-}$ polyanion, (c) $[Ln(W_5O_{18})_2]^{9-}$ polyanion and (d) $[Ln(\beta\text{-}Mo_8O_{26})_2]^{5-}$polyanion. Grey octahedra, $[WO_6]$ or $[MoO_6]$; pink polyhedral and shphere, Ln; yellow tetrahedra, $[PO_4]$.

Our group has long been studying the magnetic behaviour of lanthanoid-containing POMs. **Fig. 1.12** shows some examples of mono-lanthanoid containing POMs that were published by our group recently. They are assembled from Preyssler polyanion or lacunary polyoxoanion ligands with one metal atom, starting from simple salts of 4*f* ions as precursors.[79,81,98]

A review presenting the structural chemistry, properties, and applications of POMs incorporating one or more lanthanoid ions was reported by Pope in 2007.[167]

1.4.2.3. Mixed-Valence POMs

As mentioned before, POMs can act as electron sponges being able to host a variable number of electrons. The coexistence of localized electronic spins (on single metal ions) and delocalized electrons over a larger part of the molecule, can give rise to a variety of interesting behaviours. In particular, the effective magnetic exchange between the magnetic ions can, in principle, be tuned by the delocalized electrons. This kind of magnetic control can be achieved by electrical gating in a single-molecule setup or by chemical control at the synthetic level.

The following three electronic processes are usually present in most of the POM-based high nuclearity mixed-valence systems: i) magnetic superexchange, when two spins occupy neighbouring sites, favoring the magnetic coupling (either ferromagnetic or antiferromagnetic) between them; ii) electron transfer between the adjacent "occupied" and "empty" sites (usually meaning two metals with different oxidation states) and iii) coulombic repulsion between every pair of "blue" electrons which tends to place the electrons apart and distribute them uniformly.

One well studied example of the mixed-valence POMs is the two-electron reduced Keggin anion $[PW_{12}O_{40}]^{5-}$ (see **Fig. 1.13a**). Borrás-Almenar *et al.* have demonstrated that the large spin-triplet gap originates from the interplay between coulombic repulsion and electron transfer.[71-73] Another two electron reduced example is found in $[GeV_{14}O_{40}]^{8-}$ (see **Fig. 1.13b**),[170-171] which, in contrast to the two-electron-reduced Keggin anion, does not show any magnetic coupling between the two unpaired electrons. The main reason of this apparently anomalous behaviour comes from the poor electron transfer between the two $[V_5O_{14}]$ square pyramids and the high orbital energy of the central square $[GeV_4O_{12}]$. In view of the electronic versatility of this system, further studies have been carried out both theoretically and experimentally, in particular, to study the effect of an external electric

field on the spin coupling.[75,172] In addition, the system originally obtained by R. J. Errington[174] $[PMo_{12}O_{40}(VO)_2]^{q-}$ (see **Fig. 1.13c**), which has two $(VO)^{2+}$ units capped at opposite tetragonal site of the Keggin anion and host a spin S = 1/2, has been proposed to be used as a molecular quantum gate between two spin qubits.[173]

Mixed-valence POMs can provide great examples of magnetic molecules. Thus, the control of the spin-spin coupling might be possible via an external stimulus. The rational design and synthesis of such kind of new materials, as well as the theoretical understanding of their behaviour is crucial in POM chemistry.

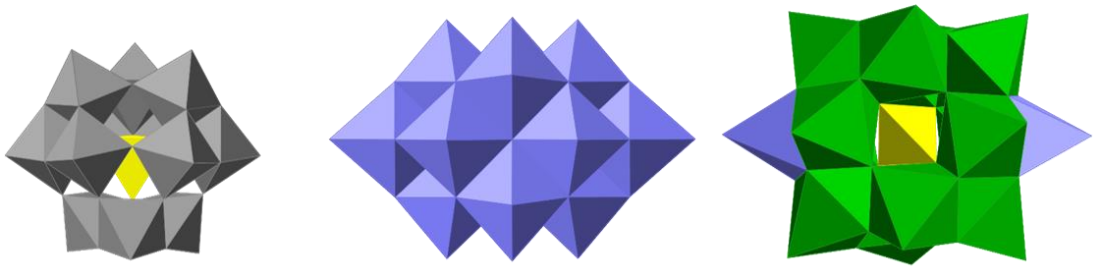

Fig. 1.13.- Polyhedral representations of some mixed-valence POMs. (a) $[PW_{12}O_{40}]^{5-}$ polyanion, (b) $[GeV_{14}O_{40}]^{8-}$ polyanion and (c) $[PMo_{12}O_{40}(VO)_2]^{q-}$ polyanion. Grey octahedra, $[WO_6]$; violet octahedra, $[VO_6]$; green octahedra, $[MoO_6]$; yellow tetrahedra, $[PO_4]$.

1.5. References

[1] T. Yamase and M. Pope, *Polyoxometalate Chemistry for Nano-Composite Design*, 2002.

[2] J. Compain, P. Mialane, A. Dolbecq, I. M. Mbomekallé, J. Marrot, F. Sécheresse, E. Rivière, G. Rogez and W. Wernsdorfer, *Angew. Chem. Int. Ed.*, 2009, **48**, 3077-3081.

[3] E. Coronado, C. Giménez-Saiz and C. J. Gómez-García, *Coord. Chem. Rev.*, 2005, **249**, 1776-1796.

[4] N. Mizuno, K. Yamaguchi and K. Kamata, *Coord. Chem. Rev.*, 2005, **249**, 1944-1956.

[5] C. Streb, T. McGlone, O. Brucher, D. Long and L. Cronin, *Chem. Eur. J.*, 2008, **14**, 8861-8868.

[6] C. Streb, R. Tsunashima, D. A. MacLaren, T. McGlone, T. Akutagawa, T. Nakamura, A. Scandurra, B. Pignataro, N. Gadegaard and L. Cronin, *Angew. Chem. Int. Ed.*, 2009, **48**, 6490-6493.

[7] J. Thiel, C. Ritchie, H. N. Miras, C. Streb, S. G. Mitchell, T. Boyd, M. N. C. Ochoa, M. H. Rosnes, J. McIvet, D. Long and L. Cronin, *Angew. Chem. Int. Ed.*, 2010, **49**, 6984-6988.

[8] J. T. Rhule, C. L. Hill and D. A. Judd, *Chem. Rev.*, 1998, **98**, 327-357.

[9] De Luyart Lubice, J. J.; De Luyar Lubice, F. C. *Extractos de las Juntas Generales celebradas por la Real Sociedad Bascongada*. 1783, **46**.

[10] J. J. Berzelius, *Poggend. Ann. Phys. Chem.*, 1826, **6**, 369-392.

[11] C. Marignac, *Ann. Chim.*, 1862, **25**, 362.

[12] L. Pauling, *J. Am. Chem. Soc.*, 1929, **51**, 2868-2880.

[13] A. H. Rosenthal, *Nature*, 1933, **132**, 350-351.

[14] J. F. Keggin, *Proceedings of the Royal Society of London Series A-Containing Papers of a Mathematical and Physical Character*, 1934, **144**, 0075-0100.

[15] J. S. Anderson, *Nature*, 1937, **140**, 850-850.

[16] H. T. Evans, *J. Am. Chem. Soc.*, 1948, **70**, 1291-1292.

[17] I. Lindqvist, *Arkiv. Kemi.*, 1950, **2**, 325.

[18] B. Dawson, *Acta Crystallogr.*, 1953, **6**, 113-126.

[19] C. Preyssler, *Bull. Soc. Chim. Fr.*, 1970, **30**.

[20] J. Yan, J. Gao, D. Long, H. N. Miras and L. Cronin, *J. Am. Chem. Soc.*, 2010, **132**, 11410-11411.

[21] A. H. Ismail, B. S. Bassil, G. H. Yassin, B. Keita and U. Kortz, *Chem. Eur. J.*, 2012, **18**, 6163-6166.

[22] H. Zang, H. N. Miras, D. Long, B. Rausch and L. Cronin, *Angew. Chem. Int. Ed.*, 2013, **52**, 6903-6906.

[23] A. Müller, Syed Q. N. Shah, H. Bögge and M. Schmidtmann, *Nature*, 1999, **397**, 48−50.

[24] A. Müller, E. Beckmann, H. Bögge, M. Schmidtmann and A. Dress, *Angew. Chem. Int. Ed.*, 2002, **41**, 1162-1167.

[25] E. Coronado and C. J. Gómez-García, *Chem. Rev.*, 1998, **98**, 273-296.

[26] T. Yamase, *Chem. Rev.*, 1998, **98**, 307-325.

[27] A. Müller, F. Peters, M. T. Pope and D. Gatteschi, *Chem. Rev.*, 1998, **98**, 239-271.

[28] J. M. Clemente-Juan and E. Coronado, *Coord. Chem. Rev.*, 1999, **193-5**, 361-394.

[29] D. Long, E. Burkholder and L. Cronin, *Chem. Soc. Rev.*, 2007, **36**, 105-121.

[30] D. Long, R. Tsunashima and L. Cronin, *Angew. Chem. Int. Ed.*, 2010, **49**, 1736-1758.

[31] S. Zheng and G. Yang, *Chem. Soc. Rev.*, 2012, **41**, 7623-7646.

[32] H. N. Miras, J. Yan, D. Long and L. Cronin, *Chem. Soc. Rev.*, 2012, **41**, 7403-7430.

[33] J. M. Clemente-Juan, E. Coronado and A. Gaita-Ariño, *Chem. Soc. Rev.*, 2012, **41**, 7464-7478.

[34] X. López, J. J. Carbó, C. Bo and J. M. Poblet, *Chem. Soc. Rev.*, 2012, **41**, 7537-7571.

[35] Y. Song and R. Tsunashima, *Chem. Soc. Rev.*, 2012, **41**, 7384-7402.

[36] A. Sartorel, M. Bonchio, S. Campagna and F. Scandola, *Chem. Soc. Rev.*, 2013, **42**, 2262-2280.

[37] S. Omwoma, W. Chen, R. Tsunashima and Y. Song, *Coord. Chem. Rev.*, 2014, **258**, 58-71.
[38] W. He, S. Li, H. Zang, G. Yang, S. Zhang, Z. Su and Y. Lan, *Coord. Chem. Rev.*, 2014, **279**, 141-160.
[39] M. D. Symes, P. J. Kitson, J. Yan, C. J. Richmond, G. J. T. Cooper, R. W. Bowman, T. Vilbrandt and L. Cronin, *Nature Chemistry*, 2012, **4**, 349-354.
[40] K. F. Jahr and J. Fuchs, *Chem. Ber.*, 1963, **96**, 2457.
[41] K. F. Jahr, J. Fuchs and R. Oherhauser, 1968, **101**.
[42] R. J. Errington, *Polyoxometalate Molecular Science*, 2003, **98**, 55-78.
[43] L. C. W. Baker and J. S. Figgis, *J. Am. Chem. Soc.*, 1970, **92**, 3794-&.
[44] L. D. Kepert, *The Early Transition Elements; Academic Press: New York, 1972*, 1972.
[45] M. T. Pope, *Inorg. Chem.*, 1976, **15**, 2008-2010.
[46] J. Canny, A. Teze, R. Thouvenot and G. Herve, *Inorg. Chem.*, 1986, **25**, 2114-2119.
[47] S. T. Nguyen, L. K. Johnson, R. H. Grubbs and J. W. Ziller, *J. Am. Chem. Soc.*, 1992, **114**, 3974-3975.
[48] *Polyoxometalate Molecular Science*, Kluwer, Dordrecht, The Nederlands, 2004.
[49] J. Zhang, A. M. Bond, P. J. S. Richardt and A. G. Wedd, *Inorg. Chem.*, 2004, **43**, 8263-8271.
[50] F. Zhang, W. Guan, L. Yan, Y. Zhang, M. Xu, E. Hayfron-Benjamin and Z. Su, *Inorg. Chem.*, 2011, **50**, 4967-4977.
[51] J. Gao, J. Yan, S. Beeg, D. Long and L. Cronin, *Angew. Chem. Int. Ed.*, 2012, **51**, 3373-3376.
[52] A. Teze and G. Herve, *Journal of Inorganic & Nuclear Chemistry*, 1977, **39**, 2151-2154.
[53] G. Herve and A. Teze, *Inorg. Chem.*, 1977, **16**, 2115-2117.
[54] R. Contant, J. P. Ciabrini, *J. Chem. Research*, 1977, **222**, 2601.
[55] M. T. Pope, *Heteropoly and Isopoly Oxometalates*, Springer-Verlag Berlin, Heidelberg, 1983.
[56] L. C. W. Baker and D. C. Glick, *Chem. Rev.*, 1998, **98**, 3-49.
[57] I. V. Kozhevnikov, *Catalysis by Polyoxometalates*, 2005.
[58] J. B. Moffat, *Metal-Oxygen Clusters: The Surface and Catalytic Properties of Heteropoly Oxometalates*, 2001.
[59] M. A. C. Stuart, W. T. S. Huck, J. Genzer, M. Mueller, C. Ober, M. Stamm, G. B. Sukhorukov, I. Szleifer, V. V. Tsukruk, M. Urban, F. Winnik, S. Zauscher, I. Luzinov and S. Minko, *Nat. Mater*, 2010, **9**, 101-113.
[60] M. Russew and S. Hecht, *Adv Mater*, 2010, **22**, 3348-3360.
[61] F. Liu and M. W. Urban, *Progress in Polymer Science*, 2010, **35**, 3-23.
[62] (a) P. Gütlich, Y. García and T. Woike, *Coord. Chem. Rev.*, 2001, **219**, 839-879; (b) S. Ohkoshi, H. Tokoro, T. Hozumi, Y. Zhang, K. Hashimoto, C. Mathonière, I. Bord, G. Rombaut, M. Verelst, C. C. D. Moulin and F. Villain, *J. Am. Chem. Soc.*, 2006, **128**, 270-277; (c) S. Ohkoshi and H. Tokoro, *Acc. Chem. Res.*, 2012, **45**, 1749-1758; (d) G. Abellán, E. Coronado, C. Martí-Gastaldo, A. Ribera, J. L. Jordá and H. García, *Adv Mater*, 2014, **26**, 4156-4162; (e) G. Abellán, C. Martí-Gastaldo, A. Ribera and E. Coronado, *Acc. Chem. Res.*, 2015, **48**, 1601-1611; (f) H. Tokoro and S. Ohkoshi, *Bull. Chem. Soc. Jpn.*, 2015, **88**, 227-239.
[63] (a) D. Bléger and S. Hecht, *Angew. Chem. Int. Ed.*, 2015, **54**, 11338-11349; (b) M. Fredersdorf, R. Göstl, A. Kolmer, V. Schmidts, P. Monecke, S. Hecht and C. M. Thiele, *Chem. Eur. J.*, 2015, **21**, 14545-14554; (c) W. Wang, J. Hu, M. Zheng, L. Zheng, H. Wang and Y. Zhang, *Org. Biomol. Chem.*, 2015, **13**, 11492-11498; (d) M. Han, Y. Luo, B. Damaschke, L. Gómez, X. Ribas, A. Jose, P. Peretzki, M. Seibt and G. H. Clever, *Angew. Chem. Int. Ed.*, 2016, **55**, 445-449.
[64] (a) E. J. Harbron, C. M. Davis, J. K. Campbell, R. M. Allred, M. T. Kovary and N. J. Economou, *J Phys Chem C*, 2009, **113**, 13707-13714; (b) S. Köytepe, M. H. Demirel, A. Gültek and T. Seçkin, *Polym. Int.*, 2014, **63**, 778-787.
[65] V. Coue, R. Dessapt, M. Bujoli-Doeuff, M. Evain and S. Jobic, *Inorg. Chem.*, 2007, **46**, 2824-2835.

[66] T. He and J. Yao, *Progress in Materials Science,* 2006, **51**, 810-879.
[67] R. Dessapt, M. Collet, V. Coue, M. Bujoli-Doeuff, S. Jobic, C. Lee and M. Whangbo, *Inorg. Chem.*, 2009, **48**, 574-580.
[68] K. Hakouk, O. Oms, A. Dolbecq, H. El Moll, J. Marrot, M. Evain, F. Molton, C. Duboc, P. Deniard, S. Jobic, P. Mialane and R. Dessapt, *Inorg. Chem.,* 2013, **52**, 555-557.
[69] K. Hakouk, O. Oms, A. Dolbecq, J. Marrot, A. Saad, P. Mialane, H. El Bekkachi, S. Jobic, P. Deniard and R. Dessapt, *J. Mater. Chem. C.*, 2014, **2**, 1628-1641.
[70] C. Pichon, P. Mialane, E. Rivière, G. Blain, A. Dolbecq, J. Marrot, F. Sécheresse and C. Duboc, *Inorg. Chem.*, 2007, **46**, 7710-7712.
[71] J. J. Borrás-Almenar, J. M. Clemente Juan, E. Coronado and B. S. Tsukerblat, *Chem. Phys.*, 1995, **195**, 1-15.
[72] J. J. Borrás-Almenar, J. M. Clemente Juan, E. Coronado and B. S. Tsukerblat, *Chem. Phys.*, 1995, **195**, 17-28.
[73] J. J. Borrás-Almenar, J. M. Clemente Juan, E. Coronado and B. S. Tsukerblat, *Chem. Phys.*, 1995, **195**, 29-47.
[74] C. J. Calzado, J. M. Clemente-Juan, E. Coronado, A. Gaita-Ariño and N. Suaud, *Inorg. Chem.*, 2008, **47**, 5889-5901.
[75] J. M. Clemente-Juan, E. Coronado, A. Gaita-Ariño and N. Suaud, *J. Phys. Chem. A.*, 2007, **111**, 9969-9977.
[76] N. Suaud, A. Gaita-Ariño, J. M. Clemente-Juan and E. Coronado, *Chem. Eur. J.*, 2004, **10**, 4041-4053.
[77] B. Tsukerblat, A. Palii, J. M. Clemente-Juan, A. Gaita-Ariño and E. Coronado, *Int. J. Quantum Chem.*, 2012, **112**, 2957-2964.
[78] C. Ritchie, A. Ferguson, H. Nojiri, H. N. Miras, Y. Song, D. Long, E. Burkholder, M. Murrie, P. Kögerler, E. K. Brechin and L. Cronin, *Angew. Chem. Int. Ed.*, 2008, **47**, 5609-5612.
[79] M. A. AlDamen, J. M. Clemente-Juan, E. Coronado, C. Martí-Gastaldo and A. Gaita-Ariño, *J. Am. Chem. Soc.*, 2008, **130**, 8874-8875.
[80] A. Giusti, G. Charron, S. Mazerat, J. Compain, P. Mialane, A. Dolbecq, E. Rivière, W. Wernsdorfer, R. N. Bibouni, B. Keita, L. Nadjo, A. Filoramo, J. Bourgoin and T. Mallah, *Angew. Chem. Int. Ed.*, 2009, **48**, 4949-4952.
[81] M. A. AlDamen, S. Cardona-Serra, J. M. Clemente-Juan, E. Coronado, A. Gaita-Ariño, C. Martí-Gastaldo, F. Luis and O. Montero, *Inorg. Chem.*, 2009, **48**, 3467-3479.
[82] X. Fang, M. Speldrich, H. Schilder, R. Cao, K. P. O'Halloran, C. L. Hill and P. Kögerler, *Chem. Commun.*, 2010, **46**, 2760-2762.
[83] M. Ibrahim, Y. Lan, B. S. Bassil, Y. Xiang, A. Suchopar, A. K. Powell and U. Kortz, *Angew. Chem. Int. Ed.*, 2011, **50**, 4708-4711.
[84] C. Ritchie, M. Speldrich, R. W. Gable, L. Sorace, P. Kögerler and C. Boskovic, *Inorg. Chem.*, 2011, **50**, 7004-7014.
[85] J. J. Baldoví, J. J. Borrás-Almenar, J. M. Clemente-Juan, E. Coronado and A. Gaita-Ariño, *Dalton. Trans.*, 2012, **41**, 13705-13710.
[86] J. J. Baldoví, S. Cardona-Serra, J. M. Clemente-Juan, E. Coronado, A. Gaita-Ariño and A. Palii, *Inorg. Chem.*, 2012, **51**, 12565-12574.
[87] S. Cardona-Serra, J. M. Clemente-Juan, E. Coronado, A. Gaita-Ariño, A. Camón, M. Evangelisti, F. Luis, M. J. Martínez-Pérez and J. Sesé, *J. Am. Chem. Soc.*, 2012, **134**, 14982-14990.
[88] H. El Moll, A. Dolbecq, J. Marrot, G. Rousseau, M. Haouas, F. Taulelle, G. Rogez, W. Wernsdorfer, B. Keita and P. Mialane, *Chem. Eur. J.*, 2012, **18**, 3845-3849.
[89] X. Fang, P. Kögerler, M. Speldrich, H. Schilder and M. Luban, *Chem. Commun.*, 2012, **48**, 1218-1220.
[90] X. Fang, K. McCallum, H. D. Pratt III, T. M. Anderson, K. Dennis and M. Luban, *Dalton. Trans.*, 2012, **41**, 9867-9870.
[91] X. Feng, W. Zhou, Y. Li, H. Ke, J. Tang, R. Clerac, Y. Wang, Z. Su and E. Wang, *Inorg. Chem.*, 2012, **51**, 2722-2724.

[92] S. Ghosh, S. Datta, L. Friend, S. Cardona-Serra, A. Gaita-Ariño, E. Coronado and S. Hill, *Dalton. Trans.*, 2012, **41**, 13697-13704.
[93] C. Lydon, M. M. Sabi, M. D. Symes, D. Long, M. Murrie, S. Yoshii, H. Nojiri and L. Cronin, *Chem. Commun.*, 2012, **48**, 9819-9821.
[94] R. Sato, K. Suzuki, M. Sugawa and N. Mizuno, *Chem. Eur. J.*, 2013, **19**, 12982-12990.
[95] Z. Zhang, S. Yao, Y. Li, H. Wu, Y. Wang, M. Rouzieres, R. Clerac, Z. Su and E. Wang, *Chem. Commun.*, 2013, **49**, 2515-2517.
[96] Y. Zhen, B. Liu, L. Li, D. Wang, Y. Ma, H. Hu, S. Gao and G. Xue, *Dalton. Trans.*, 2013, **42**, 58-62.
[97] A. Escuer, J. Esteban, S. P. Perlepes and T. C. Stamatatos, *Coord. Chem. Rev.*, 2014, **275**, 87-129.
[98] J. J. Baldoví, J. M. Clemente-Juan, E. Coronado, Y. Duan, A. Gaita-Ariño and C. Giménez-Saiz, *Inorg. Chem.*, 2014, **53**, 9976-9980.
[99] J. J. Baldoví, E. Coronado, A. Gaita-Ariño, C. Gamer, M. Giménez-Marqués and G. Mínguez Espallargas, *Chem. Eur. J.*, 2014, **20**, 10695-10702.
[100] R. Sato, K. Suzuki, T. Minato, M. Shinoe, K. Yamaguchi and N. Mizuno, *Chem. Commun.*, 2015, **51**, 4081-4084.
[101] K. Suzuki, R. Sato, T. Minato, M. Shinoe, K. Yamaguchi and N. Mizuno, *Dalton. Trans.*, 2015, **44**, 14220-14226.
[102] U. Kortz, A. Mueller, J. van Slageren, J. Schnack, N. S. Dalal and M. Dressel, *Coord. Chem. Rev.*, 2009, **253**, 2315-2327.
[103] L. C. W. Baker and T. P. Mccutcheon, *J. Am. Chem. Soc.*, 1956, **78**, 4503-4510.
[104] A. Palii, B. Tsukerblat, S. Klokishner, K. R. Dunbar, J. M. Clemente-Juan and E. Coronado, *Chem. Soc. Rev.*, 2011, **40**, 3130-3156.
[105] C. J. Gómez-García, E. Coronado, J. J. Borrás-Almenar, M. Aebersold, H. U. Güdel and H. Mutka, *Physica B*, 1992, **180**, 238-240.
[106] J. M. Clemente, H. Andrés, M. Aebersold, J. J. Borrás-Almenar, E. Coronado, H. U. Güdel, H. Buttner and G. Kearly, *Inorg. Chem.*, 1997, **36**, 2244-2245.
[107] J. M. Clemente-Juan, E. Coronado, A. Gaita-Ariño, C. Giménez-Saiz, G. Chaboussant, H. -U. Güdel, R. Burriel and H. Mutka, *Chem. Eur. J.*, 2002, **8**, 5701-5708.
[108] J. M. Clemente-Juan, E. Coronado, A. Gaita-Ariño, C. Giménez-Saiz, H. U. Güdel, A. Sieber, R. Bircher and H. Mutka, *Inorg. Chem.*, 2005, **44**, 3389-3395.
[109] J. R. Galán-Mascarós, C. J. Gómez-García, J. J. Borrás-Almenar and E. Coronado, *Adv Mater*, 1994, **6**, 221-223.
[110] J. M. Clemente-Juan, E. Coronado, A. Forment-Aliaga, J. R. Galán-Mascarós, C. Giménez-Saiz and C. J. Gómez-García, *Inorg. Chem.*, 2004, **43**, 2689-2694.
[111] Y. Hou, L. Xu, M. J. Cichon, S. Lense, K. I. Hardcastle and C. L. Hill, *Inorg. Chem.*, 2010, **49**, 4125-4132.
[112] L. Ruhlmann, J. Canny, R. Contant and R. Thouvenot, *Inorg. Chem.*, 2002, **41**, 3811-3819.
[113] N. Belai and M. T. Pope, *Chem. Commun.*, 2005, 5760-5762.
[114] R. J. Errington, G. Harle, W. Clegg and R. W. Harrington, *Eur. J. Inorg. Chem.*, 2009, 5240-5246.
[115] C. Ritchie, F. Li, C. P. Pradeep, D. Long, L. Xu and L. Cronin, *Dalton. Trans.*, 2009, 6483-6486.
[116] D. Gabb, C. P. Pradeep, H. N. Miras, S. G. Mitchell, D. Long and L. Cronin, *Dalton. Trans.*, 2012, **41**, 10000-10005.
[117] K. Suzuki, Y. Kikukawa, S. Uchida, H. Tokoro, K. Imoto, S. Ohkoshi and N. Mizuno, *Angew. Chem. Int. Ed.*, 2012, **51**, 1597-1601.
[118] B. S. Bassil, U. Kortz, A. S. Tigan, J. M. Clemente-Juan, B. Keita, P. de Oliveira and L. Nadjo, *Inorg. Chem.*, 2005, **44**, 9360-9368.
[119] M. D. Ritorto, T. M. Anderson, W. A. Neiwert and C. L. Hill, *Inorg. Chem.*, 2004, **43**, 44-49.
[120] L. Yang, J. Zhao, J. Zhao and J. Niu, *J. Coord. Chem.*, 2012, **65**, 3363-3371.

[121] L. Lisnard, P. Mialane, A. Dolbecq, J. Marrot, J. Modesto Clemente-Juan, E. Coronado, B. Keita, P. de Oliveira, L. Nadjo and F. Sécheresse, *Chem. Eur. J.*, 2007, **13**, 3525-3536.
[122] H. Lv, J. Song, Y. V. Geletii, W. Guo, J. Bacsa and C. L. Hill, *Eur. J. Inorg. Chem.*, 2013, 1720-1725.
[123] J. Wang, P. Ma, Y. Shen and J. Niu, *Cryst. Growth Des.*, 2008, **8**, 3130-3133.
[124] T. J. R. Weakley, H. T. Evans, J. S. Showell, G. F. Tourné and C. M. Tourné, *J. Chem. Soc., Chem. Commun.*, 1973, 139-140.
[125] R. G. Finke, M. W. Droege and P. J. Domaille, *Inorg. Chem.*, 1987, **26**, 3886-3896.
[126] N. Casan-Pastor, J. Bas-Serra, E. Coronado, G. Pourroy and L. C. W. Baker, *J. Am. Chem. Soc.*, 1992, **114**, 10380-10383.
[127] H. Andrés, J. M. Clemente-Juan, M. Aebersold, H. U. Güdel, E. Coronado, H. Buttner, G. Kearly, J. Melero and R. Burriel, *J. Am. Chem. Soc.*, 1999, **121**, 10028-10034.
[128] C. H. Fu, S. T. Zheng and G. Y. Yang, *Chinese J. Struct. Chem.*, 2008, **27**, 943-948.
[129] H. Liu, J. Peng, J. Sha, L. Wang, L. Han, D. Chen and Y. Shen, *J. Mol. Struct.*, 2009, **923**, 153-161.
[130] C. Ritchie, T. Boyd, D. Long, E. Ditzel and L. Cronin, *Dalton. Trans.*, 2009, 1587-1592.
[131] L. Zhang, W. Gu, X. Liu, Z. Dong, Y. Yang, B. Li and D. Liao, *Inorg. Chem. Commun.*, 2007, **10**, 1378-1380.
[132] Z. Zhang, E. Wang, Y. Li, H. An, Y. Qi and L. Xu, *J. Mol. Struct.*, 2008, **872**, 176-181.
[133] X. Zhao, Y. Li, Y. Wang and E. Wang, *Transit. Metal. Chem.*, 2008, **33**, 323-330.
[134] Q. X. Han, Y. Liu, J. Li and J. P. Wang, *Chinese J. Struct. Chem.*, 2009, **28**, 25-28.
[135] Y. Wang, Z. Zhang, E. Wang, Y. Qi and S. Chang, *Aust. J. Chem.*, 2008, **61**, 874-880.
[136] J. Wang, J. Liu and J. Niu, *J. Coord. Chem.*, 2009, **62**, 3599-3605.
[137] L. Chen, D. Shi, J. Zhao, Y. Wang, P. Ma and J. Niu, *Inorg. Chem. Commun.*, 2011, **14**, 1052-1056.
[138] Z. Wang and H. Xi, *Zeitschrift Fur Naturforschung Section B-a Journal of Chemical Sciences*, 2012, **67**, 495-498.
[139] L. H. Bi, E. B. Wang, J. Peng, R. D. Huang, L. Xu and C. W. Hu, *Inorg. Chem.*, 2000, **39**, 671-679.
[140] L. H. Bi, R. D. Huang, J. Peng, E. B. Wang, Y. H. Wang and C. W. Hu, *J. Chem. Soc., Dalton Trans.*, 2001, 121-129.
[141] Y. Kikukawa, K. Suzuki, K. Yamaguchi and N. Mizuno, *Inorg. Chem.*, 2013, **52**, 8644-8652.
[142] H. Lv, J. Song, Y. V. Geletii, J. W. Vickers, J. M. Sumliner, D. G. Musaev, P. Kögerler, P. F. Zhuk, J. Bacsa, G. Zhu and C. L. Hill, *J. Am. Chem. Soc.*, 2014, **136**, 9268-9271.
[143] R. Tan, X. Pang, H. Wang, S. Cui, Y. Jiang, C. Wang, X. Wang and W. Song, *Inorg. Chem. Commun.*, 2012, **25**, 70-73.
[144] G. Rousseau, O. Oms, A. Dolbecq, J. Marrot and P. Mialane, *Inorg. Chem.*, 2011, **50**, 7376-7378.
[145] G. Zhu, Y. V. Geletii, P. Kögerler, H. Schilder, J. Song, S. Lense, C. Zhao, K. I. Hardcastle, D. G. Musaev and C. L. Hill, *Dalton Trans.*, 2012, **41**, 2084-2090.
[146] C. M. Tourné, G. F. Tourné and F. Zonnevijlle, *J. Chem. Soc., Dalton. Trans.*, 1991, 143-155.
[147] H. Andrés, J. M. Clemente-Juan, R. Basler, M. Aebersold, H. U. Güdel, J. J. Borrás-Almenar, A. Gaita-Ariño, E. Coronado, H. Buttner and S. Janssen, *Inorg. Chem.*, 2001, **40**, 1943-1950.
[148] J. Guo, D. Zhang, L. Chen, Y. Song, D. Zhu and Y. Xu, *Dalton. Trans.*, 2013, **42**, 8454-8459.
[149] X. Wang, X. Liu, A. Tian, J. Ying, H. Lin, G. Liu and Q. Gao, *Dalton. Trans.*, 2012, **41**, 9587-9589.
[150] T. J. R. Weakley, *J. Chem. Soc., Chem. Commun.*, 1984, 1406-1407.
[151] M. A. Aldamen and S. F. Haddad, *J. Coord. Chem.*, 2011, **64**, 4244-4253.
[152] B. S. Bassil, S. Nellutla, U. Kortz, A. C. Stowe, J. van Tol, N. S. Dalal, B. Keita and L. Nadjo, *Inorg. Chem.*, 2005, **44**, 2659-2665.

[153] M. Ibrahim, Y. Lan, B. S. Bassil, Y. Xiang, A. Suchopar, A. K. Powell and U. Kortz, *Angew. Chem. Int. Ed.*, 2011, **50**, 4708-4711.
[154] X. Han, Z. Zhang, T. Zhang, Y. Li, W. Lin, W. You, Z. Su and E. Wang, *J. Am. Chem. Soc.*, 2014, **136**, 5359-66.
[155] Y. Duan, J. M. Clemente-Juan, C. Giménez-Saiz and E. Coronado, *Inorg. Chem.*, 2016, **55**, 925-938.
[156] W. Chen, X. Wang, C. Qin, K. Shao, Z. Su and E. Wang, *Chem. Commun.*, 2016, **52**, 9514-9517.
[157] S. Bareyt, S. Piligkos, B. Hasenknopf, P. Gouzerh, E. Lacôte, S. Thorimbert and M. Malacria, *J. Am. Chem. Soc.*, 2005, **127**, 6788-6794.
[158] M. Ochiai, Y. Takeuchi, T. Katayama, T. Sueda and K. Miyamoto, *J. Am. Chem. Soc.*, 2005, **127**, 12244-12245.
[159] C. Boglio, G. Lemière, B. Hasenknopf, S. Thorimbert, E. Lacôte and M. Malacria, *Angew. Chem. Int. Ed.*, 2006, **45**, 3324-3327.
[160] C. Boglio, G. Lenoble, C. Duhayon, B. Hasenknopf, R. Thouvenot, C. Zhang, R. C. Howell, B. P. Burton-Pye, L. C. Francesconi, E. Lacôte, S. Thorimbert, M. Malacria, C. Afonso and J. C. Tabet, *Inorg. Chem.*, 2006, **45**, 1389-1398.
[161] W. Chen, Y. Li, Y. Wang, E. Wang and Z. Su, *Dalton. Trans.*, 2007, 4293-4301.
[162] W. Huang, L. C. Francesconi and T. Polenova, *Inorg. Chem.*, 2007, **46**, 7861-7869.
[163] C. Boglio, K. Micoine, P. Remy, B. Hasenknopf, S. Thorimbert, E. Lacôte, M. Malacria, C. Afonso and J. Tabet, *Chem. Eur. J.*, 2007, **13**, 5426-5432.
[164] K. Micoine, B. Hasenknopf, S. Thorimbert, E. Lacôte and M. Malacria, *Org. Lett.*, 2007, **9**, 3981-3984.
[165] E. Derat, E. Lacôte, B. Hasenknopf, S. Thorimbert and M. Malacria, *J. Phys. Chem. A*, 2008, **112**, 13002-13005.
[166] C. Boglio, K. Micoine, E. Derat, R. Thouvenot, B. Hasenknopf, S. Thorimbert, E. Lacôte and M. Malacria, *J. Am. Chem. Soc.*, 2008, **130**, 4553-4561.
[167] M. T. Pope, *Handbook on the Physics and Chemistry of Rare Earths*, 2007.
[168] R. D. Peacock and T. J. R. Weakley, *J. Chem. Soc. A*, 1971, 1836-1839.
[169] J. Iball, J. N. Low and T. J. R. Weakley, *J. Chem. Soc., Dalton Trans.*, 1974, 2021-2024.
[170] L. Bi, U. Kortz, M. H. Dickman, S. Nellutla, N. S. Dalal, B. Keita, L. Nadjo, M. Prinz and M. Neumann, *J. Cluster Sci.*, 2006, **17**, 143-165.
[171] S. Cardona-Serra, J. M. Clemente-Juan, E. Coronado, A. Gaita-Ariño, N. Suaud, O. Svoboda, R. Bastardis, N. Guihéry and J. J. Palacios, *Chem. Eur. J.*, 2015, **21**, 763-769.
[172] N. Suaud, Y. Masaro, E. Coronado, J. M. Clemente-Juan and N. Guihéry, *Eur. J. Inorg. Chem.*, 2009, 5109-5114.
[173] J. Lehmann, A. Gaita-Ariño, E. Coronado and D. Loss, *Nat. Nanotechnol*, 2007, **2**, 312-317.
[174] R. Bakri, A. Booth, G. Harle, P. S. Middleton, C. Wills, W. Clegg, R. W. Harrington, R. J. Errington, *Chem. Commun*., 2012, **48**(22), 2779-2781.

Chapter 2. Cobalt-Containing POMs

In this chapter, POMs have been chosen as ligands to encapsulate different cobalt clusters exhibiting desired topologies for the study of their magnetic properties. This chapter provides a deep insight into the experimental details of the synthesis and characterisation of ten new cobalt-containing POM clusters that were obtained during the course of the thesis. For the sake of clarity, the chapter is divided into the following three parts:

In the first part, the synthesis and characterisation of four novel tetra-cobalt(II) or hepta-cobalt(II,III)-substituted POMs having cobalt cores exhibiting cubane or di-cubane topologies are described. The tetra-cobalt(II)-substituted POM $[Co_4(OH)_3(H_2O)_6(PW_9O_{34})]^{4-}$ (**2.1**) consists of a trilacunary B-α-$[PW_9O_{34}]^{9-}$ unit which accommodates a cubane-like $[Co^{II}_4O_4]$ core. The three hepta-cobalt(II,III)-containing POMs $[Co_7(OH)_6(H_2O)_6(PW_9O_{34})_2]^{9-}$ (**2.2**), $[Co_7(OH)_6(H_2O)_4(PW_9O_{34})_2]_n^{9n-}$ (**2.3**) and $[Co_7(OH)_6(H_2O)_6(P_2W_{15}O_{56})_2]^{15-}$ (**2.4**) encapsulate a dicubane-like $\{Co^{II}_6Co^{III}O_8\}$ core between two trilacunary Keggin B-α-$[PW_9O_{34}]^{9-}$ units (in **2.2** and **2.3**) or two trilacunary Dawson α-$[P_2W_{15}O_{56}]^{12-}$ (in **2.4**) units. The chemical nature and physical properties of the resulting clusters are discussed. The magnetic properties of these complexes have been fitted according to an anisotropic exchange model in the low-temperature regime and discussed on the basis of ferromagnetic interactions between Co(II) ions with angles Co-L-Co (L = O, OH) close to orthogonality and weakly antiferromagnetic interactions between Co(II) ions connected through central diamagnetic Co(III) ion.

In the second part, a synthetic procedure is presented to construct new magnetic POMs containing one or two subunits of '$[Co_4(OH)_3(H_2O)_{6-n}(PW_9O_{34})]^{3-}$' (n = 3 or 5). The substitution of the water ligands present in these subunits by oxo or hydroxo ligands belonging to other POM fragments, gives rise to the following five, larger POM anions: $[Co_7(OH)_6(H_2O)_6(PW_9O_{34})_2]^{9-}$ (**2.2**), $[Co_7(OH)_6(H_2O)_4(PW_9O_{34})_2]_n^{9n-}$ (**2.3**), $[Co_8(OH)_6(H_2O)_6\{W_8O_{28}(OH)_2\}(PW_9O_{34})_2]^{16-}$ (**2.5**), $[Co_{11}(OH)_5(H_2O)_5(W_6O_{24})(PW_9O_{34})_3]^{22-}$ (**2.6**) and $[\{Co_4(OH)_3(H_2O)(PW_9O_{34})\}_2\{K\subset(H_2W_{12}O_{41})_2\}\{Co(H_2O)_4\}_2]^{17-}$ (**2.7**). The

crystal structures, magnetic characterisation and stabilities in aqueous solutions of these POM derivatives are also presented.

In the third part, two structurally intriguing Co(II)-substituted POMs are described, formulated as $[Co^{II}_4(H_2O)_2(Co^{III}W_9O_{34})(PW_9O_{34})]^{12-}$ (**2.8**) and $[Co_2\{Co_3(H_2O)(Co(OH)_2W_7O_{26})(PW_9O_{34})\}_2]^{22-}$ (**2.9**). **2.8** contains a $[Co^{II}_4Co^{III}]$ pentacobalt cluster which represents the first asymmetric sandwich exhibiting Weakley's topology, while **2.9** is made up of two capping trilacunary B-α-$[PW_9O_{34}]^{9-}$ units and two bridging $[W_7O_{26}]^{10-}$ units that assemble to encapsulate a novel deca-Co(II) cluster core comprising octahedral and tetrahedral Co(II) ions. An original reaction consisting in a partial reductive hydrolysis of the penta-Co(II/III) cluster **2.8** leads to the formation of the novel deca-Co(II) cluster **2.9**.

2.1. Cubane cobalt clusters based on trivacant POM ligands

2.1.1. Introduction

From the magnetic point of view, cobalt containing POMs with cubane topologies can be used as model systems for the study of the anisotropic nature of the exchange interactions between Co(II) ions in such topologies. From the synthetic point of view, such species can be building blocks for the construction of POMs with larger cobalt nuclearities by linking these cubane or di-cubane cobalt cluster units with phosphate, acetate, carbonate or other ligands. The interest of these cubane or di-cubane cobalt clusters could also span to the field of catalysis. For example, special attention has been paid in the last years to the cubane-type tetranuclear metal clusters due to their potential interest as molecular water oxidation catalysts (WOCs).[1-4] Such interest stems from their structural similarity with the natural $\{Mn_3O_4Ca\}$ cubane cluster (see **Fig. 2.1a**), which is hosted within the photosystem II (PS II) complex. As POMs have been proved to be efficient WOCs due to their oxidative, thermal and hydrolytic (over pH ranges dictated by the POM metal) stability,[5-7] a promising strategy in this field consists in the use of POMs as ligands for the construction of cubane metal clusters. In addition, some cobalt-containing POMs have been found to be potent species for water oxidation.[8-21]

Previously to this work, no cobalt clusters exhibiting the isolated cubane topology shown in **Fig. 2.1b** had been reported in polyoxotungstate chemistry, although a non-isolated $\{Co^{II}_4O_4\}$ cubane cluster was encapsulated in the family of POMs formulated as $[\{Co_4(OH)_3PO_4\}_4(XW_9O_{34})_4]^{n-}$ (X = Si^{IV}, Ge^{IV}, n = 32; X = P^{V}, As^{V}, n = 28).[6,22] In contrast, for nickel and manganese, isolated cubanes cores $\{M_4O_4\}$ have been reported in the following polyoxoanions: $[Ni_4(OH)_3(H_2O)_6(H_2PW_9O_{34})]^{2-}$,[23] $[(\alpha\text{-}P_2W_{15}O_{56})Mn^{III}_3Mn^{IV}O_3(CH_3COO)_3]^{8-}$,[24-26] and $[(\alpha\text{-}P_2W_{15}O_{56})(W_{0.5}Ni_{3.5})(OH)_6(H_2O)_3]^{8-}$.[27]

On the other hand, the heptanuclear di-cubane core $\{M_7O_8\}$ shown in **Fig. 2.1c** has only been obtained for manganese in $[(\alpha\text{-}P_2W_{15}O_{56})_2Mn^{III}_6Mn^{IV}O_6(H_2O)_6]^{14-}$, which has a S = 21/2 ground state and exhibits SMM behavior.[26]

In this part of the chapter, we show that using the heptadentate trilacunary ligand B-α-$[PW_9O_{34}]^{9-}$, the POM formulated as $[Co_4(OH)_3(H_2O)_6(PW_9O_{34})]^{4-}$ (**2.1**) can be obtained, which contains an isolated cubane core $\{Co^{II}_4O_4\}$ with all four cobalt ions in the oxidation state 2+. Regarding the di-cubane topology, we show that three different POMs incorporating di-cubane $\{Co_7O_8\}$ core can be obtained:

$[Co_7(OH)_6(H_2O)_6(PW_9O_{34})_2]^{9-}$ (**2.2**) and $[Co_7(OH)_6(H_2O)_4(PW_9O_{34})_2]_n^{9n-}$ (**2.3**) (both containing the trilacunary B-α-$[PW_9O_{34}]^{9-}$ ligand) and $[Co_7(OH)_6(H_2O)_6(P_2W_{15}O_{56})_2]^{15-}$ (**2.4**) (containing the trilacunary α-$[P_2W_{15}O_{56}]^{12-}$ ligand). The main difference between **2.2** and **2.3** is that the former is an isolated polyanion, while the later is a polymeric POM in which individual neighbouring units are linked through two W–O–Co(II) bonds. **2.2**, **2.3** and **2.4** all contain Co(III) in the central position of the dicubane core and Co(II) in the other six metal positions. Owing to this feature these heptanuclear cobalt clusters can be viewed as formed by two triangular groups (**Fig. 1.11c**) linked by a diamagnetic Co(III) ion. POMs encapsulating Co(II)/Co(III) clusters are uncommon. As far as we know, there are only three previously reported examples: the $[Co^{II}(H_2O)(Co^{III}W_{11}O_{39})]^{7-}$ polyanion, which contains a dinuclear cobalt group similar to the one shown in **Fig. 1.11a**,[28] $[Co^{II}_2Co^{III}_4(OH)_5(H_2O)_2(CH_3CO_2)(Si_2W_{18}O_{66})]^{6-}$, which contains a hexanuclear cobalt cluster (**Fig. 1.11k**) comprising four Co(III) and two Co(II) ions apparently disordered between the six cobalt positions,[29] and the polyoxoniobate $[H_2Co_8O_4(Nb_6O_{19})_4]^{18-}$ which encapsulates an octanuclear cobalt cluster comprising a central $\{Co^{III}_4O_4\}$ cubane core surrounded by four Co(II) ions.[30] In this part of the thesis, the synthetic strategies to obtain four new POMs, **2.1**, **2.2**, **2.3** and **2.4**, their crystal structures, their stability studies in solution by UV-vis spectroscopy and cyclic voltammetry and their magnetic properties are described. The interest of the unique spin structures provided by these cubane and di-cubane cobalt topologies in molecular spintronics (molecular spins addressed through an electric field) and quantum computing (spin qu-gates) will be discussed.

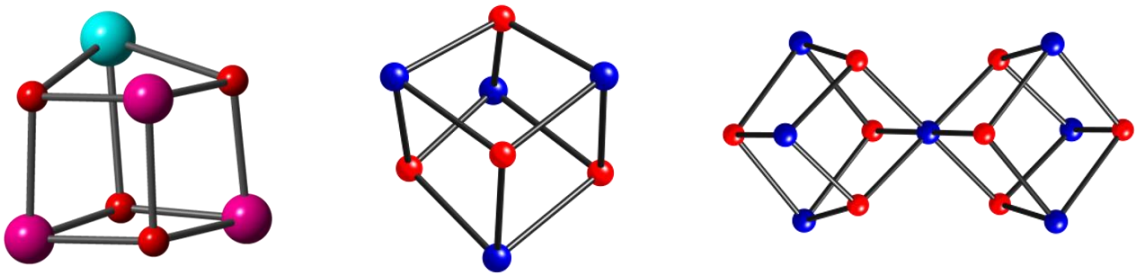

(a) $\{Mn_3O_4Ca\}$ (b) $\{M_4O_4\}$ (c) $\{M_7O_8\}$

Fig. 2.1.- Ball-and-stick representations of (a) the quasi-cubane core $\{Mn_3O_4Ca\}$ featured in many natural and synthetic water oxidation catalysts, (b) cubane and (c) dicubane cores that mimic the natural $\{Mn_3O_4Ca\}$ cluster in POMs.

2.1.2. Results and Discussion

2.1.2.1. Synthetic approach

In order to obtain cobalt clusters with the topologies shown in **Fig. 2.1**, the synthetic procedure of the previously known $[Ni_4(OH)_3(H_2O)_6(H_2PW_9O_{34})]^{2-}$ anion (which contains a cubane $\{Ni_4O_4\}$ unit)[23] is of primary importance. This POM was obtained in moderate yield (35 %) by reaction of the trilacunary Keggin anion B-α-$[PW_9O_{34}]^{9-}$ with Ni(II) ions at pH 4.8 and 80 ºC and isolated by precipitation as a cesium salt and subsequent recrystallization. However, the addition of cesium cations to an aqueous B-α-$[PW_9O_{34}]^{9-}$/Co(II) system in similar conditions results in a bulky precipitate of the well-known tetranuclear Co(II) cluster sandwiched by two POM moieties of B-α-$[PW_9O_{34}]^{9-}$ of formula $[Co_4(H_2O)_2(PW_9O_{34})_2]^{10-}$, originally reported by Weakley in 1973.[31] To obtain the tetracobalt cubane-containing polyoxoanion **2.1**, it is necessary to, first, filter out this cesium salt of the tetranuclear Co(II) sandwiched cluster and, then, the polyoxoanion **2.1** crystallizes from the mother liquor after 5 days standing, as a minor product with very low yield (7 %). The reason for the different behavior between Co(II) and Ni(II) ions lies in the higher rate of formation of $[Co_4(H_2O)_2(PW_9O_{34})_2]^{10-}$ in the pH range in which the heptadentate B-α-$[PW_9O_{34}]^{9-}$ ligand is stable (approx. 5-8).[32] This hinders the formation of the cobalt cubane cluster **2.1**, which is considered as a by-product. In contrast, reaction of B-α-$[PW_9O_{34}]^{9-}$ with Ni(II) ions does not produce significant amounts of the corresponding tetranuclear sandwiched POM, allowing the formation of other nickel-substituted POMs in higher yields, such as the aforementioned cubane-containing $[Ni_4(OH)_3(H_2O)_6(H_2PW_9O_{34})]^{2-}$ polyanion (at pH 4.8) or the tri-nickel POM $[Ni_3(H_2O)_3PW_{10}O_{39}H_2O]^{7-}$ (at pH 6-7).[33] The tetranickel sandwiched POM is more conveniently obtained by direct condensation of tungstate and phosphate ions at pH 6.5 rather that from the preformed B-α-$[PW_9O_{34}]^{9-}$ ligand.[34] An additional difference between cobalt and nickel systems, is that **2.1** is obtained at pH values of 6.6, while a significantly lower value (4.8) is required for the synthesis of the analogous nickel derivative.[23]

A polyoxoanion similar to **2.1**, *i.e.* containing a cubane cobalt cluster, can be envisioned using the trilacunary Dawson unit α-$[P_2W_{15}O_{56}]^{12-}$ instead of the trilacunary Keggin B-α-$[PW_9O_{34}]^{9-}$. In this case, the formation of the tetranuclear cobalt sandwich $[Co_4(H_2O)_2(P_2W_{15}O_{56})_2]^{16-}$, first reported by Finke,[32,35] is also highly favored in the

reaction system α-$[P_2W_{15}O_{56}]^{12-}$/Co(II). Therefore, the addition of a small amount of cesium chloride produces a bulky precipitate containing Finke's POM, while other minor POM species remain in solution (larger amounts of cesium cations cause the precipitation of these minor species too). Unexpectedly, **2.4** was obtained from the mother liquor resulting after the filtration of the precipitate, instead of the hypothetical '$[Co_4(OH)_3(H_2O)_6(P_2W_{15}O_{56})]^{7-}$'. POM **2.4** encapsulates a $\{Co_7O_8\}$ dicubane cobalt cluster (shown in **Fig. 2.1c**) in which the central cobalt atom is in oxidation state 3+. This oxidation state is probably favored because the central cobalt atom is in a coordination environment of six hydroxyl anions. This fact reduces the E^o value of the Co(III)/Co(II) couple, thereby facilitating oxidation of the central cobalt atom to the 3+ state by atmospheric O_2. This oxidation process takes place during the 14 days of slow evaporation of the solvent required to obtain the crystals of the salt **Q-2.4** and is evidenced by the gradual change of the solution from red to orange. Crystals of the salt **Q-2.1**, however, were obtained after only 4 days of evaporation at room temperature, which is probably too short time to get a significant concentration of an oxidized cobalt POM in solution by the action of atmospheric O_2. Then, when using the trilacunary ligand B-α-$[PW_9O_{34}]^{9-}$, the low solubility of **Q-2.1** seems to be the reason for which **2.1** (containing a Co(II) cubane cluster) is obtained instead of a POM containing a Co(II)/Co(III) dicubane cluster. In order to deliberately obtain this last compound the oxidation process must be accelerated by the addition of a one-electron oxidant (such as potassium persulfate). In these conditions, the main POM species in solution are the oxidized ones, which crystallize after one day as **Q-2.2**.

To obtain the cubane-containing POM with the lacunary ligand α-$[P_2W_{15}O_{56}]^{12-}$, two strategies were followed: i) addition of larger amounts of cesium cations in the synthesis of **2.4** and ii) decreasing the pH of the reaction mixture. However, larger amounts of cesium always led to a mixed precipitate containing Finke's POM ($[Co_4(H_2O)_2(P_2W_{15}O_{56})_2]^{16-}$), which was impossible to purify, while a decrease of pH produced exclusively Finke's POM.

The preparation of cubane and dicubane compounds from direct condensation of tungstate and phosphate anions instead of using the preformed lacunary ligands has also been attempted. Only compound **Q-2.3** was obtained following this strategy. **2.3** consists of a polymeric one-dimensional chain made of units that are structurally similar to **2.2** (see structural description). The reason for such a condensation likely lies in the reflux

and later concentration process followed in this synthesis. It is interesting to note that the formation of a similar polymeric chain made from the condensation of POMs of the type **2.4** is not possible, probably due to the steric hindrance imposed by the larger ligand α-$[P_2W_{15}O_{56}]^{12-}$.

2.1.2.2. Crystal Structure of $Na_{1.5}Cs_{2.5}[Co_4(OH)_3(H_2O)_6(PW_9O_{34})]\cdot 9H_2O$ (Q-2.1)

The novel polyoxoanion $[Co_4(OH)_3(H_2O)_6(PW_9O_{34})]^{4-}$ (**2.1**) consists of one heptadentate B-α-$[PW_9O_{34}]^{9-}$ ligand which incorporates a $\{Co_4O_4\}$ cubane unit arising from the tetrahedral arrangement of four edge-shared $\{CoO_6\}$ octahedra (see **Fig. 2.2**). This type of arrangement gives rise to an idealized C_{3v} symmetry for anion **2.1**. This architecture was first reported by Kortz *et al.* for the nickel(II)-containing tungstophosphate $[Ni_4(OH)_3(H_2O)_6(H_2PW_9O_{34})]^{2-}$.[23] As far as we know, **2.1** is the second example of POM exhibiting this topology. Both compounds crystallize in the same space group with similar unit cell parameters and are isostructural. In the nickel derivative, however, two protons were assumed to be bonded directly to the surface of the POM (without specific binding sites) for charge balance considerations, as only two cesium countercations were found in the crystal structure. In **Q-2.1**, a total number of 2.5 cesium cations per POM unit were found in Fourier difference maps. Hence, the electroneutrality is achieved by 1.5 extra sodium cations which are disordered (along with solvation water molecules) inside infinite channels running along the crystallographic *c* direction. The presence of these sodium atoms inside the channels was assessed by chemical analysis, making unnecessary the assumption of hydrogen atoms bonded to the surface of the POM.

As a result of the tetrahedral arrangement of the four $\{CoO_6\}$ octahedra in **2.1**, two types of chemically different cobalt atoms arise (see **Fig. 2.3**): the apical cobalt atom, which is not directly coordinated by the trivacant B-α-$[PW_9O_{34}]^{9-}$ unit (Co1), and the three central cobalt atoms, which share one common oxygen (O10) with the phosphorous atom of the POM (Co2, Co3 and Co4). Co1 has three terminal ligands (O1, O2 and O3) while the other three cobalt atoms have only one terminal ligand (O7, O8 and O9 for Co2, Co3 and Co4, respectively). The packing diagram of **2.1** is shown in **Fig. 2.4**. All bond distances and angles involved in the cubane cluster of **2.1** are listed in **Table 2.1**.

Table 2.1.- Bond Distances (Å) and Angles (º) involved in the cubane $\{Co_4O_4\}$ and di-cubane $\{Co_7O_8\}$ clusters contained in **2.1**, **2.2**, **2.3** and **2.4**.

	2.1	**2.2**	**2.3**	**2.4**
Co(1)-O(1)[O(5)^{i}]^{a}	2.134(10)	1.91(3)	1.915(10)	1.931(9)
Co(1)-O(2)[O(6)^{i}]^{a}	2.162(9)	1.93(3)	1.917(10)	1.913(9)
Co(1)-O(3)[O(4)^{i}]^{a}	2.060(11)	1.92(3)	1.912(11)	1.912(9)
Co(1)-O(4)	2.080(9)	1.92(3)	1.912(11)	1.912(9)
Co(1)-O(5)	2.113(10)	1.91(3)	1.915(10)	1.931(9)
Co(1)-O(6)	2.083(9)	1.93(3)	1.917(10)	1.913(9)
Co(2)-O(4)	2.089(9)	2.06(3)	2.092(11)	2.080(9)
Co(2)-O(6)	2.060(9)	2.06(3)	2.096(11)	2.093(8)
Co(2)-O(7)	2.139(9)	2.13(3)	2.163(11)	2.131(10)
Co(2)-O(10)	2.262(9)	2.25(3)	2.254(9)	2.179(8)
Co(2)-O(11)	2.031(8)	1.97(3)	1.991(11)	2.011(8)
Co(2)-O(16)	2.053(10)	2.04(3)	2.009(10)	2.011(9)
Co(3)-O(4)	2.070(9)	2.11(3)	2.082(10)	2.094(9)
Co(3)-O(5)	2.062(10)	2.09(2)	2.087(11)	2.085(9)
Co(3)-O(8)	2.141(11)	2.13(4)	2.139(11)	2.118(11)
Co(3)-O(10)	2.269(8)	2.24(2)	2.263(10)	2.174(8)
Co(3)-O(12)	2.072(10)	2.08(3)	2.030(11)	2.012(8)
Co(3)-O(13)	2.052(10)	2.09(3)	1.991(11)	2.026(8)
Co(4)-O(5)	2.043(9)	2.06(3)	2.069(10)	2.102(9)
Co(4)-O(6)	2.023(9)	2.07(3)	2.080(10)	2.077(9)
Co(4)-O(9)	2.127(10)	2.21(3)	2.100(10)	2.108(10)
Co(4)-O(10)	2.261(9)	2.29(2)	2.232(10)	2.189(8)
Co(4)-O(14)	2.025(10)	2.01(3)	1.986(10)	2.015(8)
Co(4)-O(15)	2.053(9)	1.98(3)	1.984(11)	2.010(9)
O(4)-Co(1)-O(5)	78.6(4)	86.8(11)	84.3(4)	84.3(4)
O(4)-Co(1)-O(6)	80.6(3)	82.5(13)	85.1(5)	85.1(4)
O(5)-Co(1)-O(6)	78.4(4)	84.2(11)	86.4(4)	86.0(4)
O(4)-Co(1)-O(3)[O(4)^{i}]^{a}	175.1(4)	180.0(17)	180.0(2)	180.000(1)
O(4)-Co(1)-O(1)[O(5)^{i}]^{a}	91.2(3)	93.2(11)	95.7(4)	95.7(4)
O(4)-Co(1)-O(2)[O(6)^{i}]^{a}	95.6(4)	97.5(13)	94.9(5)	94.9(4)
O(5)-Co(1)-O(3)[O(4)^{i}]^{a}	97.8(4)	93.2(11)	95.7(4)	95.7(4)
O(5)-Co(1)-O(1)[O(5)^{i}]^{a}	168.4(4)	180.0(14)	180.000(1)	180.000(2)
O(5)-Co(1)-O(2)[O(6)^{i}]^{a}	97.6(4)	95.8(11)	93.6(4)	94.0(4)
O(6)-Co(1)-O(3)[O(4)^{i}]^{a}	95.4(4)	97.5(13)	94.9(5)	94.9(4)
O(6)-Co(1)-O(1)[O(5)^{i}]^{a}	94.6(4)	95.8(11)	93.6(4)	94.0(4)
O(6)-Co(1)-O(2)[O(6)^{i}]^{a}	174.9(4)	180.0(18)	180.000(1)	180.000(2)
O(3)[O(4)^{i}]-Co(1)-O(1)[O(5)^{i}]^{a}	92.1(4)	86.8(11)	84.3(4)	84.3(4)
O(3)[O(4)^{i}]-Co(1)-O(2)[O(6)^{i}]^{a}	88.2(4)	82.5(13)	85.1(5)	85.1(4)
O(1)[O(5)^{i}]-Co(1)-O(2)[O(6)^{i}]^{a}	88.8(4)	84.2(11)	86.4(4)	86.0(4)
O(11)-Co(2)-O(16)	85.8(4)	85.6(13)	88.0(4)	90.5(4)
O(11)-Co(2)-O(6)	172.7(4)	169.2(14)	173.5(4)	171.2(4)
O(16)-Co(2)-O(6)	97.1(4)	99.6(13)	95.5(4)	95.5(4)
O(11)-Co(2)-O(4)	95.6(4)	97.4(13)	99.5(5)	96.9(4)
O(16)-Co(2)-O(4)	174.1(4)	171.6(13)	169.5(4)	170.8(3)
O(6)-Co(2)-O(4)	80.9(3)	76.2(13)	76.4(4)	76.6(4)
O(11)-Co(2)-O(7)	94.2(4)	98.8(13)	93.8(4)	93.1(4)
O(16)-Co(2)-O(7)	90.8(4)	100.2(13)	99.0(4)	88.8(4)
O(6)-Co(2)-O(7)	92.5(4)	89.6(11)	91.1(4)	93.5(4)
O(4)-Co(2)-O(7)	94.9(4)	87.0(12)	87.9(4)	96.3(4)

[It comes from previous page.] **Table 2.1.-** Bond Distances (Å) and Angles (º) involved in the cubane $\{Co_4O_4\}$ and di-cubane $\{Co_7O_8\}$ clusters contained in **2.1**, **2.2**, **2.3** and **2.4**.

	2.1	**2.2**	**2.3**	**2.4**
O(11)-Co(2)-O(10)	91.3(3)	89.4(12)	93.8(4)	91.9(3)
O(16)-Co(2)-O(10)	91.8(3)	89.8(11)	90.8(4)	92.9(3)
O(6)-Co(2)-O(10)	81.9(3)	81.2(9)	80.7(4)	81.3(3)
O(4)-Co(2)-O(10)	82.3(3)	82.5(10)	81.4(4)	81.4(3)
O(7)-Co(2)-O(10)	174.0(4)	167.5(10)	167.8(4)	174.7(4)
O(13)-Co(3)-O(12)	86.6(4)	91.3(10)	89.0(4)	90.1(3)
O(13)-Co(3)-O(5)	96.2(4)	92.0(10)	97.6(4)	95.9(3)
O(12)-Co(3)-O(5)	172.4(4)	172.4(11)	170.4(4)	171.1(4)
O(13)-Co(3)-O(4)	171.5(4)	167.2(12)	172.4(5)	169.7(3)
O(12)-Co(3)-O(4)	96.3(4)	98.2(11)	96.7(4)	97.1(3)
O(5)-Co(3)-O(4)	80.0(4)	77.6(11)	76.1(4)	76.2(3)
O(13)-Co(3)-O(8)	87.2(4)	99.6(14)	94.7(4)	93.0(4)
O(12)-Co(3)-O(8)	97.1(4)	88.5(11)	92.6(4)	89.3(4)
O(5)-Co(3)-O(8)	90.1(4)	97.6(10)	93.6(4)	96.9(4)
O(4)-Co(3)-O(8)	100.4(5)	89.2(13)	90.0(4)	94.5(4)
O(13)-Co(3)-O(10)	89.4(3)	89.7(12)	93.5(4)	91.3(3)
O(12)-Co(3)-O(10)	90.8(3)	92.1(9)	92.4(4)	91.1(3)
O(5)-Co(3)-O(10)	82.2(3)	81.2(9)	80.4(4)	82.2(3)
O(4)-Co(3)-O(10)	82.6(3)	81.5(11)	81.4(4)	81.2(3)
O(8)-Co(3)-O(10)	171.2(4)	170.6(13)	170.5(4)	175.7(4)
O(14)-Co(4)-O(6)	172.3(4)	171.6(14)	168.2(5)	171.9(4)
O(14)-Co(4)-O(5)	96.6(4)	96.2(12)	94.2(4)	96.4(3)
O(6)-Co(4)-O(5)	81.4(4)	77.1(12)	78.5(4)	77.7(4)
O(14)-Co(4)-O(15)	86.5(4)	87.7(14)	89.6(4)	90.8(4)
O(6)-Co(4)-O(15)	94.5(4)	97.9(15)	96.5(4)	94.5(4)
O(5)-Co(4)-O(15)	171.5(4)	169.4(11)	171.8(4)	170.5(3)
O(14)-Co(4)-O(9)	92.3(4)	93.1(17)	97.3(4)	90.7(4)
O(6)-Co(4)-O(9)	95.4(4)	92.7(17)	91.7(4)	95.3(4)
O(5)-Co(4)-O(9)	98.8(4)	94.4(13)	88.4(4)	95.0(4)
O(15)-Co(4)-O(9)	89.0(4)	95.2(13)	98.2(5)	91.1(4)
O(14)-Co(4)-O(10)	89.6(3)	93.7(11)	88.2(4)	92.2(3)
O(6)-Co(4)-O(10)	82.7(3)	80.1(11)	81.6(4)	81.5(3)
O(5)-Co(4)-O(10)	82.8(3)	80.8(9)	81.5(4)	81.5(3)
O(15)-Co(4)-O(10)	89.2(3)	89.2(10)	91.4(4)	92.0(3)
O(9)-Co(4)-O(10)	177.3(4)	172.0(15)	168.8(4)	175.7(4)
Co(1)-O(4)-Co(2)	97.2(4)	100.3(14)	98.7(5)	98.8(4)
Co(3)-O(4)-Co(1)	100.0(4)	96.3(11)	99.3(5)	99.5(4)
Co(3)-O(4)-Co(2)	102.9(4)	102.4(13)	102.9(4)	100.6(4)
Co(3)-O(5)-Co(1)	99.2(4)	97.2(12)	99.0(5)	99.2(4)
Co(4)-O(5)-Co(1)	98.1(4)	98.6(11)	96.8(4)	96.8(4)
Co(4)-O(5)-Co(3)	103.6(4)	104.4(11)	103.8(5)	100.2(4)
Co(2)-O(6)-Co(1)	98.0(3)	100.0(17)	98.4(5)	98.3(4)
Co(4)-O(6)-Co(2)	104.2(4)	105.1(12)	103.3(5)	101.1(4)
Co(4)-O(6)-Co(1)	99.7(4)	97.9(11)	96.4(4)	98.2(4)
Co(2)-O(10)-Co(3)	91.7(3)	92.5(9)	92.5(3)	95.1(3)
Co(2)-O(10)-Co(4)	90.9(3)	92.3(10)	93.7(3)	94.9(3)
Co(3)-O(10)-Co(4)	90.8(3)	92.9(8)	93.3(4)	94.8(3)

[a] For compounds **2.2**, **2.3** and **2.4** the atom labels enclosed between square brackets must be used instead the preceding atom label. Symmetry transformations: (*i*) 1–x, –y, –z (for **2.2**); 1–x, –y, 1+z (for **2.3**) and 1–x, 1–y, 1–z (for **2.4**).

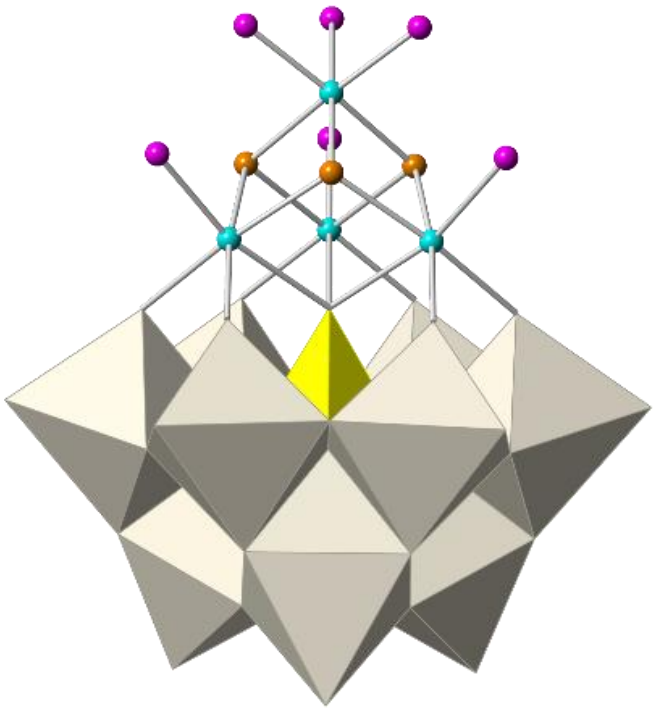

Fig. 2.2.- Polyhedral and ball-and-stick representation of the polyoxoanion $[Co_4(OH)_3(H_2O)_6(PW_9O_{34})]^{4-}$ (**2.1**). Gray octahedra, $[WO_6]$; yellow tetrahedra, $[PO_4]$; cyan spheres, Co; pink spheres, H_2O; orange spheres, OH.

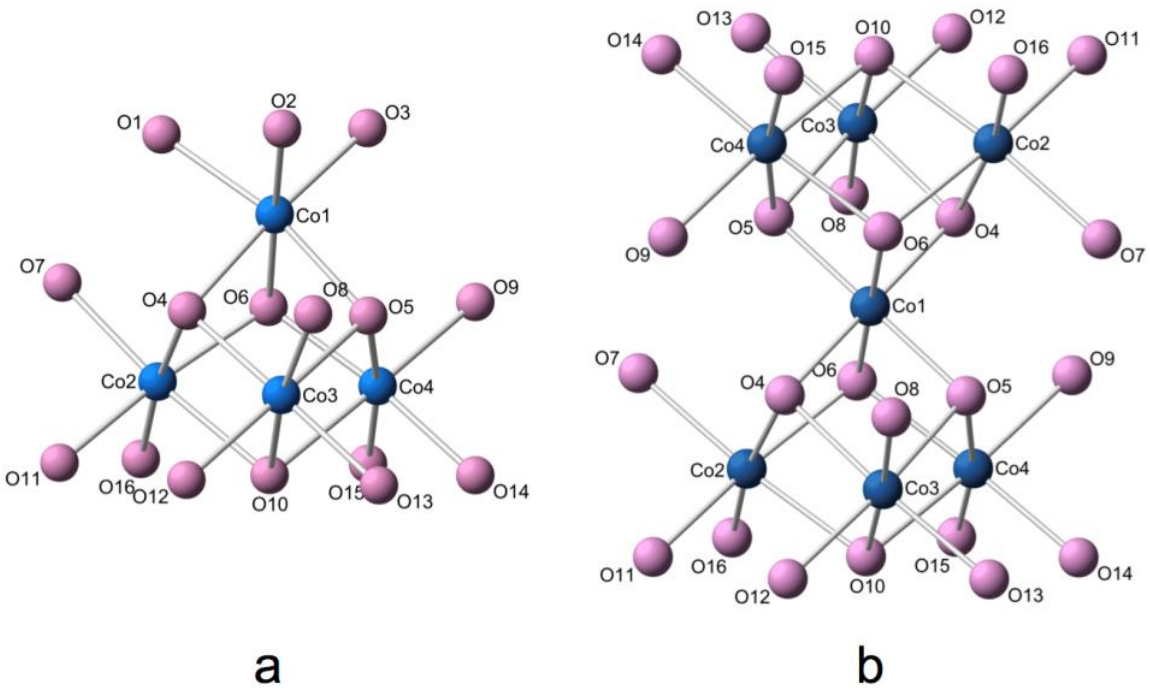

Fig. 2.3.- Ball-and-stick representations and atom labelling of the cubane (a) and dicubane (b) cobalt clusters contained in the POM derivates of this work. Blue spheres, Co; pink spheres, O.

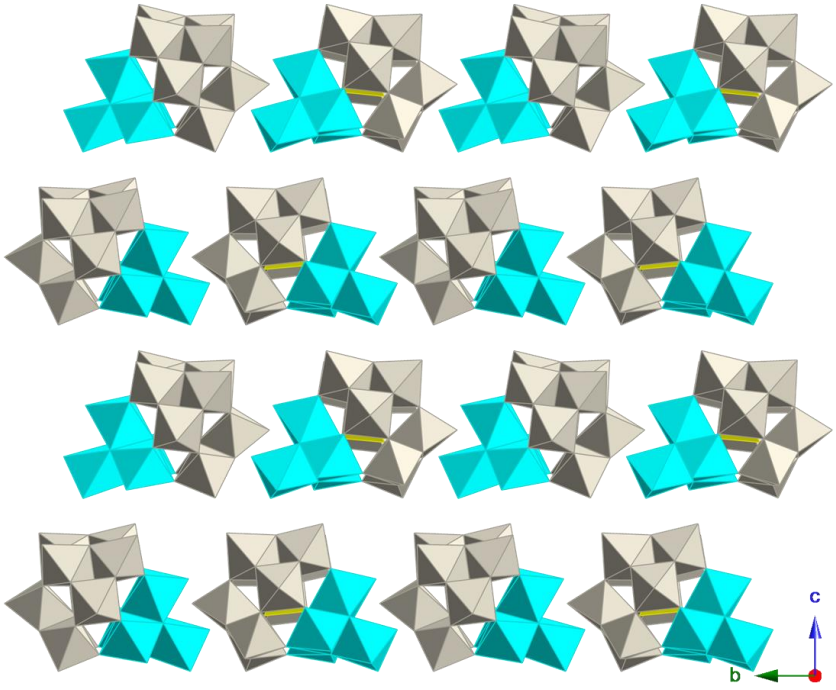

Fig. 2.4.- Polyhedral representation of the packing diagram of **2.1** along the *a*-axis. Lattice cations and water molecules are omitted for clarity. Cyan octahedra, [CoO_6]; gray octahedra, [WO_6]; yellow tetrahedra, [PO_4].

2.1.2.3. Crystal Structure of $Cs_7Na_2[Co_7(OH)_6(H_2O)_6(PW_9O_{34})_2]\cdot 20H_2O$ (Q-2.2)

The novel polyoxoanion $[Co_7(OH)_6(H_2O)_6(PW_9O_{34})_2]^{9-}$ (**2.2**) consists of two heptadentate B-α-$[PW_9O_{34}]^{9-}$ ligands which encapsulate a heptanuclear {Co_7O_8} cluster. This cluster can be conceptually constructed from two fused {Co_4O_8} cubanes sharing a common cobalt atom, which sits at the inversion center. This type of arrangement lends an overall D_{3d} symmetry of **2.2** (see **Fig. 2.5**) and gives rise to two chemically different cobalt atoms in **2.2** (see **Fig. 2.3b**): the central cobalt atom at the inversion center (Co1), which is not directly coordinated by the trivacant B-α-$[PW_9O_{34}]^{9-}$ unit and the six cobalt atoms arranged in two separated triads, each of them sharing a common oxygen with a phosphorus atom of the POM (Co2, Co3 and Co4). The packing diagram of **2.2** along *a*-axis is shown in **Fig. 2.6**. All bond distances and angles involved in the di-cubane cluster of **2.2** are listed in **Table 2.1**.

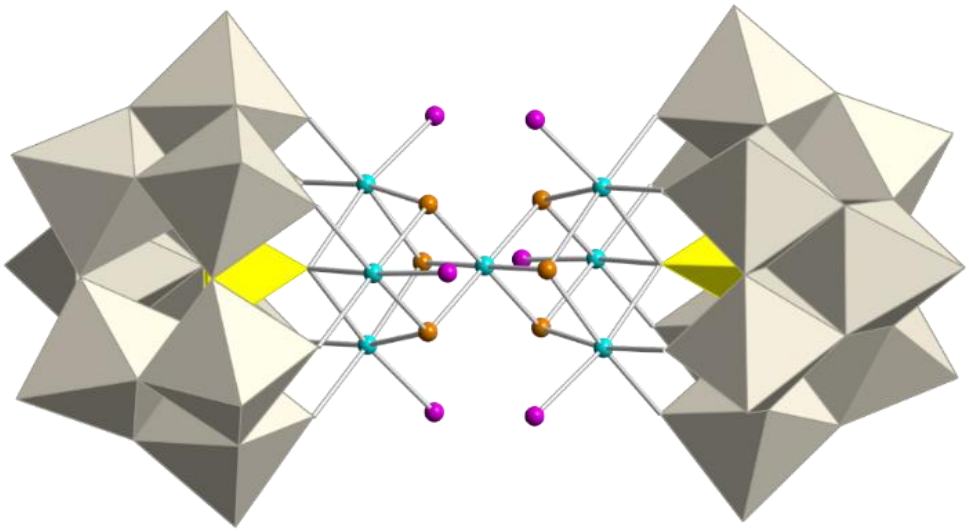

Fig. 2.5.- Polyhedral and ball-and-stick representation of the polyoxoanion $[Co_7(OH)_6(H_2O)_6(PW_9O_{34})_2]^{9-}$ (**2.2**). Gray octahedra, $[WO_6]$; yellow tetrahedra, $[PO_4]$; cyan spheres, Co; pink spheres, H_2O; orange spheres, OH.

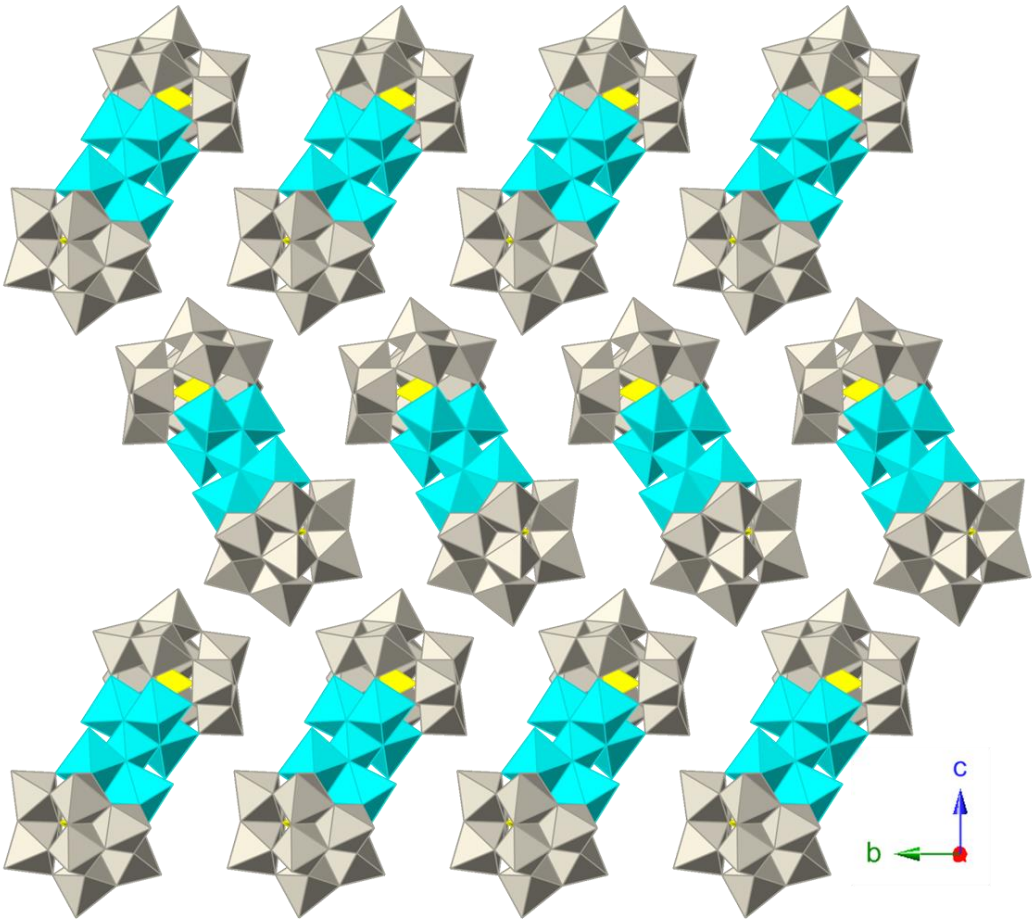

Fig. 2.6.- Polyhedral representation of the packing diagram of **2.2** along the *a*-axis. Lattice cations and water molecules are omitted for clarity. Cyan octahedra, $[CoO_6]$; gray octahedra, $[WO_6]$; yellow tetrahedra, $[PO_4]$.

2.1.2.4. Crystal structure of $K_{5n}Na_{2n}\{Co(H_2O)_2\}_n[Co_7(OH)_6(H_2O)_4(PW_9O_{34})_2]_n \cdot 20nH_2O$ (Q-2.3)

2.3 is topologically identical to **2.2** with the difference that two water molecules that coordinate two cobalt atoms in **2.2** (labeled as Co4, one in each triad) have been substituted in **2.3** by terminal oxygen atoms of two neighbouring polyoxoanions, giving rise to polymeric chains running along the *a* axis (see **Fig. 2.7**). This type of polymeric chains formed by POM units with this topology has not been reported previously. In these chains each POM unit is linked to the two nearest polyanions via four Co-O_{bridge}-W connections (two connections with each neighbour), forming a two-dimensional layer structure shown in **Fig. 2.8**. A further difference between **2.2** and **2.3** lies in that each monomeric POM unit in **2.3** is mono-capped by one additional cobalt atom (Co5), which sits in one of the tetragonal sites of the parent Keggin anion. Co5 is bonded to four surface oxygen atoms of the POM and two water molecules. Co5 has a refined occupancy of 50 % and, due to the centrosymmetric nature of **2.3**, is disordered between two positions located at both ends of the POM. From the magnetic point of view, this external Co5 atom is well separated from the cobalt atoms belonging to the $\{Co_7O_8\}$ cluster. Therefore, superexchange pathways would involve at least one O-W-O bridge and rather long cobalt-to-cobalt distances (minimum distance of 5.66 Å Co3–Co5, with the rest over 7.00 Å), so they are expected to be negligible. All bond distances and angles involved in the dicubane cluster of **2.3** are listed in **Table 2.1**.

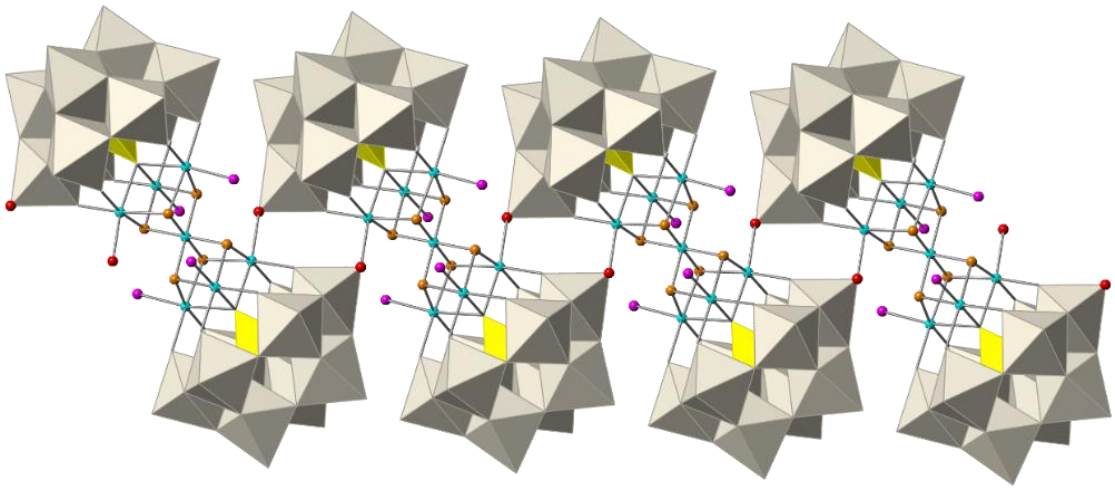

Fig. 2.7.- Polyhedral and ball-and-stick representation of the polymeric chain $[Co_7(OH)_6(H_2O)_4(PW_9O_{34})_2]_n^{9n-}$ (**2.3**). Gray octahedra, $[WO_6]$; yellow tetrahedra, $[PO_4]$; cyan spheres, Co; pink spheres, H_2O; orange sphere, OH; red sphere, O.

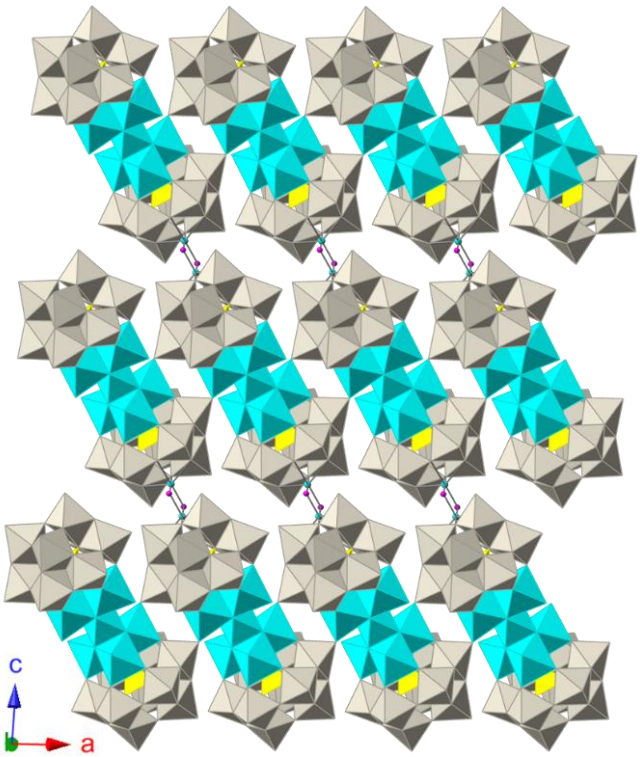

Fig. 2.8.- Polyhedral and ball-and-stick representation of the packing diagram of **2.3** along the *a*-axis. Lattice cations and water molecules are omitted for clarity. Cyan octahedra, [CoO_6]; gray octahedra, [WO_6]; yellow tetrahedra, [PO_4]; cyan spheres, Co; pink spheres, H_2O.

2.1.2.5. Crystal Structure of $Na_{15}[Co_7(OH)_6(H_2O)_6(P_2W_{15}O_{56})_2]\cdot 38H_2O$ (Q-2.4)

The novel polyoxoanion $[Co_7(OH)_6(H_2O)_6(P_2W_{15}O_{56})_2]^{15-}$ (**2.4**) consists of two heptadentate α-$[P_2W_{15}O_{56}]^{12-}$ ligands which encapsulate a heptanuclear {Co_7O_8} cluster (see **Fig. 2.3b** and **Fig. 2.9**). This cluster is structurally similar to the one described for **2.2** and BVS calculations yield the same results concerning the oxidation state of the cobalt atoms and the protonation level of the O ligands (see **Fig. 2.14**). Therefore, the only difference between POMs **2.2** and **2.4** is the phosphotungstate ligands B-α-$[PW_9O_{34}]^{9-}$ and α-$[P_2W_{15}O_{56}]^{12-}$ used in each case, respectively. The POM architecture exhibited by **2.4** was first reported by Fang, Kögerler *et al.* for the tungstophosphate $[Mn^{III}_6Mn^{IV}O_6(H_2O)_6(P_2W_{15}O_{56})_2]^{14-}$.[26] The packing diagram of **2.4** along the *a*-axis is shown in **Fig. 2.10**. As far as we know, **2.4** is the second example of a POM exhibiting this topology although there are two important differences between **2.4** and the Mn derivative. On the one hand, while in **2.4** the cobalt atom located at the inversion center exhibits an oxidation state of 3+ and all the other cobalt atoms are divalent, in the Mn derivative, the Mn atom at the inversion center exhibits a 4+ oxidation

state while all other Mn atoms are trivalent. On the other hand, while the six μ_3-O ligands bonded to the trivalent cobalt ion correspond to hydroxyl groups, in the Mn derivative they are reported to be oxo ligands. Therefore, the degree of protonation of these oxygen ligands seems to be related to the oxidation state of the central 3*d* metal ion. As previously explained, the presence of these six ligands as hydroxyl ions is likely the key of the trivalent oxidation state of the central cobalt ion, due to the decrease of the reduction potential of the Co(III)/Co(II) pair. All bond distances and angles involved in the dicubane cluster of **2.4** are listed in **Table 2.1**.

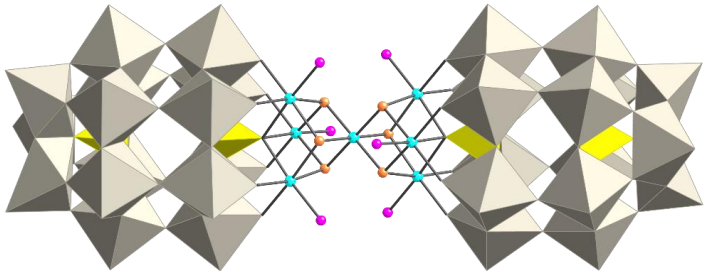

Fig. 2.9.- Polyhedral and ball-and-stick representation of the polyoxoanion $[Co_7(OH)_6(H_2O)_6(P_2W_{15}O_{56})_2]^{15-}$ (**2.4**). Gray octahedra, $[WO_6]$; yellow tetrahedra, $[PO_4]$; cyan spheres, Co; pink spheres, H_2O; orange spheres, OH.

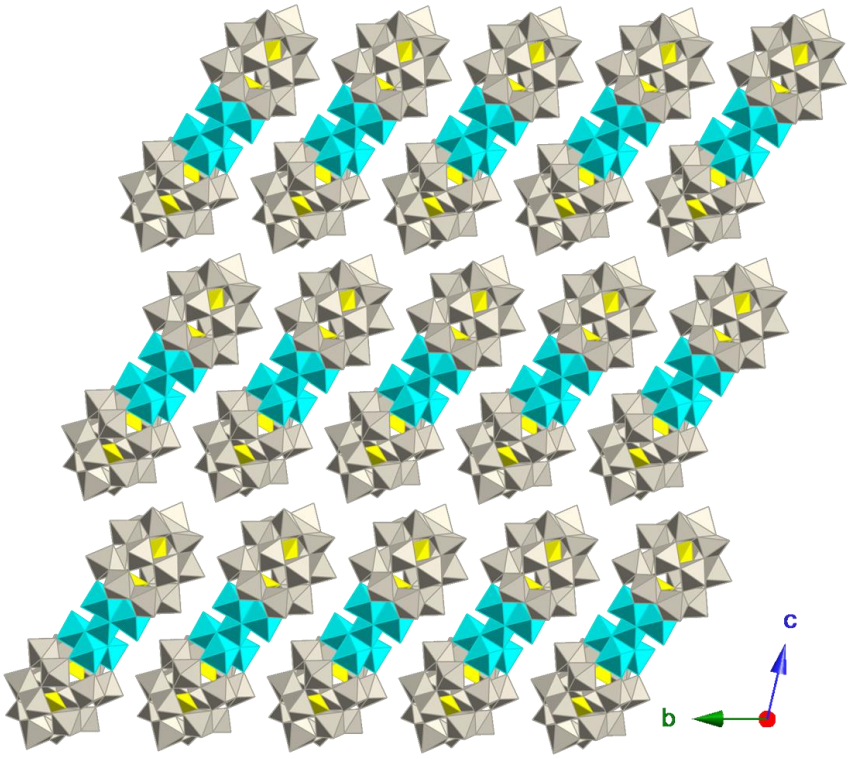

Fig. 2.10.- Polyhedral representation of the packing diagram of **2.4** along the *a*-axis. Lattice cations and water molecules are omitted for clarity. Cyan octahedra, $[CoO_6]$; gray octahedra, $[WO_6]$; yellow tetrahedra, $[PO_4]$.

2.1.2.6. Bond valence sum (BVS) calculations

For the determination of the oxidation states of metal centers and the protonation states of oxygen sites, bond valence sum (BVS) calculations were carried out using the method of I. D. Brown.[36] The calculation formula is $S_i = \exp[(R_0 - R_i)/B]$, where S_i is the bond valence of bond *i*, R_0 is a constant dependent upon the bonded elements, R_i is the bond length of bond *i*, and B equals to 0.37. R_0 values were taken from the literature for calculations performed on cobalt[37] and oxygen[37-38] sites [R_0 (Co–O) = 1.67].

For POM **2.1**, according to bond valence sum (BVS) calculations, all these terminal ligands correspond to water molecules, while the three μ_3–bridging oxygen atoms of the cubane unit correspond to hydroxyl groups (see **Fig. 2.11**). BVS calculations also confirm that all four cobalt atoms in **2.1** are Co(II) ions.

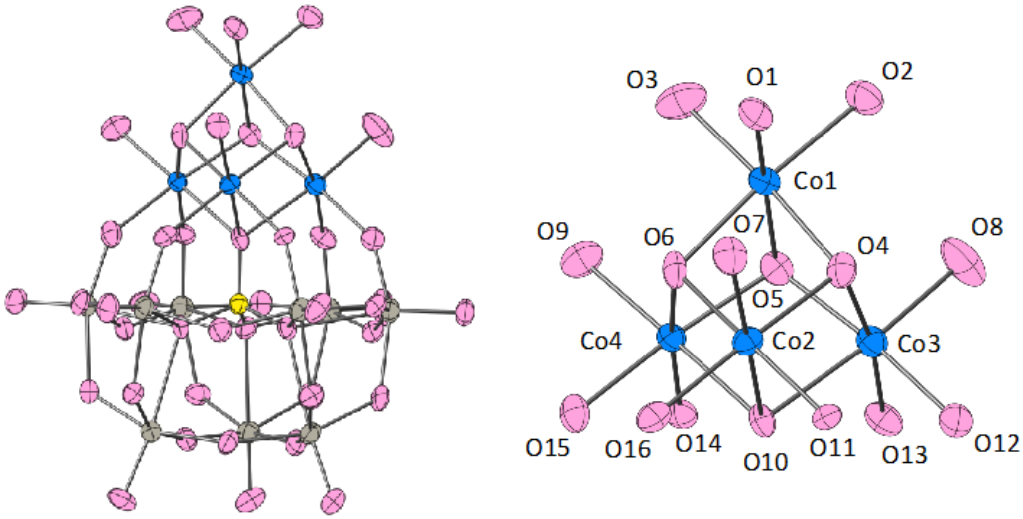

Cobalt atoms	BVS
Co1	**1.86**
Co2	**1.89**
Co3	**1.86**
Co4	**1.98**

Oxygen atoms	BVS	Assigned protonation levels
O1	**0.29**	**H_2O**
O2	**0.27**	**H_2O**
O3	**0.35**	**H_2O**
O4	**0.99**	**OH**
O5	**1.01**	**OH**
O6	**1.06**	**OH**
O7	**0.28**	**H_2O**
O8	**0.28**	**H_2O**
O9	**0.29**	**H_2O**

Fig. 2.11.- (Up) Thermal ellipsoid plot and labelling scheme for **2.1** (50 % probability). (Down) Bond valence sum (BVS) calculations for cobalt centers and relevant oxygen sites of **2.1**.

For the salt **Q-2.2**, BVS calculations strongly indicate that Co1 exhibits an oxidation state of 3+, while all other cobalt atoms are divalent (see **Fig. 2.12**). Moreover, the μ_3-O ligands coordinating to Co1 (O4, O5 and O6) atom correspond to hydroxyl groups, while the terminal oxygen ligands (O7, O8 and O9) bonded to the divalent cobalt ions correspond to water molecules (see **Fig. 2.12**).

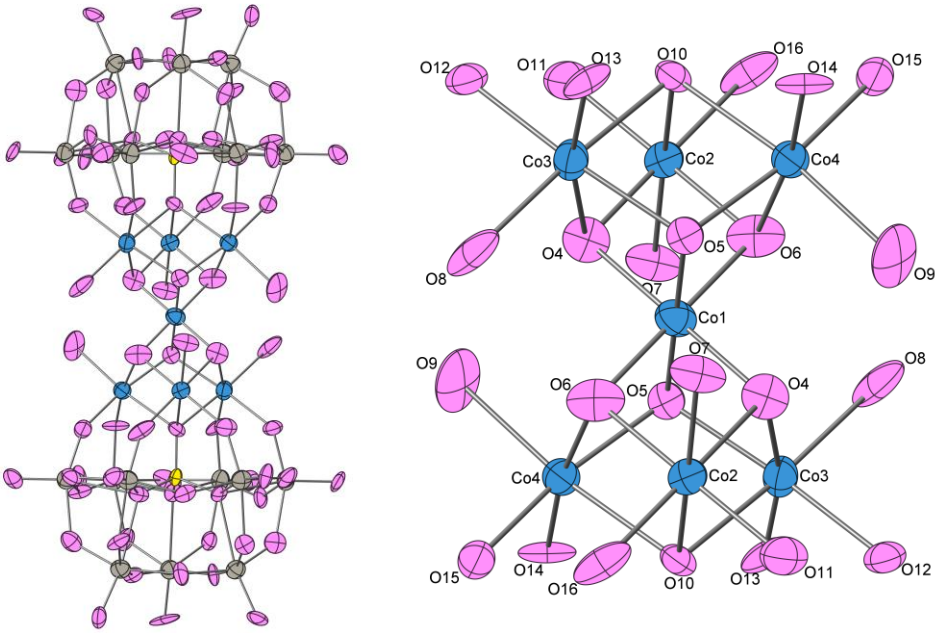

Cobalt atoms	BVS
Co1	**3.06**
Co2	**2.01**
Co3	**1.77**
Co4	**1.93**

Oxygen atoms	BVS	Assigned protonation levels
O4	**1.17**	**OH**
O5	**1.23**	**OH**
O6	**1.23**	**OH**
O7	**0.29**	**H_2O**
O8	**0.28**	**H_2O**
O9	**0.23**	**H_2O**
O10	**1.86**	**O**

Fig. 2.12.- (Up) Thermal ellipsoid plot and labelling scheme for **2.2** in the salt **Q-2.2** (50 % probability). (Down) Bond valence sum (BVS) calculations for cobalt centers and relevant oxygen sites in the same salt.

For **2.3**, BVS calculations give the same results as for **2.2**: Co1 bears an oxidation state of 3+, while all other cobalt ions are divalent, the μ_3-O ligands bonded to Co1 correspond to hydroxyl ions and all the terminal oxygen ligands of the divalent cobalt ions correspond to water molecules. In addition, the bridging O atom (O26) is non-protonated (see **Fig. 2.13**).

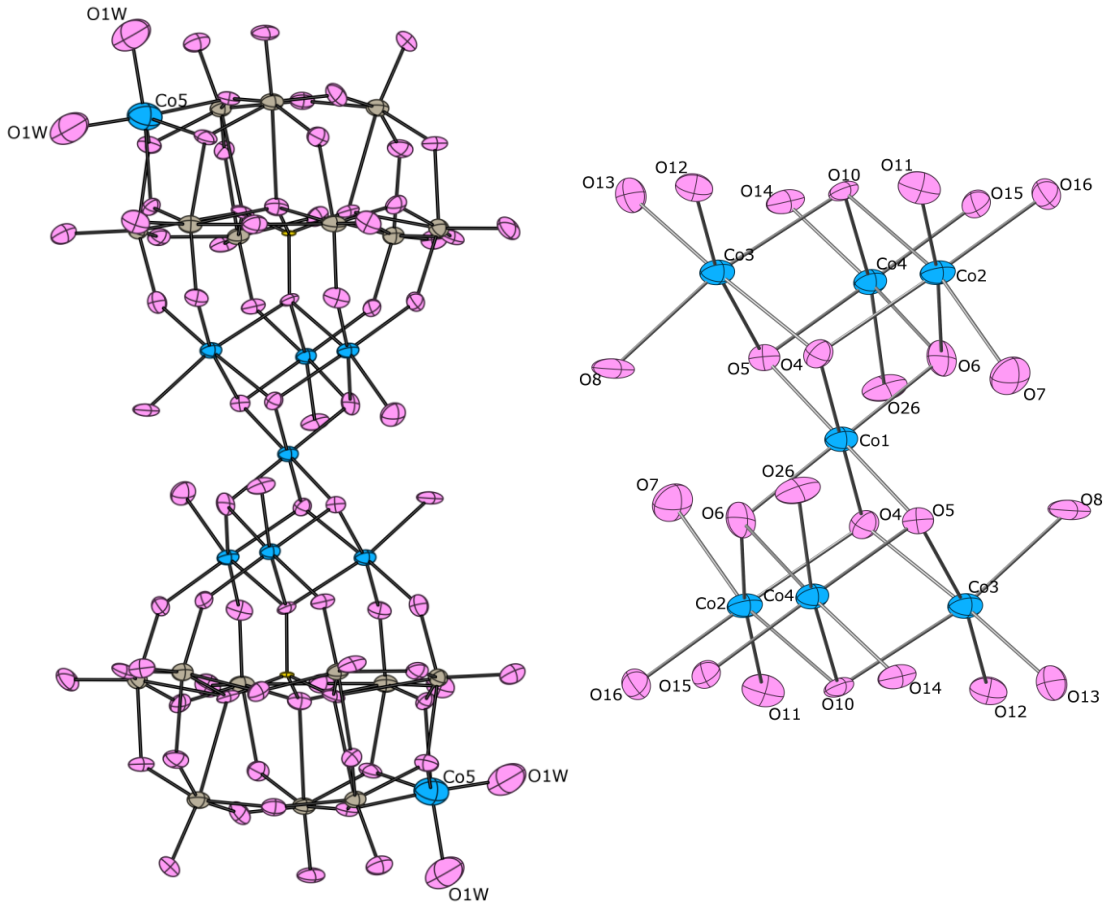

Cobalt atoms	BVS
Co1	**3.09**
Co2	**1.93**
Co3	**1.93**
Co4	**2.06**
Co5	**2.06**

Oxygen atoms	BVS	Assigned protonation levels
O4	**1.17**	**OH**
O5	**1.18**	**OH**
O6	**1.16**	**OH**
O7	**0.26**	**H_2O**
O8	**0.28**	**H_2O**
O10	**1.79**	**O**
O26	**1.55**	**O**

Fig. 2.13.- (Up) Thermal ellipsoid plot and labelling scheme for **2.3** (50 % probability). (Down) Bond valence sum (BVS) calculations for cobalt centers and relevant oxygen sites of **2.3**.

For **2.4**, the cobalt atom Co1 located at the inversion center exhibits an oxidation state of 3+ and the other cobalt atoms are divalent. The six μ_3-O ligands bonded to the trivalent cobalt ion correspond to hydroxyl groups (see **Fig. 2.14**).

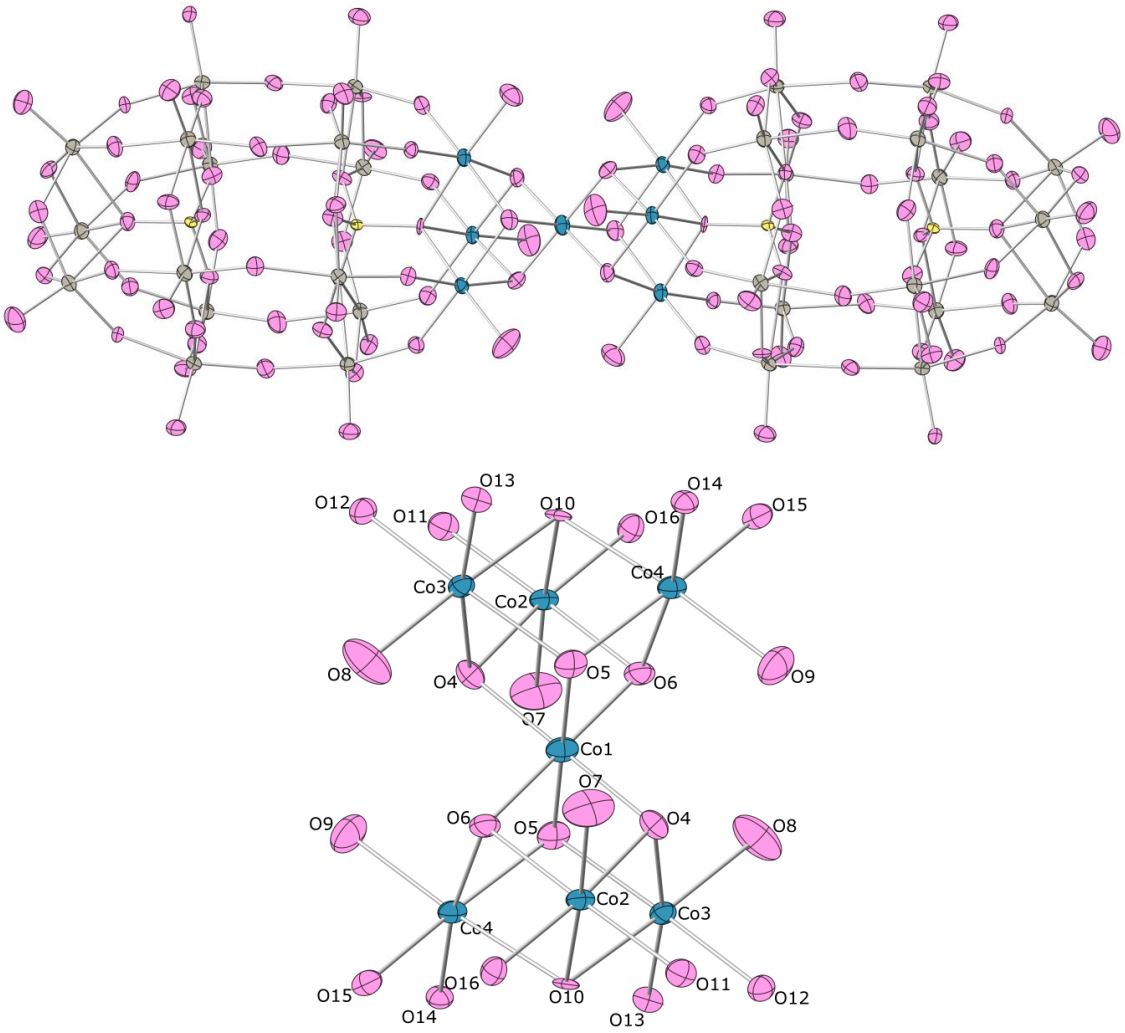

Cobalt atoms	BVS
Co1	**3.06**
Co2	**1.97**
Co3	**1.98**
Co4	**1.99**

Oxygen atoms	BVS	Assigned protonation levels
O4	**1.17**	**OH**
O5	**1.17**	**OH**
O6	**1.21**	**OH**
O7	**0.29**	**H_2O**
O8	**0.30**	**H_2O**
O9	**0.31**	**H_2O**
O10	**1.84**	**O**

Fig. 2.14.- (Up) Thermal ellipsoid plot and labelling scheme for **2.4** (50 % probability). (Down) Bond valence sum (BVS) calculations for cobalt centers and relevant oxygen sites of POM **2.4**.

2.1.2.7. Stabilities in aqueous solution

Given the interest of Co-based POMs in catalysis, the stabilities in solution of the discrete species (**2.1**, **2.2** and **2.4**) were studied using UV-vis spectroscopy at the following conditions: 0.2 M sodium sulfate (pH 3.0), 0.4 M sodium acetate (pH 5.0) and 25 mM sodium borate (pH 9) buffer solutions over a period of 24 h. **2.3** was not included in the study due to its polymeric nature. All the other three POMs exhibit absorption bands in the range 200–250 nm which are attributed to ligand-to-metal charge-transfer transitions (O → W) characteristic of the presence of POMs.[39] A comparison between the initial spectrum of **2.1** in a pH 3 buffer solution and the spectrum recorded after 24 h of standing is shown in **Fig. 2.15a**. It can be seen that the last spectrum develops a new peak at 252 nm, a situation reminiscent of the behavior of the isostructural POM $[Ni_4(OH)_3(H_2O)_6(H_2PW_9O_{34})]^{2-}$ which was shown to be unstable in a wide pH range, decomposing into $[PNi(H_2O)W_{11}O_{39}]^{5-}$ as the major product.[40] This is also the case for **2.1**, as a comparison of the UV spectra of **2.1** at pH 3, recorded after 24 h of standing, and the spectrum of $[PCo(H_2O)W_{11}O_{39}]^{5-}$ (which is stable in these conditions) reveals that both are very similar (see **Fig. 2.15a**). The remaining differences can be attributed to the presence of other minor, unidentified decomposition compounds and to Co^{2+}(aq) ions, which are released from **2.1** as it decomposes. The same conclusion can be deduced from the UV spectra of **2.1** at pH 5 (see **Fig. 2.15d**), while at pH 9, the evolution of the UV spectra of **2.1** (**Fig. 2.15g**) shows that, although the positions of the absorption bands do not change significantly after 24h, the characteristic bands become weaker, suggesting that **2.1** also decomposes partially in this medium. The same behavior is observed for **2.2** in aqueous solution, as the evolution of the UV spectra of **2.2** after 24h of standing (**Fig. 2.15b**, **Fig. 2.15e** and **Fig. 2.15h**) is the same as for **2.1** at the three different pH values studied. **2.4**, however, has a higher stability in aqueous solutions than **2.1** and **2.2** at pH 5 and 9, as deduced from the minimal variation observed in the UV spectra of **2.4** after 24h (**Fig. 2.15c**, **Fig. 2.15f** and **Fig. 2.15i**).

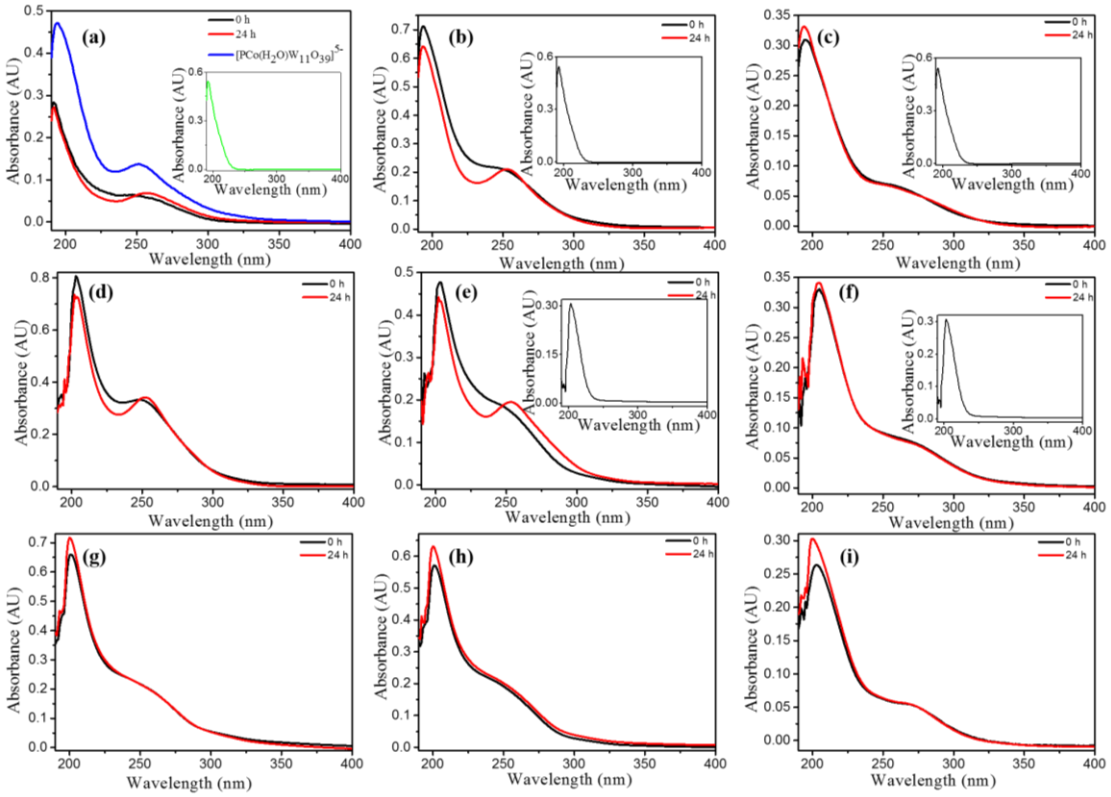

Fig. 2.15.- Evolution of the UV spectrum of aqueous solutions of the POMs (**2.1**, **2.2** and **2.4**) in this work. (**a**) Evolution of the UV spectrum of a solution of **2.1** ($2.5\cdot10^{-6}$ M) with time, recorded in a pH 3 medium (red and black lines) and UV spectrum of $[PCo(H_2O)W_{11}O_{39}]^{5-}$ ($2.5\cdot10^{-7}$ M) in the same medium (blue line). Inset: UV spectrum of a solution of $CoSO_4$ ($7.4\cdot10^{-4}$ M) in the same medium. (**b**) Evolution of the UV-vis spectrum of a solution of **2.2** ($2.5\cdot10^{-5}$ M) with time, recorded in a pH 3 medium (red and black lines). (**c**) Evolution of the UV-vis spectrum of a solution of **2.4** ($2.5\cdot10^{-5}$ M) with time, recorded in a pH 3 medium (red and black lines). (**d**) Evolution of the UV-vis spectrum of a solution of **2.1** ($5\cdot10^{-5}$ M) with time, recorded in a pH 5 medium (red and black lines). (**e**) Evolution of the UV-vis spectrum of a solution of **2.2** ($2.5\cdot10^{-5}$ M) with time, recorded in a pH 5 medium (red and black lines). (**f**) Evolution of the UV-vis spectrum of a solution of **2.4** ($2.5\cdot10^{-5}$ M) with time, recorded in a pH 5 medium (red and black lines). (**g**) Evolution of the UV-vis spectrum of a solution of **2.1** ($5\cdot10^{-5}$ M) with time, recorded in a pH 9 medium (red and black lines). (**h**) Evolution of the UV-vis spectrum of a solution of **2.2** ($2.5\cdot10^{-6}$ M) with time, recorded in a pH 9 medium (red and black lines). (**i**) Evolution of the UV-vis spectrum of a solution of **2.4** ($2.5\cdot10^{-5}$ M) with time, recorded in a pH 9 medium (red and black lines).

The partial decomposition of **2.1** into $[PCo(H_2O)W_{11}O_{39}]^{5-}$ as the major product has also been confirmed by cyclic voltammetry experiments. The initial cyclic voltammogram of **2.1** in pH 3 (sulfate medium) exhibits a composite reduction wave comprised between −0.75 and −1.00 V and a small oxidation shoulder at *ca.* −0.6 V (*vs.* Ag/AgCl) which correspond to redox processes involving W (see **Fig. 2.16**). At more negative potentials than −1.00 V a proton reduction wave, not shown, takes place and is

accompanied by the deposition of a solid thin film on the platinum working electrode. After 30 minutes, this shoulder becomes better and better defined in the subsequent cyclic voltammograms, developing in a separated wave centered at –0.65 V. The resulting cyclic voltammogram is very similar to that of a solution of the 'true' $[PCo(H_2O)W_{11}O_{39}]^{5-}$ in the same buffer solution (see inset in **Fig. 2.16**). The same results are observed in the cyclic voltammograms of **2.1** at pH 5 (see **Fig. 2.17**), although the voltammetric waves experience a shift to more negative potentials as a result of the pH increase, a general feature in POM electrochemistry. For **2.2** and **2.4** the cyclic voltammograms between 0.1 and –0.7 V are almost featureless, as a proton reduction wave (accompanied by a thin film deposition on the working electrode) takes place at lower potentials, avoiding the observation of the W reduction processes (see **Fig. 2.18** and **Fig. 2.19**).

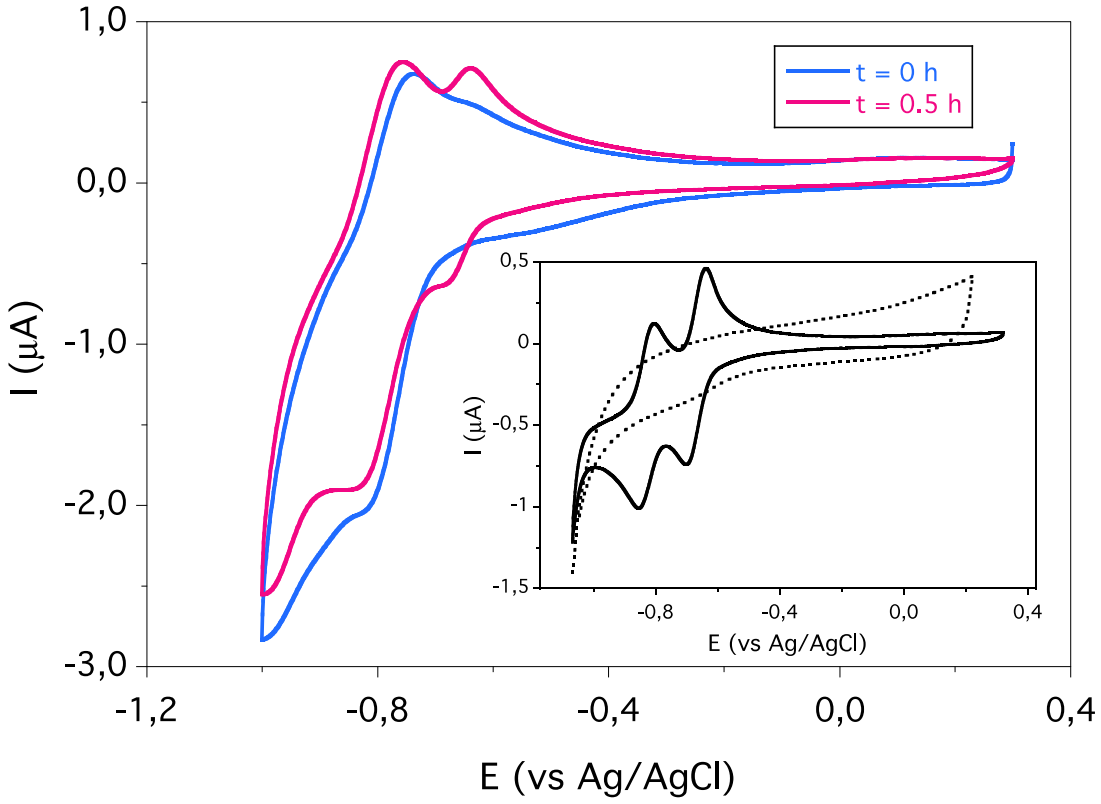

Fig. 2.16.- Comparison of an initial cyclic voltammogram of **2.1** ($5\cdot10^{-5}$ M) with the cyclic voltammogram recorded after 0.5 h (pH = 3). Inset: cyclic voltammograms of $[PCo(H_2O)W_{11}O_{39}]^{5-}$ ($3\cdot10^{-5}$ M, solid line) and $[Co(H_2O)_6]^{2+}$ ($2.5\cdot10^{-5}$ M, dotted line) in the same medium.

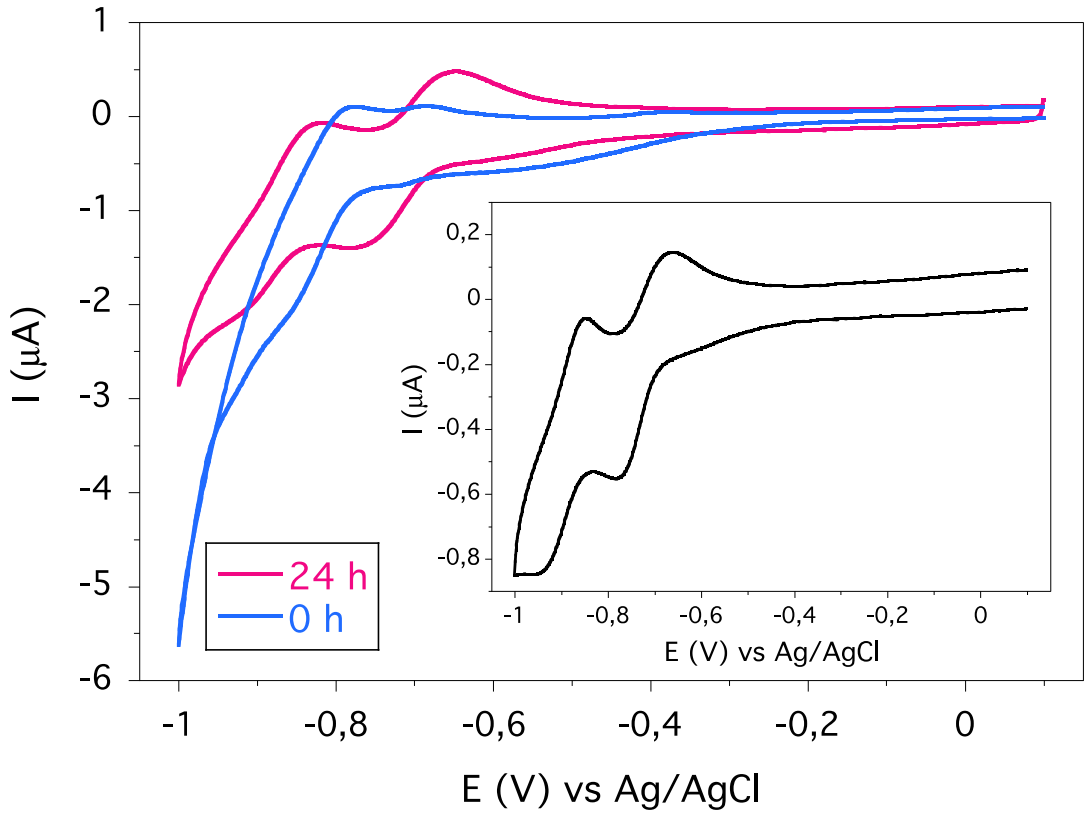

Fig. 2.17.- Comparison of an initial cyclic voltammogram of **2.1** ($5 \cdot 10^{-5}$ M) with the cyclic voltammogram recorded after 24 h (pH = 5). Inset: cyclic voltammogram of $[PCo(H_2O)W_{11}O_{39}]^{5-}$ ($3 \cdot 10^{-5}$ M) in the same medium.

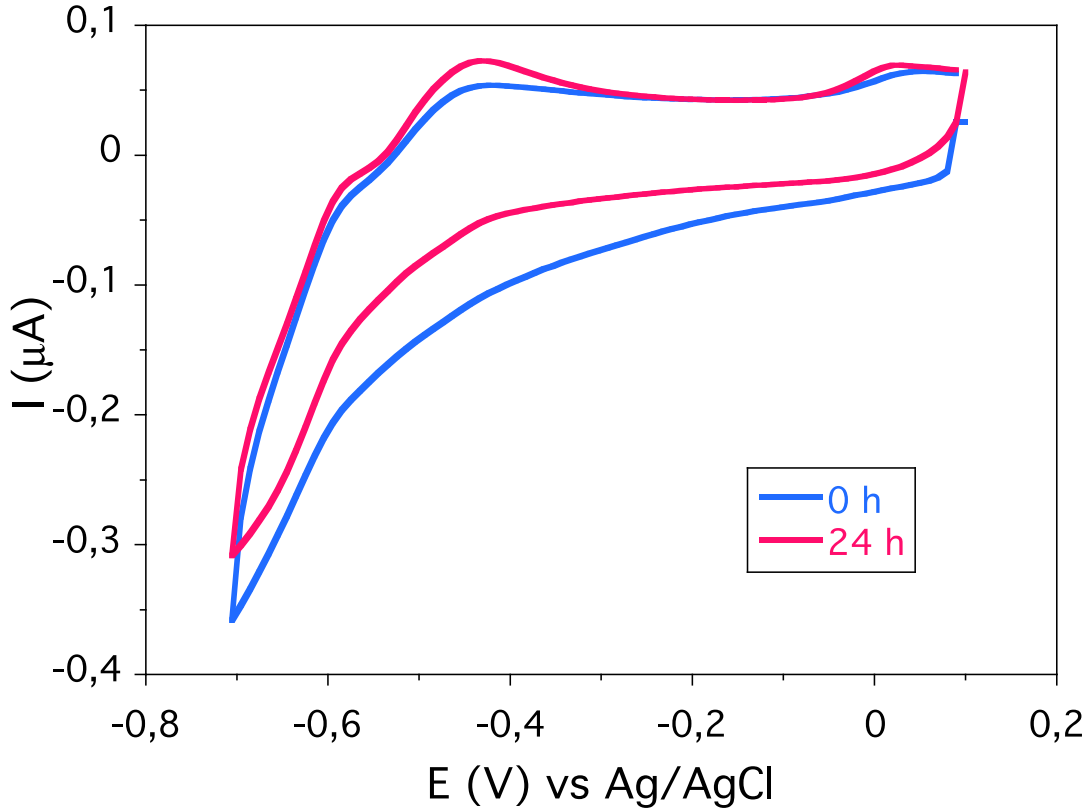

Fig. 2.18.- Comparison of an initial cyclic voltammogram of **2.4** ($5 \cdot 10^{-5}$ M) with the cyclic voltammogram recorded after 24 h (pH = 5).

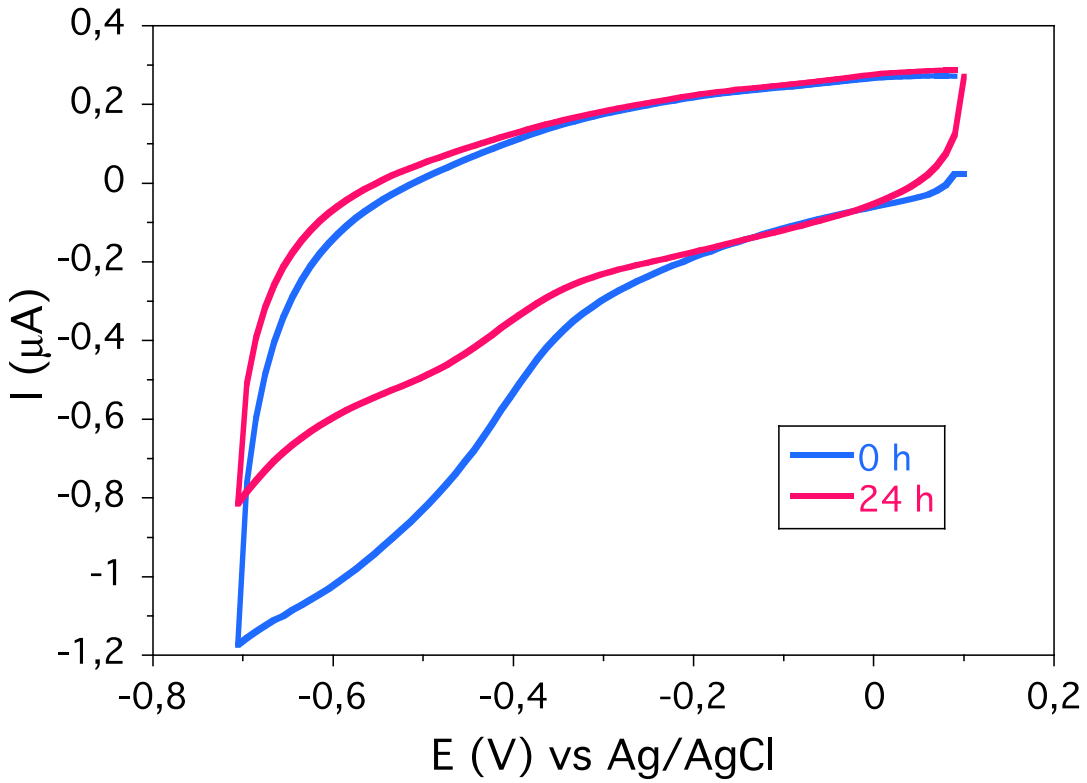

Fig. 2.19.- Comparison of an initial cyclic voltammogram of **2.4** ($5 \cdot 10^{-5}$ M) with the cyclic voltammogram recorded after 24 h (pH = 9).

Therefore, while **2.4** appears to be quite stable during the first 24h between pH 5 and 9, **2.1** and **2.2** quickly decompose upon standing in aqueous solutions in a wide pH range. The result is a mixture of decomposition products in which $[PCo(H_2O)W_{11}O_{39}]^{5-}$ appears to be the major species. Decomposition of **2.1** and **2.2** can be roughly described by the following overall chemical equations:[41]

$$11\ [Co_4(OH)_3(H_2O)_6(PW_9O_{34})]^{4-} + 63\ H^+ + 105\ H_2O \rightarrow$$
$$9\ [Co(H_2O)(PW_{11}O_{39})]^{5-} + 35\ [Co(H_2O)_6]^{2+} + 2\ (PO_4)^{3-}$$

$$44\ [Co_7(OH)_6(H_2O)_6(PW_9O_{34})_2]^{9-} + 460\ H^+ + 862\ H_2O \rightarrow$$
$$72\ [Co(H_2O)(PW_{11}O_{39})]^{5-} + 236\ [Co(H_2O)_6]^{2+} + 16\ (PO_4)^{3-} + 11\ O_2$$

2.1.2.8. Magnetic Properties

The magnetic behavior of the tetranuclear cobalt(II) cluster isolated in **2.1** is displayed in **Fig. 2.20** as a plot of the product $\chi_m T$ *vs.* T and in **Fig. 2.21** as a plot of the isothermal magnetization *vs.* H measured from 0 to 5 T at 2 and 5 K. The $\chi_m T$ *vs.* T curve exhibits a smooth and continuous decrease from room temperature ($\chi_m T$ = 16.0 emu K mol^{-1}) to a minimum at 43 K. Below this temperature, a sharp peak is observed with a maximum at 6.0 K ($\chi_m T$ = 17.6 emu K mol^{-1}). The maximum clearly depends on the magnetic field and, when the magnetic field increases, it decreases in value, shifts to higher temperature and becomes broader. The decrease in $\chi_m T$ is due to the depopulation of the single-ion Co(II) doublets upon cooling down, while the sharp increase at lower temperature indicates a ferromagnetic Co-Co interaction within the cluster (*vide infra*). Finally, the presence of a maximum is indicative of the anisotropic nature of the exchange interactions.

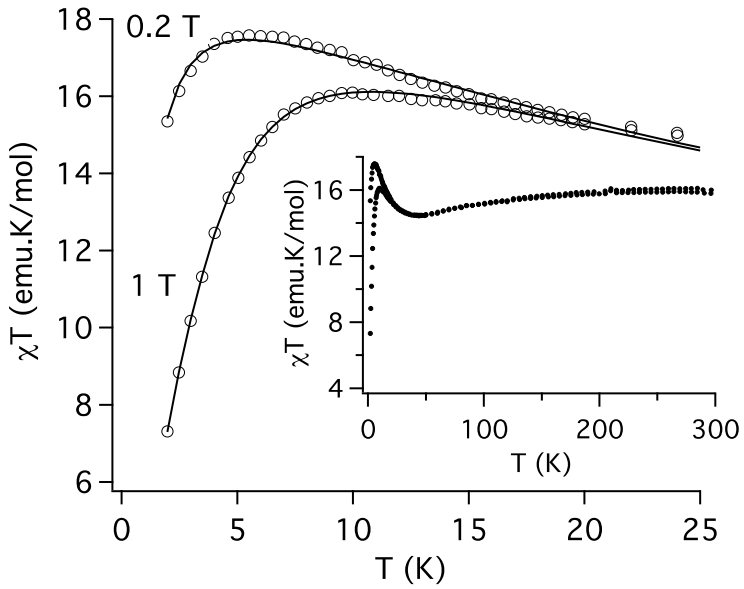

Fig. 2.20.- Thermal behavior of product susceptibility and temperature for **2.1** at 0.2 and 1.0 T. Expansion of low temperature range and fitting results are shown at inset. Solid lines represent the best fitting with the anisotropic model proposed.

The magnetic behavior of the cobalt samples containing heptameric units **2.2**, **2.3** and **2.4** are displayed in **Fig. 2.22** as a plot of $\chi_m T$ *vs.* T. **Fig. 2.23** shows a plot of the isothermal magnetization *vs.* H measured from 0 to 5 T at 2 and 5 K for **2.4**. The $\chi_m T$ *vs.* T curves exhibit a smooth and continuous decrease from room temperature

(χ_mT = 24.4 emu K mol^{-1} for **2.2**, χ_mT = 27.9 emu K mol^{-1} for **2.3**, χ_mT = 24.5 emu K mol^{-1} for **2.4**) and tend to a levelling around 30-40 K. Below this temperature, a sharp decrease is observed indicating strong antiferromagnetic interactions inside the heptameric units.

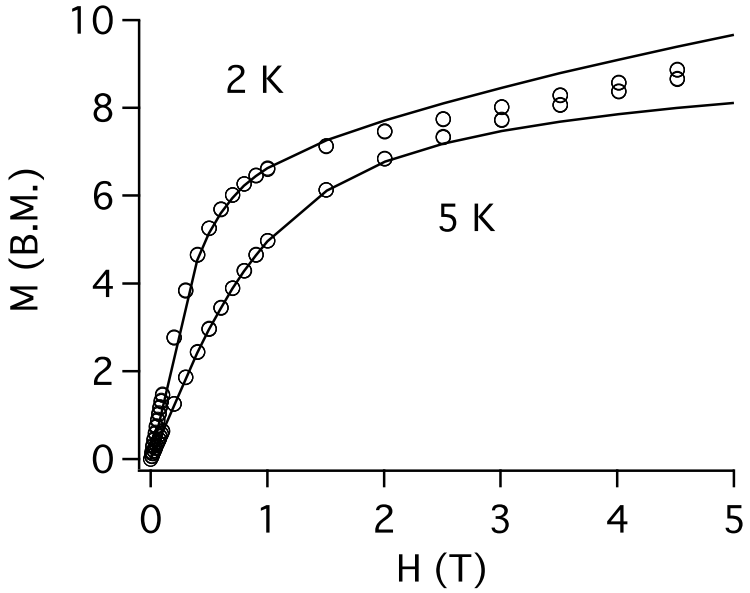

Fig. 2.21.- Magnetization *vs.* field for **2.1** at 2 and 5 K. Solid lines represent the simulation of properties with the parameter set obtained from the susceptibility fit.

Let us now analyze the experimental results using a quantitative approach. High-spin octahedral Co(II) is an orbitally degenerate ion with a $^4T_1$ ground electronic term. Due to spin-orbit coupling and the low-symmetry crystal field, this ground term splits into six Kramers doublets. The smooth decrease from room temperature in all measurements can be attributed to the depopulation of the higher Kramers doublets. Moreover, the cobalt atom in the center of the heptameric units presents typical distances of oxidation state 3+. This central cobalt should be diamagnetic due to the strong field associated with the hydroxyl groups and only plays a role of exchange pathway between the other spins. Typically, magnetic interactions between paramagnetic sites through diamagnetic metal ions are negligibly small or weakly antiferromagnetic.

At low temperature (below 30-40 K) only the lowest Kramers doublet is significantly populated so that the exchange interaction between two octahedral Co(II) ions can be conveniently described by assuming a coupling between these fully anisotropic Kramers doublets with fictitious spins 1/2.[42,43]

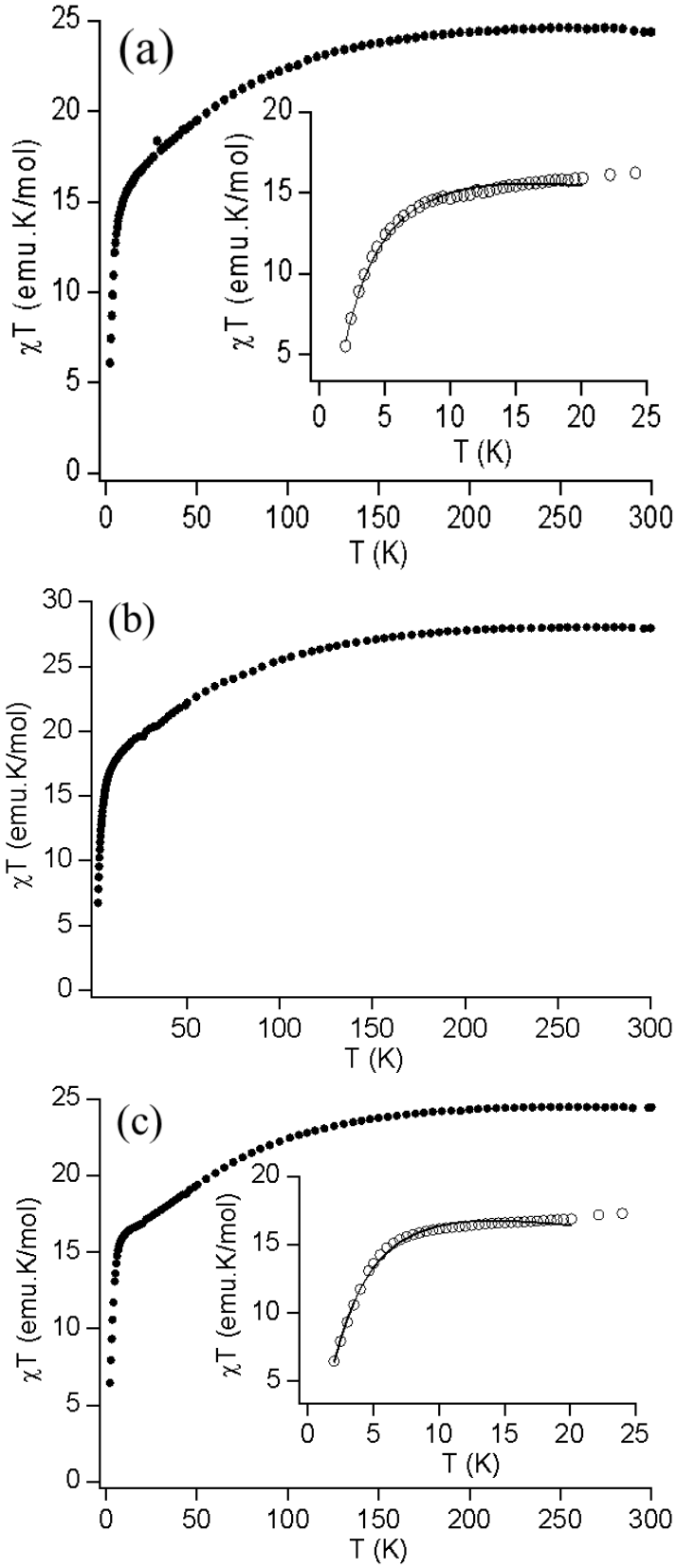

Fig. 2.22.- Thermal behavior of product susceptibility and temperature for **2.2** (a), **2.3** (b) and **2.4** (c) at 0.1 T. Expansion of low temperature range and fitting results are shown as insets. Solid lines represent the best fittings with the anisotropic model proposed.

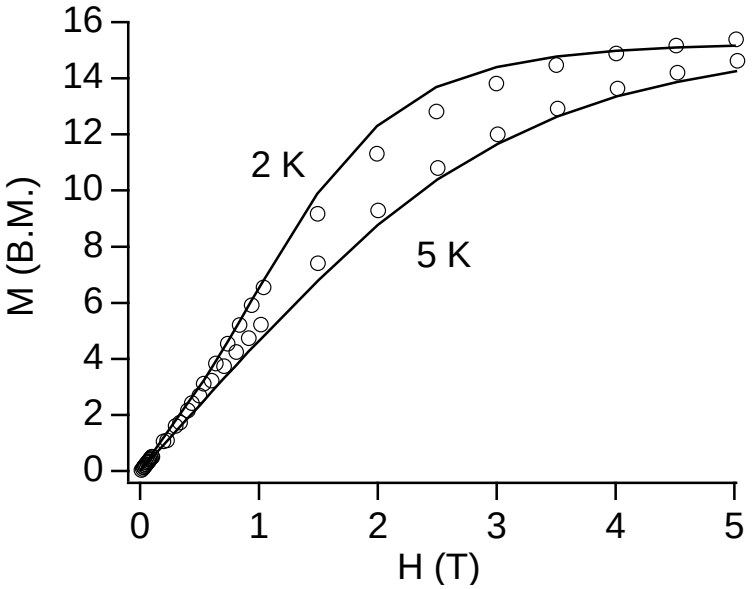

Fig. 2.23.- Magnetization *vs.* field for **2.4** at 2 and 5 K. Solid lines represent the simulation of properties with the parameter set obtained from susceptibility fit.

Taking into account all the aspects mentioned above, the effective exchange Hamiltonian for the cobalt cluster contained in **2.1** can be written as the following equation:

$$\widehat{H} = -2 \sum_{i=x,y,z} \{J_i(\hat{S}_i^2\hat{S}_i^3 + \hat{S}_i^2\hat{S}_i^4 + \hat{S}_i^3\hat{S}_i^4) + rJ_i\hat{S}_i^1(\hat{S}_i^2 + \hat{S}_i^3 + \hat{S}_i^4)\}$$

where J_i refers to the exchange components associated to the coupling between the three magnetically equivalent Co(II) coordinated to the POM (see **Fig. 2.24**). In order to avoid overparametrization, the exchange coupling between these three central cobalt ions with the apical one has been considered to be proportional to J_i, $J'_i = rJ_i$ (r is the proportionality parameter). A simultaneous fit of the two magnetic susceptibilities at two fields (0.2 and 1.0 T) was performed by numerical diagonalization of the full eigenmatrix[44,45] and gives the following sets of parameters: J_x = 15.0 cm^{-1}, J_y = 12.6 cm^{-1}, J_z = 9.3 cm^{-1}, r = 0.123, g_{av} = 5.02 where $g_{av}=(g_x+g_y+g_z)/3$ ($R=4.6\cdot10^{-5}$). To reduce the number of adjustable parameters, the three components of the tensor g were considered proportional to the square root of the corresponding component of the tensor exchange. This proportionality factor is the same for all components and the only adjustable parameter. The ferromagnetic sign of the exchange parameters for edge-sharing [CoO_6] octahedra can be associated to the orthogonality of the magnetic orbitals (Co-O-Co angles close to 90º). The validity of the exchange model and fit is confirmed by the magnitude of the exchange parameters, which is in good agreement with previously

published analogous edge-sharing oxo-cobalt clusters encapsulated by POMs.[46-52] The comparatively small value of *J'* (r ≈ 0.123) can be associated to the different nature of the ligand bridge (a double bridge formed by –O and –OH for the pairwise interaction between basal cobalt ions and a single –OH bridge for the interaction between the basal cobalt ions and the apical one) and to small changes in averaged angle Co-L-Co (values very close to orthogonality, 91°, for the basal cobalt ions, and larger values, 97.1º and 98.3º, for the angles connecting the basal cobalt ions with the apical one). Further confirmation of the model is obtained by the low-temperature behavior of the magnetization as a function of external field, which can be fitted with the same set of parameters (**Fig. 2.20**). Deviations from experimental curves at fields higher than 3 T can be due to contributions coming from excited Kramers doublets not included in the model.

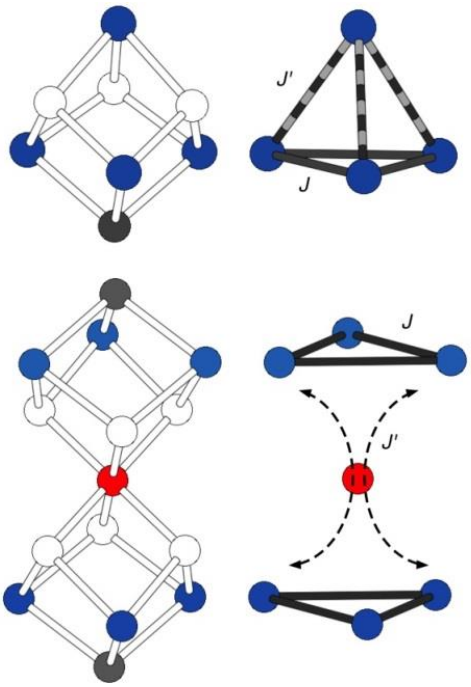

Fig. 2.24.- Schematic representation of tetranuclear $\{Co^{II}_4O_4\}$ and heptanuclear $\{Co^{II}_6Co^{III}O_8\}$ cores (colour code: Co(II) blue, Co(III) red, O^{2-} grey and OH^- white). Exchange networks of the corresponding magnetic clusters show a dominant intratrimer exchange pathway, *J* (depicted as full rod) and a weaker exchange interaction (depicted as a dashed rod in the tetramer and as a dashed line in the heptamer), which corresponds to the magnetic coupling between the basal triangular unit and the apical one.

In the case of the heptanuclear cobalt clusters isolated in **2.2**, **2.3** and **2.4**, the effective exchange Hamiltonian can be written as the following equation:

$$\hat{H} = -2 \sum_{i=x,y,z} \{J_i(\hat{S}_i^1\hat{S}_i^2 + \hat{S}_i^1\hat{S}_i^3 + \hat{S}_i^2\hat{S}_i^3 + \hat{S}_i^4\hat{S}_i^5 + \hat{S}_i^4\hat{S}_i^6 + \hat{S}_i^5\hat{S}_i^6) + 2J'(\hat{S}^1 + \hat{S}^2 + \hat{S}^3)(\hat{S}^4 + \hat{S}^5 + \hat{S}^6)\}$$

where J_i is the exchange components associated to the pathway between the three magnetically equivalent cobalt ions on each trinuclear units. On the other hand, J' is associated to the exchange interaction between cobalt ions from different trinuclear units through the diamagnetic central Co(III). In order to simplify the number of parameters, this last interaction has been considered isotropic and equal between all of them. For **2.2** and **2.4**, fittings of magnetic susceptibilities at 0.1 T were performed by numerical diagonalization of the full eigenmatrix and give the following sets of parameters: J_x = 12.7 cm^{-1}, J_y = 11.0 cm^{-1}, J_z = 10.23 cm^{-1}, J' = –0.333 cm^{-1}, g_{av} = 4.29 (R = $2.5 \cdot 10^{-4}$) for **2.2** and J_x = 10.6 cm^{-1}, J_y = 7.7 cm^{-1}, J_z = 9.9 cm^{-1}, J' = –0.380 cm^{-1}, g_{av}= 4.41 (R = $2.9 \cdot 10^{-4}$) for **2.4**. Again, the exchange coupling between the Co(II) ions belonging to the trinuclear units is ferromagnetic due to the same reasons explained above and with similar magnitude to other previously studied cobalt systems. In this case, the antiferromagnetic interaction between trimeric units through the Co(III) leads to antiferromagnetic S = 0 ground state for the heptameric cluster. This also results in the fact that the susceptibility is far less sensitive to anisotropy; therefore, the extracted ferromagnetic exchange tensor is more isotropic in these clusters than in **2.1**. **2.3** has not been fitted due to the presence of an additional isolated cobalt atom outside heptanuclear cluster, leading to overparametrization. However, the magnetic behavior of this cluster is similar to that observed in the previous compounds suggesting that the exchange parameters inside the heptanuclear unit should be very close to those of **2.2**.

2.1.3. Conclusions

Four new cobalt-substituted POMs have been synthesized containing cobalt cores exhibiting cubane (**2.1**) or dicubane topologies (**2.2**, **2.3** and **2.4**). These cobalt clusters are encapsulated by the heptadentate lacunary POM units B-α-$[PW_9O_{34}]^{9-}$ (in **2.1**, **2.2** and **2.3**) or α-$[P_2W_{15}O_{56}]^{15-}$ (in **2.4**) and represent the first isolated cobalt clusters of this type in POM chemistry. Additionally, the dicubane clusters contain six Co(II) ions and one central Co(III) ion and, then, represent rare examples of cobalt clusters encapsulated by POMs having cobalt in both oxidation states. The occurrence of the oxidation state 3+ is due to the coordination environment of the central cobalt, which is made of six hydroxyl ligands. The preparation of all these POMs has been elusive till now because they are formed as minor byproducts during the synthesis of the more stable and well known

tetracobalt sandwich POMs $[Co_4(H_2O)_2(PW_9O_{34})_2]^{10-}$ and $[Co_4(H_2O)_2(P_2W_{15}O_{56})_2]^{16-}$. Hence, these species must be removed from the reaction mixture (for example, by precipitation with Cs^+ cations) to achieve the isolation and crystallization of **2.1**, **2.2**, **2.3** and **2.4**. From the structural point of view, **2.1**, **2.2** and **2.4** crystallize as alkaline ion salts of isolated polyoxoanions, while **2.3** consists of polymeric chains formed by individual POM units similar to the ones found in **2.2** that are connected through two Co-O-W bridges. The stability of **2.1**, **2.2** and **2.4** in aqueous solution has been assessed using UV-vis spectroscopy suggesting that, while **2.1** and **2.2** partially decompose into the species $[PCo(H_2O)W_{11}O_{39}]^{5-}$, **2.4** is more stable in the pH range 5-9.

From the magnetic point of view, the tetrameric Co_4 cluster contained in **2.1** exhibits ferromagnetic interactions between the three magnetically equivalent Co(II) coordinated to the POM (trimer) and also between each of them and the apical Co(II). Its magnetic behavior has been modeled assuming a dominant anisotropic exchange interaction within the trimer, and a much weaker exchange interaction of this trimer with the apical Co(II). The ferromagnetic nature of these exchange interactions is consistent with the angles Co-L-Co (L = O, OH), which are close to orthogonality. Complexes **2.2**, **2.3** and **2.4** exhibit an antiferromagnetic behavior at very low temperature due to the antiferromagnetic interaction between the two trimeric Co_3 units, which are ferromagnetically coupled.

At this point, one can notice that the spin structures exhibited by these two cluster topologies show some unique features. Thus, since the coupling within the basal Co_3 triangle is much stronger than that between these cobalt atoms and the apical one, the ground state of the tetranuclear Co(II) cluster (compound **2.1**) can be viewed as resulting from a weak interaction between two different spin doublets: a doublet, $|S, M\rangle = |3/2, \pm 1/2\rangle$, coming from a ferromagnetic anisotropic interaction between the three basal cobalt atoms, and the fundamental Kramers doublet coming from the apical cobalt. This feature is in sharp contrast with that encountered in other cobalt trimers (with triangular or linear topologies)[46,47] and in rhomb-like centrosymmetrical cobalt tetramers encapsulated by POMs.[50] In the trimeric clusters, direct access to energy levels by INS spectroscopy shows that these systems have a doublet ground state well separated in energy from the first excited one.[46,47] As for the rhomblike tetramer formed by four coplanar edge-sharing $[CoO_6]$ octahedra, its energy scheme consists of a doublet ground state very stable compared to other levels due to strong ferromagnetic anisotropic coupling between the four cobalt atoms.[53] In contrast, complex **2.1** presents, as a result of the interaction between two nonequivalent spin doublets coming from two different units

(mononuclear and trinuclear), an energy scheme with 4 levels ranging over 5 cm^{-1}. This situation may be useful to provide a 2-qubit quantum gate.[54] Obviously, a detailed description of its low-lying energy levels and wave functions, as that provided by INS, will be also very useful to check this possibility.

In the case of the heptanuclear systems (**2.2**, **2.3** and **2.4**), its magnetic properties can be interpreted on the basis of an antiferromagnetic coupling between two identical ferromagnetically coupled trinuclear units. As discussed above, each trinuclear unit has an energy scheme with only doubly degenerate levels. The antiferromagnetic coupling between these two units results in a complex level scheme with a diamagnetic ground state (S = 0) quasidegenerate with an antisymmetric combination of ±M functions. In view of this result, this molecule can be a candidate of electrically responsive magnetic molecule in which its ground spin state can be changed by application of an external electric field.[55-58]

2.1.4. Experimental Section

2.1.4.1. General Methods and Materials

All reagents were of high purity grade quality, obtained from commercial sources, and used without further purification. Pure water ($\rho > 18$ MΩ·cm) was used throughout. It was obtained using an Elix-3/Millipore-Q Academic water purification system. IR spectra were recorded with KBr pellets on a Thermo NICOLET-5700 FT-IR spectrophotometer. The UV-vis spectra of the relevant POM were recorded on an Agilent 8453 UV-vis spectrophotometer from 190 to 400 nm using 10-mm-optical-path quartz cuvettes in three different buffer solutions: 0.2 M sodium sulfate (pH 3), 0.4 M sodium acetate (pH 5) and 25 mM sodium borate (pH 9). Elemental analysis was performed at the Universidad Complutense de Madrid (CAI de Técnicas Geológicas) by inductively-coupled-plasma optical-emission-spectroscopy (ICP-OES) on solutions prepared by treating the POMs in a hydrofluoric acid/hydrochloric acid mixture of ratio 1:8 and diluted with water to a known volume. Thermogravimetric analyses were performed on a Mettler Toledo TGA/SDTA851e analyzer. Cyclic voltammetry measurements were carried out on an Autolab PGSTAT12 potentiostat using a three-electrode single compartment cell supplied by IJ Cambria. It was equipped with a 3 mm glassy carbon disc working electrode (which was polished sequentially with 0.3, 0.1 and 0.05 μm

alumina powders and washed with distilled water before each experiment), a platinum wire counter electrode and a Ag/AgCl (3M KCl) reference electrode. All cyclic voltammograms were recorded at a scan rate of 10 $mV \cdot s^{-1}$ using the same media and concentrations as for UV-vis spectroscopy. The solutions were deaerated during at least 15 min with argon and kept under a positive pressure of this gas during the experiments.

2.1.4.2. Synthesis

*2.1.4.2.1. Synthesis of $Na_{1.5}Cs_{2.5}[Co_4(OH)_3(H_2O)_6(PW_9O_{34})]\cdot 9H_2O$ (**Q-2.1**)*

2.05 g (25 mmol) of CH_3COONa and 1.24 g (4.41 mmol) of $CoSO_4\cdot 7H_2O$ were dissolved in 50 mL of water, producing an aqueous solution with a pH of 7.5. Then, 2.42 g (1 mmol) of freshly prepared, solid $Na_8H[B\text{-}\alpha\text{-}PW_9O_{34}]$ (synthetized according to a literature method)[59] were added in small portions, with stirring, to the previous solution. When the addition was completed, the solution was stirred during 30 min, heated to 80 ºC for 20 min and then allowed to cool down to room temperature (pH 6.6). At this point, 0.854 g (5.07 mmol) of CsCl were added in small portions producing a violet precipitate which was filtered out (dry weight 1.84 g) and identified as a mixed cesium/sodium salt of the well-known tetracobalt sandwich polyoxoanion $[Co_4(H_2O)_2(PW_9O_{34})_2]^{10-}$ by IR spectroscopy (see **Fig. 2.25**). The filtrate was kept in an open container at room temperature and, after five days, pink, needle-shaped crystals were obtained, filtered, washed with cold water and air dried (yield: 0.143 g; 5 % based on $B\text{-}\alpha\text{-}[PW_9O_{34}]^{9-}$).

Anal. Calcd (Found) for $Na_{1.5}Cs_{2.5}[Co_4(OH)_3(H_2O)_6(PW_9O_{34})]\cdot 9H_2O$: P, 0.98 (0.90); W 52.47 (50.4); Co 7.48 (6.8); Cs 10.54 (11.0); Na 1.09 (0.84). IR (2 % KBr pellet 1100–400 cm^{-1}, see **Fig. 2.26**): 1077 (m), 1026 (s), 951(m, sh), 933 (s), 887 (s), 793 (w), 728 (s), 588 (w), 484 (w). The TG curve of **Q-2.1** (**Fig. 2.27**) shows a total weight loss of 10.34 % in the range 30-500 ºC, which agrees with the loss of 15 water molecules and 3 hydroxyls in the structure (calcd 10.19 %). The powder X-ray diffraction pattern of this compound has been collected to confirm the phase purity of the bulk compound (**Fig. 2.28**).

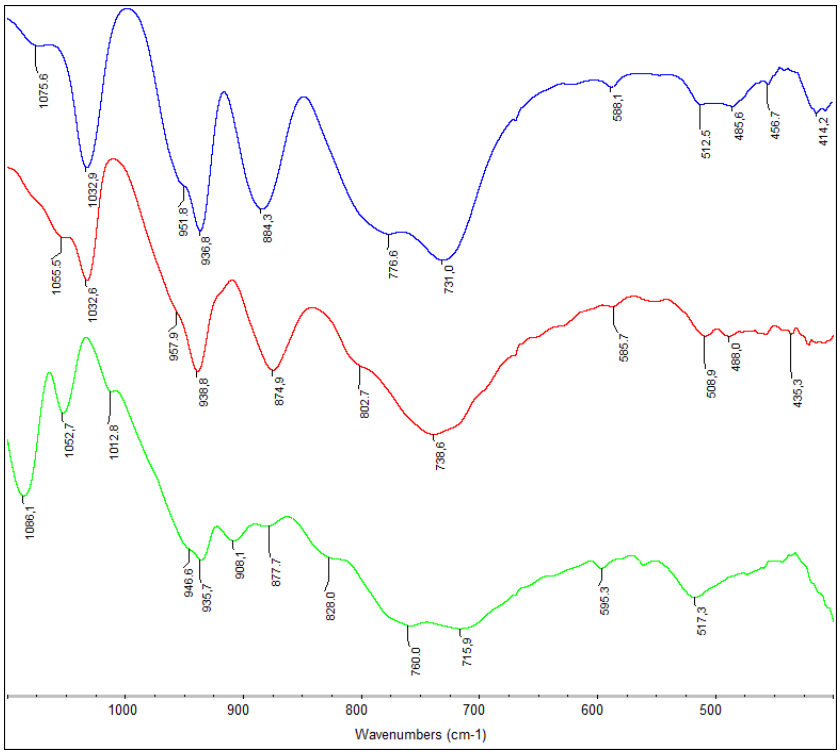

Fig. 2.25.- FT-IR spectra of the precipitates obtained when CsCl is added during the synthesis of **Q-2.1** (blue), **Q-2.3** (red), and **Q-2.4** (cyan) which allow their identification as mixed cesium/sodium salts of the tetracobalt sandwich compounds $[Co^{II}_4(H_2O)_2(PW_9O_{34})_2]^{10-}$, $[(Co^{II}/Co^{III})_4(H_2O)_2(PW_9O_{34})_2]^{n-}$ and $[Co_4(H_2O)_2(P_2W_{15}O_{56})_2]^{16-}$ respectively, by comparison with the spectra of the original potassium or sodium salts of these polyanions.[32]

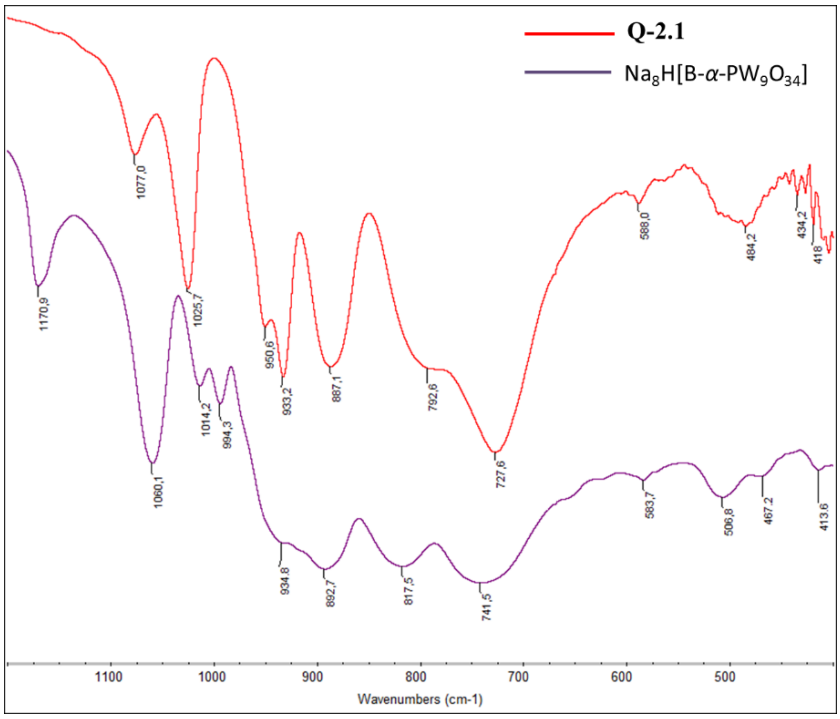

Fig. 2.26.- FT-IR spectra of the precursor $Na_8H[B\text{-}\alpha\text{-}PW_9O_{34}]$ and the product **Q-2.1**.

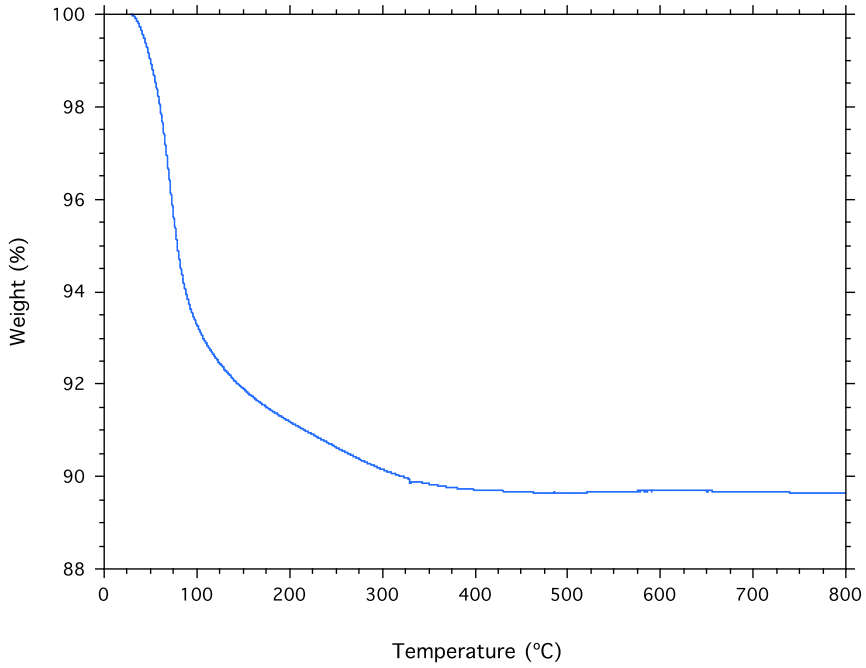

Fig. 2.27.- Thermogram of **Q-2.1** from room temperature to 800 °C (experimental total weight loss 10.34 %).

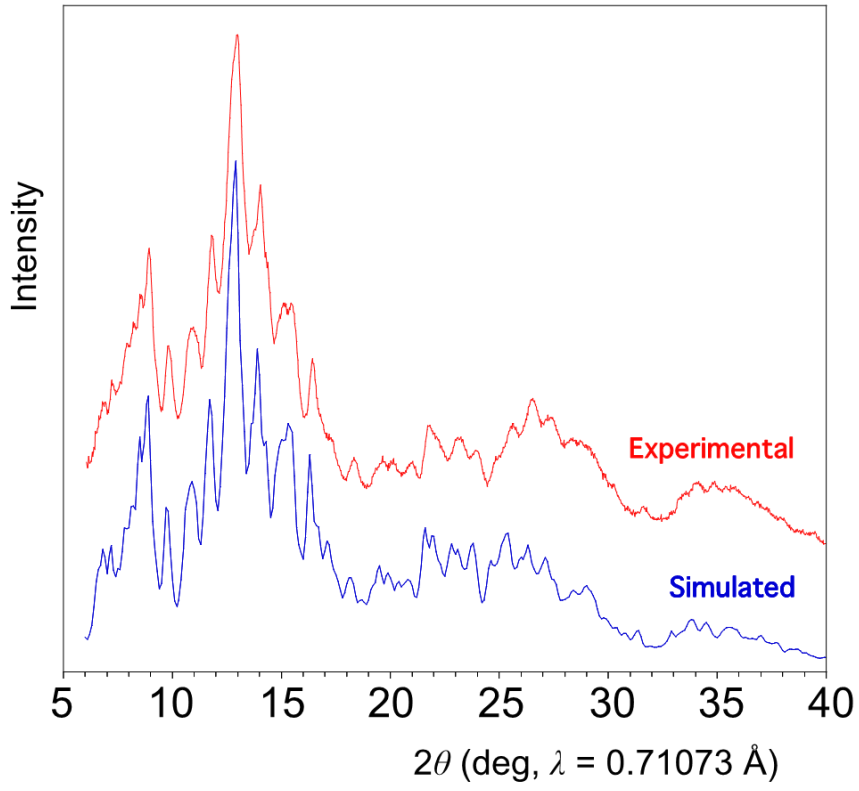

Fig. 2.28.- Comparison of simulated and experimental powder X-ray diffraction patterns for compound **Q-2.1**. The experimental powder X-ray diffraction pattern was obtained from powdered samples in an *Oxford Diffraction Supernova* diffractometer. The simulated pattern was generated from the atomic coordinates of the single-crystal structure solution using the program Mercury 3.0 (copyright CCDC, http://www.ccdc.cam.ac.uk/mercury/) and a FWHM (full width at half maximum) of 0.2.

*2.1.4.2.2. Synthesis of $Cs_7Na_2[Co_7(OH)_6(H_2O)_6(PW_9O_{34})_2]\cdot 20H_2O$ (**Q-2.2**)*

The synthetic procedure was similar to that for **Q-2.1** but, after the filtration of the violet precipitate, 0.024 g (0.09 mmol) of $K_2S_2O_8$ was added to the filtrate and the solution heated again to 80 ºC for 1 hour. The mixture was allowed to cool down to room temperature and filtered again. The resultant orange solution was kept in an open container and after 1 day orange, thin, layered crystals were obtained, filtered, washed with cold water and air dried (yield: 0.224 g; 7 % based on B-α-$[PW_9O_{34}]^{9-}$).

Anal. Calcd (Found) for $Cs_7Na_2[Co_7(OH)_6(H_2O)_6(PW_9O_{34})_2]\cdot 20H_2O$: P, 0.97 (0.84); W 51.56 (51.4); Co 6.43 (5.9); Cs 14.50 (13.5); Na 0.72 (0.57). IR (2 % KBr pellet 1100–400 cm^{-1}, see **Fig. 2.29**): 1062 (m), 1027 (s), 977 (m, sh), 952 (m, sh), 935 (s), 878 (s), 806 (s), 779 (m, sh), 721 (s), 588 (w), 540 (w), 514 (w), 484 (w), 444 (w), 422 (w). The TG curve of **Q-2.2** (**Fig. 2.30**) shows a total weight loss of 9.25 % in the range 30-500 ºC, which agrees with the loss of 26 water molecules and 6 hydroxyls in the structure (calcd 8.89 %). The powder X-ray diffraction pattern of this compound has been collected to confirm the phase purity of the bulk compound (**Fig. 2.31**).

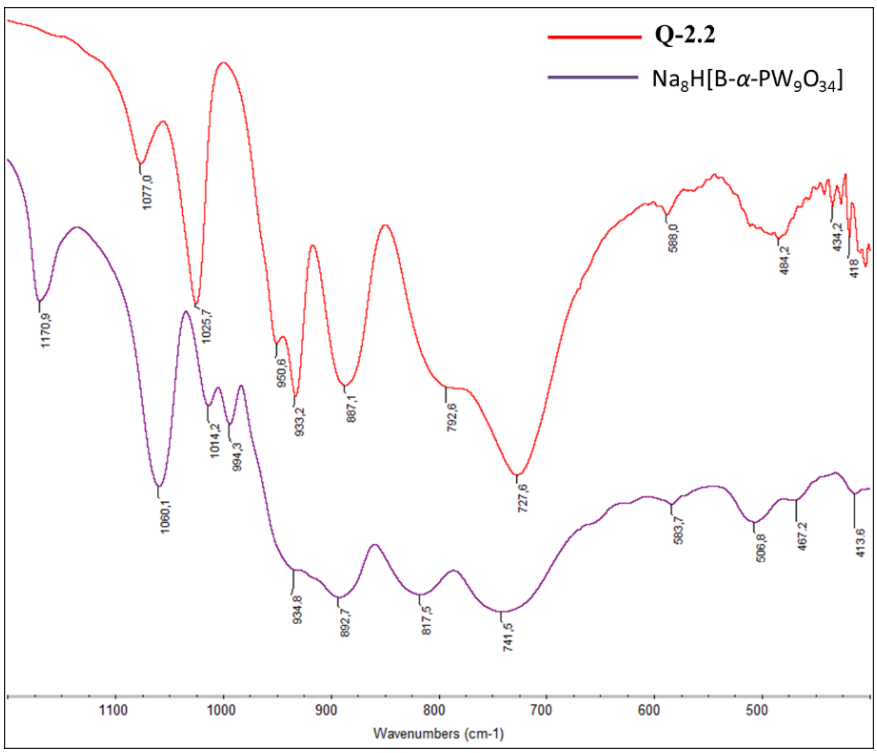

Fig. 2.29.- FT-IR spectra of the POM precursor $Na_8H[B\text{-}\alpha\text{-}PW_9O_{34}]$ and the product **Q-2.2.**

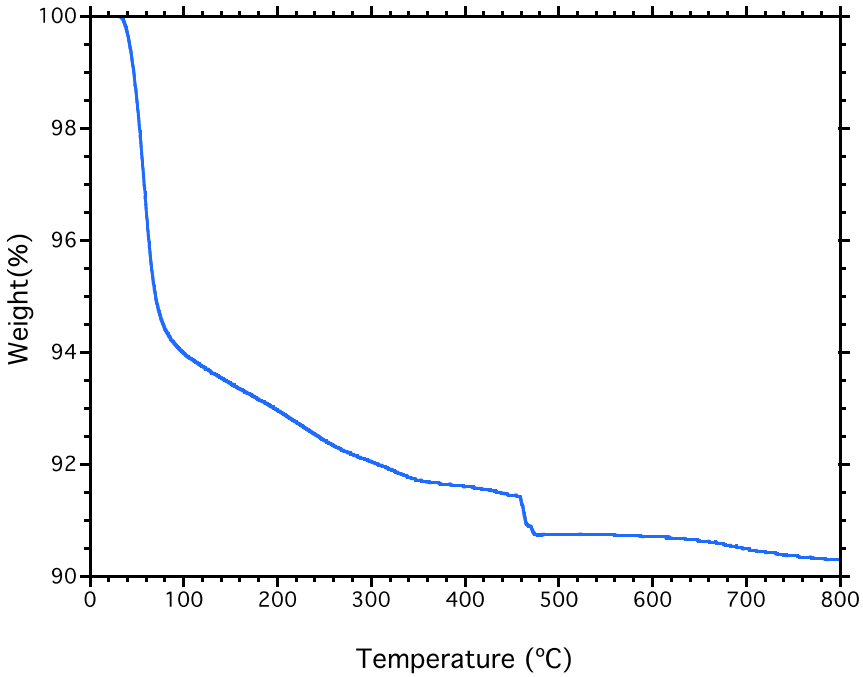

Fig. 2.30.- Thermogram of **Q-2.2** from room temperature to 800 °C (experimental total weight loss 9.25 %).

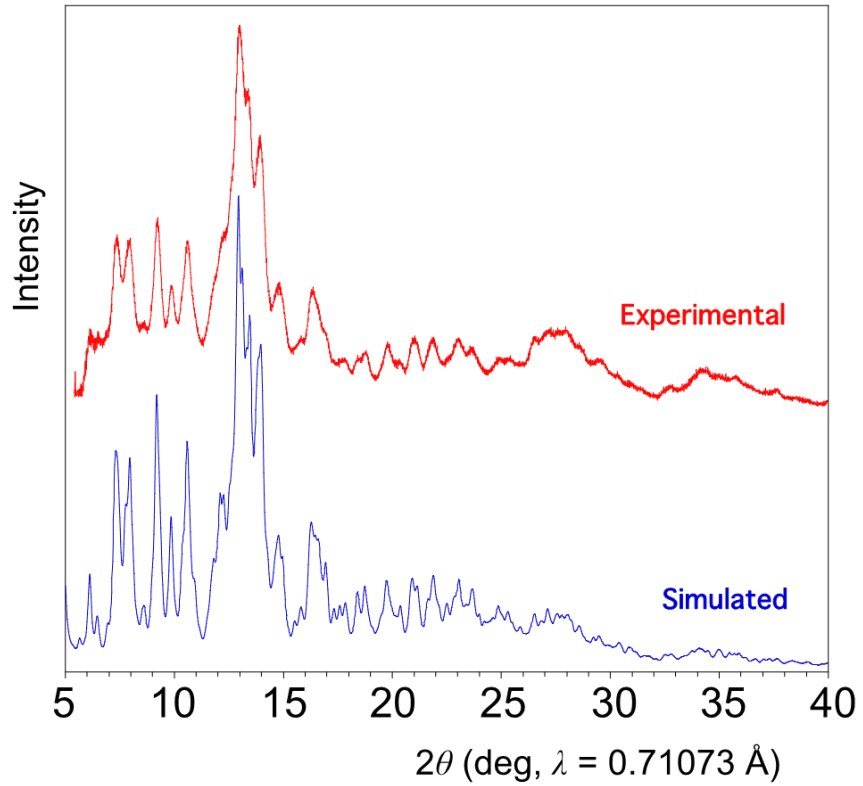

Fig. 2.31.- Comparison of simulated and experimental powder X-ray diffraction patterns for compound **Q-2.2**. The experimental powder X-ray diffraction pattern was obtained from powdered samples in an *Oxford Diffraction Supernova* diffractometer. The simulated pattern was generated from the atomic coordinates of the single-crystal structure solutions using the program Mercury 3.0 (copyright CCDC, http://www.ccdc.cam.ac.uk/mercury/) and a FWHM (full width at half maximum) of 0.2.

*2.1.4.2.3. Synthesis of $K_{5n}Na_{2n}\{Co(H_2O)_2\}_n[Co_7(OH)_6(H_2O)_4(PW_9O_{34})_2]_n \cdot 20nH_2O$ (**Q-2.3**)*

21.60 g (65.6 mmol) of $Na_2WO_4 \cdot 2H_2O$ and 0.84 g (5.92 mmol) of Na_2HPO_4 were dissolved in 60 mL of water and the pH of the solution adjusted to 5.5 using glacial acetic acid. Another aqueous solution containing 5.16 g (20.72 mmol) of $Co(CH_3COO)_2 \cdot 4H_2O$ in 100 mL of water was added dropwise to the first one and the pH of the resultant solution adjusted again to 5.5 using glacial acetic acid. Then, the solution was refluxed for 2 hours and hot filtered. To the hot filtrate, 8.96 g (91.2 mmol) of potassium acetate and 0.44 g (1.63 mmol) of $K_2S_2O_8$ were successively added in small portions. After the addition of the solids, the solution was concentrated at 80 ºC until a final volume of 120 mL was attained. Then, the solution was allowed to cool down to room temperature and a large amount of black precipitate was formed which was filtered, washed with cold water and air-dried (9.42 g). The IR spectra of this precipitate (see **Fig. 2.25**) is almost identical to the corresponding spectra of the tetracobalt sandwich polyoxoanion $[Co^{II}_4(H_2O)_2(PW_9O_{34})_2]^{10-}$, although its black colour indicates that one or more cobalt ions bear an oxidation state of 3+. The filtrate was allowed to stand at room temperature in an open container and, after one night, a brown precipitate was formed which was filtered and recrystallized in water to afford 35 mg (yield < 1 %) of orange-brown, plate-like crystals.

Anal. Calcd (Found) for $K_{5n}Na_{2n}\{Co(H_2O)_2\}_n[Co_7(OH)_6(H_2O)_4(PW_9O_{34})_2] \cdot 20nH_2O$: P, 1.08 (1.30); W 57.63 (57.4); Co 8.21 (7.5); K 3.40 (3.6); Na 0.80 (0.61). IR (2 % KBr pellet 1100–400 cm^{-1}, see **Fig. 2.32**): 1062 (m), 1028 (s), 952 (m, sh), 935 (s), 880 (s), 804 (s), 780 (m, sh), 721 (s), 588 (w), 539 (w), 508 (w), 481 (w), 415 (w). The TG curve of **Q-2.3** (**Fig. 2.33**) shows a total weight loss of 10.14 % in the range 30-380 ºC, which agrees with the loss of 26 water molecules and 6 hydroxyls in the structure (calcd 9.93 %). The powder X-ray diffraction pattern of this compound has been collected to confirm the phase purity of the bulk compound (**Fig. 2.34**).

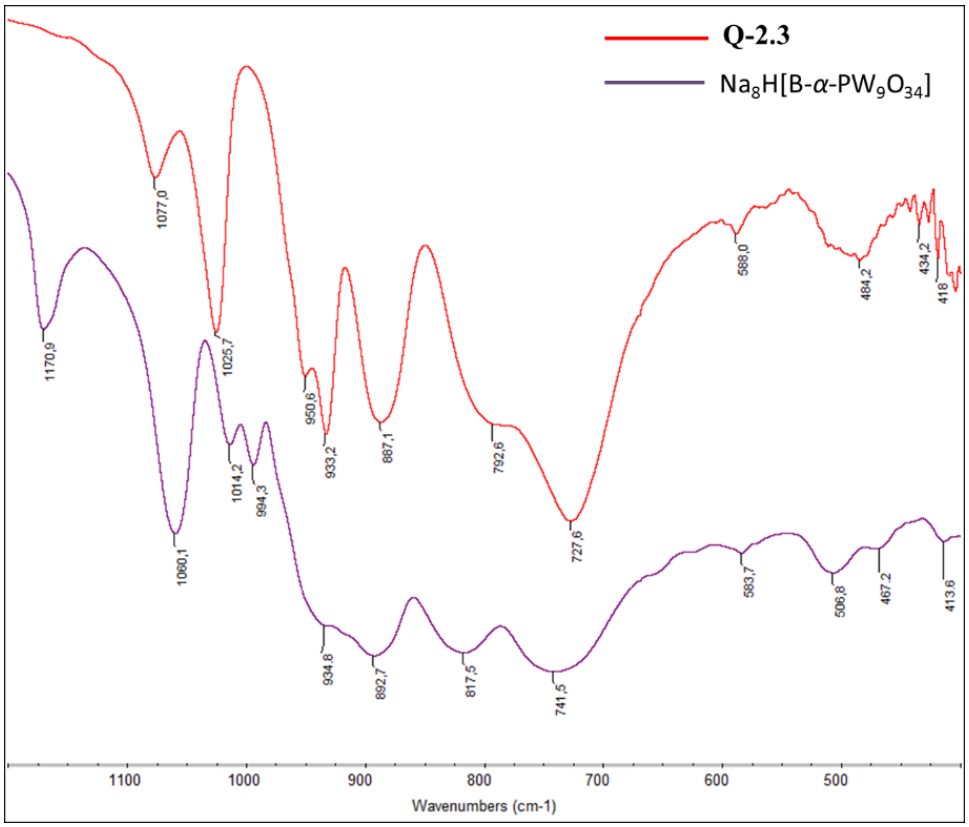

Fig. 2.32.- FT-IR spectra of the POM precursor $Na_8H[B\text{-}\alpha\text{-}PW_9O_{34}]$ and the product **Q-2.3**.

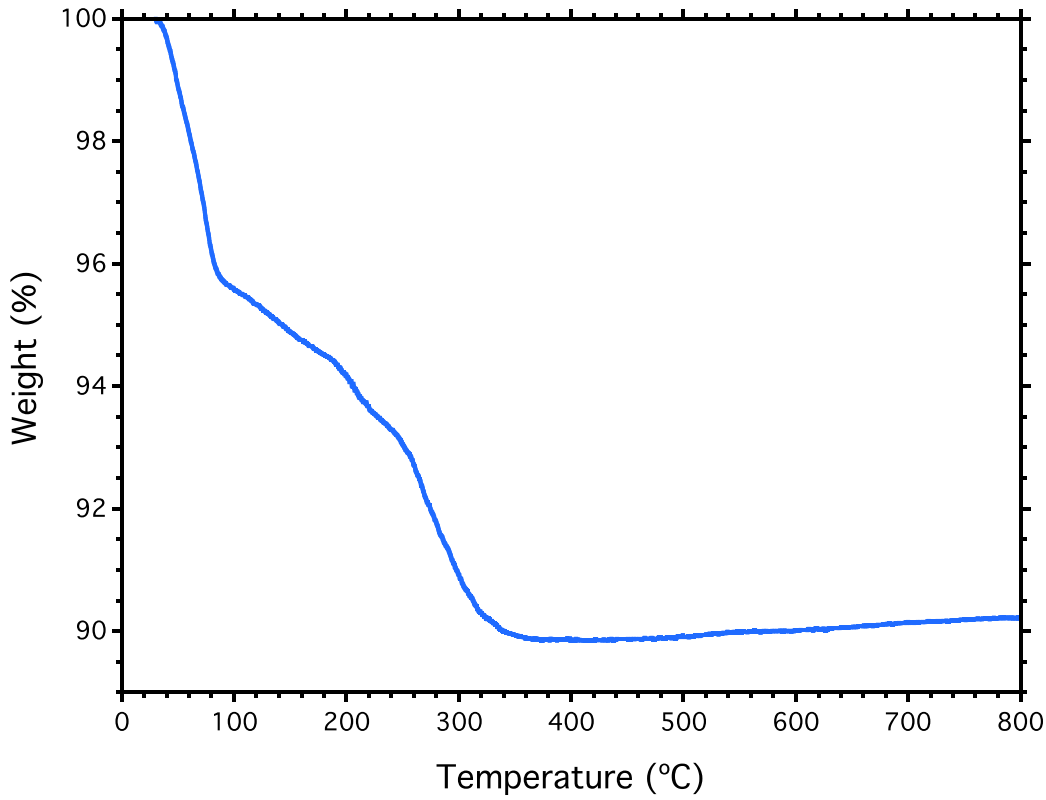

Fig. 2.33.- Thermogram of **Q-2.3** from room temperature to 800 °C (experimental total weight loss 10.14 %).

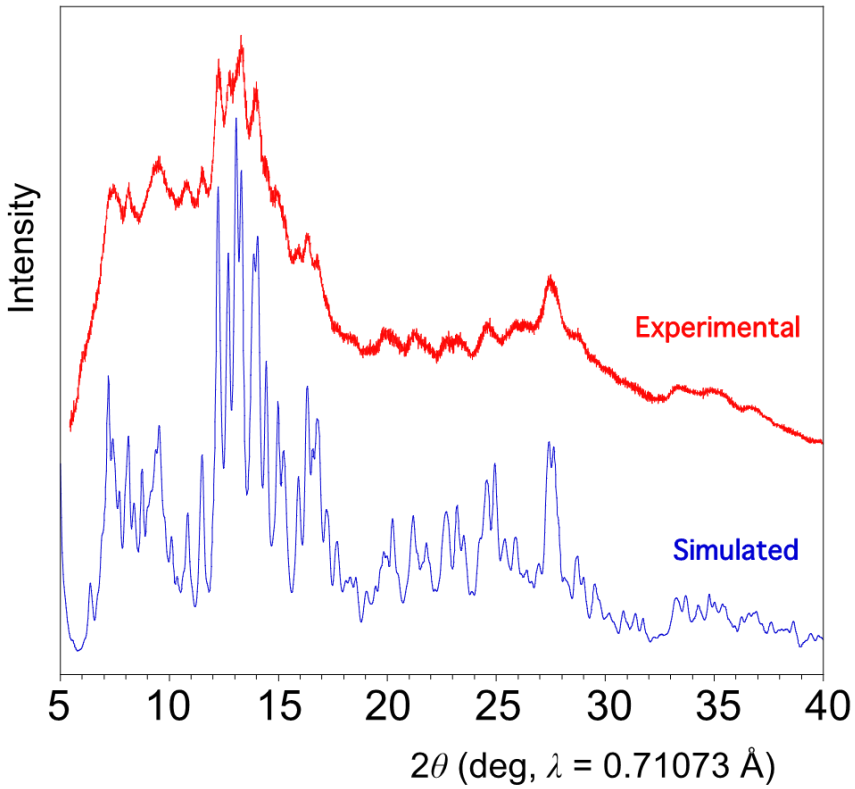

Fig. 2.34.- Comparison of simulated and experimental powder X-ray diffraction patterns for compound **Q-2.3**. The experimental powder X-ray diffraction pattern was obtained from powdered samples in an *Oxford Diffraction Supernova* diffractometer. The simulated pattern was generated from the atomic coordinates of the single-crystal structure solutions using the program Mercury 3.0 (copyright CCDC, http://www.ccdc.cam.ac.uk/mercury/) and a FWHM (full width at half maximum) of 0.2.

*2.1.4.2.4. Synthesis of $Na_{15}[Co_7(OH)_6(H_2O)_6(P_2W_{15}O_{56})_2]\cdot 38H_2O$ (**Q-2.4**)*

A solution of 0.192 g (1.30 mmol) of $CH_2(COONa)_2$ in 10 mL of water was added to 15 mL of an aqueous solution containing 0.527 g (1.81 mmol) of $Co(NO_3)_2\cdot 6H_2O$. To the resulting pink solution (pH 6.8), 0.800 g (0.181 mmol) of solid $Na_{12}[\alpha\text{-}P_2W_{15}O_{56}]\cdot 24H_2O$ (synthetized according to a literature method)[59] were added in small portions with stirring causing a colour change, from pink to light red. The solution was stirred during 2 h (pH 5.9), heated to 80 ºC for 30 min and then allowed to cool down to room temperature. At this point, 0.018 g (0.011 mmol) of CsCl were added in small portions producing a reddish precipitate which was filtered out and identified as a cesium/sodium salt of $[Co_4(H_2O)_2(P_2W_{15}O_{56})_2]^{16-}$ by IR spectroscopy (see **Fig. 2.25**). The filtrate was kept in an open container at room temperature and, over the next days, its colour changed gradually from red to orange. After 14 days, orange, plate-like crystals

were obtained, filtered, washed with cold water and air dried (yield: 0.128 g; 8 % based on α-$[P_2W_{15}O_{56}]^{12-}$).

Anal. Calcd (Found) for $Na_{15}[Co_7(OH)_6(H_2O)_6(P_2W_{15}O_{56})_2]\cdot 38H_2O$: P, 1.36 (1.30); W 60.7 (57.2); Co 4.54 (5.2); Na 3.80 (2.2). IR (2 % KBr pellet 1100–400 cm^{-1}, see **Fig. 2.35**): 1085 (s), 1043 (m), 1007 (m, sh), 976 (m, sh), 947 (m, sh), 934 (s), 908 (s), 881 (s), 823 (s), 728 (s), 599 (w), 561(w), 528 (w), 456 (w). The TG curve of **Q-2.4** (**Fig. 2.36**) shows a total weight loss of 9.78 % in the range 30-500 ºC which agrees with the loss of 44 water molecules and 6 hydroxyls in the structure (calcd 9.85 %). The powder X-ray diffraction pattern of this compound has been collected to confirm the phase purity of the bulk compound (**Fig. 2.37**).

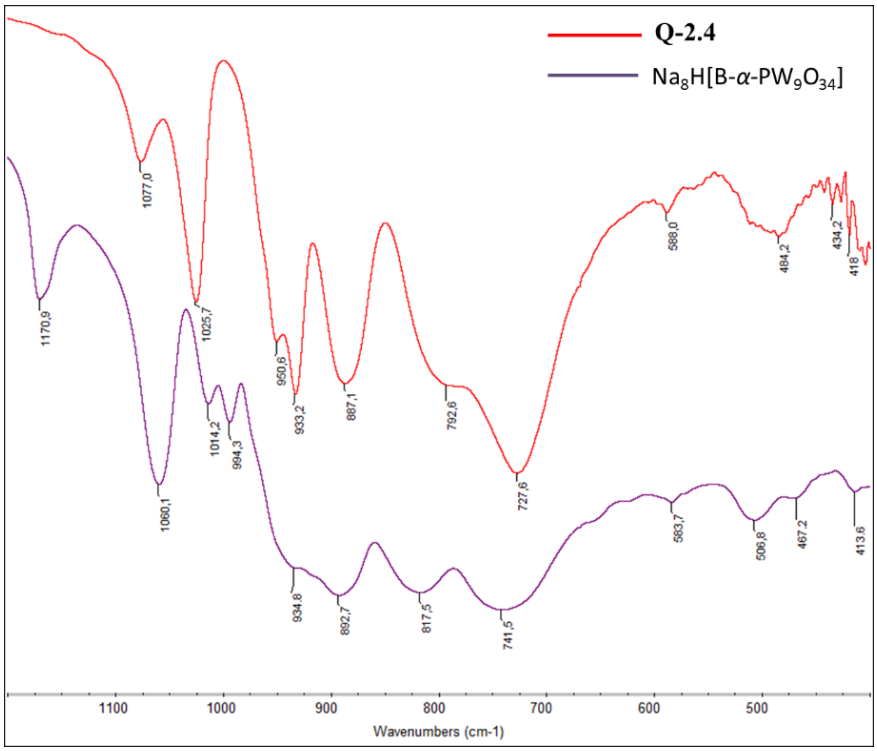

Fig. 2.35.- FT-IR spectra of the POM precursor $Na_8H[B\text{-}\alpha\text{-}PW_9O_{34}]$ and the product **Q-2.4.**

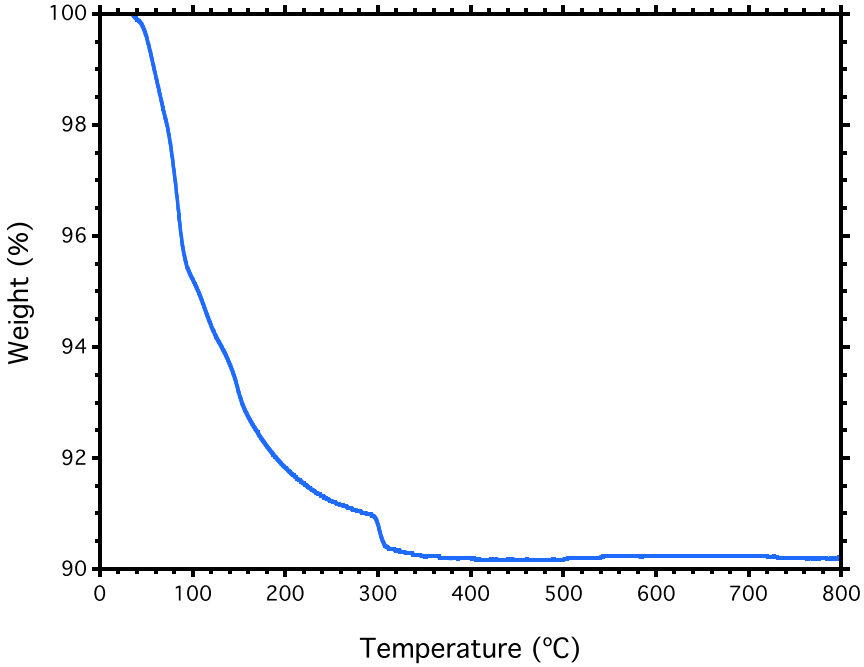

Fig. 2.36.- Thermogram of **Q-2.4** from room temperature to 800 °C (experimental total weight loss 9.78 %).

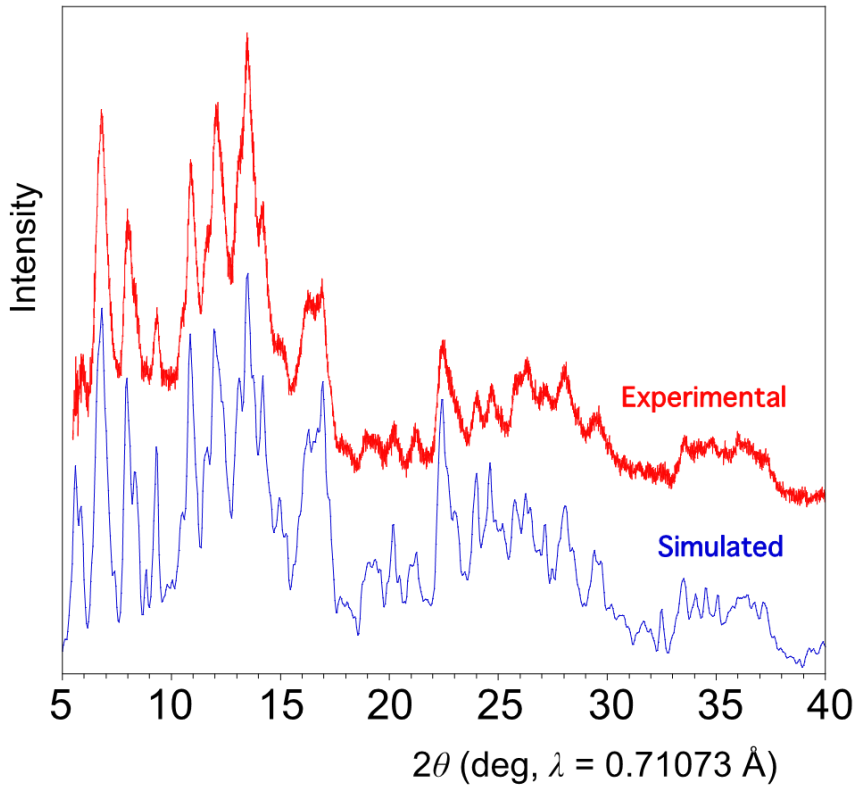

Fig. 2.37.- Comparison of simulated and experimental powder X-ray diffraction patterns for compound **Q-2.4**. The experimental powder X-ray diffraction pattern was obtained from powdered samples in an *Oxford Diffraction Supernova* diffractometer. The simulated pattern was generated from the atomic coordinates of the single-crystal structure solutions using the program Mercury 3.0 (copyright CCDC, http://www.ccdc.cam.ac.uk/mercury/) and a FWHM (full width at half maximum) of 0.2.

2.1.4.3. X-ray Crystallography

Suitable crystals of **Q-2.1**, **Q-2.2**, **Q-2.3** and **Q-2.4** were coated with Paratone N oil, suspended on small fiber loops, and placed in a stream of cooled nitrogen (120 K) on an Oxford Diffraction Supernova diffractometer equipped with a graphite-monochromated Enhance (Mo) X-ray Source (λ = 0.71073 Å). The data collection routines, unit cell refinements and data processing were carried out using the CrysAlis software package[60] and structure solution and refinement were carried out using SHELXS-97 and SHELXL-97.[61]

In **Q-2.1**, four well-behaved water molecules of solvation and 2.5 cesium counter-cations could be found in difference electron density maps. One of the cesium ions was located on the *b*-glide plane (Cs1), a second one in general position (Cs2), and a third one was disordered between two positions (Cs3 and Cs4). The crystal structure of **Q-2.1** contains channels parallel to the *c* axis in which, further, disordered water molecules and sodium countercations (detected by chemical analysis) lay. According to the TGA and chemical analysis results, 5 water molecules and 1.5 sodium countercations per POM reside in these channels. These additional water molecules and sodium ions were added to the final formula of **Q-2.1** using the SQUEEZE procedure implemented in the PLATON program.[62]

The X-ray diffraction pattern of **Q-2.2** reveals diffuse diffraction spots which gave rise to diffuse streaks along the *c**-axis. This fact is indicative of the presence of stacking disorders of the POMs, which form layers in the crystallographic *ab* plane. These stacking disorders are the origin of the high *R* factors obtained for the crystal structure of **Q-2.2**, which can be considered as an "average" structure. According to the TGA and chemical analysis results, this compound contains ten additional water molecules per POM, which were added to the formula of **Q-2.2** using the SQUEEZE procedure implemented in the PLATON program.[62]

In **Q-2.3**, apart from the cobalt atoms forming the dicubane core, a further cobalt atom was found in Fourier maps, which is bonded to four surface oxygen atoms of the POM and two water molecules. This cobalt atom (Co5) and the water molecules bonded to it have 50 % refined occupancies, which (due to the centrosymmetric nature of the POM) gives a total of one of such cobalt atoms per POM. Ten water molecules of crystallization were found in the asymmetric unit and no significant voids with disordered solvent were detected.

The refinement of the crystal structure of **Q-2.4** reveals that the polyoxoanion exhibits an 8 % disorder consisting in a 60º rotation of the full POM around a hypothetical pseudo-senary axis coincident with the long axis of the POM. This disorder was only evident for the W atoms of the capping triads of the two α-$[P_2W_{15}O_{56}]^{12-}$ lacunary units and also for the cobalt atoms which occupy the three vacant sites in both units. Therefore, the disorder was modeled only for those W and Co atoms. The disorder is not shown in the remaining W atoms belonging to the six-membered belts of the lacunary α-$[P_2W_{15}O_{56}]^{12-}$ unit because a 60º rotation brings these W atoms into coincidence. The disorder is neither apparent for the much lighter O atoms of the POM due to the small extent of the disorder. The disorder was modeled separately for the W and Co atoms giving exactly the same extent (8 %) for both of them, which points to a rotational disorder of the whole POM and rules out the possibility of a $\alpha \rightarrow \beta$ conformational disorder. Fifteen sodium countercations per POM (in full agreement with the anionic charge of **2.4**) and 32 water molecules of solvation were found in difference electron density maps. However, there are regions of the unit cell of **Q-2.4** that contain additional disordered water molecules which, according to the TGA and chemical analysis results, were estimated as six additional water molecules per POM. These water molecules were added to the formula of **Q-2.4** using the SQUEEZE procedure implemented in the PLATON program.[62]

All atoms were refined anisotropically in the four crystal structures except some sodium cations and water molecules of solvation having partial occupancies. Absorption corrections were applied to the four crystal structures. Hydrogen atoms of water molecules or hydroxyl anions were not located. The cif files of all these structures have been deposited in the inorganic crystal structure database (ICSD) with the deposition number CSD-430365. The crystallographic data for the four structures are summarized in **Table 2.2**.

Table 2.2.- Crystallographic Data for $Na_{1.5}Cs_{2.5}[Co_4(OH)_3(H_2O)_6(PW_9O_{34})]\cdot 9H_2O$ (**Q-2.1**), $Cs_7Na_2[Co_7(OH)_6(H_2O)_6(PW_9O_{34})_2]\cdot 20H_2O$ (**Q-2.2**), $K_{5n}Na_{2n}\{Co(H_2O)_2\}_n[Co_7(OH)_6(H_2O)_4(PW_9O_{34})_2]_n\cdot 20nH_2O$ (**Q-2.3**), and $Na_{15}[Co_7(OH)_6(H_2O)_6(P_2W_{15}O_{56})_2]\cdot 38H_2O$ (**Q-2.4**).

Compound	**Q-2.1**	**Q-2.2**	**Q-2.3**	**Q-2.4**
empirical formula	$Co_4Cs_{2.50}H_{33}Na_{1.50}O_{52}PW_9$	$Co_7Cs_7H_{58}Na_2O_{100}P_2W_{18}$	$Co_8H_{58}K_5Na_2O_{100}P_2W_{18}$	$Co_7H_{94}Na_{15}O_{162}P_4W_{30}$
formula weight	3153.36	6418.56	5742.62	9083.49
space group	*Pbcn*	*P2₁/c*	*P–1*	*P–1*
a/Å	24.7139(2)	12.4982(5)	10.2222(3)	12.7112(3)
b/Å	21.6677(2)	12.6768(6)	12.6115(4)	12.7409(4)
c/Å	20.02760(10)	33.332(2)	17.8646(6)	23.7998(6)
α/°	90	90	77.041(3)	101.199(2)
β/°	90	96.416(5)	83.369(3)	93.011(2)
γ/°	90	90	73.088(3)	105.768(2)
V/Å³	10724.65(14)	5248.0(5)	2144.23(11)	3616.04(17)
Z	8	2	1	1
T/K	120.00(10)	120.00(10)	120.00(10)	120.00(14)
λ/Å	0.71073	0.71073	0.71073	0.71073
ρ_{calcd}/g cm^{-3}	3.906	4.062	4.447	4.171
μ/mm^{-1}	22.243	23.249	25.952	24.745
$R[F_o^2 > 2\sigma(F_o^2)]$[a]	0.0470	0.1495	0.0519	0.0470
$R_w[F_o^2 > 2\sigma(F_o^2)]$[b]	0.1346[c]	0.3933[d]	0.1184[e]	0.1044[f]

[a] $R = \Sigma(||F_o| - |F_c||)/\Sigma|F_o|$. [b] $R_w = \{\Sigma[w(F_o^2 - F_c^2)^2]/\Sigma[w(F_o^2)^2]\}^{1/2}$. $w = 1/[\sigma^2(F_o^2) + (AP)^2 + BP]$, where $P = (F_o^2 + 2F_c^2)/3$. [c] $A = 0.0899$, $B = 0$. [d] $A = 0.2000$, $B = 0$. [e] A = 0.0537, B = 44.75. [f] $A = 0.0345$, $B = 189.1526$.

2.1.4.4. Magnetic Measurements

Samples of **Q-2.1**, **Q-2.2**, **Q-2.3**, and **Q-2.4** were prepared by compacted powder molded from ground crystalline samples. Each sample was covered with the minimum amount of liquid eicosane (40 ºC) in order to prevent crystallite torquering. Variable-temperature susceptibility measurements were carried out in the temperature range 2-300 K on a magnetometer equipped with a SQUID sensor (Quantum Design MPMS-XL-5). The data were corrected for diamagnetic contribution from eicosane and for the diamagnetic contributions of the polyanions as deduced by using the Pascal's constant tables. Isothermal magnetization measurements at low temperature (2 K and 5 K) were performed up to a field of 5 T in the same apparatus.

2.2. Construction of large magnetic POMs containing '$[Co_4(OH)_3(H_2O)_{6-n}(PW_9O_{34})]^{3-}$' (n = 3 or 5) as a common subunit

2.2.1. Introduction

As pointed out in **chapter 1**, two main synthetic strategies have been followed to obtain transition metal substituted POMs with new topologies: (i) reacting preformed lacunary POM species with transition metal ions and/or additional oxoanions (step-by-step approach) and (ii) direct self-assembly of tungstate (or molybdate, vanadate, *etc.*) anions, transition metal ions and/or additional oxoanions (one-pot approach). Both strategies require strict control of the key synthetic parameters, such as pH, temperature, concentration of reagents, *etc.* While the first approach is more directed towards the preparation of a specific POM species, the second one is prone to generate multiple POM products in solution which could need to be separated in the workup or by crystallization/recrystallization steps.[63]

In the first part of this chapter, we described a series of POM compounds containing cubane $[Co_4O_4]$ or dicubane $[Co_7O_8]$ cobalt clusters and B-α-$[PW_9O_{34}]^{9-}$ or α-$[P_2W_{15}O_{56}]^{9-}$ trilacunary ligands.[64] The cubane containing POM, formulated as $[Co_4(OH)_3(H_2O)_6(PW_9O_{34})]^{4-}$ (**2.1**), has three water molecules coordinated to the apical cobalt atom (in the following 'apical water') and three more to each of the three basal cobalt atoms (in the following 'basal water'), see **Fig. 2.38**. Since D. E. Katsoulis and M. T. Pope first demonstrated that water molecules coordinated to 3*d* metal ions could be substituted by other organic or inorganic ligands,[65] numerous examples of hybrid POMs have been reported in the literature.[7,66] These water molecules can also be substituted by oxo ligands belonging to other polyoxoanions giving rise to larger POM species, which are usually polymeric, such as: $[PMnW_{11}O_{39}]_n^{5n-}$,[67] $[XCo^{II}W_{11}O_{39}]_n^{5n-}$ (X = P^V or As^V),[68] α-$[XCuW_{11}O_{39}]_n^{6n-}$ (X = Si^{IV} or Ge^{IV})[69] and α-$[PCuW_{11}O_{39}]_{2n}^{10n-}$.[70] In these examples, one water molecule acting as ligand of each 3*d* metal has been replaced by an oxo group of a similar POM species, giving rise to infinite linear chains.

In the case of **Q-2.1**, the three apical water molecules lie in an almost equilateral triangle of side length 2.6-2.8 Å and so, they are in an ideal position to be replaced by three oxo (or hydroxo) ligands belonging to an edge-shared $[W_3O_{13}]$ group of any other POM (see green dashed lines in **Fig. 2.38**). In addition, the basal water molecules can be also substituted by oxo (or hydroxo) ligands to afford polymeric POM species. Therefore,

the six water molecules in **Q-2.1** provide the possibility to build larger POMs with new topologies by replacing some of them with oxo (or hydroxo) ligands belonging to other POMs.

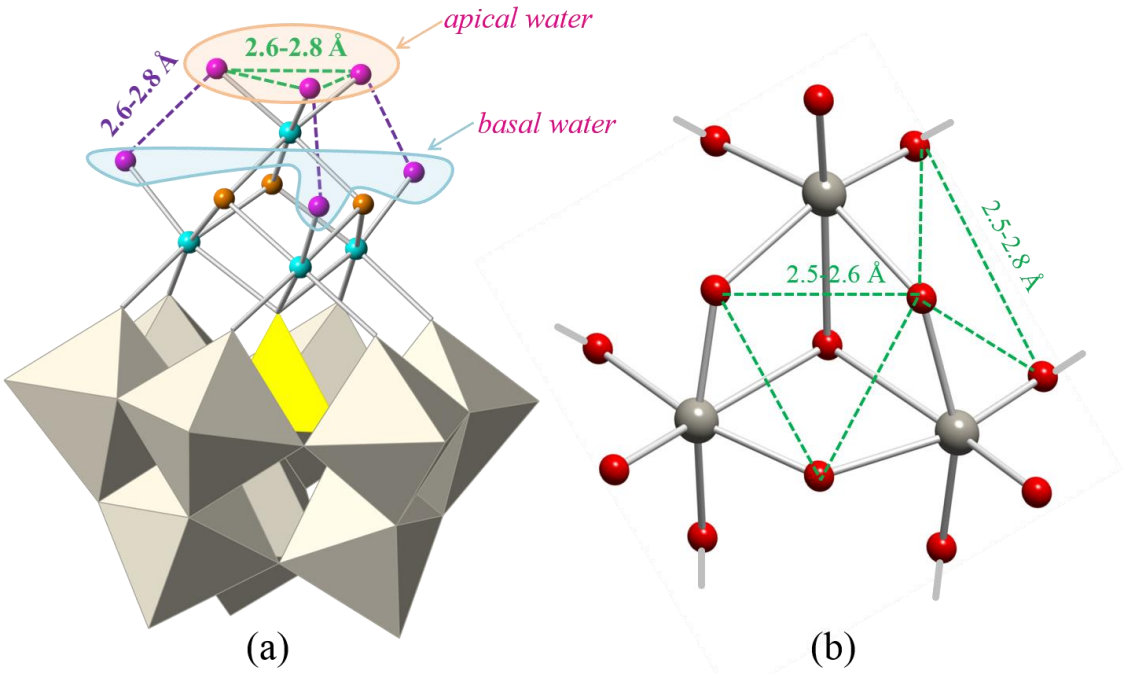

Fig. 2.38.- (a) Polyhedral and ball-and-stick representation of the polyoxoanion $[Co_4(OH)_3(H_2O)_6(PW_9O_{34})]^{4-}$ (**2.1**) in which the range of distances between water molecules have been indicated. (b) Ball-and-stick representation of an edge-shared $[W_3O_{13}]$ group, with indication of some O···O distances to illustrate the correspondence with the figure on the left and the possibilities of water substitution. Gray octahedra, $[WO_6]$; yellow tetrahedron, $[PO_4]$; cyan spheres, Co; red spheres, O; orange spheres, OH; pink spheres, H_2O.

Here, we develop a one-pot synthetic approach to construct new magnetic POMs containing one or two subunits of $[Co_4(OH)_3(H_2O)_{6-n}(PW_9O_{34})]^{3-}$ (n = 3 or 5). In these subunits, some water ligands have been substituted by oxo or hydroxo ligands belonging to other POM fragments, giving rise to five POM anions: $[Co_7(OH)_6(H_2O)_6(PW_9O_{34})_2]^{9-}$ (**2.2**), $[Co_7(OH)_6(H_2O)_4(PW_9O_{34})_2]_n^{9n-}$ (**2.3**), $[Co_8(OH)_6(H_2O)_6\{W_8O_{28}(OH)_2\}(PW_9O_{34})_2]^{16-}$ (**2.5**), $[Co_{11}(OH)_5(H_2O)_5(W_6O_{24})(PW_9O_{34})_3]^{22-}$ (**2.6**) and $[\{Co_4(OH)_3(H_2O)(PW_9O_{34})\}_2\{K\subset(H_2W_{12}O_{41})_2\}\{Co(H_2O)_4\}_2]^{17-}$ (**2.7**).

2.2.2. Results and Discussion

2.2.2.1. Synthetic approach

2.1 was described in the first part of this chapter. This POM was obtained using the trilacunary anion B-α-$[PW_9O_{34}]^{9-}$ in the presence of Co(II) ions at pH 6.6. Although this synthetic approach is more convergent than a one-pot synthesis starting from WO_4^{2-}, Co^{2+} and PO_4^{3-}, it still produces a mixture of several species that needs to be separated in the workup. The main product obtained during the synthesis of **2.1** is the sandwich POM $[Co_4(H_2O)_2(PW_9O_{34})_2]^{10-}$ which was eliminated from the solution by precipitation as an insoluble Cs^+ salt. This allowed the subsequent crystallization of the salt **Q-2.1** as a side product in very low yield.

In contrast, the synthesis of **2.2**, **2.3**, **2.5**, **2.6** and **2.7** was accomplished by the self-assembly of WO_4^{2-}, Co^{2+} and PO_4^{3-} ions in the presence of $S_2O_8^{2-}$ as one-electron oxidant (see **Scheme 2.1**). The occurrence of the cubane $[Co_4O_4]$ cluster in all compounds is likely to be related to the use of $S_2O_8^{2-}$ as oxidant and, therefore, to the presence of Co(III) in the reaction medium. In all compounds, Co(III) ions are located in the apical position of the $[Co_4O_4]$ cubane clusters, in which they are coordinated by six hydroxyl ligands (in **2.2** and **2.3**) or three hydroxo and three oxo ligands (in **2.5**, **2.6** and **2.7**). In both cases, the apical position is particularly suitable to accommodate Co(III) ions (specially in **2.2** and **2.3**) because hydroxo ligands stabilize Co(III) in comparison with water ligands, as evidenced by the E^o values of the Co(III)/Co(II) redox couple.* In contrast, in the cubane cluster of **2.1**, the cobalt is coordinated by three hydroxo and three water ligands, favoring the stabilization of Co(II). If the synthesis of POMs containing cubane clusters is performed in the presence of an oxidant, the three apical water molecules will likely be substituted by oxo or hydroxo ligands in order to accommodate a Co(III) ion.

The synthesis of all these compounds involves the preparation of a starting solution in which the experimental conditions favor the formation of the trivacant polyanion B-α-$[PW_9O_{34}]^{9-}$ in the presence of Co(II) ions (see experimental section). The W:P ratio used in this starting solution (11:1) is higher than the necessary to obtain the trivacant POM ligand; then, the formation of additional polyoxoanions coexisting in the solution can be expected. This explains the formation of **2.5**, **2.6** and **2.7**, which consist of the

* $[Co(H_2O)_6]^{3+} + e^- \rightarrow [Co(H_2O)_6]^{2+}$ $\quad E^o = 1.92$ V
$Co(OH)_3 + e^- \rightarrow Co(OH)_2 + OH^-$ $\quad E^o = 0.17$ V

assembly of one or more subunits of **2.1** with different polyoxoanion fragments. The isolation of each compound requires the implementation of different experimental conditions to the starting solution. For example, **2.2** and **2.3** were obtained at higher pH (5.5) than **2.6** (pH = 5.4, the difference being approx. 10 drops of glacial acetic acid), favoring the coordination of the apical Co(III) by six hydroxo ligands. The reason for which **2.2** is an isolated POM while **2.3** is a polymeric chain lies in the concentration step performed in the synthesis of the salt **Q-2.3** (**Q'-2.2** crystallises from a more diluted solution).

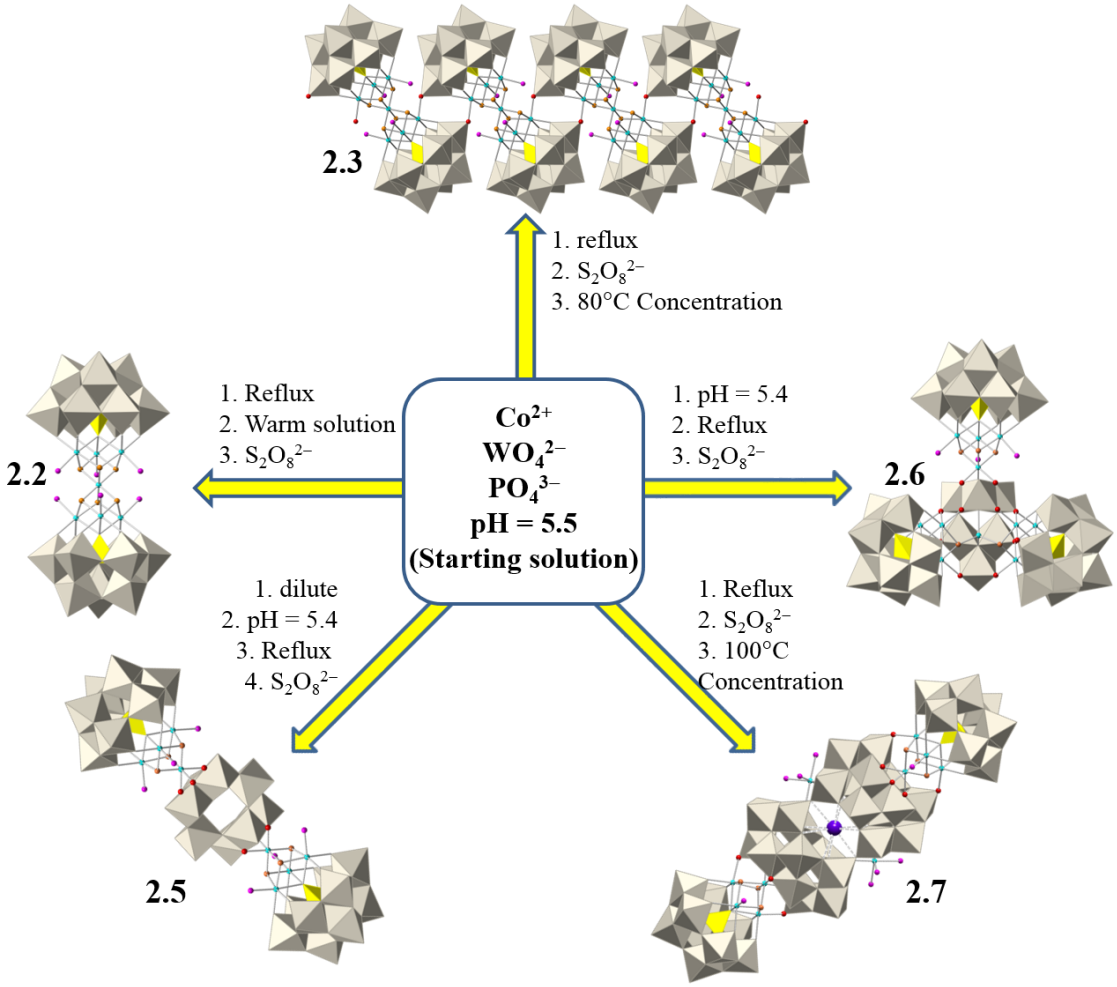

Scheme 2.1.- Synthetic approach for **2.2**, **2.3**, **2.5**, **2.6** and **2.7**. Colour code: Gray octahedra, [WO_6]; yellow tetrahedra, [PO_4]; cyan spheres, Co; red spheres, O; orange spheres, OH; pink spheres, H_2O; violet sphere, K.

In the synthesis of **2.6** and **2.7**, the addition of the oxidant (potassium persulfate) was performed under boiling conditions, favoring the formation of the previously reported asymmetric sandwich POM $[Co^{II}_4(H_2O)_2(Co^{III}W_9O_{34})(PW_9O_{34})]^{12-}$, which contains Co(III) in tetrahedral coordination.[71] This asymmetric sandwich POM precipitates as a black solid (due to the concentration process followed during the synthesis of **2.6** and **2.7**)

and was filtered out. The main differences in the synthesis of **2.6** and **2.7** lies in the pH values (5.4 and 5.5, respectively) and the concentration processes, carried out at boiling conditions for **2.6** and room temperature for **2.7**.

Salt **Q-2.5** was obtained only once. Several attempts were conducted to obtain further amounts of this material, but were unsuccessful. For this reason, the conditions of the synthesis are not discussed in this section and the synthesis is included in the experimental part only to illustrate that the general synthetic strategy exposed in this part can give rise to additional POMs that contain the fragment '$[Co_4(OH)_3(H_2O)_{6-n}(PW_9O_{34})]^{3-}$' (n = 3 or 5) as a subunit.

2.2.2.2. Crystal structure of $Na_{1.5}Cs_{2.5}[Co_4(OH)_3(H_2O)_6(PW_9O_{34})]\cdot 9H_2O$ (Q-2.1)

Salt **Q-2.1** contains the polyoxoanion $[Co_4(OH)_3(H_2O)_6(PW_9O_{34})]^{4-}$ (**2.1**), which has been described in the first part of this chapter. Basically, the architecture of **2.1** consists of one heptadentate B-α-$[PW_9O_{34}]^{9-}$ ligand which incorporates a $[Co_4O_4]$ cubane unit arising from the tetrahedral arrangement of four edge-shared $[CoO_6]$ octahedra (see **Fig. 2.38a**), giving rise to an idealized C_{3v} symmetry for **2.1**. The three μ_3-bridging oxygen atoms of the cubane unit correspond to hydroxo groups. The apical cobalt atom is coordinated by three water ligands, while the three basal cobalt atoms are coordinated by only one water ligand. **2.1** is the common building unit for the following described five POMs. **2.2**, **2.3**, **2.5**, **2.6** and **2.7** are formed by replacing some of the water molecules in **2.1** by oxo or hydroxo ligands belonging to other POM units, giving rise to the crystal structures described below.

2.2.2.3. Crystal Structure of $K_{4.2}Na_{2.8}\{Co(H_2O)_6\}[Co_7(OH)_6(H_2O)_6(PW_9O_{34})_2]\cdot 19H_2O$ (Q'-2.2)

Salt **Q'-2.2** crystallizes in the triclinic $P\bar{1}$ space group and contains the polyoxoanion $[Co_7(OH)_6(H_2O)_6(PW_9O_{34})_2]^{9-}$ (**2.2**). This POM can be considered to be constructed from one subunit of **2.1** in which the three 'apical water' molecules have been replaced by the three hydroxo ligands of a hypothetical unit formulated as '$[Co^{II}_3(OH)_3(H_2O)_3(PW_9O_{34})]^{6-}$' (see **Fig. 2.39**). As a result, a heptanuclear $[Co_7O_8]$ cluster is encapsulated by two heptadentate B-α-$[PW_9O_{34}]^{9-}$ ligands. The central cobalt atom of this cluster exhibits an oxidation state of 3+, while the other six cobalt atoms are divalent. According to BVS calculations (**Fig. 2.47**), the six μ_3-O ligands coordinating

the central cobalt correspond to hydroxyl groups. In salt **Q'-2.2** the POM forms layers parallel to the crystallographic *ab* plane which are separated by external $[Co(H_2O)_6]^{2+}$ cations. The long axis of the POMs forms an angle of 69.7º with the packing plane and keeps parallel in adjacent layers, giving rise to a ⋯AA⋯ packing mode (see **Fig. 2.40c**). **2.2** was found to crystallise also as a mixed cesium/sodium salt (**Q-2.2**) described in the first part of this chapter. Unlike **Q'-2.2**, salt **Q-2.2** crystallises in a monoclinic space group ($P2_1/c$) and does not contain any external Co(II) acting as counterion of the negative charge of the POM. Salt **Q-2.2** is made of layers perpendicular to the *b* axis, in which the POMs are parallel and form an angle of 79.6º with the packing plane. POMs in the adjacent layers are forming the same angle but in the opposite direction, giving rise to a ⋯ABAB⋯ mode of layer packing (see **Fig. 2.40a**). In contrast, the structure of **2.3** is made of units of **2.2**, in which one of the basal water molecules is replaced by a terminal oxo ligand of an adjacent POM giving rise to one-dimensional polymeric chains running along the crystallographic *a*-axis (see **Fig. 2.40b**).

2.2.2.4. Crystal Structure of $K_2Na_{14}[Co_8(OH)_6(H_2O)_6\{W_8O_{28}(OH)_2\}(PW_9O_{34})_2]\cdot 44H_2O$ (Q-2.5)

The novel polyoxoanion $[Co_8(OH)_6(H_2O)_6\{W_8O_{28}(OH)_2\}(PW_9O_{34})_2]^{16-}$ (**2.5**) consists of two subunits of **2.1** and one bridging ligand '$[W_8O_{28}(OH)_2]^{10-}$', which replaces the three 'apical water' ligands of **2.1** by three oxo ligands. The bridging ligand consists of two $[W_3O_{13}]$ triads, which are linked together by two equivalent *cis*-$[WO_2]$ groups. The linking $[WO_6]$ units exhibit octahedral coordination to two terminal oxo ligands and four doubly bridging oxo ligands with a typical two short (1.75-1.76 Å), two intermediate (1.95-1.96 Å) and two long (2.15-2.17 Å) bonding pattern. The only previously reported example of this fragment is the organoruthenium-supported polyoxotungstate $Na_6[\{Ru(C_6H_6)\}_2W_8O_{28}(OH)_2]\cdot 16H_2O$.[72] **2.5** exhibits an overall C_{2h} symmetry, which gives rise to three crystallographically different cobalt atoms (see **Fig. 2.41**). In this salt, all the POMs are parallel forming layers parallel to the *ab* crystallographic plane (see **Fig. 2.42**).

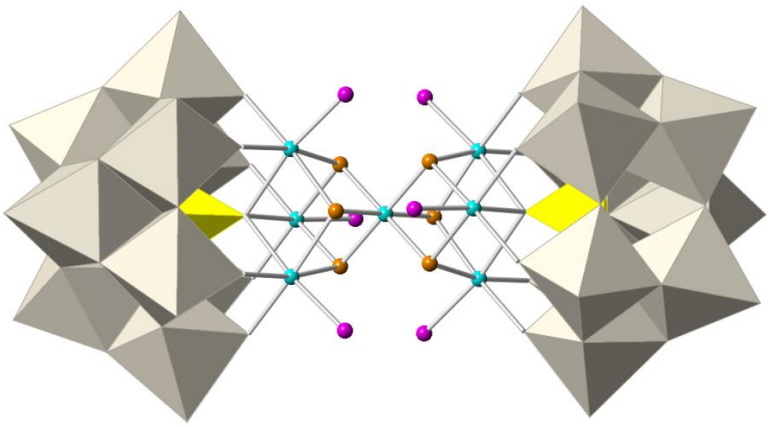

Fig. 2.39.- Polyhedral and ball-and-stick representation of the polyoxoanion $[Co_7(OH)_6(H_2O)_6(PW_9O_{34})_2]^{9-}$ (**2.2**). Grey octahedra, $[WO_6]$; yellow tetrahedra, $[PO_4]$; cyan spheres, Co; red spheres, O; orange spheres, OH; pink spheres, H_2O.

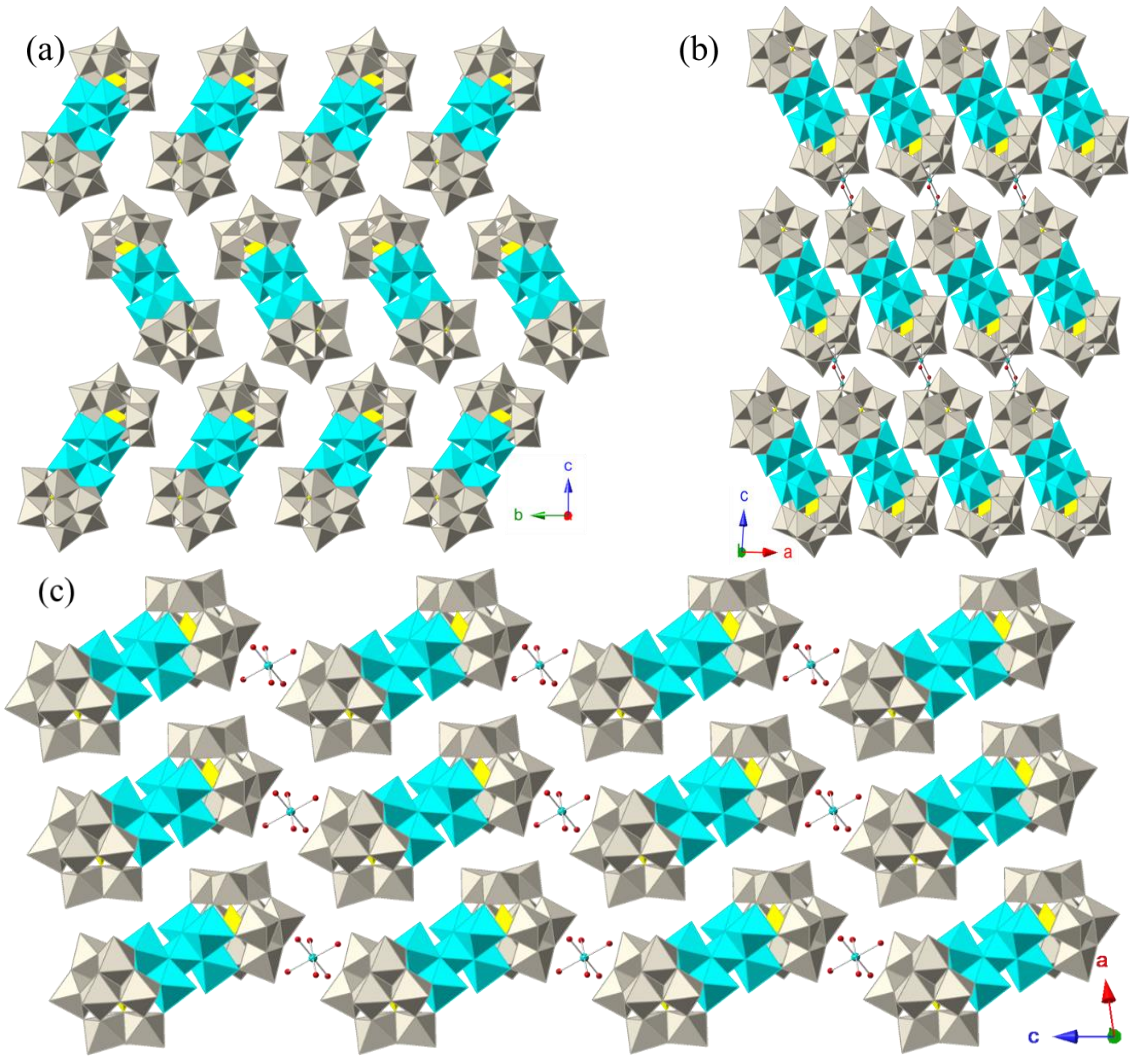

Fig. 2.40.- Polyhedral and ball-and-stick representations of the packing of the POMs in: (a) $Cs_7Na_2[Co_7(OH)_6(H_2O)_6(PW_9O_{34})_2]\cdot 20H_2O$ (**Q-2.2**); (b) $K_{5n}Na_{2n}\{Co(H_2O)_2\}_n[Co_7(OH)_6(H_2O)_4(PW_9O_{34})_2]_n\cdot 20nH_2O$ (**Q-2.3**); and (c) $K_{4.2}Na_{2.8}\{Co(H_2O)_6\}[Co_7(OH)_6(H_2O)_6(PW_9O_{34})_2]\cdot 19H_2O$ (**Q'-2.2**). Alkali countercations and water molecules of solvation are omitted for clarity. Grey octahedra, $[WO_6]$; yellow tetrahedra, $[PO_4]$; cyan octahedra, $[CoO_6]$; cyan spheres, Co; red spheres, O.

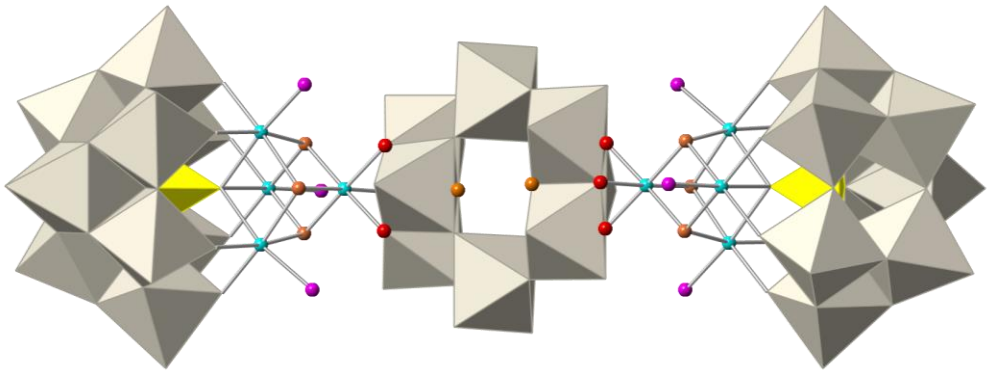

Fig. 2.41.- Polyhedral and ball-and-stick representation of the polyoxoanion $[Co_8(OH)_6(H_2O)_6\{W_8O_{28}(OH)_2\}(PW_9O_{34})_2]^{16-}$ (**2.5**). Gray octahedra, $[WO_6]$; yellow tetrahedra, $[PO_4]$; cyan spheres, Co; red spheres, O; orange spheres, OH; pink spheres, H_2O.

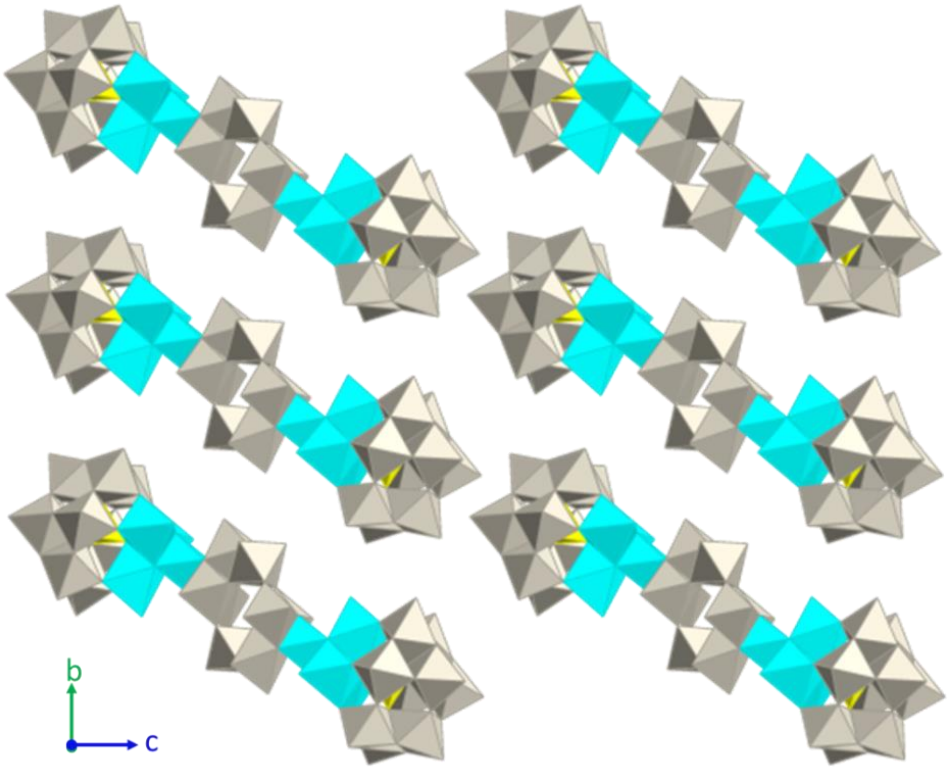

Fig. 2.42.- Polyhedral and ball-and-stick representation of the packing mode of **2.5** along the *a* axis. Alkaline countercations and water molecules of solvation are omitted for clarity. Gray octahedra, $[WO_6]$; yellow tetrahedra, $[PO_4]$; cyan octahedra, $[CoO_6]$.

2.2.2.5. Crystal Structure of $K_{12}Na_4H_3\{Co_{1.5}(H_2O)_{5.5}\}[Co_{11}(OH)_5(H_2O)_5(W_6O_{24})(PW_9O_{34})_3]\cdot 37.5H_2O$ (Q-2.6)

The novel polyoxoanion $[Co_{11}(OH)_5(H_2O)_5(W_6O_{24})(PW_9O_{34})_3]^{22-}$ (**2.6**) can be considered to be formed by one subunit of **2.1** and one heptameric cobalt fragment

formulated as '{[$Co_3(H_2O)]_2[Co(OH)_2W_6O_{24}](PW_9O_{34})_2$}$^{18-}$', giving rise to a C_s symmetry for the whole assembly. This fragment replaces the three apical water molecules in **2.1** by three oxo ligands (see **Fig. 2.43**) and can be constructed from the previously reported POM {[$Co_3(H_2O)]_2[Co(OH)_2W_7O_{26}](PW_9O_{34})_2$}$^{16-}$ by removal of one [WO_2] group from the central '[$Co^{II}(OH)_2W_7O_{26}$]$^{10-}$' unit.[52] In addition, the heptameric cobalt fragment in **2.6** is topologically similar to the previously reported series formulated as {[$M_3(H_2O)]_2[XW_6O_{26}](X'W_9O_{34})_2$}$^{n-}$ (X = X' = P^V and M = Co^{II}, Mn^{II}, Ni^{II};[73,74] X = X' = V^V and M = Co^{II};[75] X = X' = As^V and M = Co^{II}, Mn^{II}, and Zn^{II};[76] and X = X' = Ge^{IV} and M = Fe^{III};[77]). Therefore, the corresponding fragment in **2.6** represents the first example in which X ≠ X' and X = M = Co^{II}. Salt **Q-2.6** crystallizes in the triclinic space group $P\bar{1}$ (**Table 2.3**) and contains chains of POMs **2.6** (running along the *a*-axis) linked by one external Co(II) disordered in two close positions (see **Fig. 2.44**). BVS calculations confirm that the apical cobalt atom exhibits an oxidation state of 3+, while all other cobalt atoms are divalent (see **Fig. 2.47**). From the magnetic point of view, both the heptameric and tetrameric cobalt cores are expected to be isolated from each other and from the external Co(II) ions by the diamagnetic polyoxotungstate framework.

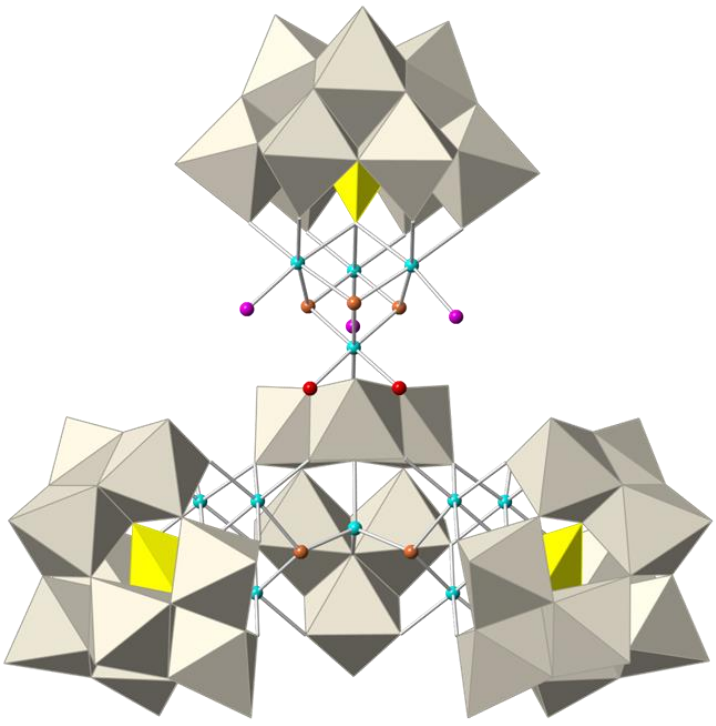

Fig. 2.43.- Polyhedral and ball-and-stick representation of the $[Co_{11}(OH)_5(H_2O)_5(W_6O_{24})(PW_9O_{34})_3]^{22-}$ polyoxoanion (**2.6**). Grey octahedra, [WO_6]; yellow tetrahedra, [PO_4]; cyan spheres, Co; red spheres, O; orange spheres, OH; pink spheres, H_2O.

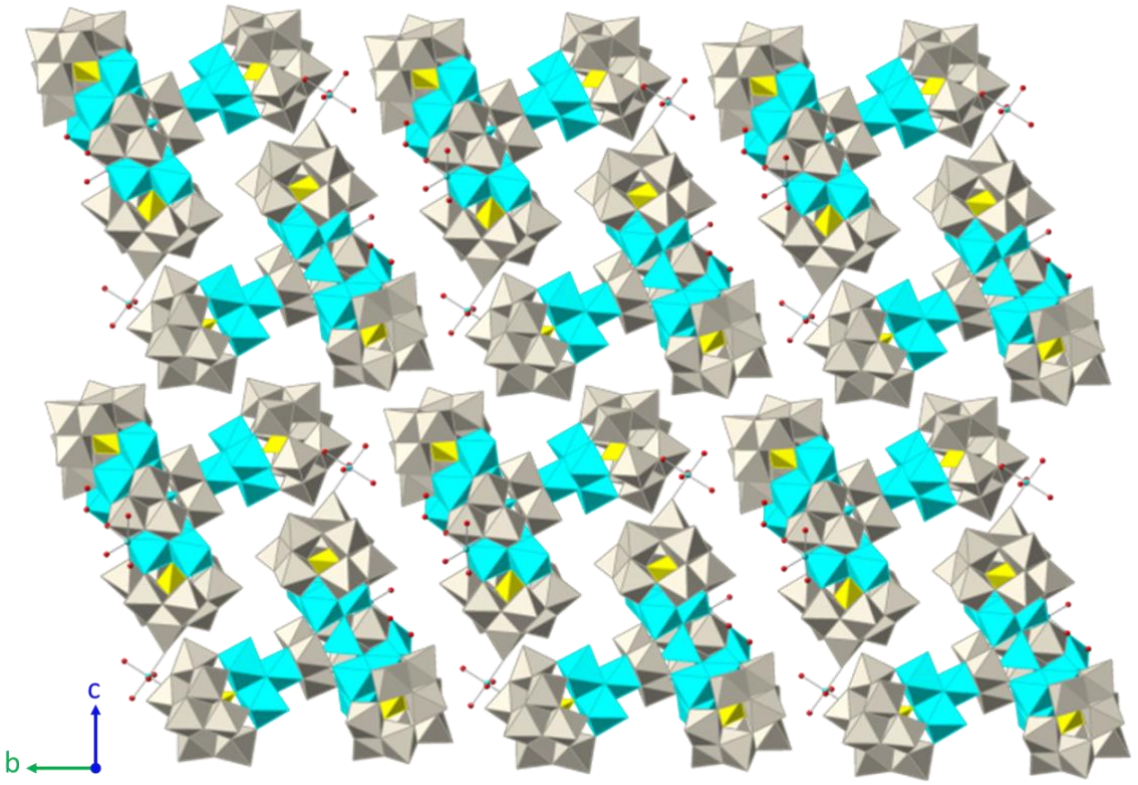

Fig. 2.44.- Polyhedral and ball-and-stick representation of the packing mode in **Q-2.6** along the *a* axis. Alkali countercations and water molecules of solvation are omitted for clarity. Grey octahedra, [WO_6]; yellow tetrahedra, [PO_4]; cyan octahedra, [CoO_6]; cyan spheres, Co; red spheres, H_2O.

2.2.2.6. Crystal Structure of $K_{12}Na\{Co_2(H_2O)_{10}\}[\{Co_4(OH)_3(H_2O)(PW_9O_{34})\}_2\{K\subset(H_2W_{12}O_{41})_2\}\{Co(H_2O)_4\}_2]\cdot 71H_2O$ (Q-2.7)

The novel elongated-shaped polyoxoanion $[\{Co_4(OH)_3(H_2O)(PW_9O_{34})\}_2\{K\subset(H_2W_{12}O_{41})_2\}\{Co(H_2O)_4\}_2]^{17-}$ (**2.7**) consists of a central fragment formulated as '$[K\subset(H_2W_{12}O_{41})_2\{Co(H_2O)_4\}_2]^{11-}$' bicapped by two subunits of **2.1** (see **Fig. 2.45**). This central fragment is made by condensation of two paratungstate-B anions $[H_2W_{12}O_{42}]^{10-}$ associated through two common oxygen atoms which were terminal in the parent paratungstate-B anions. The two paratungstate-B subunits are connected in an open arrangement in such a way that they leave an internal cavity occupied by a K^+ cation. The K^+ cation is coordinated by ten μ_2-O atoms from corner-shared [WO_6] octahedra, with K···O distances ranging between 2.77-2.97 Å. In addition, the open configuration of the central fragment delimits two coordination sites for two extra Co(II) cations, which are *cis*-chelated by two terminal oxygen atoms belonging to different paratungstate-B subunits.

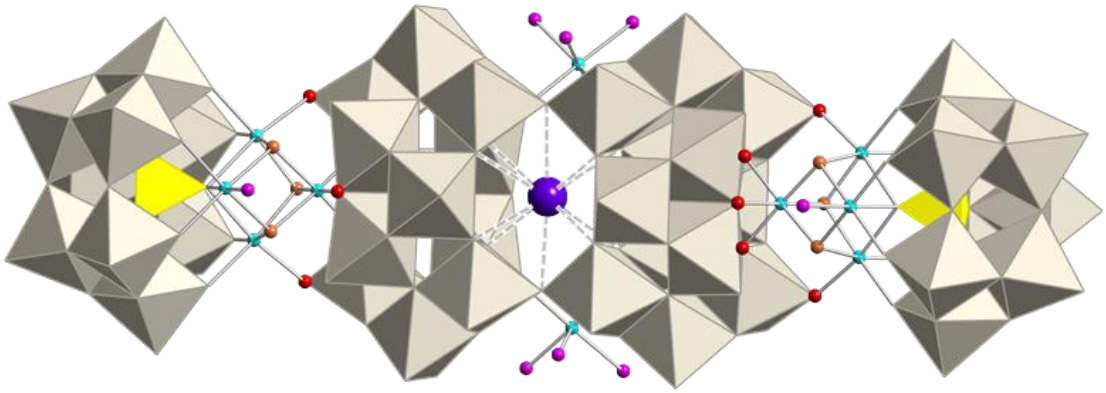

Fig. 2.45.- Polyhedral and ball-and-stick representation of the polyoxoanion $[\{Co_4(OH)_3(H_2O)(PW_9O_{34})\}_2\{K\subset(H_2W_{12}O_{41})_2\}\{Co(H_2O)_4\}_2]^{17-}$ (**2.7**). Grey octahedra, $[WO_6]$; yellow tetrahedra, $[PO_4]$; cyan spheres, Co; red spheres, O; orange spheres, OH; pink spheres, H_2O; violet sphere, K.

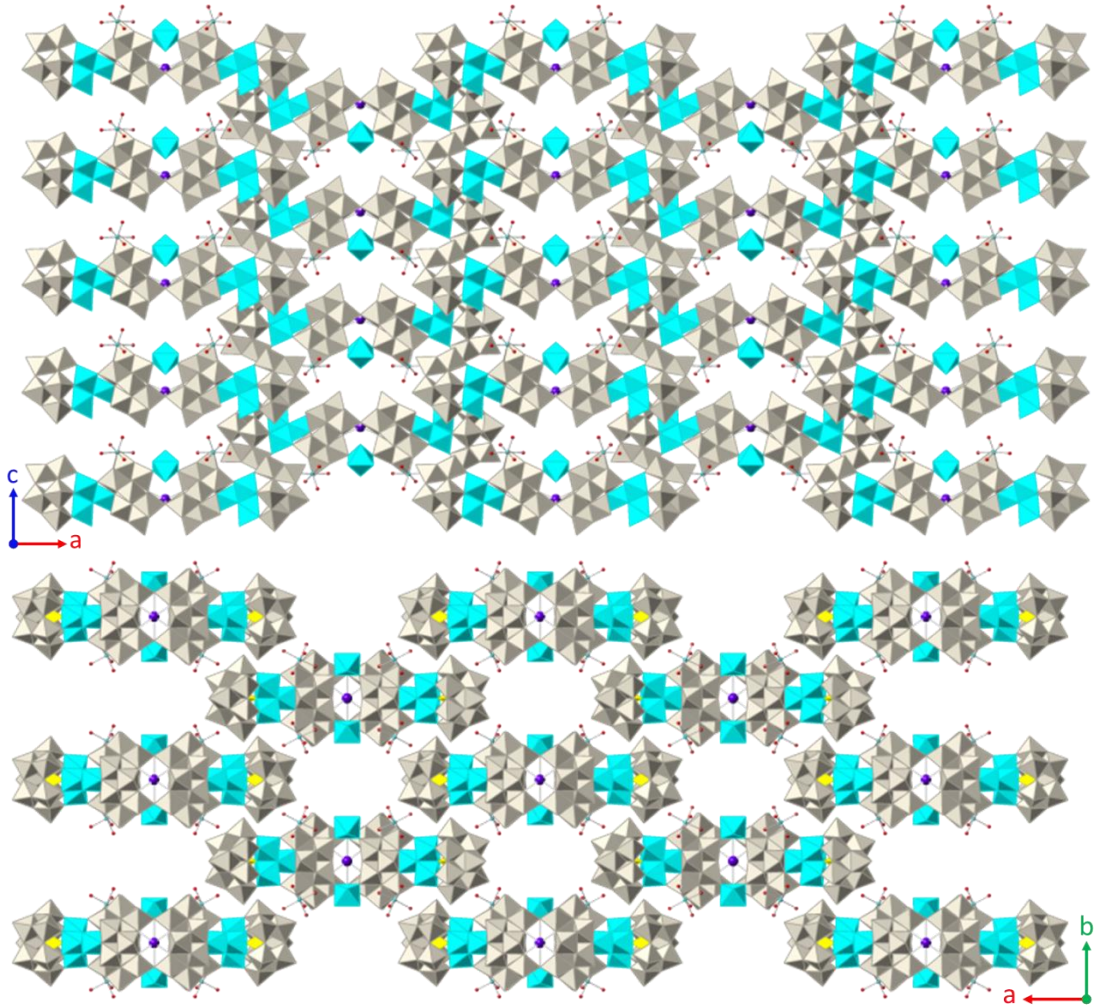

Fig. 2.46.- Polyhedral and ball-and-stick representations of the packing mode in **Q-2.7** along the *b* axis (up) and the *c* axis (down). Alkali countercations and water molecules of solvation are omitted for clarity. Grey octahedra, $[WO_6]$; yellow tetrahedra, $[PO_4]$; cyan octahedra, $[CoO_6]$; cyan spheres, Co; red spheres, O; violet spheres, K.

The subunits **2.1** are linked to the central fragment through substitution of five water ligands. The three apical water molecules of subunit **2.1** are substituted by three μ_2-O atoms (from two corner-shared and one edge-shared WO_6 octahedra), while two basal water molecules are substituted by two terminal oxygen atoms from each paratungstate-B subunit. The arrangement of all fragments leads to an overall C_{2v} symmetry for polyanion **2.7**. BVS calculations yield the same results as in **2.2**, **2.3**, **2.5** and **2.6** concerning the oxidation state of the cobalt atoms, *i.e.* the apical cobalt atom bears an oxidation state of 3+, while the basal cobalt atoms are divalent (see **Fig. 2.48**). Salt **Q-2.7** crystallizes in the orthorhombic space group *Pmmn*, forming columns of eclipsed POMs in which the long axis of **2.7** is perpendicular to the stacking *c* direction (see **Fig. 2.46**). Each stack is surrounded by other four stacks, creating channels along the *c* direction in which water molecules of crystallization reside.

2.2.2.7. Bond valence sum (BVS) calculations

According to bond valence sum (BVS) calculations, for all these POMs **2.2**, **2.5**, **2.6** and **2.7**, the apical cobalt atoms exhibit an oxidation state of 3+, while all other cobalt atoms are divalent (**Fig. 2.47** to **Fig. 2.51**). In addition, in the salt **Q'-2.2**, the μ_3-O ligands coordinating Co1 (O4, O5 and O6) correspond to hydroxyl groups, while the terminal ligands (O7, O8 and O9) bonded to the divalent cobalt ions correspond to water molecules (see **Fig. 2.47**). This BVS results are similar to the ones obtained for the same POM (**2.2**) in the salt **Q-2.2**, previously discussed in section 2.1.2.6.

2.2.2.8. Stabilities in aqueous solution

The aqueous solution stability of **2.1** was previously studied by UV-vis spectroscopy and cyclic voltammetry in the first part of this chapter. It was concluded that aqueous solutions of **2.1** mainly decompose into the mono-substituted POM $[PCo(H_2O)W_{11}O_{39}]^{5-}$, as evidenced by the appearance of a characteristic peak in the UV-vis spectrum at 252 nm within 24 hours of standing. We have also investigated the stability of aqueous solutions of POMs **2.2**, **2.5**, **2.6** and **2.7** in 0.5 M NaOAc/HOAc buffer solution at pH 4.8 at room temperature (see **Fig. 2.52**). The evolution of the UV-vis spectra of **2.2**, **2.5** and **2.6** clearly indicate that, similarly to **2.1**, a new peak develops in all cases within 24 h at 252 nm, suggesting that these POMs decompose producing the mono-substituted $[PCo(H_2O)W_{11}O_{39}]^{5-}$ as the major product. By comparison with the decomposition of **2.1**,

these mono-substituted species should come from the decomposition of the corresponding fragment of **2.2**, **2.5** and **2.6**, which is topologically identical to **2.1**. In contrast, the UV-vis spectra of **2.7** remains almost unchanged during the first 48 h of standing, suggesting that this POM is stable in aqueous solution at pH 4.8 during this period. We have also checked that **2.7** is stable at pH values 4.3 and 3.8 (see **Fig. 2.53**). In fact, **2.7** can be recrystallised from hot water (80 ºC) and recovered from solution after one week in high yield, in accordance with the UV-vis spectra results. Compared to **2.1**, **2.2**, **2.5** and **2.6**, the higher stability of **2.7** is likely due to the fact that five water molecules from subunit **2.1** (the three 'apical water' and two 'basal water' molecules) have been substituted by oxo ligands from the central fragment of **2.7**, providing rigidity to the cubane cobalt cluster [Co_4O_4] and, therefore, hindering its decomposition.

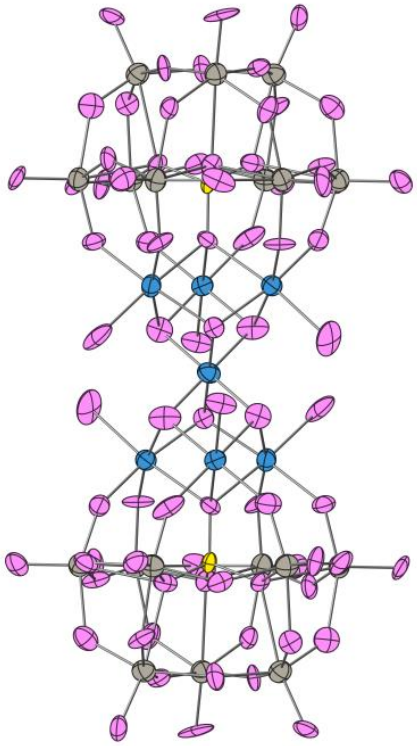

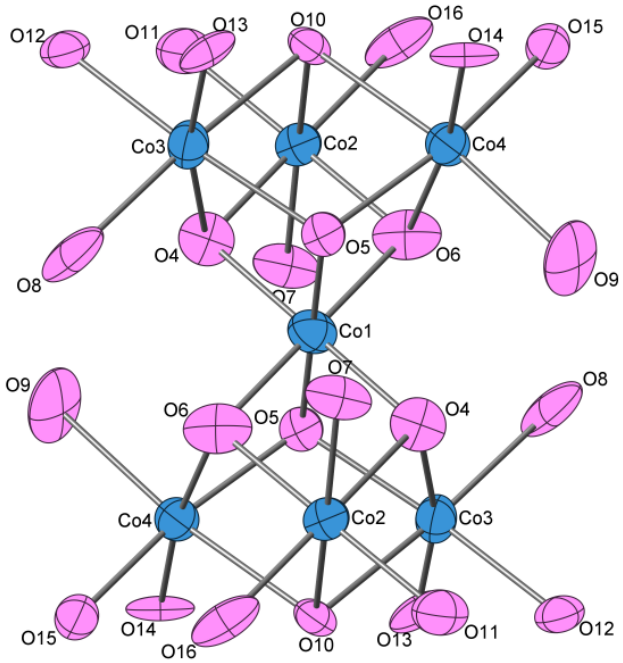

Cobalt atoms	BVS
Co1	**3.11**
Co2	**1.96**
Co3	**1.95**
Co4	**2.03**

Oxygen atoms	BVS	Assigned protonation levels
O4	**1.14**	**OH**
O5	**1.17**	**OH**
O6	**1.23**	**OH**
O7	**0.29**	**H_2O**
O8	**0.30**	**H_2O**
O9	**0.31**	**H_2O**
O10	**1.84**	**O**

Fig. 2.47.- (Up) Thermal ellipsoid plot and numbering scheme for the POM **2.2** in the salt **Q'-2.2** (50 % probability). (Down) Bond valence sum (BVS) calculations for cobalt centers and relevant oxygen sites in the same salt.

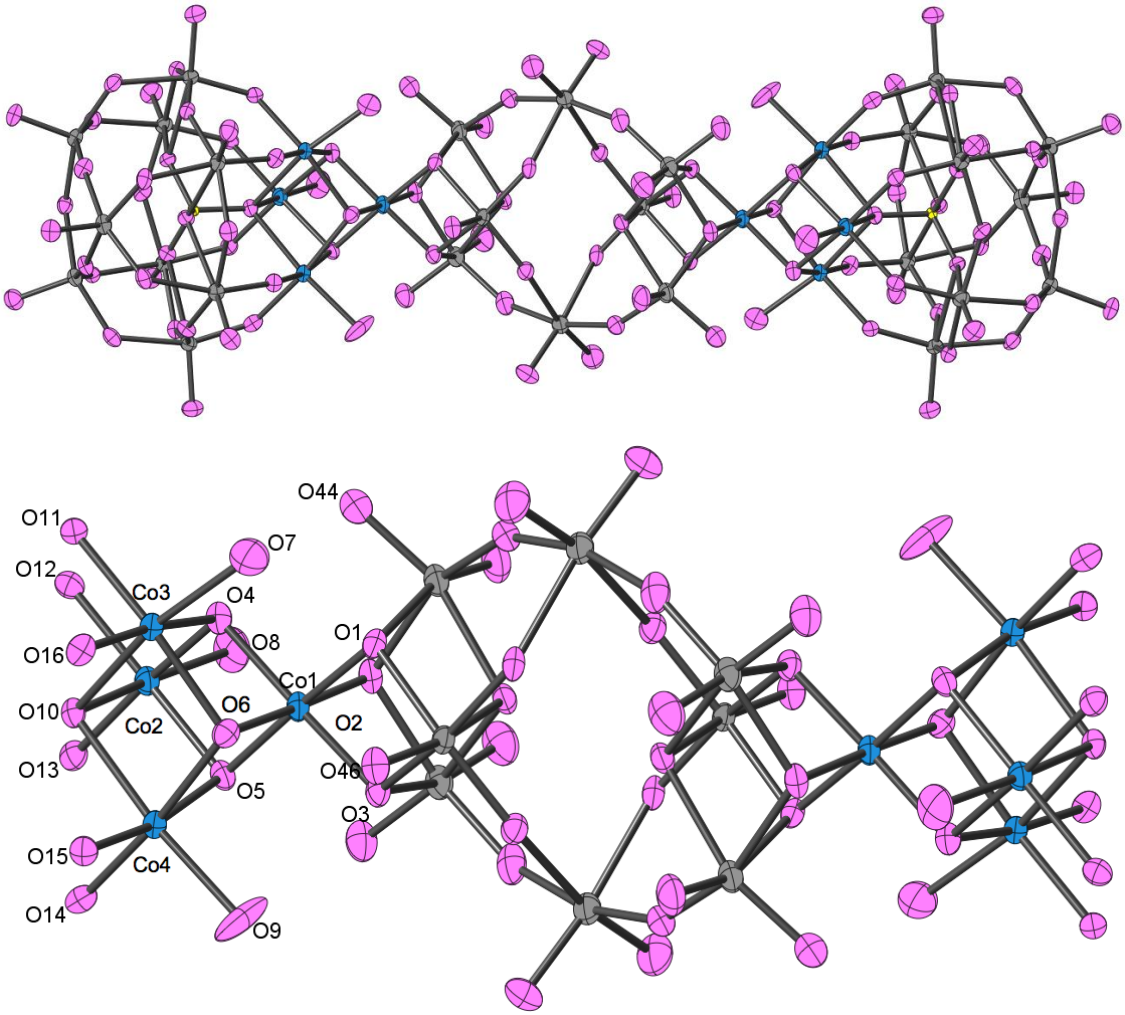

Cobalt atoms	BVS
Co1	**3.12**
Co2	**1.95**
Co3	**1.98**
Co4	**2.05**

Oxygen atoms	BVS	Assigned protonation levels
O1	**1.83**	**O**
O2	**1.95**	**O**
O3	**1.88**	**O**
O4	**1.16**	**OH**
O5	**1.17**	**OH**
O6	**1.18**	**OH**
O7	**0.29**	**H_2O**
O8	**0.31**	**H_2O**
O9	**0.63**	**H_2O**
O47	**1.27**	**OH**

Fig. 2.48.- (Up) Thermal ellipsoid plots and numbering scheme for **2.5** (50 % probability). (Down) Bond valence sum (BVS) calculations for cobalt centers and relevant oxygen sites of **2.5**.

2.2.2.9. Electrochemical experiments

Due to the instability of **2.2**, **2.5** and **2.6** in aqueous solutions, only the electrochemical behaviour of **2.7** has been studied between –0.9 to +1.3 V (*vs.* Ag/AgCl), in the same medium where the UV-vis spectra measurements were performed. **Fig. 2.49** shows that the reduction of the W centers in **2.7** is chemically irreversible, exhibiting a single wave at –0.60 V and no counterpart in the oxidation scan. The central fragment of **2.7** consists of two fused paratungstate-B units (see structural description), which can be considered as type III species, according to Pope's classification of isopoly- and heteropolyanions.[78] Type I (or type II) species have one (or two *cis*) terminal oxygen atom(s) per [WO_6] octahedron, respectively. Type III species have both types of [WO_6] octahedra. Generally, type I species exhibit reversible electrochemical behaviour, while type II species are electrochemically inactive or exhibit irreversible behaviour. The cyclic voltammogram of the paratungstate-B isopolyanion has been previously reported,[79] and exhibits a cathodic peak at –1.08 V at pH 5.0 with an anodic couple appearing only at pH values lower than 4.5. In the case of **2.7**, the irreversible cathodic peak and the reduction of water appear at less negative potentials (–0.60 and –0.90 V, respectively) than for the paratungstate-B polyanion.

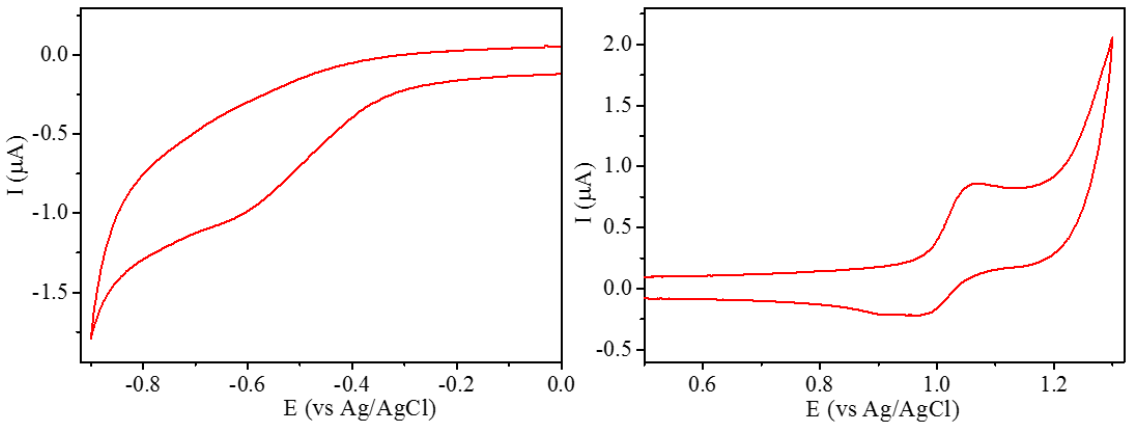

Fig. 2.49.- Cyclic voltammograms of **2.7** ($5 \cdot 10^{-5}$ M) at pH = 4.8 (0.5 M sodium acetate/acetic acid buffer solution), addressing the redox processes of W (left) and Co centers (right). Scan rate: 10 mV/s.

In the positive potential domain, one quasi-reversible oxidation wave is observed (E_{pa} = 1.06 V) which exhibits a composite reduction wave with two components at E_{pc1} = 0.97 V and E_{pc2} = 0.91 V. By analogy with other cobalt-containing POMs, this wave can be assigned to redox processes involving the cobalt cluster of **2.7**.[66,80] Therefore,

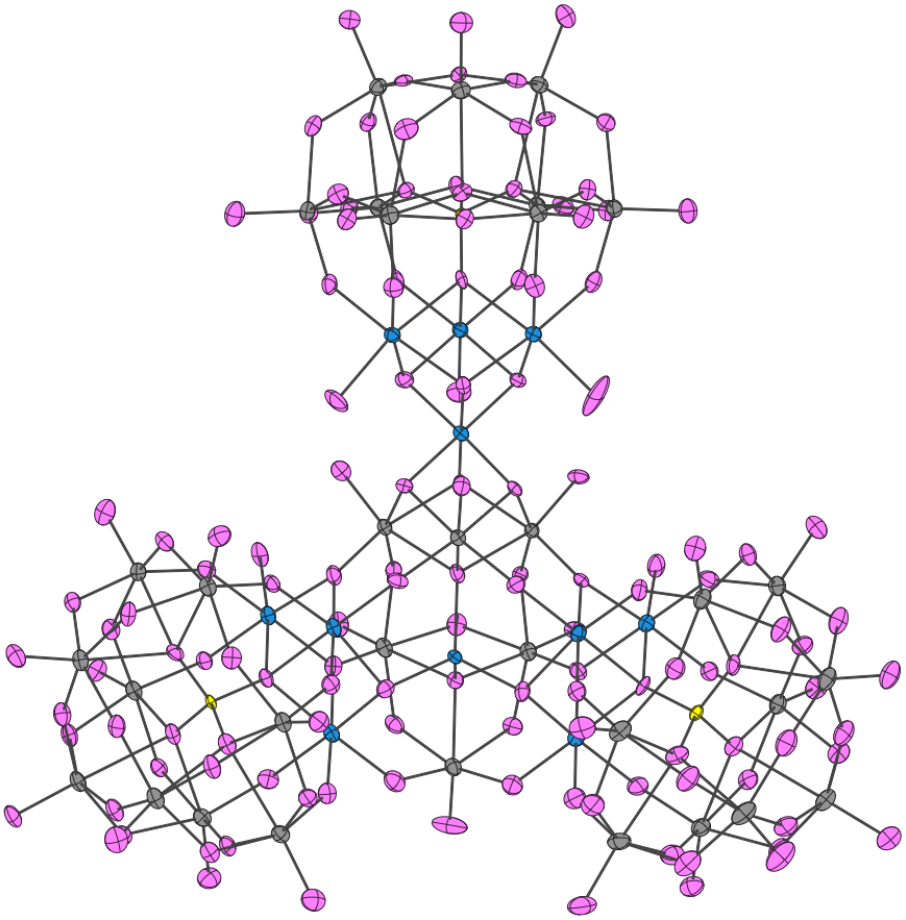

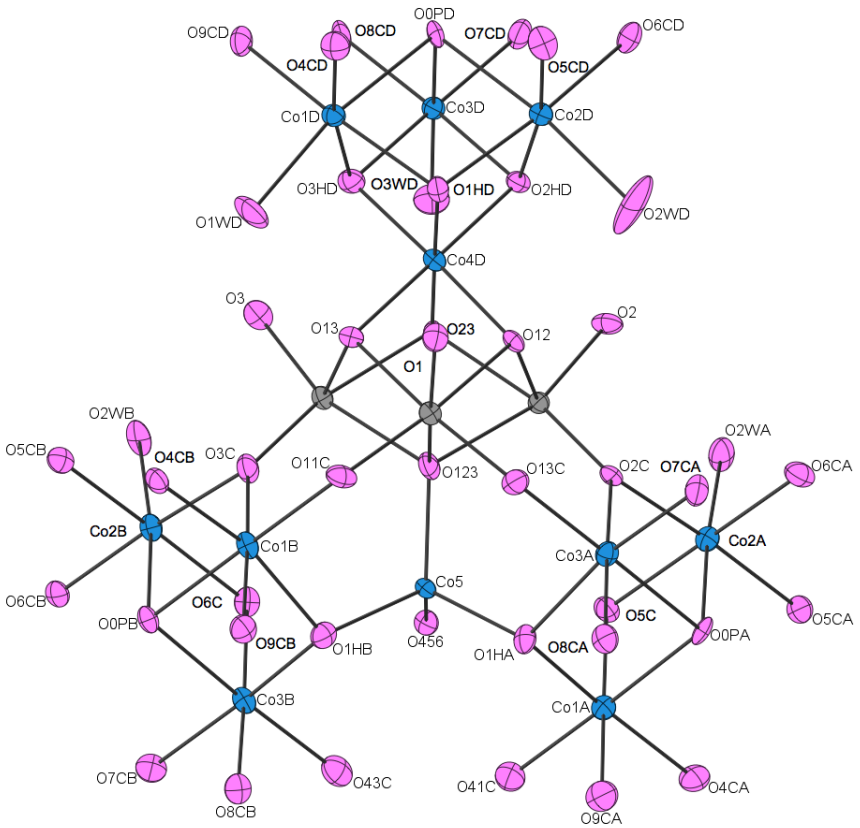
O0PD
O9CD
O8CD
O7CD
O6CD
O4CD
O5CD
Co1D
Co3D
Co2D
O3HD
O3WD
O1HD
O2HD
O1WD
O2WD
Co4D
O3
O13
O23
O12
O2
O1
O2WB
O5CB
O4CB
O3C
O11C
O123
O13C
O2C
O7CA
O2WA
O6CA
Co2B
Co1B
Co3A
Co2A
Co5
O6CB
O6C
O5C
O5CA
O0PB
O9CB
O1HB
O456
O1HA
O8CA
O0PA
Co3B
Co1A
O7CB
O43C
O41C
O4CA
O8CB
O9CA

Cobalt atoms	BVS
Co1D	**1.96**
Co2D	**1.97**
Co3D	**2.01**
Co4D	**3.06**
Co1A	**1.95**
Co2A	**1.87**
Co3A	**2.01**
Co5	**1.86**
Co1B	**2.01**
Co2B	**1.92**
Co3B	**1.96**

Oxygen atoms	BVS	Assigned protonation levels
O0PD	**1.79**	**O**
O1	**1.50**	**O**
O2	**1.58**	**O**
O3	**1.63**	**O**
O12	**1.86**	**O**
O23	**1.81**	**O**
O13	**1.84**	**O**
O1HD	**1.15**	**OH**
O2HD	**1.18**	**OH**
O3HD	**1.20**	**OH**
O1WD	**0.29**	**H_2O**
O2WD	**0.30**	**H_2O**
O3WD	**0.28**	**H_2O**
O4CD	**1.87**	**O**
O5CD	**1.84**	**O**
O6CD	**1.86**	**O**
O7CD	**1.83**	**O**
O8CD	**1.88**	**O**
O9CD	**1.83**	**O**
O41C	**1.80**	**O**
O1HA	**1.13**	**OH**
O1HB	**1.11**	**OH**
O13C	**1.90**	**O**
O5C	**1.84**	**O**
O2C	**1.90**	**O**
O2WA	**0.30**	**H_2O**
O2WB	**0.28**	**H_2O**
O4CA	**1.88**	**O**
O5CA	**1.84**	**O**
O6CA	**1.80**	**O**
O7CA	**1.89**	**O**
O8CA	**1.90**	**O**
O9CA	**1.86**	**O**
O0PA	**1.78**	**O**

Fig. 2.50.- (Previous page) Thermal ellipsoid plots and numbering scheme for **2.6** (50 % probability). (This page) Bond valence sum (BVS) calculations for cobalt centers and relevant oxygen sites of **2.6**.

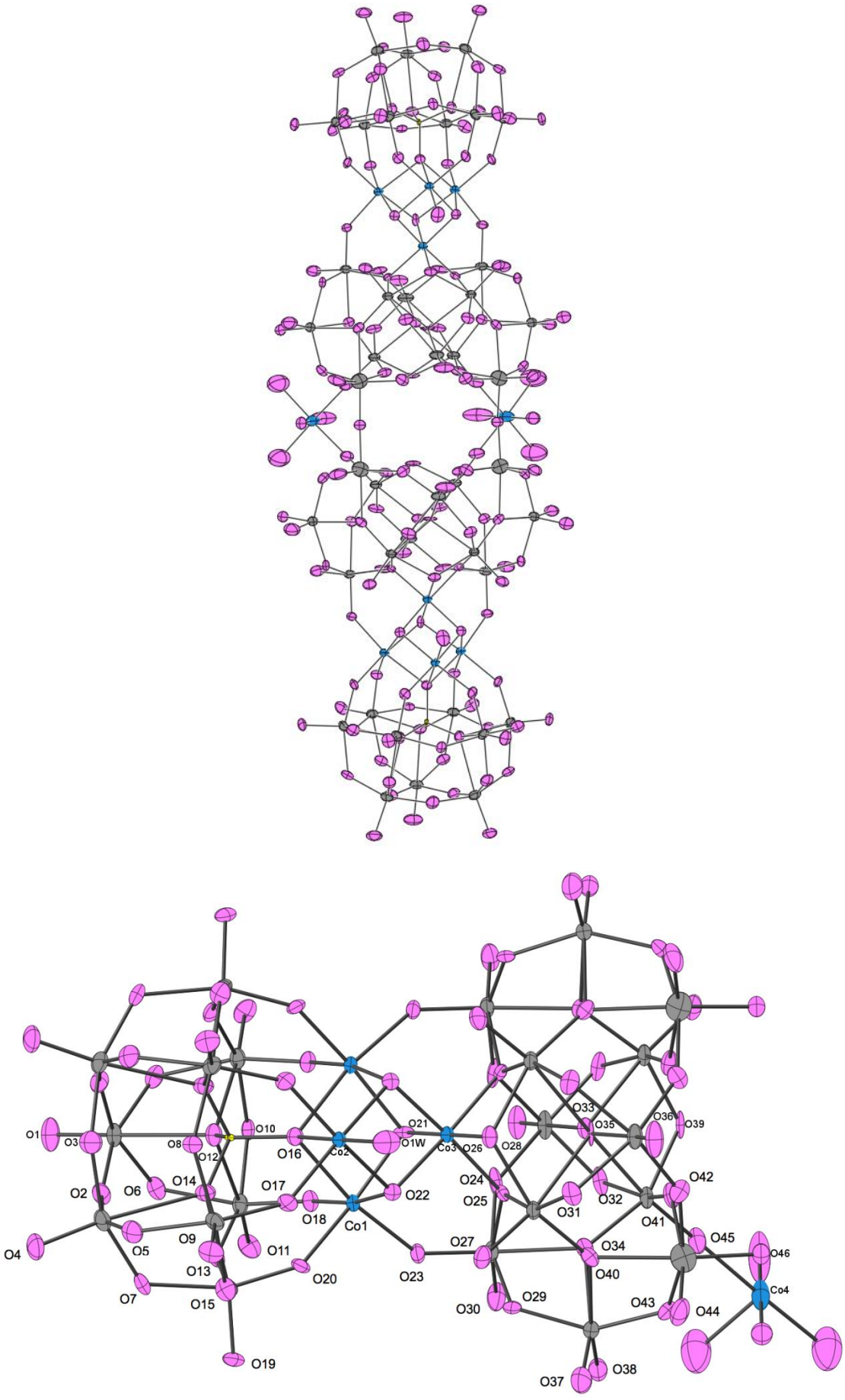
O1
O3
O8
O12
O10
O16
Co2
O21
O1W
Co3
O26
O28
O33
O35
O36
O39
O2
O6
O14
O17
O18
Co1
O22
O24
O25
O31
O32
O41
O42
O4
O5
O9
O11
O13
O20
O23
O27
O34
O40
O45
O46
O7
O15
O19
O30
O29
O43
O44
Co4
O37
O38

Cobalt atoms	BVS
Co1	**2.00**
Co2	**1.96**
Co3	**2.86**
Co4	**1.95**

Oxygen atoms	BVS	Assigned protonation levels
O1	**1.69**	**O**
O2	**1.95**	**O**
O3	**2.01**	**O**
O4	**1.80**	**O**
O5	**1.92**	**O**
O6	**1.89**	**O**
O7	**1.81**	**O**
O8	**2.03**	**O**
O9	**1.76**	**O**
O10	**1.91**	**O**
O11	**1.72**	**O**
O12	**1.82**	**O**
O13	**2.04**	**O**
O14	**1.87**	**O**
O15	**1.82**	**O**
O16	**1.78**	**O**
O17	**1.88**	**O**
O18	**1.81**	**O**
O19	**1.72**	**O**
O20	**1.89**	**O**
O21	**1.19**	**OH**
O22	**1.15**	**OH**
O23	**1.87**	**O**
O24	**2.00**	**O**

Oxygen atoms	BVS	Assigned protonation levels
O25	**1.79**	**O**
O26	**1.91**	**O**
O27	**1.65**	**O**
O28	**1.66**	**O**
O29	**2.01**	**O**
O30	**1.93**	**O**
O31	**1.86**	**O**
O32	**1.76**	**O**
O33	**1.23**	**OH**
O34	**1.87**	**O**
O35	**1.15**	**OH**
O36	**1.73**	**O**
O37	**1.69**	**O**
O38	**1.73**	**O**
O39	**1.89**	**O**
O40	**2.08**	**O**
O41	**1.91**	**O**
O42	**2.16**	**O**
O43	**1.18**	**O**
O44	**1.99**	**O**
O45	**2.22**	**O**
O46	**2.46**	**O**
O1W	**0.29**	**H2O**

Fig. 2.51.- (Previous page) Thermal ellipsoid plots and numbering scheme for **2.7** (50 % probability). (This page) Bond valence sum (BVS) calculations for cobalt centers and relevant oxygen sites of **2.7**.

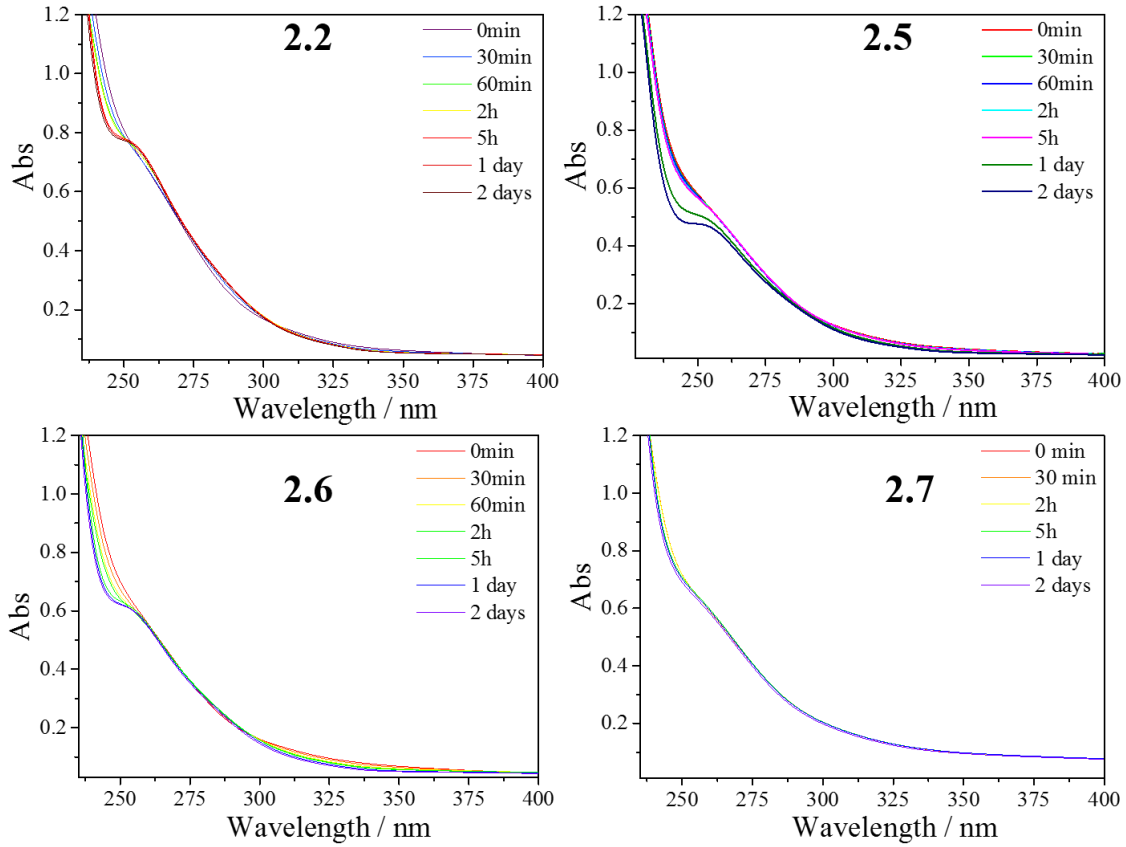

Fig. 2.52.- The evolution of UV spectra of solutions of **2.2** (a), **2.5** (b), **2.6** (c) and **2.7** (d) at concentration of 10^{-5} M with time, recorded in pH = 4.8 buffer solution.

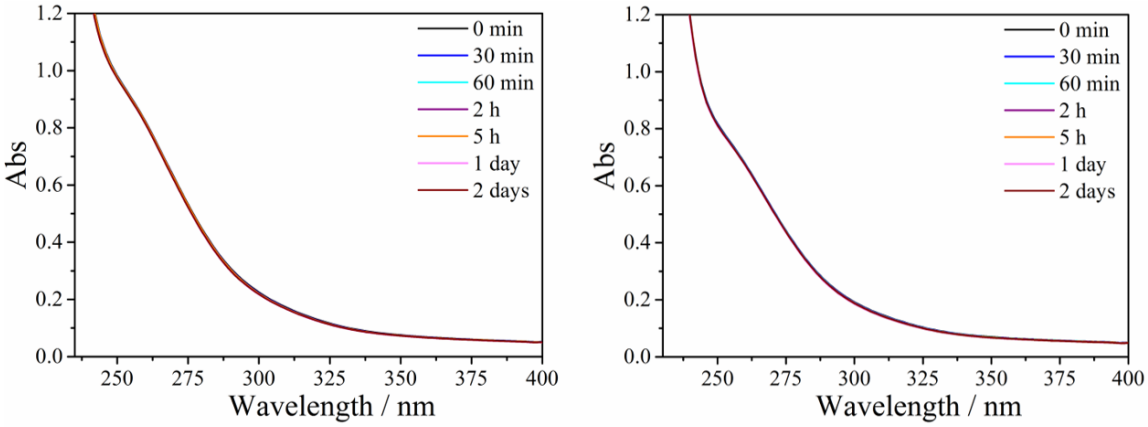

Fig. 2.53.- Evolution of UV spectra of aqueous solutions of **2.7** (10^{-5} M) with time, recorded in pH = 4.3 (left) and 3.8 (right) buffer solution.

2.7 is one of the few cobalt-substituted POMs that exhibit evident electroactivity of the encapsulated cobalt cluster in a multi-cobalt-containing POM. However, due to the complexity imposed by the presence of several different cobalt ions in **2.7** (isolated or from the cluster) with different oxidation states (for the apical and basal cobalt ions), a deeper electrochemical study has not been performed.

2.2.2.10. Magnetic properties

The magnetic studies of salts containing POMs **2.1**, **2.2** and **2.3** have been previously described in section 2.1.4.4. Therefore, here we report the magnetic properties of the salts containing the POMs **2.6** and **2.7** polyoxoanion (**Fig. 2.54** and **Fig. 2.55**). For **2.6** the $\chi_m T$ *vs.* T curve shows a smooth decrease from room temperature ($\chi_m T$ = 37.5 emu K mol^{-1}) down to 50 K ($\chi_m T$ = 32.0 emu K mol^{-1}). Below this temperature, a sharp peak is observed with a maximum at 5.0 K ($\chi_m T$ = 52 emu K mol^{-1}), which clearly depends on the magnetic field: as it increases, the maximum decreases, shifts to higher temperatures and becomes broader. In the case of **2.7**, the $\chi_m T$ *vs.* T curve exhibits a smooth and continuous decrease from room temperature ($\chi_m T$ = 35.0 emu K mol^{-1}) down to 15 K. Below this temperature, a sharp decrease is observed.

To analyse these results it is necessary to take into account the contributions of the different cobalt ions. As already pointed out, octahedral Co(II) ions are described by a high-spin ground electronic term $^4T_1$ with first-order spin–orbit coupling. This ground state is split into six anisotropic Kramers doublets.[42-43] At low temperature, only the lowest anisotropic Kramers doublet is populated. The apical cobalt atom in the cubane unit bears an oxidation state of 3+ and is diamagnetic due to the strong field associated with the hydroxyl groups, having no net contribution to the magnetic properties.

We discuss first the magnetic behavior of the salt **Q-2.7** because it contains two identical cubane cobalt clusters, while the salt **Q-2.6** contains one of such cubane clusters and one additional, independent, heptameric cluster. The magnetic behaviour of the salt **Q-2.7** can be explained by the superposition of two different contributions: the two cubane units present in **2.7**, and four isolated Co(II) (two of them are bridging the two central paratungstate units and the remaining two are external cobalt atoms acting as countercations). Due to the diamagnetic behaviour of the apical cobalt, the magnetic

exchange scheme of **2.7** can be described as an equilateral triangle of Co(II) ions coupled with a single anisotropic interaction.

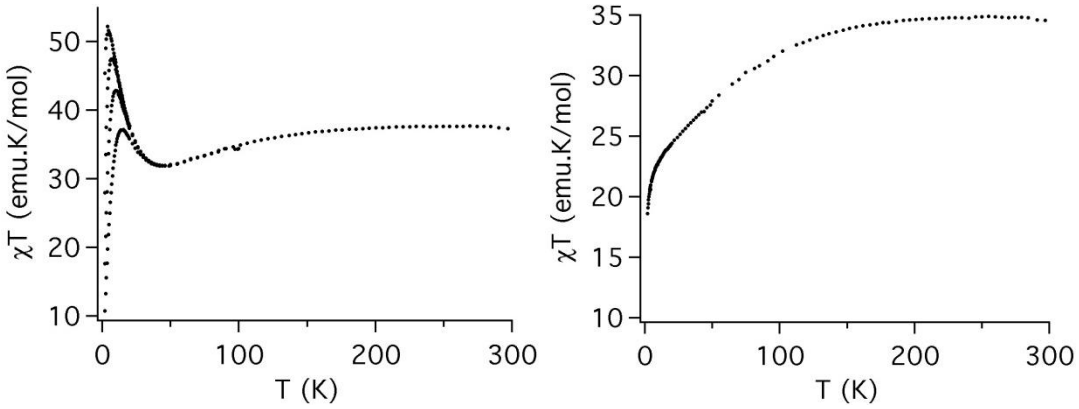

Fig. 2.54.- Thermal dependence of $\chi_m T$ for salts containing **2.6** (left) and **2.7** (right) anions at different fields (0.1, 0.5, 1 and 2 T for **2.6**; 0.1 T for **2.7**) in the range 2–300 K.

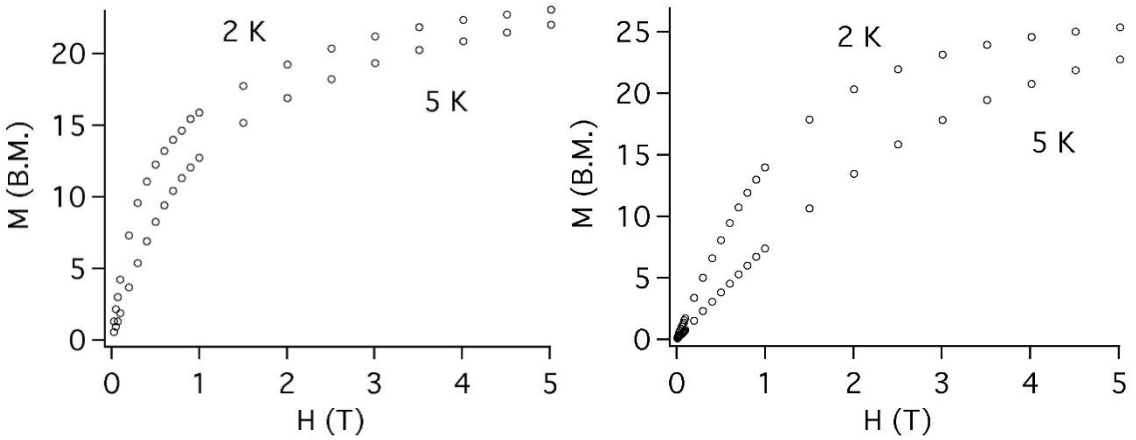

Fig. 2.55.- Magnetization versus field for **Q-2.6** (left) and **Q-2.7** (right) at 2 and 5 K.

We have recently studied several POMs containing similar triangular units, which present ferromagnetic interactions.[66,81-83] In these triangular units, the ferromagnetic sign of the exchange parameter was explained by the orthogonality of the magnetic orbitals in the edge-sharing CoO_6 octahedra (Co-O-Co angles close to 90º). All these systems present a sharp maximum at low temperature due to the ferromagnetic interaction between the lowest Kramers doublets of each Co(II) atom. The height of this maximum depends greatly on the position of the anisotropy axes of the cobalt atoms involved in the triangular unit. However, for **2.7**, no maximum is observed and only a change in the slope of the curve is observed upon cooling from room temperature to 8 K, where a sudden drop occurs. This may be due to the presence in the salt of a large number (four) of

monomeric external cobalt ions, which dominate the magnetic behaviour, masking the contribution of the triangular cobalt units.

In contrast to **Q-2.7**, **Q-2.6** exhibits the characteristic maximum in $\chi_m T$ at low temperature, clearly indicating the presence of dominant ferromagnetic interactions. To explain this behaviour, it is necessary to take into account the three different contributions present in this system: the first arises from a cobalt cubane unit (similar to that found in **2.7**), the second from a heptameric cobalt unit and, the third, from some external and isolated Co(II) ions. An identical heptameric unit was reported in the POM $\{[Co_3(H_2O)]_2[Co(OH)_2W_7O_{26}](PW_9O_{34})_2\}^{16-}$.[84] In this case the $\chi_m T$ curve exhibited a maximum in the same temperature region. This heptameric unit exhibits ferrimagnetic behavior, with ferromagnetic interaction between the cobalt atoms of each triangular unit and antiferromagnetic interaction between the central cobalt atom and the outer cobalt trimers. The cubane unit, together with the outer Co(II) ions, should show similar behaviour as in **Q-2.7**. Thus, the experimental behavior may result from the sum of the three different contributions with a dominant contribution at low temperature coming from the heptameric ferrimagnetic unit. Unfortunately, the large overparameterisation and the existence of external Co(II) ions make a quantitative analysis of the data impossible in this case.

2.2.3. Conclusions

We have reported a one-pot synthetic approach which gives rise to five cobalt-containing POM clusters (**2.2**, **2.3**, **2.5**, **2.6** and **2.7**) by carrying out slight variations to a common starting solution containing WO_4^{2-}, PO_4^{3-}, and Co^{2+} at pH 5.5. Each synthetic procedure includes the addition of persulfate, which causes the oxidation of some cobalt ions and promotes the formation of the $[Co^{II}_3Co^{III}O_4]$-cubane-containing fragment '$[Co_4(OH)_3(H_2O)_{6-n}(PW_9O_{34})]^{3-}$' (n = 3 or 5), which acts as a common subunit (**Fig. 2.56**). This subunit is topologically similar to the $[Co^{II}_4O_4]$-cubane-containing POM $[Co_4(OH)_3(H_2O)_3(PW_9O_{34})]^{4-}$ (**2.1**), which exists as an individual entity and has been described in the first part of this chapter. The use of persulfate as oxidant is responsible for the oxidation of the apical cobalt in the cubane cluster. This Co(III) ion is stabilized by the substitution of the three apical water molecules in **2.1** by oxo or hydroxo groups of other POM fragments present in solution, giving rise to larger final POM entities. Thus,

an heptacobalt-containing POM $[Co_7(OH)_6(H_2O)_6(PW_9O_{34})_2]^{9-}$ (**2.2**) is formed by substitution of the three apical water molecules in a subunit of **2.1** by the fragment '$\{Co_3(OH)_3(H_2O)_3(PW_9O_{34})\}^{6-}$' (see **Fig. 2.56a**). The additional substitution of one basal water molecule in the subunit of **2.1** gives rise to an infinite polymeric chain formulated as $[Co_7(OH)_6(H_2O)_4(PW_9O_{34})_2]_n^{9n-}$ (**2.3**). On the other hand, if three apical water molecules in **2.1** are replaced by the heptanuclear fragment '$\{[Co_3(H_2O)]_2[Co(OH)_2W_6O_{24}](PW_9O_{34})_2\}^{18-}$', a novel undecacobalt-containing POM $[Co_{11}(OH)_5(H_2O)_5(W_6O_{24})(PW_9O_{34})_3]^{22-}$ (**2.6**) is obtained (see **Fig. 2.56b**). Finally, a new decacobalt-containing POM $[\{Co_4(OH)_3(H_2O)(PW_9O_{34})\}_2\{K\subset(H_2W_{12}O_{41})_2\}\{Co(H_2O)_4\}_2]^{17-}$ (**2.7**) is formed by the substitution of the three apical water molecules and two basal water molecules of two subunits of **2.1** by bridging the di-paratungstate fragment '$[\{K\subset(H_2W_{12}O_{41})_2\}\{Co(H_2O)_4\}_2]^{11-}$' (see **Fig. 2.56c**).

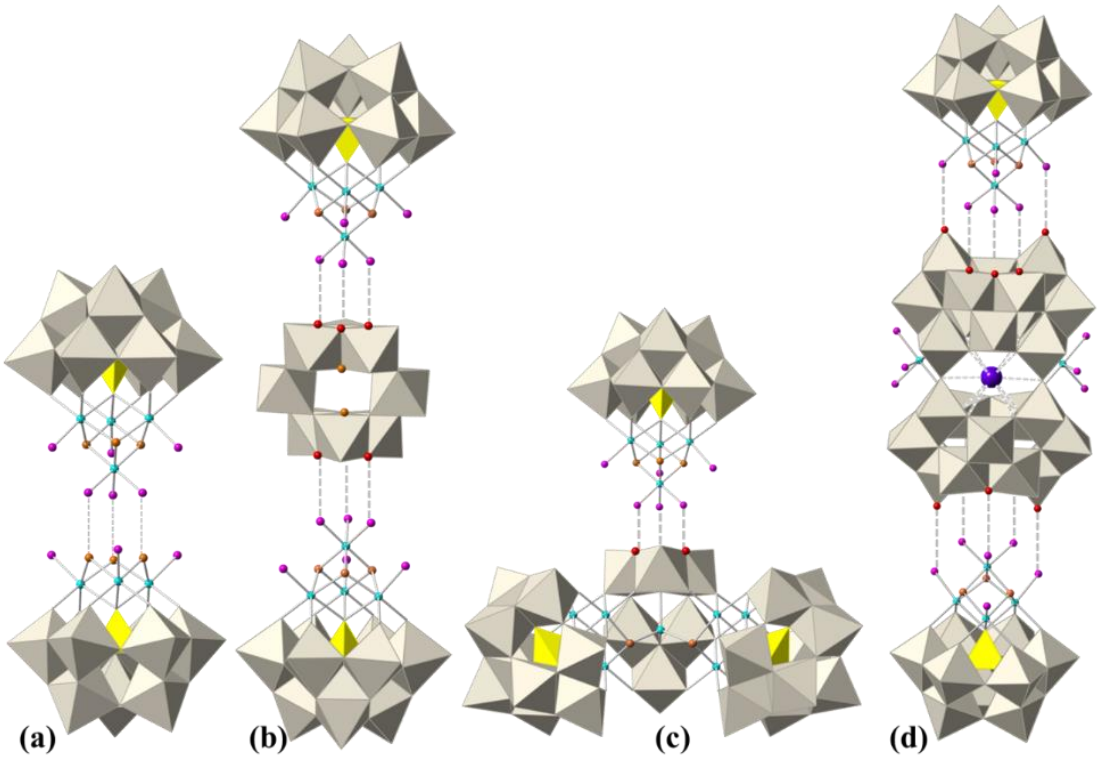

Fig. 2.56.- Polyhedral and ball-and-stick representations of the assembling of polyoxoanions (a) $[Co_7(OH)_6(H_2O)_6(PW_9O_{34})_2]^{9-}$ (**2.2**); (b) $[Co_8(OH)_6(H_2O)_6\{W_8O_{28}(OH)_2\}(PW_9O_{34})_2]^{16-}$ (**2.5**); (c) $[Co_{11}(OH)_5(H_2O)_5(W_6O_{24})(PW_9O_{34})_3]^{22-}$ (**2.6**) and (d) $[\{Co_4(OH)_3(H_2O)(PW_9O_{34})\}_2\{K\subset(H_2W_{12}O_{41})_2\}\{Co(H_2O)_4\}_2]^{17-}$ (**2.7**). Gray octahedra, $[WO_6]$; yellow tetrahedral, $[PO_4]$; cyan spheres, Co; red spheres, O; orange spheres, OH; pink spheres, H_2O; violet sphere, K.

As far as the stability of these POMs is concerned, we have observed that **2.7** is stable in aqueous solutions for at least 48 hours, as confirmed by UV-vis spectroscopy,

while **2.2**, **2.5** and **2.6** slowly decompose forming the mono-substituted Keggin anion $[PCo(H_2O)W_{11}O_{39}]^{5-}$ as the major product. Cyclic voltammetry of **2.7** shows an irreversible reduction of the oxo-tungsten framework and a quasi-reversible electrochemical oxidation of the cobalt centers. Concerning the magnetic properties, we have focused on the new POMs (**2.6** and **2.7**). In the corresponding salts, the presence of several isolated octahedrally coordinated Co(II) ions acting as counterions have made impossible to carry out a quantitative analysis. Nonetheless, the magnetic properties of **2.6** can be understood qualitatively from the known magnetic interactions existing in previously reported cobalt clusters encapsulated in POMs. In fact, the magnetic behavior of this large POM (formed by the fusion of a heptanuclear Co(II) cluster with the $[Co^{II}_3Co^{III}]$ cubane unit) is dominated at low temperatures by the ferrimagnetic coupling within the heptanuclear cluster.

Finally, it has to be noted that the synthetic strategy reported in this work can be further exploited to obtain other POMs with larger nuclearities made from the linkage of subunits of **2.1** with other polyoxoanion fragments, by substitution of the water ligands coordinated to the cobalt atoms of the cubane cluster.

2.2.4. Experimental section

2.2.4.1. General methods and materials

All reagents were of high purity grade quality, obtained from commercial sources, and used without further purification. The preparation and characterisation of the POM salts $Na_{1.5}Cs_{2.5}[Co_4(OH)_3(H_2O)_6(PW_9O_{34})]\cdot 9H_2O$ (**Q-2.1**) and $K_{5n}Na_{2n}\{Co(H_2O)_2\}_n[Co_7(OH)_6(H_2O)_4(PW_9O_{34})_2]_n\cdot 20nH_2O$ (**Q-2.3**) have been previously described in the first part of this chapter. Pure water ($\rho > 18$ MΩ·cm) was used throughout. It was obtained using an Elix-3/Millipore-Q Academic water purification system. IR spectra were recorded with KBr pellets on a Thermo NICOLET-5700 FT-IR spectrophotometer. Elemental analysis was carried out with a Philips XL-30 scanning electron microscope coupled with a Philips EDAX Microanalysis system. Thermogravimetric analysis was performed on a Mettler Toledo TGA/SDTA851e analyzer. The UV-vis spectra of the relevant POMs (10^{-5} M) were recorded on an Agilent 8453 UV-vis spectrophotometer from 190 to 400 nm using 10-mm-optical-path quartz cuvettes in buffer solutions of 0.5 M sodium acetate (pH 4.8). Cyclic voltammetry

measurements were carried out on an Autolab PGSTAT128N potentiostat using a three-electrode single compartment cell supplied by IJ Cambria. It was equipped with a 3 mm glassy carbon disc working electrode (which was polished sequentially with 0.3, 0.1 and 0.05 μm alumina powders and washed with distilled water before each experiment), a platinum wire counter electrode and a Ag/AgCl (3 M KCl) reference electrode. Cyclic voltammograms were recorded at a scan rate of 10 $mV \cdot s^{-1}$ using the same media as for UV-vis spectroscopy. The solutions were deaerated during at least 15 min with argon and kept under a positive pressure of this gas during the experiments.

2.2.4.2. Synthesis

2.2.4.2.1. Preparation of the starting solution

5.40 g (16.4 mmol) of $Na_2WO_4 \cdot 2H_2O$ and 0.21 g (1.48 mmol) of Na_2HPO_4 were dissolved in 15 mL of water and the pH of the solution was adjusted to 5.4 using glacial acetic acid. Another aqueous solution containing 1.29 g (5.18 mmol) of $Co(CH_3COO)_2 \cdot 4H_2O$ in 20 mL of water was added dropwise to the first solution, giving rise to a solution with pH = 5.5.

*2.2.4.2.2. Synthesis of $K_{4.2}Na_{2.8}\{Co(H_2O)_6\}[Co_7(OH)_6(H_2O)_6(PW_9O_{34})_2] \cdot 19H_2O$ (**Q'-2.2**)*

The starting solution was refluxed for two hours and hot filtered. To the warm filtrate, 2.24 g (22.8 mmol) of potassium acetate and 0.11 g (0.41 mmol) of potassium persulfate were successively added in small portions. After the addition, the dark solution was allowed to stand at room temperature in an open beaker. A big amount of orange precipitate appeared overnight, which was filtered and recrystallized in 15 mL of water. After one week, orange plate-shaped crystals were formed (yield: 0.352 g, 6.6 % based on W). The P:Co:W ratio obtained by SEM-EDX for **Q'-2.2** is 1.79:11.79:86.42 (calcd for $P_2Co_8W_{18}$: 1.61:12.26:86.12). IR (2 % KBr pellet 1100–400 cm^{-1}) (**Fig. 2.57**): 1056(m), 1033(s), 982(m, sh), 953(sh), 938(s), 883(s), 792(w), 715(m, sh), 588(w), 540(m), 479(m, sh), 415(s). The TGA curve of **Q'-2.2** (**Fig. 2.58**) shows a total weight loss of 11.36 % in the range 25-800 ºC, which agrees with the loss of 31 water molecules and 6 hydroxyls in the structure (calcd 11.29 %).

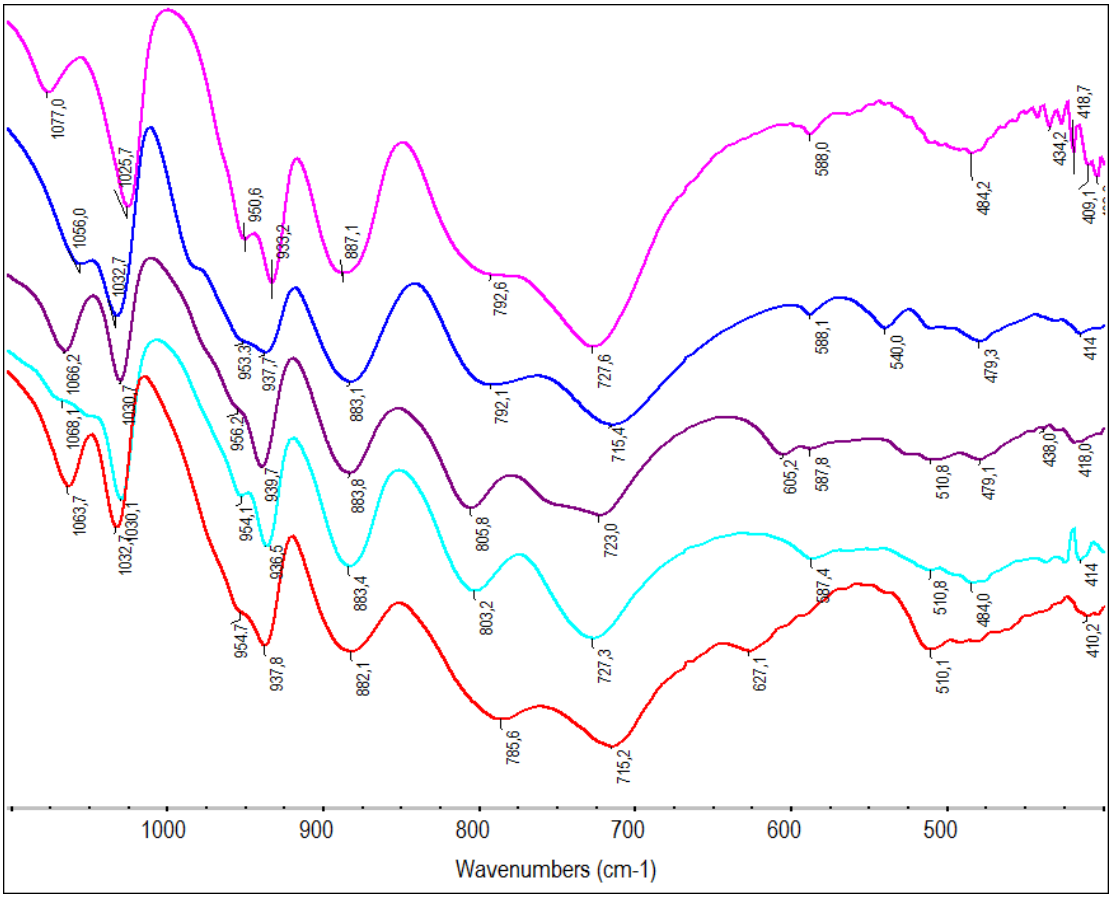

Fig. 2.57.- FT-IR spectra of salts **Q-2.1** (pink), **Q'-2.2** (blue), **Q-2.5** (violet), **Q-2.6** (cyan) and **Q-2.7** (red).

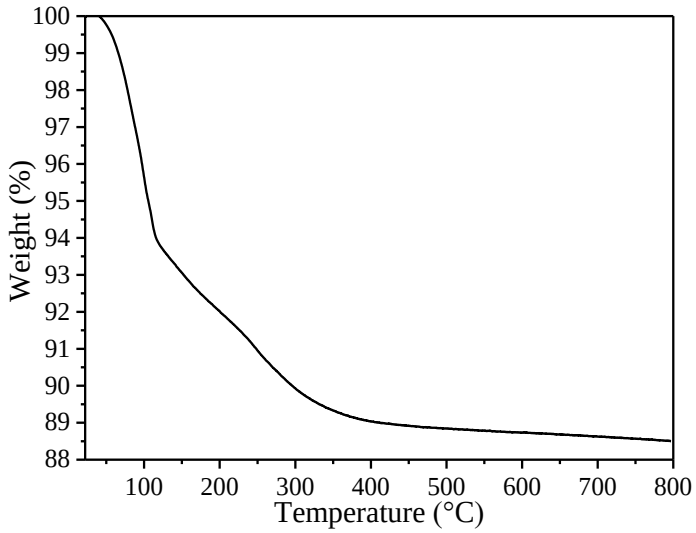

Fig. 2.58.- Thermogram of **Q'-2.2** from room temperature to 800 ºC (experimental total weight loss 11.36 %).

*2.2.4.2.3. Synthesis of $K_2Na_{14}[Co_8(OH)_6(H_2O)_6\{W_8O_{28}(OH)_2\}(PW_9O_{34})_2]\cdot 44H_2O$ (**Q-2.5**)*

*<u>WARNING</u>: This compound was obtained only once. Several attempts were conducted to obtain further amounts of this material, but all were unsuccessful. The formula of **Q-2.5** is derived solely on the basis of the crystallographic analysis and the P:Co:W ratio obtained by SEM-EDX.*

The starting solution (see section 2.2.4.2.1) was diluted with 20 mL of water and the pH readjusted to 5.4 with glacial acetic acid (approx. 10 drops). Then, the solution was refluxed for two hours and hot filtered. To the hot filtrate, 2.24 g (22.8 mmol) of potassium acetate and 0.11 g (0.41 mmol) of potassium persulfate were successively added in small portions. After the addition of the solids, the dark solution was allowed to stand at room temperature in a beaker covered with Parafilm to prevent evaporation. After 4 months, grey plate-shaped crystals were obtained (yield: 0.078 g, < 0.1 % based on W). The P:Co:W ratio obtained by SEM-EDX for **Q-2.5** is 1.62:8.68:89.70 (calcd for $P_2Co_8W_{26}$: 1.16:8.87:89.97). IR (2 % KBr pellet 1100–400 cm^{-1}): 1066(m), 1031(s), 958(m, sh), 940(s), 884(s), 806(w), 723(m, sh), 605(w), 588(w), 511(m), 479(m, sh), 418(s). For a general synthetic scheme of compounds, see **Scheme 2.1**.

*2.2.4.2.4. Synthesis of $K_{12}Na_4H_3\{Co_{1.5}(H_2O)_{5.5}\}[Co_{11}(OH)_5(H_2O)_5(W_6O_{24})(PW_9O_{34})_3]\cdot 37.5H_2O$ (**Q-2.6**)*

The pH of the starting solution was readjusted to 5.4 with glacial acetic acid. Then, the solution was refluxed for two hours, hot filtered, and to the hot filtrate 2.24 g (22.8 mmol) of potassium acetate and 0.11 g (0.41 mmol) of potassium persulfate were successively added in small portions. After the addition of the solids, the solution was concentrated at 100 ºC until a final volume of 20 mL was attained. Then, the solution was allowed to cool to room temperature and a large amount of black precipitate, (identified as $K_{10.5}Na_{0.3}\{Co_{0.6}(H_2O)_{3.6}\}[Co_4(H_2O)_2(CoW_9O_{34})(PW_9O_{34})]\cdot 19.4H_2O$)[71] was formed and filtered out. The filtrate was allowed to stand at room temperature in an open beaker and, after one week, blue needle-shaped crystals were formed (yield: 0.128 g, 2.7 % based on W). The P:Co:W ratio obtained by SEM-EDX for **Q-2.6** is 1.55:10.39:88.06 (calcd for $P_3Co_{12.5}W_{33}$: 1.35:10.67:87.98). IR (2 % KBr pellet 1100–400 cm^{-1}) (**Fig. 2.57**): 1068(m), 1048(w), 1030(s), 954(m, sh), 937(s), 883(s), 803(w), 727(m, sh), 587(w), 511(m), 484(m, sh), 415(s). The TGA curve of **Q-2.6** (**Fig. 2.59**) shows a total weight loss of 9.10 % in

the range 25-800 ºC which agrees with the loss of 48 water molecules and 5 hydroxyls in the structure (calcd 9.02 %).

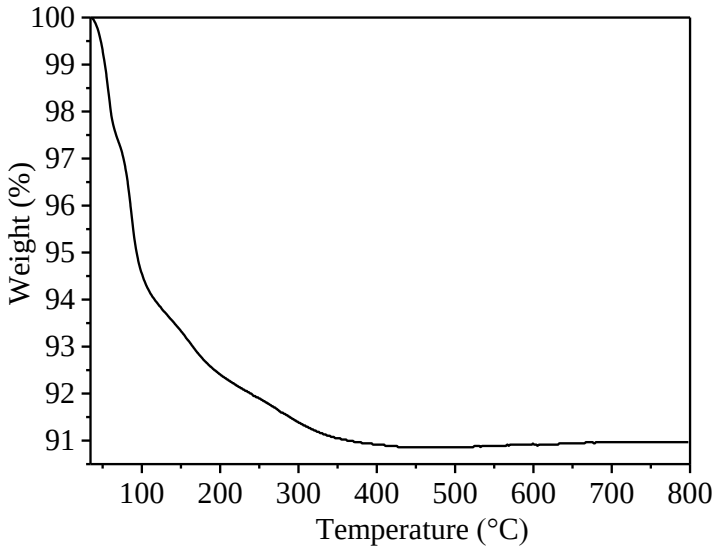

Fig. 2.59.- Thermogram of **Q-2.6** from room temperature to 800 ºC (experimental total weight loss 9.02 %).

2.2.4.2.5. Synthesis of $K_{12}Na\{Co_2(H_2O)_{10}\}[\{Co_4(OH)_3(H_2O)(PW_9O_{34})\}_2\{K\subset(H_2W_{12}O_{41})_2\}\{Co(H_2O)_4\}_2]\cdot 71H_2O$ ***(Q-2.7)***

The starting solution was refluxed for two hours and, then, 2.24 g (22.8 mmol) of potassium acetate and 0.11 g (0.41 mmol) of potassium persulfate were successively added to the hot solution. After the addition of the solids, the solution was filtered and kept in an open beaker and a black precipitate appeared overnight which was filtered and identified as $K_{10.5}Na_{0.3}\{Co_{0.6}(H_2O)_{3.6}\}[Co_4(H_2O)_2(CoW_9O_{34})(PW_9O_{34})]\cdot 19.4H_2O$.[71] The filtrate was left to evaporate at room temperature in an open beaker until the volume of the reaction mixture reached approx. 20 mL and a large amount of orange precipitate appeared. This solid was filtered and recrystallized in boiling water. After one week, orange block shaped crystals were formed, filtered and washed with a small amount of cold water (yield: 0.180 g, < 0.1 % based on W). The P:Co:W ratio obtained by SEM-EDX for **Q-2.7** is 1.07:8.81:90.12 (calcd for $P_2Co_{12}W_{42}$: 0.73:8.32:90.95). IR (2 % KBr pellet 1100–400 cm^{-1}) (**Fig. 2.57**): 1064(m), 1033(s), 954(m, sh), 938(s), 882(s), 786(w), 715(m, sh), 627(w), 510(m), 410(m, sh). The TGA curve of **Q-2.7** (**Fig. 2.60**) shows a total weight loss of 13.65 % in the range 25-800 ºC which agrees with the loss of 91 water molecules and 10 hydroxyls in the structure (calcd 13.74 %).

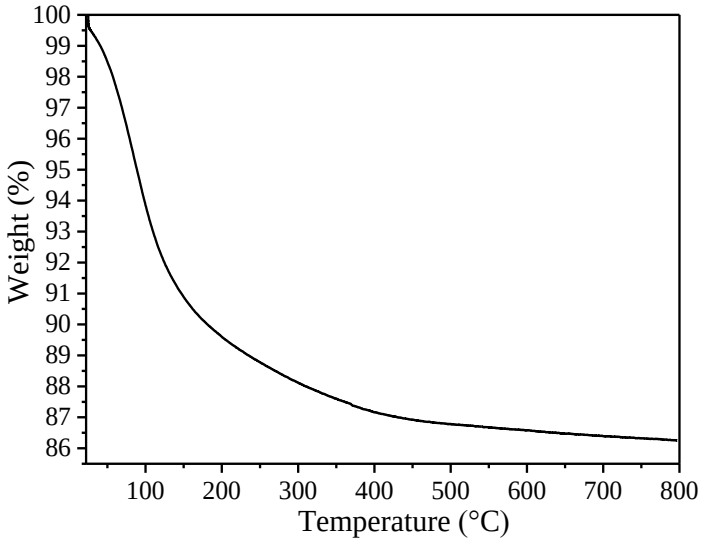

Fig. 2.60.- Thermogram of **Q-2.7** from room temperature to 800 ºC (experimental total weight loss 13.65 %).

2.2.4.3. X-ray Crystallography

Suitable crystals of **Q'-2.2**, **Q-2.5**, **Q-2.6** and **Q-2.7** were coated with Paratone N oil, suspended on small fiber loops, and placed in a stream of cooled nitrogen (120 K) on an Oxford Diffraction Supernova diffractometer equipped with a graphite-monochromated Enhance (Mo) X-ray Source (λ = 0.71073 Å). The data collection routines, unit cell refinements and data processing were carried out using the CrysAlis software package[60] and structure solution and refinement were carried out using SHELXS-97 and SHELXL-2016/4.[61]

All atoms were refined anisotropically in the four crystal structures except some disordered counter cations and water molecules of solvation having partial occupancies. Analytical absorption corrections were performed for all compounds based on face indexations of the single crystals. Hydrogen atoms of water molecules and hydroxyl anions were not included in the models.

The structure of **Q-2.7** contains channels parallel to the crystallographic *c* axis containing disordered water molecules that could not be modeled as discrete atomic sites. We employed PLATON SQUEEZE[62] to calculate the contribution to the diffraction from the solvent/cation region and thereby produced a set of solvent-free diffraction intensities. According to the TGA, 44 water molecules per POM reside in these channels in accordance with the volume of the void and electron count found by SQUEEZE. These additional water molecules were added to the final formula of **Q-2.7**.

In the case of **Q-2.6**, 31 solvation water molecules were found in Fourier maps and included in the structural model. The TGA indicated the presence of 6.5 additional water molecules of solvation, which were included in the final formula of **Q-2.6**. In this case, the SQUEEZE procedure was considered to be unnecessary.

CSD reference number and CCDC reference number for **Q'-2.2**, **Q-2.5**, **Q-2.6** and **Q-2.7** are 432446 and 1538254, respectively. A summary of the crystallographic data for all compounds is given in **Table 2.3**.

2.2.4.4. Magnetic Measurements

Samples of **2.6** and **2.7** were prepared by compacted powder molded from ground crystalline samples. Each sample was covered with the minimum amount of liquid eicosane (40 ºC) in order to prevent crystallite torquering. Variable-temperature susceptibility measurements were carried out in the temperature range 2-300 K on a magnetometer equipped with a SQUID sensor (Quantum Design MPMS-XL-5). The data were corrected for diamagnetic contribution from eicosane and for the diamagnetic contributions of the polyanions as deduced by using the Pascal's constant tables. Isothermal magnetization measurements at low temperature (2 K and 5 K) were performed up to a field of 5 T in the same apparatus.

Table 2.3.- Crystallographic Data for $K_{4.2}Na_{2.8}\{Co(H_2O)_6\}[Co_7(OH)_6(H_2O)_6(PW_9O_{34})_2]\cdot 19H_2O$ (**Q'-2.2**), $K_2Na_{14}[Co_8(OH)_6(H_2O)_6\{W_8O_{28}(OH)_2\}(PW_9O_{34})_2]\cdot 44H_2O$ (**Q-2.5**), $K_{12}Na_4H_3\{Co_{1.5}(H_2O)_{5.5}\}[Co_{11}(OH)_5(H_2O)_5(W_6O_{24})(PW_9O_{34})_3]\cdot 37.5H_2O$ (**Q-2.6**) and $K_{12}Na\{Co_2(H_2O)_{10}\}[\{Co_4(OH)_3(H_2O)(PW_9O_{34})\}_2\{K\subset(H_2W_{12}O_{41})_2\}\{Co(H_2O)_4\}_2]\cdot 71H_2O$ (**Q-2.7**).

Compound	**Q'-2.2**	**Q-2.5**	**Q-2.6**	**Q-2.7**
empirical formula	$Co_8H_{68}K_{4.20}Na_{2.80}O_{105}P_2W_{18}$	$Co_8H_{108}K_2Na_{14}O_{154}P_2W_{26}$	$Co_{12.5}H_{104}K_{12}Na_4O_{179}P_3W_{33}$	$Co_{12}H_{192}K_{13}NaO_{247}P_2W_{42}$
formula weight	5819.82	8286.40	10426.58	13167.63
space group	*P–1*	*P–1*	*P–1*	*Pmmn*
a/Å	11.5505(3)	11.6458(2)	12.30440(12)	46.3907(3)
b/Å	12.4263(3)	12.87367(19)	24.7192(2)	19.63375(16)
c/Å	20.3358(8)	25.4990(3)	27.2759(2)	12.80597(7)
α/°	75.365(3)	89.4689(10)	85.7259(7)	90
β/°	76.876(3)	86.5366(11)	86.8164(7)	90
γ/°	68.308(2)	71.6439(14)	89.0860(8)	90
V/Å^3	2594.94(14)	3621.59(9)	8259.68(12)	11663.98(14)
Z	1	1	2	2
T/K	120.00(10)	120.00(10)	120.00(10)	120.00(10)
λ/Å	0.71073	0.71073	0.71073	0.71073
ρ_{calcd}/g cm^{-3}	3.724	3.799	4.192	3.749
μ/mm^{-1}	21.422	21.684	24.555	21.883
$R[F_o^2 > 2\sigma(F_o^2)]$[a]	0.0571	0.0403	0.0473	0.0627
$R_w[F_o^2 > 2\sigma(F_o^2)]$[b]	0.1425[c]	0.0932[d]	0.1052[e]	0.1554[f]

[a] $R = \Sigma(||F_o| - |F_c||)/\Sigma|F_o|$. [b] $R_w = \{\Sigma[w(F_o^2 - F_c^2)^2]/\Sigma[w(F_o^2)^2]\}^{1/2}$. $w = 1/[\sigma^2(F_o^2) + (AP)^2 + BP]$, where $P = (F_o^2 + 2F_c^2)/3$. [c] $A = 0.0441$, $B = 271.6505$. [d] $A = 0.0353$, $B = 80.1873$. [e] $A = 0.0381$, $B = 405.0507$. [f] $A = 0.0506$, $B = 1340.3177$.

2.3. A decacobalt(II) cluster with triple-sandwich structure obtained by partial reductive hydrolysis of a pentacobalt(II/III) Weakley-type polyoxometalate

2.3.1. Introduction

A relevant family of Co-containing polyoxotungstates consists of a single layer of up to four CoO_6 octahedra sandwiched between two trilacunary capping ligands derived from the parent Keggin structure (i.e. $[XW_9O_{34}]^{n-}$, with X = Si^{IV}, Ge^{IV}, P^{V}, As^{V}, Zn^{II}, Co^{II}, V^{V}, *etc.*). The most representative example of this family is the tetracobalt sandwich POM $[Co^{II}_4(H_2O)_2(PW_9O_{34})_2]^{10-}$ originally obtained by Weakley (see **Fig. 2.61**).[31] These compounds can be obtained by reaction of Co(II) ions with the preformed $[XW_9O_{34}]^{n-}$ capping ligand or by direct polycondensation of tungstate and the necessary heteroatoms (i.e., phosphate, silicate, *etc.*) in the presence of Co(II) ions at the appropriate pH.[85] To our knowledge, all POMs with Weakley's topology reported to date are formed by two identical capping ligands, *i.e.* the heteroatom X is the same in both $[XW_9O_{34}]^{n-}$ moieties.

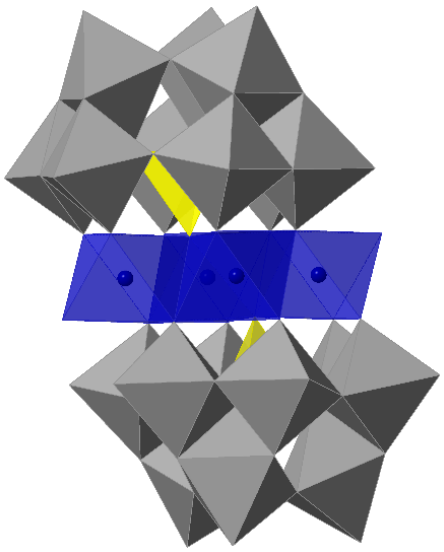

Fig. 2.61.- Polyhedral representation of the tetracobalt sandwich POM $[Co^{II}_4(H_2O)_2(PW_9O_{34})_2]^{10-}$. Gray octahedra, $[WO_6]$; yellow tetrahedra, $[PO_4]$; blue octahedra, $[CoO_6]$; blue spheres, Co.

In this part of the work, we have obtained and characterised the first example of an asymmetric sandwich POM with this topology ($[Co^{II}_4(H_2O)_2(Co^{III}W_9O_{34})(PW_9O_{34})]^{12-}$, **2.8**). The subsequent reaction of this POM with hydrazine by partial reductive hydrolysis gave rise to a new triple-layered sandwich POM containing an unprecedented deca-Co(II) cluster ($[Co_2\{Co_3(H_2O)(Co(OH)_2W_7O_{26})(PW_9O_{34})\}_2]^{22-}$, **2.9**).

2.3.2. Results and Discussion

2.3.2.1. Synthetic approach

2.8 was synthesized in a one-pot reaction of Co(II) ions with tungstate and phosphate in aqueous medium at pH 5.5 in the presence of persulfate as oxidant, and isolated as a hydrated potassium and sodium mixed salt. In the absence of persulfate, the POM obtained is the Weakley's POM formulated as $[Co^{II}_4(H_2O)_2(PW_9O_{34})_2]^{10-}$, which contains P(V) in the two tetrahedral positions available for this topology. Therefore, the key point to obtain **2.8** (which contains cobalt in one of the tetrahedral positions) appears to be the presence of cobalt ions with oxidation state 3+ in the reaction solution, giving rise to the formation of an asymmetric sandwich structure. The formation of a symmetric sandwich structure containing Co(III) ions in both tetrahedral positions was attempted by removing the phosphate ions from the reaction mixture without success. This suggests that the phosphate ions are necessary for the formation of this kind of sandwich structure by giving rise first in solution to the fragment $[PW_9O_{34}]^{9-}$ which act as a template for the further assembling of the asymmetric sandwich.

The reaction of **2.8** with hydrazine gave rise to the higher nuclearity POM (**2.9**), which was isolated as the hydrated salt $K_6\{Co_9(H_2O)_{42}\}[Co_2\{Co_3(H_2O)(Co(OH)_2W_7O_{26})(PW_9O_{34})\}_2]\cdot 26H_2O$ (**Q-2.9**). This reaction can be considered as a condensation of two units of **2.8**, proceeding through partial reductive hydrolysis and the elimination of the smaller paratungstate polyanion (see **Fig. 2.62**).

$$12\ [Co^{II}_4(H_2O)_2(Co^{III}W_9O_{34})(PW_9O_{34})]^{12-}\ (\mathbf{2.8}) + 3\ N_2H_4 + 8\ OH^- \rightarrow$$
$$6\ [Co^{II}_2\{Co^{II}_3(H_2O)(Co^{II}(OH)_2W_7O_{26})(PW_9O_{34})\}_2]^{22-}\ (\mathbf{2.9})$$
$$+ 2\ [H_2W_{12}O_{42}]^{10-} + 3N_2 + 8\ H_2O$$

2.9 is obtained by the slight basification of an aqueous solution of **2.8**, which is produced with hydrazine (pH ~7.6). This basification produces a partial hydrolysis in the $[Co^{III}W_9O_{34}]^{11-}$ moiety, giving rise to lacunary polydentate building blocks with the ability to coordinate two extra Co(II) metal ions to form the dimeric POM, **2.9**. It is noteworthy that the hydrolysis takes place only in the $[Co^{III}W_9O_{34}]^{11-}$ moiety and not in the $[PW_9O_{34}]^{9-}$ fragment, which points to a lower stability of the former in comparison with the latter, which would require higher pH values to undergo further hydrolysis. The

other essential role of hydrazine in this synthesis consists of reducing the Co(III) ions to Co(II). A final point that deserves to be mentioned is the isomerization produced by the rotation of the B-$[PW_9O_{34}]^{9-}$ capping ligand as it loses one cobalt atom from the tetrameric Co_4 unit to transform into **2.9**. The heating process likely induces this isomerization during the synthesis of **2.9**.

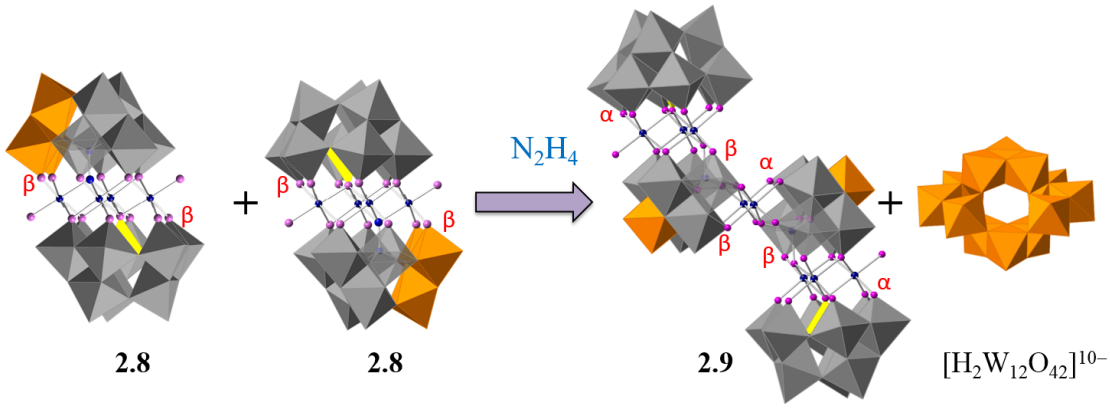

Fig. 2.62.- Polyhedral and ball-and-stick representation of the partial reductive hydrolysis of **2.8** to the formation of a new triple-layered sandwich **2.9**.

2.3.2.2. Crystal Structure of $K_{10.5}Na_{0.3}\{Co_{0.6}(H_2O)_{3.6}\}[Co^{II}_4(H_2O)_2(Co^{III}W_9O_{34})(PW_9O_{34})]\cdot 19.4H_2O$ (Q-2.8)

Polyoxoanion **2.8** crystallizes as the mixed salt $K_{10.5}Na_{0.3}\{Co_{0.6}(H_2O)_{3.6}\}[Co_4(H_2O)_2(CoW_9O_{34})(PW_9O_{34})]\cdot 19.4H_2O$ (**Q-2.8**) in the centrosymmetric space group $P\bar{1}$ (*i.e.* the asymmetric unit contains only half POM unit). The crystal structure reveals that **2.8** has the same topology as $[Co_4(H_2O)_2(PW_9O_{34})_2]^{10-}$ (**Fig. 2.61**). However, a close inspection of the bond distances of the heteroatom that occupies the tetrahedral position, reveals that they are longer than expected for P-O bonds, but shorter than expected for Co-O bonds (**Table 2.4**), pointing to an occupational disorder between P and Co. A refinement of this disorder leads to an occupation of approx. 50 % for P and Co. The crystallographic disorder avoids the use of BVS calculations to estimate the oxidation state of the cobalt atom in the tetrahedral position, but clearly indicates an oxidation state of 2+ for the other four cobalt ions with octahedral coordination (**Table 2.5**).

The crystallographic disorder between P^V and Co^{III} located in the tetrahedral position of **2.8** is compatible with either of the following possibilities: (*i*) the sample consists of a

mixture (ca. 1:1) of sandwich POMs in which the tetrahedral positions are occupied only by P or Co, (*ii*) the sample consists mainly of one type of POM in which the two tetrahedral positions are occupied by one Co and one P atom within the same polyanion. This second possibility is a far better match to the mass spectrometry and ^{31}P NMR results than the first one (see below).

Table 2.4.- Comparison of the tetrahedral P^{V}-O, Co^{II}-O or Co^{III}-O bond distances in **2.8**,[a] **2.9**,[b] and selected compounds from the literature: $[Co_4(H_2O)_2(PW_9O_{34})_2]^{10-}$,[c] $[Co^{II}W_{12}O_{40}]^{6-}$,[d] and $[Co^{III}W_{12}O_{40}]^{5-}$.[e]

P^{V}/Co^{III}-O[a]	Co^{II}-O[b]	P^{V}-O[c]	Co^{II}-O[d]	Co^{III}-O[e]
1.6515(17)	1.950(7)	1.528(17)	1.931(14)	1.836(10)
1.6962(9)	1.950(7)	1.532(12)	1.931(14)	1.836(10)
1.715(2)	1.953(11)	1.547(14)	1.931(14)	1.836(10)
1.7352(16)	1.964(10)	1.552(13)	1.931(14)	1.836(10)

[a] **2.8** (this work, T = 120 K). P^{V} and Co^{III} occupy the same crystallographic position inside the tetrahedral cavity of **2.8** (refined occupancy ca. 50 %). [b] **2.9** (this work, T = 120 K). [c] $[Co_4(H_2O)_2(PW_9O_{34})_2]^{10-}$ (T = 172 K).[8] [d] $[Co^{II}W_{12}O_{40}]^{6-}$ (T = 298 K).[86] [e] $[Co^{III}W_{12}O_{40}]^{5-}$ (T = 298 K).[86]

Table 2.5.- Selected Co-O Bond Distances (Å) and O-Co-O Angles (º) involved in **2.8** (see **Fig. 2.66** for the labelling of the relevant atoms).

Co(1)-O(1)	1.654(13)	Co(2)-O(1)	2.139(11)
Co(1)-O(2)	1.697(12)	Co(2)-O(10)^{i}	2.021(10)
Co(1)-O(4)	1.711(12)	Co(2)-O(7)	2.030(10)
Co(1)-O(3)	1.733(13)	Co(2)-O(8)	2.111(11)
Co(2)-O(9)^{i}	2.112(11)	Co(3)-O(6)	2.056(10)
Co(2)-O(1)^{i}	2.140(11)	Co(3)-O(8)^{i}	2.116(10)
Co(3)-O(1)	2.123(11)	Co(3)-O(1W)	2.123(12)
Co(3)-O(5)	2.039(10)	Co(3)-O(9)^{i}	2.122(10)
O(1)-Co(1)-O(2)	115.3(5)	O(10)^{i}-Co(2)-O(9)^{i}	93.2(4)
O(1)-Co(1)-O(4)	112.2(5)	O(7)-Co(2)-O(9)^{i}	93.5(4)
O(2)-Co(1)-O(4)	106.2(5)	O(8)-Co(2)-O(9)^{i}	170.9(4)
O(1)-Co(1)-O(3)	111.5(5)	O(10)^{i}-Co(2)-O(1)^{i}	91.4(4)
O(2)-Co(1)-O(3)	105.8(5)	O(7)-Co(2)-O(1)^{i}	173.7(4)
O(4)-Co(1)-O(3)	105.0(5)	O(8)-Co(2)-O(1)^{i}	84.1(4)
O(10)^{i}-Co(2)-O(7)	94.2(4)	O(9)^{i}-Co(2)-O(1)^{i}	88.9(4)
O(10)^{i}-Co(2)-O(8)	92.8(4)	O(10)^{i}-Co(2)-O(1)	173.1(4)
O(7)-Co(2)-O(8)	92.9(4)	O(7)-Co(2)-O(1)	92.3(4)
O(8)-Co(2)-O(1)	89.1(4)	O(5)-Co(3)-O(1)	90.2(4)
O(9)^{i}-Co(2)-O(1)	84.1(4)	O(6)-Co(3)-O(1)	91.0(4)
O(1)^{i}-Co(2)-O(1)	82.1(5)	O(8)^{i}-Co(3)-O(1)	84.4(4)
O(5)-Co(3)-O(6)	90.7(4)	O(1W)-Co(3)-O(1)	177.4(5)
O(5)-Co(3)-O(8)^{i}	91.1(4)	O(5)-Co(3)-O(9)^{i}	174.0(4)
O(6)-Co(3)-O(8)^{i}	175.0(4)	O(6)-Co(3)-O(9)^{i}	91.8(4)
O(5)-Co(3)-O(1W)	88.1(5)	O(8)^{i}-Co(3)-O(9)^{i}	86.0(4)
O(6)-Co(3)-O(1W)	91.0(4)	O(1W)-Co(3)-O(9)^{i}	97.3(5)
O(8)^{i}-Co(3)-O(1W)	93.7(4)	O(1)-Co(3)-O(9)^{i}	84.3(4)

Symmetry transformations: (*i*) –x+2, –y+1, –z.

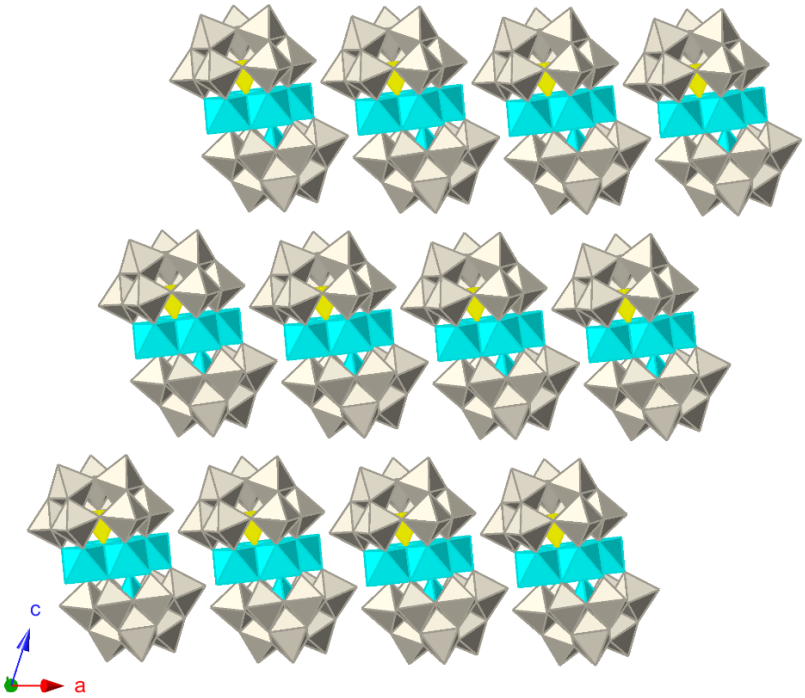

Fig. 2.63.- Polyhedral and ball-and-stick representation of the packing mode of **2.8** along *b*-axis. Lattice cations and water molecules are omitted for clarity. Cyan octahedra, [CoO_6]; gray octahedra, [WO_6]; blue spheres, Co; red spheres, O.

2.3.2.3. Crystal Structure of $K_6\{Co_9(H_2O)_{42}\}[Co_2\{Co_3(H_2O)(Co(OH)_2W_7O_{26})(PW_9O_{34})\}_2]\cdot 26H_2O$ (Q-2.9)

The crystal structure of **2.9** exhibits an idealized C_{2h} symmetry and encapsulates a deca-Co(II) cluster. This cluster is made of two terminal Co_3 triads, one central Co_2 dimer and two tetrahedral cobalt atoms that connect the dimer with the triads (**Fig. 2.64a**). Both Co_3 triads are capped by trilacunary $[PW_9O_{34}]^{9-}$ ligands and bridged to the central Co_2 dimer with two $[Co(OH)_2W_7O_{26}]^{10-}$ fragments, which contain the tetrahedral cobalt atoms. An important structural aspect of **2.9** concerns the junctions between the Co_3 triads and the $[PW_9O_{34}]^{9-}$ or $[Co(OH)_2W_7O_{26}]^{10-}$ moieties in **2.9** (α and β, respectively, **Fig. 2.64a**). In POM **2.8**, however, the junctions between the central tetrameric Co_4 unit and the two $[XW_9O_{34}]^{n-}$ (X = P^V and Co^{III}) capping ligands are both β type (**Fig. 2.64**). Therefore, one effect of the reaction of **2.8** with hydrazine consists on a 60° rotation of the B-$[PW_9O_{34}]^{9-}$ capping ligand as it loses one of the Co atoms of the tetrameric Co_4 unit to transform into **2.9**. This agrees with the fact that all known B-type Keggin tetranuclear sandwich POMs containing first row transition metals present β junctions, while trinuclear sandwich POMs always exhibit the α junction.[82,87-89]

The structural features of **2.9** are reminiscent of the hydrothermally prepared $[Fe_2\{Fe_3(H_2O)(H_2AsW_6O_{26})(H_4AsW_9O_{34})\}_2]^{4-}$,[90] although there are several important differences between the latter and **2.9**: on the one hand, the Fe-containing POM encapsulates two Fe_3 triads and one Fe_2 dimer (all isolated from each other), while **2.9** contains two additional Co(II) (substituting the tetrahedral As^V) which connect the Co_3 triads with the Co_2 dimer, giving rise to a deca-Co(II) cluster. On the other hand, the bridging $[Co(OH)_2W_7O_{26}]^{10-}$ units contain one additional tungsten compared to the corresponding bridging $[H_2AsW_6O_{26}]^{9-}$ unit in the Fe-containing POM. For this reason, it is more enlightening to compare **2.9** with the previously reported polyoxoanion $\{[Co_3(H_2O)]_2[Co(OH)_2W_7O_{26}](PW_9O_{34})_2\}^{16-}$.[52] This hepta-Co(II)-containing POM is made of two terminal Co_3 triads capped by $[PW_9O_{34}]^{9-}$ ligands (as in **2.9**) and only one bridging $[Co(OH)_2W_7O_{26}]^{10-}$ (**Fig. 2.64b**). Therefore, **2.9** can be considered as an extended version of the hepta-Co(II)-containing POM, which contains an extra $[Co(OH)_2W_7O_{26}]^{10-}$ bridging fragment and a Co_2 dimer.

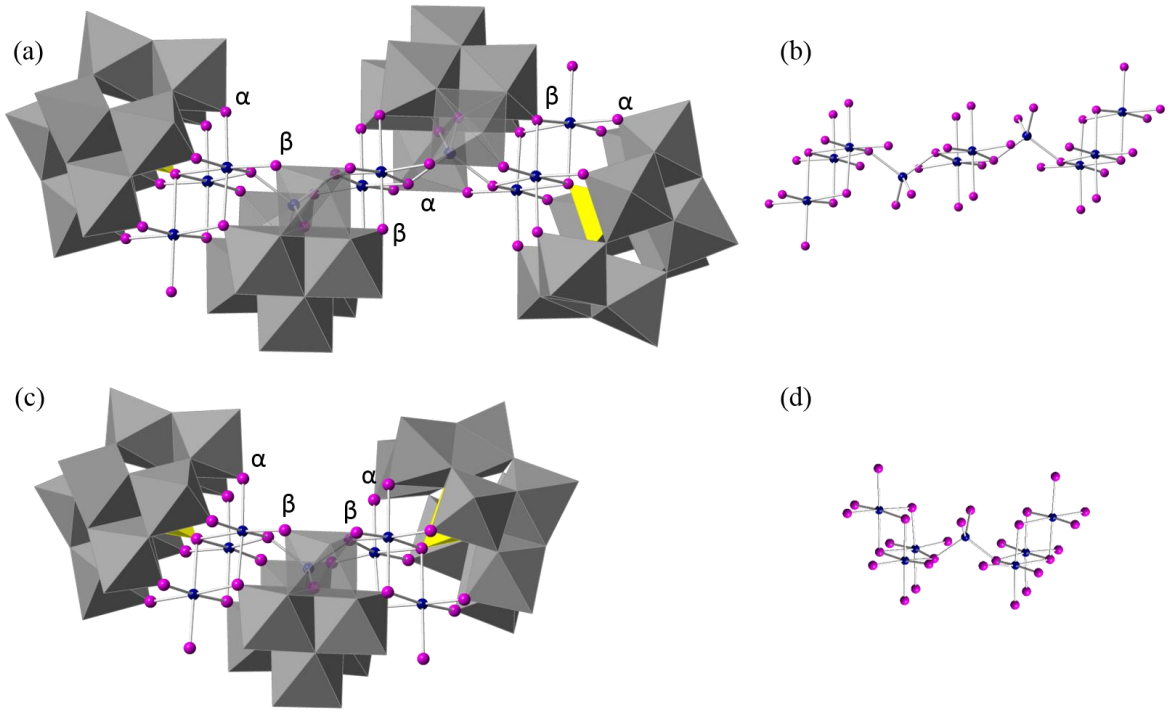

Fig. 2.64.- (a) Polyhedral and ball-and-stick representation of **2.9**; (b) ball-and-stick representation of the Co(II)-core of **2.9**; (c) Polyhedral and ball-and-stick representations of the polyoxoanion $\{[Co_3(H_2O)]_2[Co(OH)_2W_7O_{26}](PW_9O_{34})_2\}^{16-}$; (d) ball-and-stick representation of the Co(II)-core. Gray octahedra, $[WO_6]$; yellow tetrahedra, $[PO_4]$; blue spheres, Co; pink spheres, O.

Table 2.6.- Selected Co-O Bond Distances (Å) and O-Co-O Angles (º) involved in **2.9** (see **Fig. 2.67** for the labelling of the relevant atoms).

Co(1)-O(3C)	2.025(9)	Co(2)-O(1P)	2.261(8)
Co(1)-O(3C)^{i}	2.025(9)	Co(3)-O(678)^{i}	1.946(8)
Co(1)-O(1W)	2.103(14)	Co(3)-O(678)	1.946(8)
Co(1)-O(6C)^{i}	2.115(8)	Co(3)-O(2H)	1.951(12)
Co(1)-O(6C)	2.115(8)	Co(3)-O(1H)	1.972(11)
Co(1)-O(1P)	2.227(11)	Co(4)-O(74C)^{ii}	2.073(8)
Co(2)-O(4C)	2.003(9)	Co(4)-O(74C)	2.073(8)
Co(2)-O(73C)	2.041(8)	Co(4)-O(8C)	2.089(8)
Co(2)-O(5C)	2.046(9)	Co(4)-O(8C)^{ii}	2.089(8)
Co(2)-O(1H)	2.064(7)	Co(4)-O(2H)^{iii}	2.109(8)
Co(2)-O(6C)	2.104(8)	Co(4)-O(2H)	2.109(8)
O(3C)-Co(1)-O(3C)^{i}	87.4(5)	O(73C)-Co(2)-O(1P)	174.4(3)
O(3C)-Co(1)-O(1W)	89.3(4)	O(5C)-Co(2)-O(1P)	90.8(4)
O(3C)^{i}-Co(1)-O(1W)	89.3(4)	O(1H)-Co(2)-O(1P)	80.7(3)
O(3C)-Co(1)-O(6C)^{i}	174.2(4)	O(6C)-Co(2)-O(1P)	83.2(4)
O(3C)^{i}-Co(1)-O(6C)^{i}	93.0(3)	O(678)^{i}-Co(3)-O(678)	114.9(5)
O(1W)-Co(1)-O(6C)^{i}	96.5(4)	O(678)^{i}-Co(3)-O(2H)	108.1(3)
O(3C)-Co(1)-O(6C)	93.0(3)	O(678)-Co(3)-O(2H)	108.1(3)
O(3C)^{i}-Co(1)-O(6C)	174.2(4)	O(678)^{i}-Co(3)-O(1H)	109.4(3)
O(1W)-Co(1)-O(6C)	96.5(4)	O(678)-Co(3)-O(1H)	109.4(3)
O(6C)^{i}-Co(1)-O(6C)	85.9(4)	O(2H)-Co(3)-O(1H)	106.6(5)
O(3C)-Co(1)-O(1P)	90.4(3)	O(74C)^{ii}-Co(4)-O(74C)	91.4(5)
O(3C)^{i}-Co(1)-O(1P)	90.4(3)	O(74C)^{ii}-Co(4)-O(8C)	92.7(3)
O(1W)-Co(1)-O(1P)	179.5(5)	O(74C)-Co(4)-O(8C)	87.7(3)
O(6C)^{i}-Co(1)-O(1P)	83.8(3)	O(74C)^{ii}-Co(4)-O(8C)^{ii}	87.7(3)
O(6C)-Co(1)-O(1P)	83.8(3)	O(74C)-Co(4)-O(8C)^{ii}	92.7(3)
O(4C)-Co(2)-O(73C)	94.2(4)	O(8C)-Co(4)-O(8C)^{ii}	179.5(4)
O(4C)-Co(2)-O(5C)	86.7(4)	O(74C)^{ii}-Co(4)-O(2H)^{iii}	94.6(3)
O(73C)-Co(2)-O(5C)	92.8(4)	O(74C)-Co(4)-O(2H)^{iii}	170.8(4)
O(4C)-Co(2)-O(1H)	169.2(4)	O(8C)-Co(4)-O(2H)^{iii}	85.1(4)
O(73C)-Co(2)-O(1H)	95.1(3)	O(8C)^{ii}-Co(4)-O(2H)^{iii}	94.5(4)
O(5C)-Co(2)-O(1H)	87.5(4)	O(74C)^{ii}-Co(4)-O(2H)	170.8(4)
O(4C)-Co(2)-O(6C)	94.0(3)	O(74C)-Co(4)-O(2H)	94.6(3)
O(73C)-Co(2)-O(6C)	93.1(3)	O(8C)-Co(4)-O(2H)	94.5(4)
O(5C)-Co(2)-O(6C)	174.0(4)	O(8C)^{ii}-Co(4)-O(2H)	85.1(4)
O(1H)-Co(2)-O(6C)	90.9(4)	O(2H)^{iii}-Co(4)-O(2H)	80.4(5)
O(4C)-Co(2)-O(1P)	90.2(3)		

Symmetry transformations: (*i*) x, –y+1, z; (*ii*) –x, y, –z and (*iii*) –x, –y+1, –z.

The crystal structure shows the presence of nine additional Co(II) ions outside the polyanion. Some of them are bonded to the external oxygen atoms of **2.9**, connecting the POMs in two dimensions and forming layers parallel to the crystallographic *ab* plane (see **Fig. 2.65**).

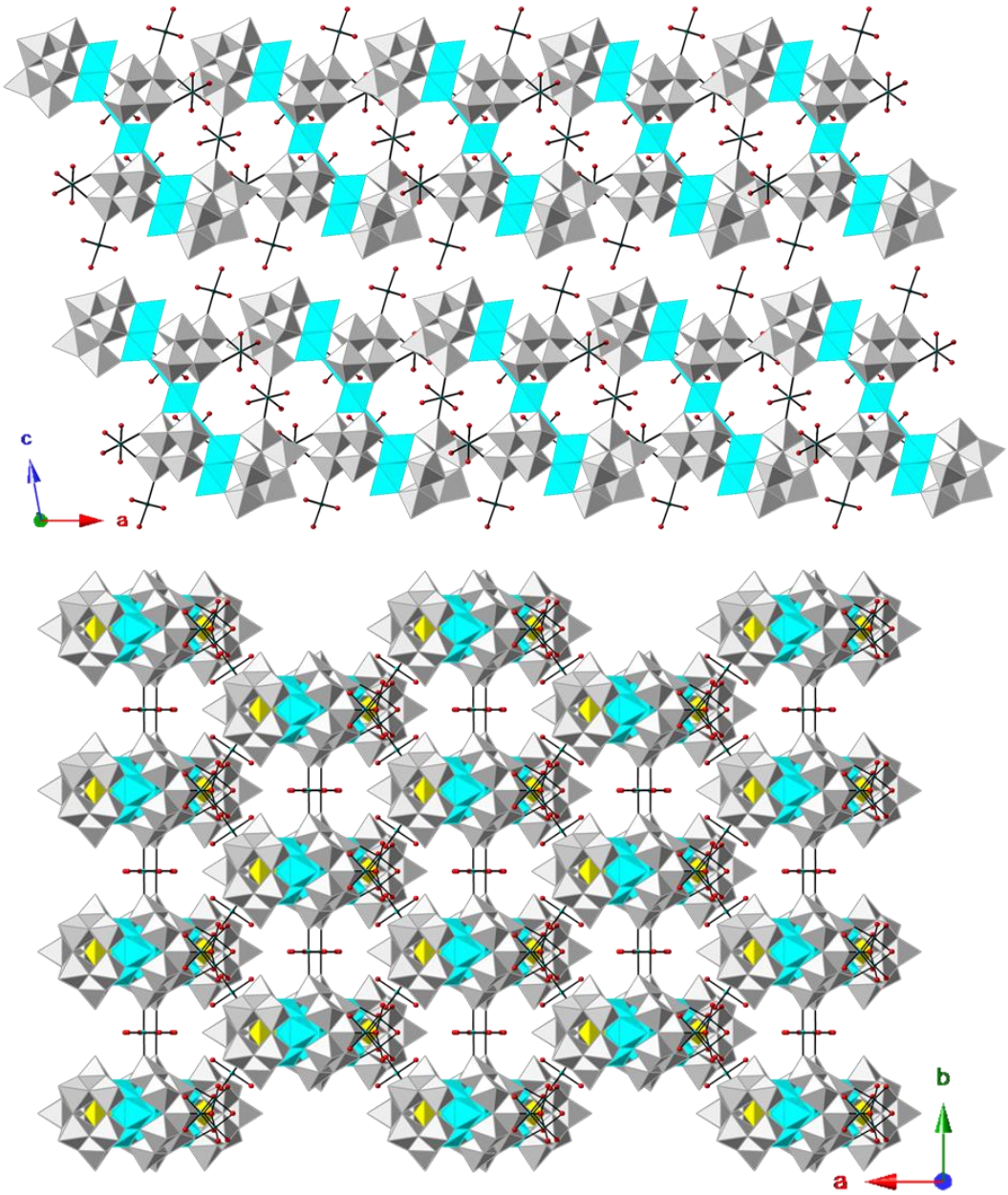

Fig. 2.65.- Polyhedral and ball-and-stick representations for **2.9**. (Up) Packing mode of $[Co_2\{Co_3(H_2O)(Co(OH)_2W_7O_{26})(PW_9O_{34})\}_2]^{22-}$ layers along b axis. (Down) The 2-D sheet architecture constructed from $[Co_2\{Co_3(H_2O)(Co(OH)_2W_7O_{26})(PW_9O_{34})\}_2]^{22-}$ and Co(III) linkers along *c* axis in **2.9**. Lattice cations and water molecules have been omitted for clarity. Cyan octahedra, $[CoO_6]$; gray octahedra, $[WO_6]$; blue spheres, Co; red spheres, O.

2.3.2.4. Bond valence sum (BVS) calculations

BVS calculations confirm that all these ten cobalt ions encapsulated in **2.9** bear an oxidation state 2+. Likewise, the μ_3-bridging oxygen atoms bonded to the tetrahedral cobalt atoms are monoprotonated, while the two terminal oxygen atoms associated to the two Co_3 triads are diprotonated (**Table 2.8**).

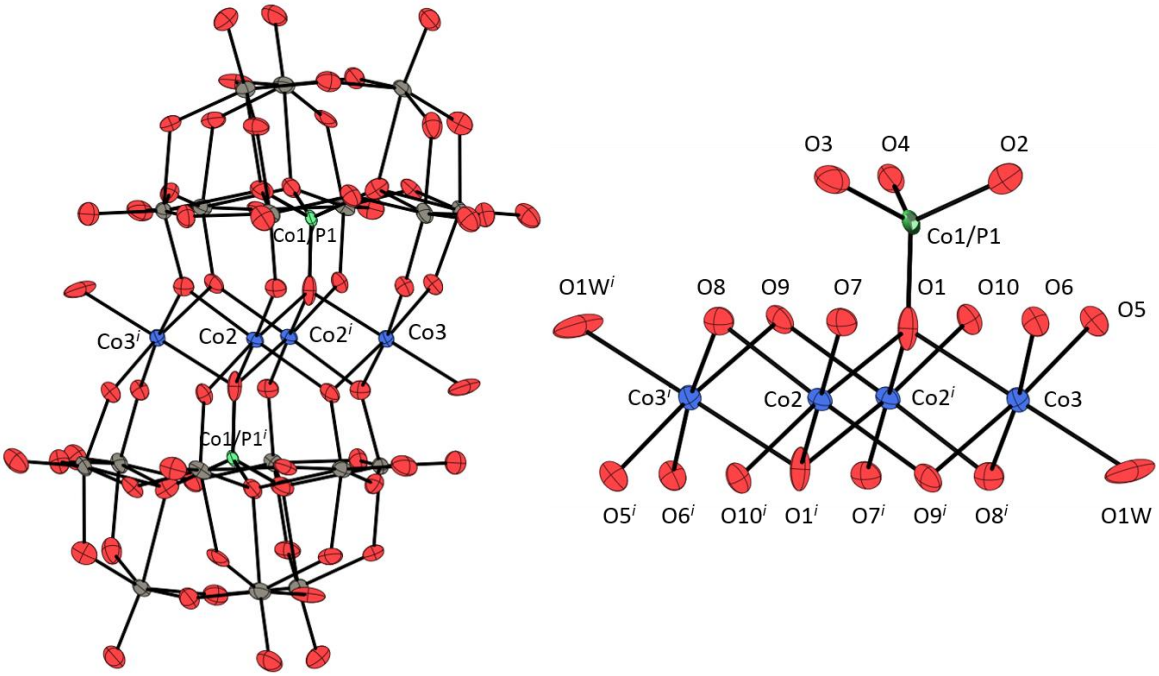

Fig. 2.66.- Thermal ellipsoid plot and numbering scheme for polyoxoanion **2.8** (50 % probability). Symmetry transformations: (*i*) –x+2, –y+1, –z.

Table 2.7.- Bond valence sum (BVS) calculations for cobalt centres and relevant oxygen sites of **2.8**.

Cobalt atoms	BVS
Co1/P1	ǂ
Co2	**1.90**
Co3	**1.93**

Oxygen atoms	BVS	Assigned protonation levels
O1	#	-
O2	#	-
O3	#	-
O4	#	-
O1W	**0.30**	**H_2O**
O5	**1.76**	**O**
O6	**1.82**	**O**
O7	**1.83**	**O**
O8	**1.89**	**O**
O9	**1.91**	**O**
O10	**1.75**	**O**
O11	**1.66**	**O**
O12	**1.84**	**O**
O13	**1.69**	**O**
O15	**1.75**	**O**
O17	**1.67**	**O**
O19	**1.64**	**O**
O21	**1.69**	**O**
O32	**1.78**	**O**
O33	**1.63**	**O**
O34	**1.74**	**O**

ǂ This atomic position is occupied by cobalt (Co1) and phosphorous (P1) (50 % / 50 %), so the bond distances are not adequate to perform BVS calculations.
These oxygen atoms are bonded to the disordered Co1/P1 position. Therefore the BVS calculations have not been performed for these oxygen atoms, although, reasonably they should not be protonated, as they are internal O atoms of **2.8**.

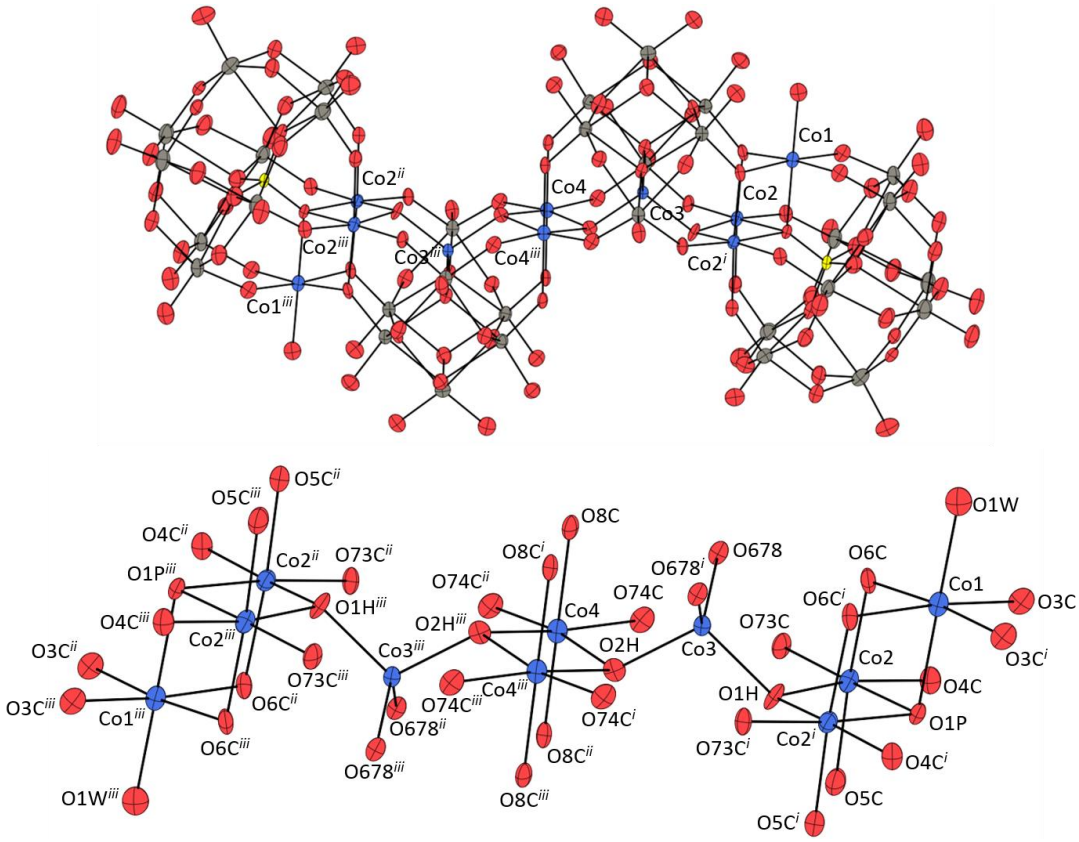

Fig. 2.67.- Thermal ellipsoid plot and numbering scheme for polyoxoanion **2.9** (50 % probability). Symmetry transformations: (*i*) x, –y+1, z; (*ii*) –x, y, –z and (*iii*) –x, –y+1, –z.

Table 2.8.- Bond valence sum (BVS) calculations for cobalt centres and relevant oxygen sites of **2.9**.

Cobalt atoms	BVS
Co1	**1.90**
Co2	**1.98**
Co3	**1.85**
Co4	**1.93**

Oxygen atoms	BVS	Assigned protonation levels
O1H	**1.14**	**OH**
O2H	**1.08**	**OH**
O1W	**0.31**	**H_2O**
O1P	**1.80**	**O**
O3C	**1.87**	**O**
O4C	**1.89**	**O**
O5C	**1.86**	**O**
O6C	**1.94**	**O**
O73C	**1.77**	**O**
O74C	**1.77**	**O**
O8C	**1.91**	**O**
O678	**1.98**	**O**
O9A	**1.69**	**O**
O9B	**1.61**	**O**

2.3.2.5. X-ray photoelectron spectroscopy

We have carried out X-ray photoelectron spectroscopy measurements of **2.8** and two other known POMs: $K_6[Co^{II}W_{12}O_{40}]$ and $K_5[Co^{III}W_{12}O_{40}]$, which contain tetrahedrally coordinated Co(II) and Co(III), respectively. Co2p core-level spectra of the three samples are displayed in **Fig. 2.68** and the corresponding binding energies of the most intense peak of the doublet (Co2$p_{3/2}$) are collected in **Table 2.9**. All samples show intense satellite structures on the high binding-energy side of the main lines indicating that a certain proportion of Co(II) are presented in all samples. The relative Co(II)/Co(III) ratios in these samples can be estimated by looking at the satellite/Co2p ratios (red values shown in **Table 2.9**). These values indicate that the proportion of Co(III) ions increases in the samples following the order $K_6[Co^{II}W_{12}O_{40}]$, **2.8** and $K_5[Co^{III}W_{12}O_{40}]$, as expected. This result demonstrates the presence of Co(III) ions in solid samples of **Q-2.8**.

Table 2.9.- Binding energies (eV) of core-levels of Co-containing samples: $K_6[Co^{II}W_{12}O_{40}]$, $K_5[Co^{III}W_{12}O_{40}]$ and **Q-2.8**. The red values correspond to the ratio between the satellite line and the overall Co2$p_{3/2}$ line (satellite included).

Compound	**W4f$_{7/2}$**	**Co2p$_{3/2}$**	**O1s**
$K_6[Co^{II}W_{12}O_{40}]$	35.0	779.8 **(0.436)**	530.1
$K_5[Co^{III}W_{12}O_{40}]$	34.8	781.2 **(0.341)**	529.9
Q-2.8	35.4	781.2 **(0.393)**	530.3

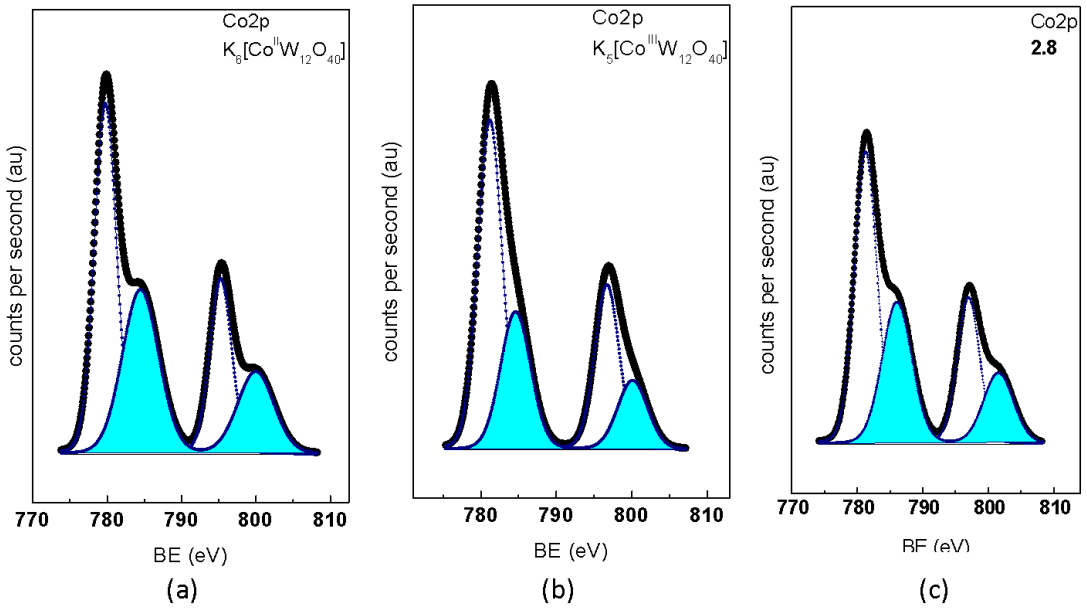

Fig. 2.68.- XPS spectra of Co-containing samples: (a) $K_6[Co^{II}W_{12}O_{40}]$, (b) $K_5[Co^{III}W_{12}O_{40}]$ and (c) **2.8**. The bold solid lines are the experimental measurements; the dashed lines are the Co2P peaks and the blue solid lines are the satellite peaks.

2.3.2.6. Mass spectrometry

The negative-mode electrospray-ionization mass spectrometry of **Q-2.8** in unbuffered aqueous solution shows three series of signals (**Fig. 2.69a**). At the *m/z* range of 1560-1700, the observed distribution envelopes could be assigned exclusively to **2.8**, with the formula $[Co^{II}_4(H_2O)_2(Co^{III}W_9O_{34})(PW_9O_{34})]^{12-}$ (with or without the coordinated water molecules). The peaks in the region *m/z* 1160–1250 could be assigned mainly to **2.8** (either with or without coordinated water molecules, as before), with only the minor peak located at *m/z* = 1174.2 being assigned to the previously known $[Co^{II}_4(H_2O)_2(PW_9O_{34})_2]^{10-}$ (without the coordinated water molecules). Finally, the minor peaks in the *m/z* range 920-980 correspond to the $[Co^{II}_4(H_2O)_2(PW_9O_{34})_2]^{10-}$ POM (either with or without coordinated water molecules). The occasional loss of the coordinated water molecules is due to the experimental conditions used during the ionization process of the species in the gas phase. These results support the partial decomposition of **2.8** into POM $[Co^{II}_4(H_2O)_2(PW_9O_{34})_2]^{10-}$ in aqueous solution (see **Fig. 2.69** and **Fig. 2.70**), in agreement with the dominant species being **2.8** as previously shown by UV-vis spectroscopy (see **Fig. 2.72**).

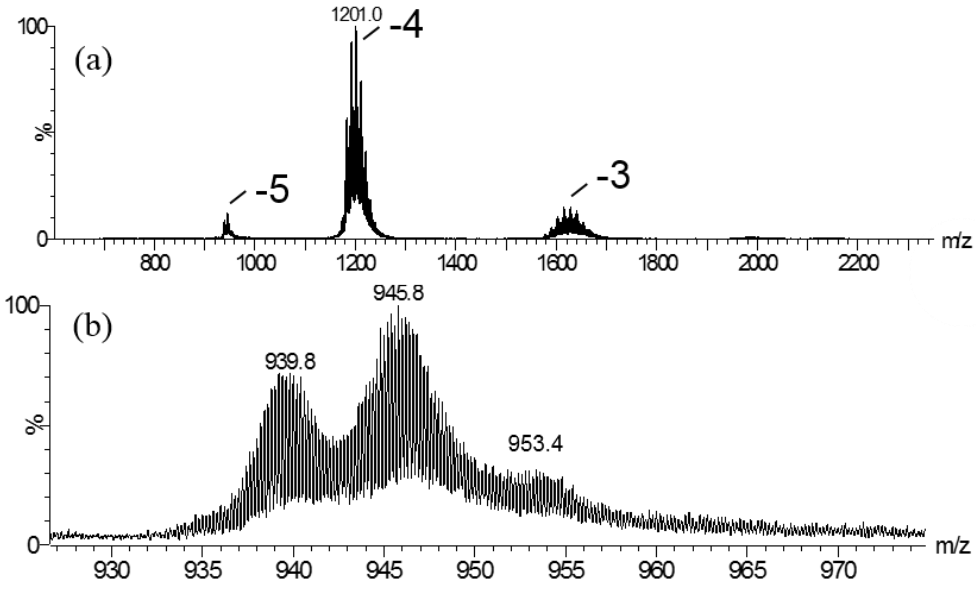

Cluster shell	m/z
$H_5\ [Co^{II}_4(PW_9O_{34})_2]^{5-}$	939.8
$H_5\ [Co^{II}_4(H_2O)_2(PW_9O_{34})_2]^{5-}$	945.8
$KH_4\ [Co^{II}_4(H_2O)_2(PW_9O_{34})_2]^{5-}$	953.4

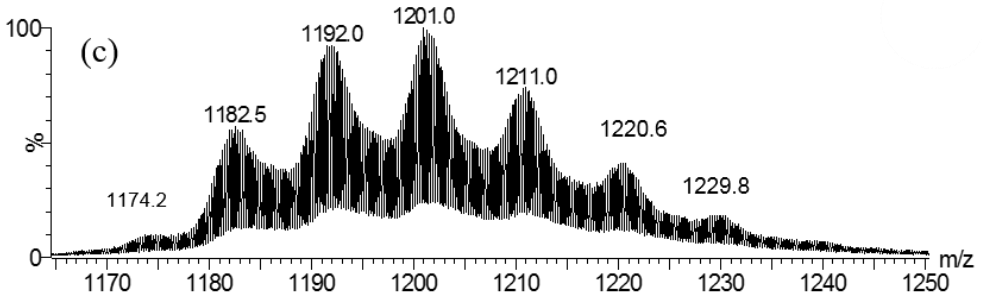

Cluster shell	m/z
$H_6\ [Co^{II}_4\ (PW_9O_{34})_2]^{4-}$	1175.2
$H_8\ [Co^{II}_4\ (Co^{III}W_9O_{34})(PW_9O_{34})]^{4-}$	1183.5
$H_8\ [Co^{II}_4(H_2O)_2(Co^{III}W_9O_{34})(PW_9O_{34})]^{4-}$	1192.5
$KH_7\ [Co^{II}_4(H_2O)_2(Co^{III}W_9O_{34})(PW_9O_{34})]^{4-}$	1202.0
$K_2H_6\ [Co^{II}_4(H_2O)_2(Co^{III}W_9O_{34})(PW_9O_{34})]^{4-}$	1211.5
$K_3H_5\ [Co^{II}_4(H_2O)_2(Co^{III}W_9O_{34})(PW_9O_{34})]^{4-}$	1221.0
$K_4H_4\ [Co^{II}_4(H_2O)_2(Co^{III}W_9O_{34})(PW_9O_{34})]^{4-}$	1230.5

Fig. 2.69.- (a) Mass spectrum (ESI-MS) in negative mode of **Q-2.8** in the *m/z* range of 600–2400 in unbuffered water solution. (b) Expanded view of the –5 charge state (*m/z* range 920–980). (c) Expanded view of the –4 charge state (*m/z* range 1160–1250).

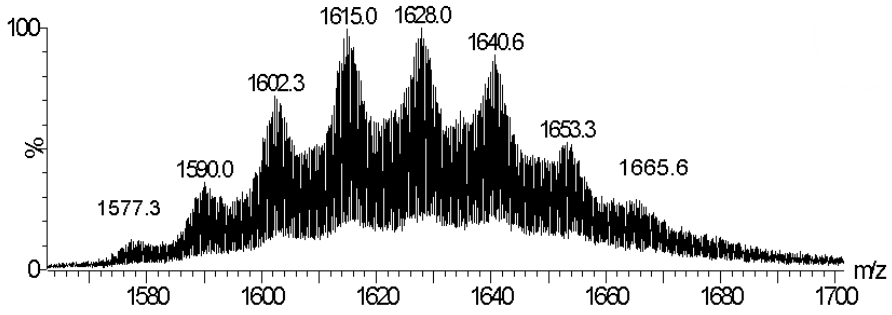

Cluster shell	m/z
H_9 $[Co^{II}_4(Co^{III}W_9O_{34})(PW_9O_{34})]^{3-}$	1577.3
H_9 $[Co^{II}_4(H_2O)_2(Co^{III}W_9O_{34})(PW_9O_{34})]^{3-}$	1590.0
KH_8 $[Co^{II}_4(H_2O)_2(Co^{III}W_9O_{34})(PW_9O_{34})]^{3-}$	1602.3
K_2H_7 $[Co^{II}_4(H_2O)_2(Co^{III}W_9O_{34})(PW_9O_{34})]^{3-}$	1615.0
K_3H_6 $[Co^{II}_4(H_2O)_2(Co^{III}W_9O_{34})(PW_9O_{34})]^{3-}$	1628.0
K_4H_5 $[Co^{II}_4(H_2O)_2(Co^{III}W_9O_{34})(PW_9O_{34})]^{3-}$	1640.6
K_5H_4 $[Co^{II}_4(H_2O)_2(Co^{III}W_9O_{34})(PW_9O_{34})]^{3-}$	1653.3
K_6H_3 $[Co^{II}_4(H_2O)_2(Co^{III}W_9O_{34})(PW_9O_{34})]^{3-}$	1665.6

Fig. 2.70.- Expanded view of the –3 charge state mass spectrum (ESI-MS) in negative mode of **Q-2.8** in the *m/z* range of 1560-1700 in unbuffered water solution.

2.3.2.7. ^{31}P NMR spectroscopy

The solution ^{31}P NMR spectrum of **Q-2.8** shows two broad signals centred at 1846.7 and 2123.3 ppm (**Fig. 2.71**). The signal at 1846.7 ppm corresponds to $[Co_4(H_2O)_2(PW_9O_{34})_2]^{10-}$,[91] while the signal at 2123.3 ppm can be assigned to **2.8**. This last signal appears at lower field due to the presence of one additional cobalt atom in the paramagnetic cluster. Both signals are broadened due to the proximity to the cobalt clusters. The evolution with time of the ^{31}P NMR spectra of the same solution shows an increase of the intensity of the upfield signal with respect to the downfield signal, pointing to an increase of the concentration of Weakley's POM with respect to **Q-2.8**. Therefore, the presence of this POM in the aqueous solutions of **Q-2.8** (as evident from ESI-MS and ^{31}P NMR) seems to be originated from slow decomposition of **2.8** in solution, as solid **Q-2.8** appears to be pure by elemental analysis. This slow decomposition is also supported by the evolution of the UV-vis spectra (**Fig. 2.72**). Thus, the UV-vis spectrum of a fresh

aqueous solution of **2.8** slowly evolves towards the spectrum of the Weakley's POM when the solution is measured after 15 and 30 days.

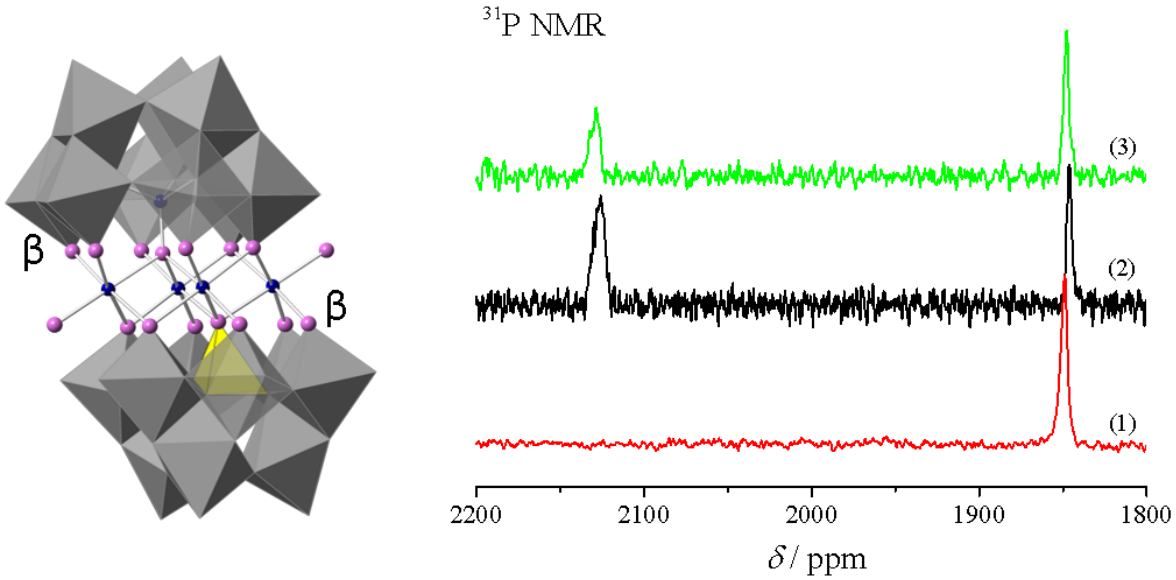

Fig. 2.71.- (Left) Polyhedral and ball-and-stick representation of $[Co^{II}_4(H_2O)_2(Co^{III}W_9O_{34})(PW_9O_{34})]^{12-}$, **2.8**. Gray octahedra, $[WO_6]$; yellow tetrahedron, $[PO_4]$; blue spheres, Co; pink spheres, O. (Right) ^{31}P NMR spectrum of $K_{10}[Co_4(H_2O)_2(PW_9O_{34})_2]$ (1), and time evolution of the ^{31}P NMR spectrum of **Q-2.8** in unbuffered D_2O: freshly prepared solution (2), and same solution after two days (3). The chemical shifts are externally referenced to 85 % H_3PO_4.

2.3.2.8. UV-visible spectroscopy

The UV-vis spectra of the relevant POM were recorded on an Agilent 8453 UV-vis spectrophotometer from 190 to 700 nm using 10-mm-optical-path quartz cuvettes in unbuffered water solution and in 0.5 M NaOAc/HOAc buffered solution at pH 4.8.

The brown colour of **2.8** suggests that the tetrahedral cobalt atom bears an oxidation state of 3+ (as is the case for $[Co^{III}Co^{II}(H_2O)W_{11}O_{39}]^{7-}$, which contains one tetrahedral Co(III) and one octahedral Co(II)).[14] This is supported by comparing the visible absorption spectra of **2.8** and other related POMs containing tetrahedral Co(II) or Co(III) (**Fig. 2.73**). Indeed, the visible spectrum of $[Co^{III}W_{12}O_{40}]^{5-}$ exhibits a band centred at 400 nm, which can be assigned to a charge transfer transition from a ligand oxygen atom to the central tetrahedral Co(III) ion.[92] This band is absent in other POMs containing tetrahedral Co(II) (as $[Co^{II}_3W(H_2O)_2(Co^{II}W_9O_{34})_2]^{12-}$) or in $[Co^{II}_4(H_2O)_2(PW_9O_{34})_2]^{10-}$ (which contains phosphorus in the tetrahedral positions). In contrast, the visible spectrum of **2.8**

exhibits a weak shoulder at ca. 400 nm that can be attributed to the O → Co(III) CT transition.

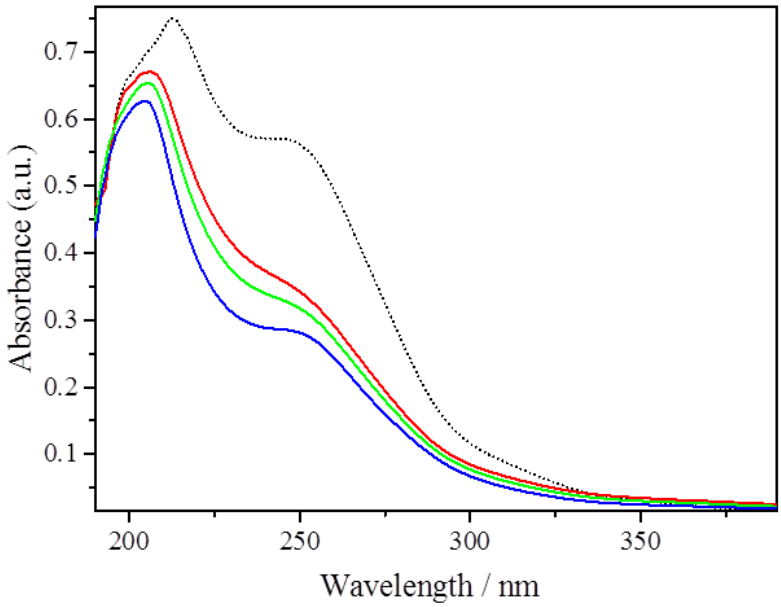

Fig. 2.72.- UV spectra of an aqueous solution of $[Co^{II}_4(H_2O)_2(PW_9O_{34})_2]^{10-}$ ($2\cdot10^{-5}$ M) (black dotted line). UV spectrum of a solution of **Q-2.8** ($2\cdot10^{-5}$ M) in a fresh aqueous solution (red line). UV spectra of the same solution after 15 days (green line), and after 30 days (blue line).

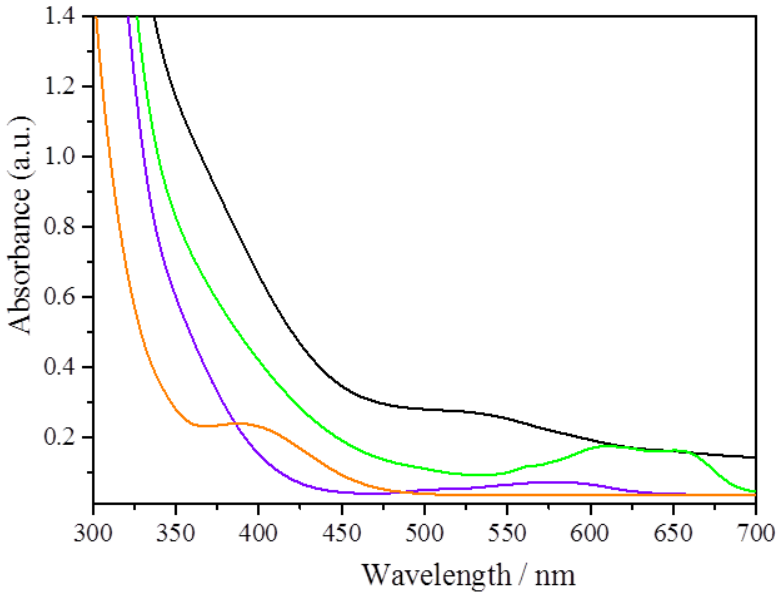

Fig. 2.73.- Visible spectra of **Q-2.8** ($2\cdot10^{-5}$ M) (black line), $[Co^{II}_4(H_2O)_2(PW_9O_{34})_2]^{10-}$ ($2\cdot10^{-5}$ M) (violet line), $[Co^{III}W_{12}O_{40}]^{5-}$ ($2\cdot10^{-5}$ M) (orange line) and $[Co^{II}_3W(H_2O)_2(Co^{II}W_9O_{34})_2]^{12-}$ ($2\cdot10^{-5}$ M) (green line) in 0.5 M NaOAc/HOAc buffered solution at pH 4.8.

2.3.2.9. Electrochemistry

Fig. 2.74 shows a comparison of the cyclic voltammograms of **2.8** and $[Co_4(H_2O)_2(PW_9O_{34})_2]^{10-}$ at pH 4.8. In the case of $[Co_4(H_2O)_2(PW_9O_{34})_2]^{10-}$, we observe two separated, reversible peaks originating from the oxo-tungstate framework, a behavior similar to the one previously reported[93] in which the E_p values of the two redox waves are –0.534 V and –0.364 V when pH is 4.4. In our case the cathodic (E_{pc}) and anodic (E_{pa}) peak potentials for these couples appear at more negative values (E_{pc1} = –0.800 V, E_{pa1} = –0.869 V and E_{pc2} = –0.954 V, E_{pa2} = –1.008 V). For **2.8**, a composite reduction wave is observed with a main peak at –0.989 V and up to three badly defined oxidation waves associated with it in the range –0.655 to –0.894 V. **Fig. 2.74b** shows the CVs of **2.8** and $[Co_4(H_2O)_2(PW_9O_{34})_2]^{10-}$ (pH 4.8) in the region of positive potential. In this region, the $[Co_4(H_2O)_2(PW_9O_{34})_2]^{10-}$ polyoxoanion does not exhibit clear redox waves corresponding to the cobalt centers, in agreement with the previously reported study of this compound.[93] In contrast, POM **2.8** exhibits three reversible couples with the following anodic and cathodic potentials: E_{pc1} = 0.496 V, E_{pa1} = 0.380 V, E_{pc2} = 0.974 V, E_{pa2} = 0.882 V, and E_{pc3} = 1.130 V, E_{pa3} = 1.048 V. The redox couple at less positive potentials is assigned to oxidation/reduction of the tetrahedral cobalt in **2.8**, while the remaining two redox couples at more positive potentials are assigned to the redox processes of the octahedral tetracobalt cluster. These last two waves exhibit potential values which are similar to the redox cobalt couples of other previously reported POMs.[94] They are presumably associated to the oxidation/reduction of the two different types of cobalt atoms present in **2.8**: the two more external cobalt atoms bound to the water molecule (which would be oxidized at less positive potentials) and the remaining two octahedral cobalt atoms. Anyway, the slow decomposition process of **2.8** in aqueous solution, shown by UV-vis and mass spectrometry, prevents further quantitative analysis of the electrochemical results and requires prudence in the assignment of the redox peaks.

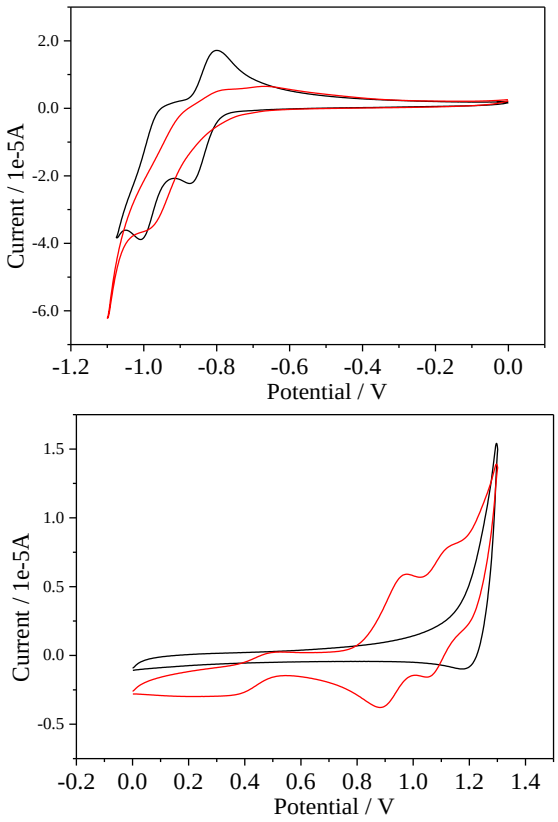

Fig. 2.74.- Comparison of cyclic voltammogram of **Q-2.8** ($5\cdot10^{-4}$ M) (red) with the cyclic voltammogram of Weakley POM $K_{10}[Co_4(H_2O)_2(PW_9O_{34})_2]\cdot20H_2O$ (black) (pH = 4.8) from –1.1 V to 1.4 V. The voltammograms addressing just the redox processes of the W centers (left); Voltammogram addressing just the redox processes of the Co centers (right).

2.3.2.10. Magnetic properties

Magnetic properties of **Q-2.8** and **Q-2.9** are shown in **Fig. 2.75** and **Fig. 2.76**. Both compounds exhibit a continuous decrease of χT from room temperature (13.5 emu·K·mol^{-1} for **Q-2.8** and 57.4 emu·K·mol^{-1} for **Q-2.9**) to minima at 24.0 K (for **Q-2.8**) and 38.0 K (for **Q-2.9**). Below these temperatures, smooth peaks are observed with maxima, which clearly depend on the applied magnetic field (5.5 K for **Q-2.8** and 9.5 K for **Q-2.9**, at 0.1 T). The decrease in χT can be attributed to the first-order spin-orbit coupling of Co(II) combined with its octahedral distortion, which leads to a splitting into six anisotropic Kramers doublets of the $^4T_1$ ground state.[95] At low temperature, when the χT *vs.* T curves present a peak, only the lowest Kramers doublet is populated and can be approximated to an effective anisotropic spin 1/2. The ground state of the tetrahedral Co(II) ion in **Q-2.9** is a spin-only S = 3/2. The ground state of the tetrahedral Co(III) ion

in **Q-2.8** is S = 2 with large anisotropy.[96] Finally, at low temperatures the isolated octahedral Co(II) charge-compensating ions are treated as isotropic S = 1/2 with g = 4.33.

Taking into account all the aspects mentioned above and the exchange network scheme shown in **Fig. 2.75**, the effective exchange Hamiltonian for the magnetic cluster in **2.8** can be written as:

$$\hat{H} = -2\sum_{\alpha=x,z} J_\alpha\left(\hat{S}_1^\alpha\hat{S}_3^\alpha + \hat{S}_1^\alpha\hat{S}_4^\alpha + \hat{S}_2^\alpha\hat{S}_3^\alpha + \hat{S}_2^\alpha\hat{S}_4^\alpha\right) - 2\sum_{\alpha=x,z} J'_\alpha\hat{S}_1^\alpha\hat{S}_2^\alpha - 2\sum j\left(\hat{S}_1\hat{S}_5 + \hat{S}_2\hat{S}_5 + \hat{S}_3\hat{S}_5\right) + D\hat{S}_5^2$$

where J_α and J'_α are anisotropic exchange parameters associated with the sides and short diagonal pathways inside the Co(II) rhombic unit, j is the exchange parameter from the interaction between tetrahedral and octahedral cobalt atoms, and D is the zero field splitting (ZDS) parameter for tetrahedral Co(III). In order to avoid overparametrisation, j has been assumed isotropic and its anisotropy included in the D parameter.

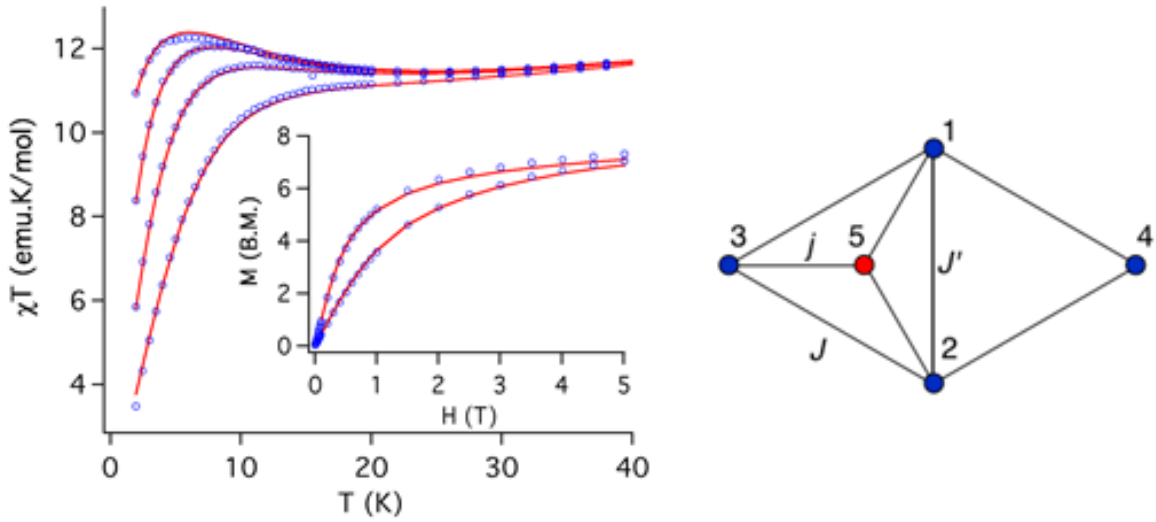

Fig. 2.75.- (Left) Thermal behavior of χT for **Q-2.8** at different fields (0.1, 0.5, 1, and 2.5 T) in the range 2–40 K. Inset: Magnetization of the same sample at 2 and 5 K in the range 0–5 T. Solid lines represent the simulation of properties with the parameter set obtained from the susceptibility fit. (Right) Exchange network scheme of the magnetic cluster in **2.8**.

A simultaneous fit of the four magnetic susceptibilities at different fields and the two magnetizations was performed by numerical diagonalization of the full eigenmatrix[44-45] giving the following set of parameters: J_z = 7.4 cm^{-1}, J_x = 4.0 cm^{-1}, J_z' = J_x' = 6.2 cm^{-1}, j = –38.1 cm^{-1}, D = –34.2 cm^{-1}, g_{Oh}= 5.1 and g_{Td} = 2.00 (R = 5.8·10^{-5}). j and D parameters are closely interrelated, and similar solutions are obtained by simultaneously reducing

one parameter and increasing the other parameter inside the ranges −30 to −44 cm^{-1} (for *j*) and −25 to −41 cm^{-1} (for *D*).

In the case of **Q-2.9**, the presence of nine isolated octahedrally coordinated Co(II) ions outside the POM makes it impossible to carry out a simple numerical fit.‡ Nonetheless, the magnetic properties of **Q-2.9** can be understood qualitatively from the antiferromagnetic interaction between the ferromagnetic Co_2 or Co_3 units, and the tetrahedral Co(II) ions. This result was obtained from the fitting of the previously mentioned hepta-Co(II)-containing POM $\{[Co_3(H_2O)]_2[Co(OH)_2W_7O_{26}](PW_9O_{34})_2\}^{16-}$, which has less isolated cobalt ions outside the polyoxoanion.[52] The use of similar parameters obtained from this compound leads to susceptibility curve shapes which are qualitatively similar to the experiment. This indicates that the interactions in both clusters are quite comparable.

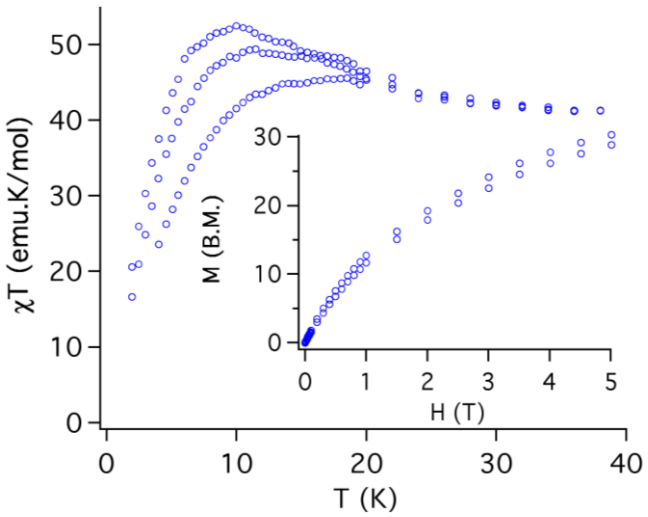

Fig. 2.76.- Thermal behavior of χT for **Q-2.9** at different fields (0.5, 1, and 2.5 T) in the range 2 – 40 K. Inset: Magnetization of the same sample at 2 and 5 K in the range 0 – 5 T.

The alternating current susceptibility measurement for **Q-2.8** was also performed with an *ac* field amplitude of 3 Oe and in the absence of dc field. The in-phase and out-of-phase *ac* susceptibilities of compound **Q-2.8** are shown in **Fig. 2.77**. As we can see, **2.8** does not show an out-of-phase magnetic susceptibility. This is not strange even if the tetrahedral cobalt has a large negative zero-field splitting, because this cobalt atom is

‡The magnetic cluster with ten Co^{2+} ions (eight octahedral and two tetrahedral) gives rise to 4096 spin functions. This matrix size and the large number of parameters for the decanuclear unit and independent Co^{2+} ions make it impossible the use of a quick method of least squares adjustment.

coupled anti-ferromagnetically with other four octahedral cobalt atoms. Therefore, the large anisotropy of isolated cobalt does not directly indicate a large anisotropy of the entire system a fundamental state, in fact in this case the ground state is mainly S = 0.

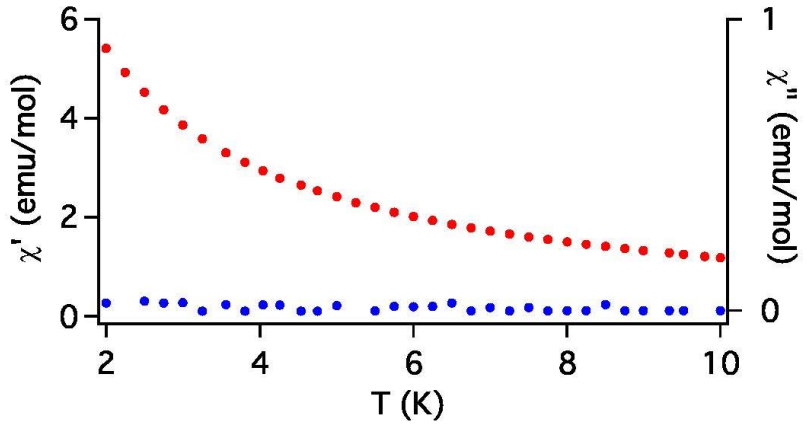

Fig. 2.77.- In-phase (blue) and Out-of-phase (red) *ac* susceptibility of **2.8** in the range 2–10 K.

2.3.3. Conclusions

In conclusion, two novel POMs containing penta-Co(II/III) (**2.8**) and deca-Co(II) (**2.9**) clusters have been obtained and characterised. **2.8** is the first reported POM which, being isostructural to the archetypical sandwich POM $[Co^{II}_4(H_2O)_2(PW_9O_{34})_2]^{10-}$ first reported by Weakley, has two different heteroatoms in the $[XW_9O_{34}]^{n-}$ capping ligands (X = P^V and Co^{III}). **2.9** was synthetized by partial reductive hydrolysis of **2.8** using hydrazine and consists of one Co_2 dimer and two Co_3 triads bridged with two $[Co(OH)_2W_7O_{26}]^{10-}$ fragments. By comparing the structure of **2.8** and **2.9** we can conclude that the reaction of **2.8** with hydrazine has three main effects: (i) the reduction of the tetrahedral Co(III) in **2.8** to Co(II) in **2.9**, (ii) the partial hydrolysis of the capping $[Co^{III}W_9O_{34}]^{11-}$ moiety, which converts to the bridging $[Co(OH)_2W_7O_{26}]^{10-}$ fragments (the $[PW_9O_{34}]^{9-}$ moiety persists under these conditions) and (iii) the loss of one Co(II) from the Co_4 cluster in **2.8**, giving rise to two Co_3 triads in **2.9** (with the concomitant 60° rotation of the $[PW_9O_{34}]^{9-}$ capping ligand). The tungsten atoms that are lost during the hydrolysis process condensate to form the paratungstate anion, which appears as a by-product. These results open the possibility to synthesize new high-nuclearity POMs containing *d*-transition metal ions from smaller ones through reaction with hydrazine. Hence, a future research task that stems from this work consists in exploring if the partial

reductive hydrolysis approach used in this work can be a general method to obtain new and large POMs with interesting magnetic and/or catalytic properties.

2.3.4. Experimental section

2.3.4.1. General methods and materials

All reagents were of high purity grade quality, obtained from commercial sources and used without further purification. Pure water ($\rho > 18$ MΩ·cm) was used throughout. It was obtained using an Elix-3/Millipore-Q Academic water purification system. IR spectra were recorded with KBr pellets on a Thermo NICOLET-5700 FT-IR spectrophotometer. The UV-vis spectra of the relevant POMs were recorded on an Agilent 8453 UV-vis spectrophotometer from 190 to 700 nm using 10-mm-optical-path quartz cuvettes in unbuffered aqueous solution and also in 0.5 M sodium acetate buffered solution (pH 4.8). Elemental analysis was performed by inductively-coupled-plasma optical-emission-spectroscopy (ICP-OES) on solutions prepared by treating the POMs in a hydrofluoric acid/hydrochloric acid mixture of ratio 1:8 and diluted with water to a known volume. Thermogravimetric analysis was performed on a Metler Toledo TGA/SDTA851e analyzer. Cyclic voltammetry measurements of **2.8** and $[Co_4(H_2O)_2(PW_9O_{34})_2]^{10-}$ were carried out on an Autolab PGSTAT128N potentiostat using a three-electrode single compartment cell supplied by IJ Cambria. It was equipped with a 3 mm glassy carbon disc working electrode (which was polished sequentially with 0.3, 0.1 and 0.05 μm alumina powders and washed with distilled water before each experiment), a platinum wire counter electrode and a Ag/AgCl (3M KCl) reference electrode. All cyclic voltammograms were recorded at a scan rate of 100 $mV \cdot s^{-1}$ using the same media (0.5M NaOAc/HOAc with pH = 4.8) and concentrations ($5 \cdot 10^{-4}$ M). The solutions were deaerated during at least 15 min with argon and kept under a positive pressure of this gas during the experiments. ^{31}P-NMR (161.70 MHz) spectra in D_2O solution were recorded in 5-mm outer diameter tubes on a JEOL JNM-EX 400 FT-NMR spectrometer with a JEOL EX-400 NMR data processing system. ^{31}P-NMR spectra were measured in D_2O solution with reference to an external standard of 25 % H_3PO_4 in H_2O in a sealed capillary.

2.3.4.2. Synthesis

2.3.4.2.1. Synthesis of $K_{10.5}Na_{0.3}\{Co_{0.6}(H_2O)_{3.6}\}[Co^{II}_4(H_2O)_2(Co^{III}W_9O_{34})(PW_9O_{34})]\cdot 19.4H_2O$ **(Q-2.8)**

$Na_2WO_4\cdot 2H_2O$ (21.60 g, 65.6 mmol) and Na_2HPO_4 (0.84 g, 5.92 mmol) were dissolved in 60 mL of water and the pH of the solution adjusted to 5.5 using glacial acetic acid. Another aqueous solution containing $Co(CH_3COO)_2\cdot 4H_2O$ (5.16 g, 20.72 mmol) in 100 mL of water was added dropwise to the first one and the pH of the resultant solution was adjusted again to 5.5 using glacial acetic acid. Then, the solution was refluxed for 2 h and hot filtered. To the hot filtrate, potassium acetate (8.96 g, 91.2 mmol) and potassium persulfate (0.44 g, 1.63 mmol) were successively added in small portions. After the addition of the solids, the solution was concentrated at 80 ºC until a final volume of 120 mL was attained. Then, the solution was allowed to cool back to room temperature and a large amount of black precipitate (9.42 g) was formed. This precipitate was recrystallized from the minimum amount of water at 80 ºC to obtain 6.75 g of dark brown prismatic crystals (yield 33 %, based on $Na_2WO_4\cdot 2H_2O$).

IR (2 % KBr pellet 1200 – 400 cm^{-1}) (**Fig. 2.78**): 1050(m), 1030(s), 937(s), 874(s), 808(w), 738(m, sh), 587(w), 513(m), 425(m, sh). The TGA curve of **Q-2.8** (**Fig. 2.79**) shows a total weight loss of 8.20 % in the range 30 – 800 ºC, which agrees with the loss of 25 water molecules (calcd 8.20 %). Anal. Calcd (Found) for **Q-2.8**: P, 0.55 (0.57); W 58.8 (57.4); Co 5.9 (6.0); K 7.3 (6.9); Na 0.12 (0.15). Powder X-ray diffraction pattern of this compound has been collected to confirm the phase purity of the bulk compound (**Fig. 2.80**).

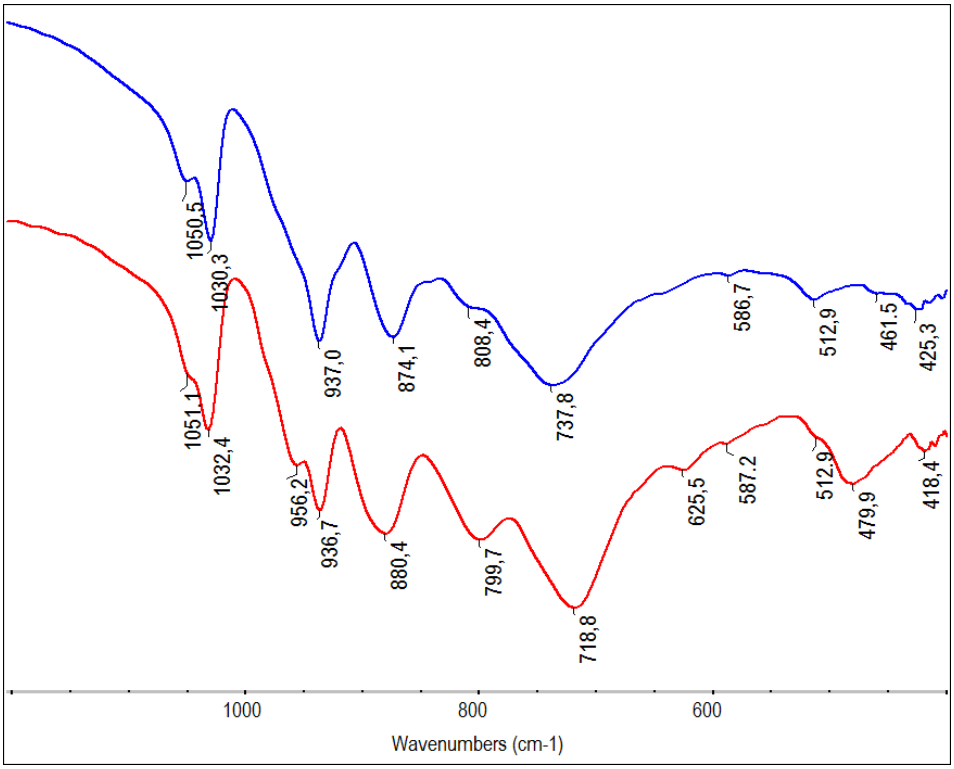

Fig. 2.78.- FT-IR spectra of **Q-2.8** (blue) and **Q-2.9** (red).

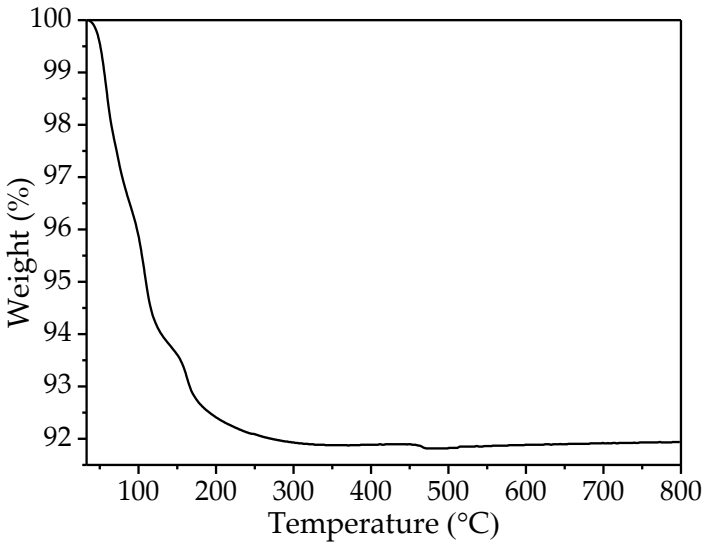

Fig. 2.79.- Thermogram of **Q-2.8** from room temperature to 800 ºC (experimental total weight loss 8.20 %).

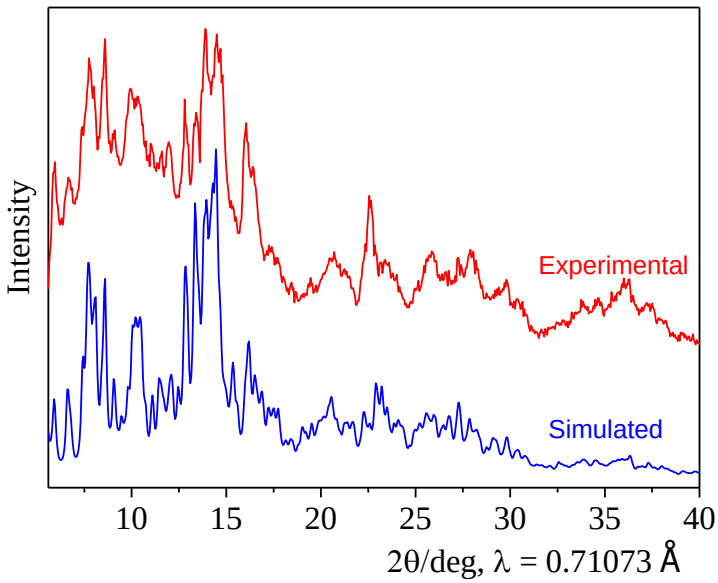

Fig. 2.80.- Comparison of simulated and experimental powder X-ray diffraction patterns for **Q-2.8**. The experimental powder X-ray diffraction pattern was obtained from powdered samples in an *Oxford Diffraction Supernova* diffractometer. The simulated pattern was generated from the atomic coordinates of the single-crystal structure solution using the program Mercury 3.0 (copyright CCDC, http://www.ccdc.cam.ac.uk/mercury/) and a FWHM (full width at half maximum) of 0.2.

*2.3.4.2.2. Synthesis of $K_6\{Co_9(H_2O)_{42}\}[Co_2\{Co_3(H_2O)(Co(OH)_2W_7O_{26})(PW_9O_{34})\}_2]\cdot 26H_2O$ (**Q-2.9**)*

Solid **Q-2.8** (0.045 g, $7.9\cdot10^{-3}$ mmol) was dissolved in 8 mL of water with gentle warming (~65 ºC) under stirring, giving rise to a dark brown solution. Then, 1 mL of hydrazine solution (1.0 M in THF) was added dropwise to the warm solution, causing a gradual colour change from dark brown to light violet. After the addition, the solution (pH ~ 7.6) was stirred for 30 min at ~ 65 ºC, filtered with paper and allowed to stand at room temperature in an open vial. Upon standing, an upper-light-pink-clear phase and a lower-violet-cloudy phase formed, which were mechanically separated using a Pasteur pipette. The light pink solution was allowed to evaporate further at room temperature during one month until pink needle-like crystals were obtained and identified by IR and X-ray single-crystal diffraction as the previously known $K_6[Co(H_2O)_4]_2[H_2W_{12}O_{42}]\cdot 14H_2O$.[97] To the lower violet suspension, 5 mL of water were added so a clear violet solution was obtained (pH ~ 7.4). After one week of evaporation at room temperature in an open vial, violet needle shaped crystals of **Q-2.9** were formed, collected by filtration, washed with a small amount of cold water and air-dried (18 mg, 43 % based on **Q-2.9**).

IR (2 % KBr pellet 1200 – 400 cm^{-1}) (**Fig. 2.78**): 1032(s), 956(m, sh), 937(s), 880(s), 800(w), 719(s), 626(w), 480(m, sh), 415(s). The TGA curve of **Q-2.9** (**Fig. 2.81**) shows a total weight loss of 12.75 % in the range 30–800 ºC, which agrees with the loss of 70 water molecules and 4 hydroxyls in the structure (calcd 12.72 %). Anal. Calcd (Found) for **Q-2.9**: P, 0.59 (0.58); W 56.2 (55.5); Co 10.7 (10.5); K 1.5 (1.2); Na 0 (0.012). Powder X-ray diffraction pattern of this compound has been collected to confirm the phase purity of the bulk compound (**Fig. 2.82**).

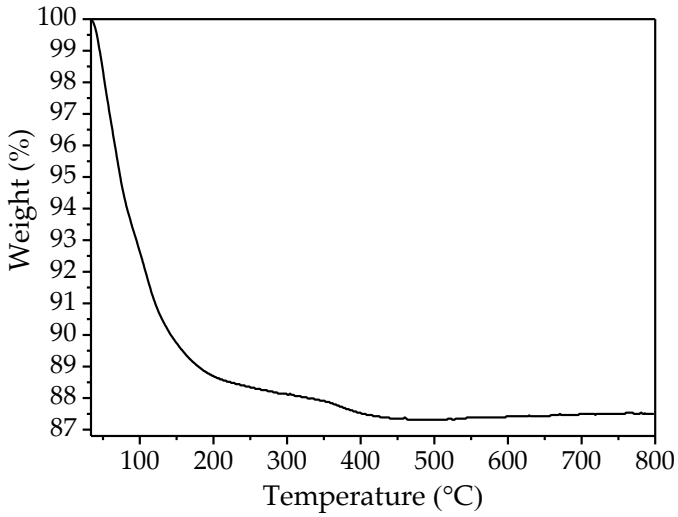

Fig. 2.81.- Thermogram of **Q-2.9** from room temperature to 800 ºC (experimental total weight loss 12.75 %).

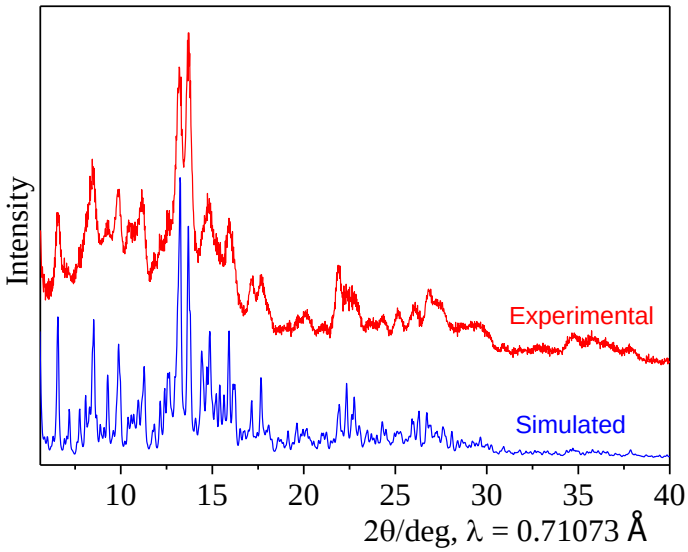

Fig. 2.82.- Comparison of simulated and experimental powder X-ray diffraction patterns for **Q-2.9**. The experimental powder X-ray diffraction pattern was obtained from powdered samples in an *Oxford Diffraction Supernova* diffractometer. The simulated pattern was generated from the atomic coordinates of the single-crystal structure solution using the program Mercury 3.0 (copyright CCDC, http://www.ccdc.cam.ac.uk/mercury/) and a FWHM (full width at half maximum) of 0.2.

2.3.4.3. X-ray crystallography

Suitable crystals of **Q-2.8** and **Q-2.9** were coated with Paratone N oil, suspended on small fiber loops and placed in a stream of cooled nitrogen (120 K) on an Oxford Diffraction Supernova diffractometer equipped with a graphite-monochromated Enhance (Mo) X-ray Source (λ = 0.71073 Å). The data collection routines, unit cell refinements and data processing were carried out using the CrysAlis software package[60] and structure solution and refinement were carried out using SHELXS-86 and SHELXL-97.[61]

All atoms were refined anisotropically in the two crystal structures except some disordered counter cations and water molecules of solvation having partial occupancies. Analytical absorption corrections were performed for both compounds based on face indexations of the single crystals. Hydrogen atoms of water molecules and hydroxyl anions were not included in the models.

The refinement of the crystal structure of **Q-2.9** reveals a 4.6 % disorder, which is likely due to a 60º rotation of the whole polyoxoanion. This disorder is only evident for the capping $[W_3O_{15}]$ triad of the $[PW_9O_{34}]^{9-}$ moiety and is not revealed in the remaining W atoms belonging to the six-membered belt of the B-$[PW_9O_{34}]^{9-}$ moiety because a 60º rotation brings these W atoms almost into coincidence. The disorder is not apparent for the lighter Co or O atoms due to its small extent (4.6 %). In addition, **Q-2.9** exhibits also disorder in the solvent/cation region (typical in many POM structures). For this reason, some crystalline water molecules and counter cations could not be located. The formula, however, reflects the total number of counter cations and crystalline water molecules (based on elemental analysis and TGA), as they represent the true bulk composition. The cif files of both structures have been deposited in the inorganic crystal structure database (ICSD) with the deposition number CSD-431286. The crystallographic data for the two structures are summarized in **Table 2.10**.

Table 2.10.- Crystallographic Data for $K_{10.5}Na_{0.3}\{Co_{0.6}(H_2O)_{3.6}\}[Co^{II}_4(H_2O)_2(Co^{III}W_9O_{34})(PW_9O_{34})]\cdot 19.4H_2O$ (**Q-2.8**), and $K_6\{Co_9(H_2O)_{42}\}[Co_2\{Co_3(H_2O)(Co(OH)_2W_7O_{26})(PW_9O_{34})\}_2]\cdot 26H_2O$ (**Q-2.9**).

Compound	**Q-2.8**	**Q-2.9**
empirical formula	$Co_{5.6}H_{50}K_{10.5}Na_{0.3}O_{93}PW_{18}$	$Co_{19}H_{144}K_4O_{194}P_2W_{32}$
formula weight	5626.13	10470.36
space group	$P\bar{1}$	$C2/m$
a/Å	12.2682(3)	30.4947(10)
b/Å	12.3236(3)	14.6754(5)
c/Å	16.6887(4)	23.0718(9)
α/°	89.4872(18)	90
β/°	74.8719(19)	100.584(4)
γ/°	60.736(2)	90
V/Å^3	2103.66(9)	10149.5(6)
Z	1	2
T/K	120(2)	120.00(10)
λ/Å	0.71073	0.71073
ρ_{calcd}/g cm^{-3}	4.441	3.426
μ/mm^{-1}	26.229	19.761
$R[F_o^2 > 2\sigma(F_o^2)]^a$	0.0557	0.0551
$R_w[F_o^2 > 2\sigma(F_o^2)]^b$	0.1358^c	0.1383^d

^{a} $R = \Sigma(||F_o| - |F_c||)/\Sigma|F_o|$. ^{b} $R_w = \{\Sigma[w(F_o^2 - F_c^2)^2]/\Sigma[w(F_o^2)^2]\}^{1/2}$. $w = 1/[\sigma^2(F_o^2) + (AP)^2 + BP]$, where $P = (F_o^2 + 2F_c^2)/3$. ^{c} $A = 0.0510$, $B = 130.8570$. ^{d} $A = 0.0643$, $B = 917.7090$.

2.3.4.4. X-ray photoelectron spectroscopy

XPS measurements in this work was carried out in collaboration with Prof. José Luis García Fierro from CSIC - Instituto de Catálisis y Petroleoquímica (ICP), Madrid, Spain.

X-ray photoelectron spectra were recorded with a VG 200R spectrometer equipped with a hemispherical electron analyzer and an Al Kα (hν = 1486.6.6 eV) X-ray source. The X-ray source operated at 10 keV and 10 mA. Survey and high-resolution spectra were collected at 65° to the detector with pass energy resolutions of 200 and 50 eV, respectively. The linearity of the binding energy scale was calibrated against the Au $4f_{7/2}$ (84.0 eV) and the Cu $2p_{3/2}$ (932.6 eV) photoemission lines by standard procedures. Each sample was first placed in an aluminum holder mounted on a sample-rod placed in the pre-treatment chamber of the spectrometer and then it was degassed at ambient temperature for 1 h before being transferred to the analysis chamber. Residual pressure within the ion-pumped analysis chamber was kept below $7\cdot10^{-9}$ mbar during data acquisition. Binding energies were calculated with respect to the C-(C, H) component of

the C1*s* peak fixed at 284.8 eV. The high-resolution spectra for the regions of interest were curve fitted using XPS Peak software. After subtraction of a Shirley background, the peaks were fitted using a nonlinear, least squares routine with mixed Gauss–Lorentz (90/10) functions. A minimum set of Gauss–Lorentz functions was chosen in order to obtain a reasonable fit. It is possible to distinguish Co oxidation states using photoelectron spectroscopy. Although the binding energies alone of Co2p lines in compounds containing Co(II) and Co(III) ions do not allow unambiguously to discriminate between them, it is feasible when looking at the satellite lines which accompany the principal Co2p ones.

2.3.4.5. Magnetic Measurements

Samples of **Q-2.8** and **Q-2.9** were prepared by compacted powder molded from ground crystalline samples. Each sample was covered with the minimum amount of liquid eicosane (40 ºC) in order to prevent crystallite torquering. Variable-temperature susceptibility measurements were carried out in the temperature range 2-300 K on a magnetometer equipped with a SQUID sensor (Quantum Design MPMS-XL-5). The data were corrected for diamagnetic contribution from eicosane and for the diamagnetic contributions of the polyanions, as deduced by using the Pascal's constant tables. Isothermal magnetization measurements at low temperature (2 K and 5 K) were performed up to a field of 5 T in the same apparatus.

2.3.4.6. Mass spectrometry

Electrospray ionization mass spectrometry was performed on a Q-TOF Premier mass spectrometer with an orthogonal Z-spray electrospray source (Waters, Manchester, UK). The temperature of the source block was set to 100 °C and the desolvation temperature to 200 °C. A capillary voltage of 3.3 kV was used in the negative scan mode and the cone voltage was set to *Uc* = 10 V to control the extent of fragmentation of the identified species). Aqueous sample solutions of compound **2.8** (ca. $1 \cdot 10^{-5}$ M) were infused via a syringe pump, directly connected to the ESI source, at a flow rate of 10 $\mu L \cdot min^{-1}$.

2.4. References

[1] H. Lv, Y. V. Geletii, C. Zhao, J. W. Vickers, G. Zhu, Z. Luo, J. Song, T. Lian, D. G. Musaev and C. L. Hill, *Chem. Soc. Rev.*, 2012, **41**, 7572-7589.

[2] F. Evangelisti, R. More, F. Hodel, S. Luber and G. R. Patzke, *J. Am. Chem. Soc.*, 2015, **137**, 11076-11084.

[3] X. Han, Y. Li, Z. Zhang, H. Tan, Y. Lu and E. Wang, *J. Am. Chem. Soc.*, 2015, **137**, 5486-5493.

[4] B. Schwarz, J. Forster, M. K. Goetz, D. Yuecel, C. Berger, T. Jacob and C. Streb, *Angew. Chem. Int. Ed.*, 2016, **55**, 6329-6333.

[5] Y. V. Geletii, B. Botar, P. Kögerler, D. A. Hillesheim, D. G. Musaev and C. L. Hill, *Angew. Chem. Int. Ed.*, 2008, **47**, 3896-3899.

[6] X. Han, Z. Zhang, T. Zhang, Y. Li, W. Lin, W. You, Z. Su and E. Wang, *J. Am. Chem. Soc.*, 2014, **136**, 5359-5366.

[7] R. Al-Oweini, A. Sartorel, B. S. Bassil, M. Natali, S. Berardi, F. Scandola, U. Kortz and M. Bonchio, *Angew. Chem. Int. Ed.*, 2014, **53**, 11182-11185.

[8] Q. Yin, J. M. Tan, C. Besson, Y. V. Geletii, D. G. Musaev, A. E. Kuznetsov, Z. Luo, K. I. Hardcastle and C. L. Hill, *Science*, 2010, **328**, 342-345.

[9] Z. Huang, Z. Luo, Y. V. Geletii, J. W. Vickers, Q. Yin, D. Wu, Y. Hou, Y. Ding, J. Song, D. G. Musaev, C. L. Hill and T. Lian, *J. Am. Chem. Soc.*, 2011, **133**, 2068-2071.

[10] J. J. Stracke and R. G. Finke, *J. Am. Chem. Soc.*, 2011, **133**, 14872-14875.

[11] J. J. Stracke and R. G. Finke, *ACS Catal.*, 2013, **3**, 1209-1219.

[12] J. J. Stracke and R. G. Finke, *ACS Catal.*, 2014, **4**, 79-89.

[13] J. W. Vickers, H. Lv, J. M. Sumliner, G. Zhu, Z. Luo, D. G. Musaev, Y. V. Geletii and C. L. Hill, *J. Am. Chem. Soc.*, 2013, **135**, 14110-14118.

[14] F. Song, Y. Ding, B. Ma, C. Wang, Q. Wang, X. Du, S. Fua and J. Song, *Energy Environ. Sci.*, 2013, **6**, 1170-1184.

[15] S. Tanaka, M. Annaka and K. Sakai, *Chem. Commun.*, 2012, **48**, 1653-1655.

[16] P. Car, M. Guttentag, K. K. Baldridge, R. Alberto and G. R. Patzke, *Green Chem.*, 2012, **14**, 1680-1688.

[17] G. Zhu, Y. V. Geletii, P. Kögerler, H. Schilder, J. Song, S. Lense, C. Zhao, K. I. Hardcastle, D. G. Musaev and C. L. Hill, *Dalton Trans.*, 2012, **41**, 2084-2090.

[18] S. Goberna-Ferron, L. Vigara, J. Soriano-Lopez and J. Ramon Galán-Mascarós, *Inorg. Chem.*, 2012, **51**, 11707-11715.

[19] J. Soriano-Lopez, S. Goberna-Ferron, L. Vigara, J. J. Carbo, J. M. Poblet and J. R. Galán-Mascarós, *Inorg. Chem.*, 2013, **52**, 4753-4755.

[20] D. Barats-Damatov, L. J. W. Shimon, L. Weiner, R. E. Schreiber, P. Jimenez-Lozano, J. M. Poblet, C. de Graaf and R. Neumann, *Inorg. Chem.*, 2014, **53**, 1779-1787.

[21] X. Han, Z. Zhang, T. Zhang, Y. Li, W. Lin, W. You, Z. Su and E. Wang, *J. Am. Chem. Soc.*, 2014, **136**, 5359-5366.

[22] M. Ibrahim, Y. Lan, B. S. Bassil, Y. Xiang, A. Suchopar, A. K. Powell and U. Kortz, *Angew. Chem. Int. Ed.*, 2011, **50**, 4708-4711.

[23] U. Kortz, A. Teze and G. Herve, *Inorg. Chem.*, 1999, **38**, 2038-2042.

[24] X. Fang, M. Speldrich, H. Schilder, R. Cao, K. P. O'Halloran, C. L. Hill and P. Kögerler, *Chem. Commun.*, 2010, **46**, 2760-2762.

[25] X. Fang, K. McCallum, H. D. Pratt III, T. M. Anderson, K. Dennis and M. Luban, *Dalton Trans.*, 2012, **41**, 9867-9870.

[26] X. Fang, P. Kögerler, M. Speldrich, H. Schilder and M. Luban, *Chem. Commun.*, 2012, **48**, 1218-1220.

[27] R. Wan, Y. Wang, M. Han, P. Ma, J. Niu and J. Wang, *Inorg. Chem. Commun.*, 2016, **68**, 72-75.

[28] L. C. W. Baker and T. P. Mccutcheon, *J. Am. Chem. Soc.*, 1956, **78**, 4503-4510.

[29] J. Guo, D. Zhang, L. Chen, Y. Song, D. Zhua and Y. Xu, *Dalton Trans.*, 2013, **42**, 8454-8459.

[30] Z. Liang, D. Zhang, P. Ma, J. Niu and J. Wang, *Chemistry-a European Journal*, 2015, **21**, 8380-8383.
[31] T. J. R. Weakley, H. T. Evans, J. S. Showell, G. F. Tourne and C. M. Tourne, *J. Chem. Soc., Chem. Commun.*, 1973, **0**, 139-140.
[32] R. G. Finke, M. W. Droege and P. J. Domaille, *Inorg. Chem.*, 1987, **26**, 3886-3896.
[33] C. J. Gómez-García, E. Coronado and L. Ouahab, *Angew. Chem. Int. Ed.*, 1992, **31**, 649-651.
[34] J. M. Clemente-Juan, E. Coronado, J. R. Galán-Mascarós and C. J. Gómez-García, *Inorg. Chem.*, 1999, **38**, 55-63.
[35] R. G. Finke and M. W. Droege, *Inorg. Chem.*, 1983, **22**, 1006-1008.
[36] I. D. Brown and D. Altermatt, *Acta Crystallogr. Sect. B: Struct. Sci.*, 1985, **41**, 244-247.
[37] R. M. Wood and G. J. Palenik, *Inorg. Chem.*, 1998, **37**, 4149-4151.
[38] N. E. Brese and M. Okeeffe, *Acta Crystallogr. Sect. B: Struct. Sci.*, 1991, **47**, 192-197.
[39] T. Yamase, *Chem. Rev.*, 1998, **98**, 307-325.
[40] D. Jabbour, B. Keita, I. M. Mbomekalle, L. Nadjo and U. Kortz, *Eur. J. Inorg. Chem.*, 2004, **10**, 2036-2044.
[41] P. H. Aubert, L. Groenendaal, F. Louwet, L. Lutsen, D. Vanderzande and G. Zotti, *Synth. Met.*, 2002, **126**, 193-198.
[42] A. P. Ginsberg, *Inorg. Chim. Acta Rev.*, 1971, **5**, 45.
[43] M. E. Lines, *J. Chem. Phys.*, 1971, **55**, 2977.
[44] J. J. Borrás-Almenar, J. M. Clemente-Juan, E. Coronado and B. S. Tsukerblat, *J. Comput. Chem.*, 2001, **22**, 985-991.
[45] J. J. Borrás-Almenar, J. M. Clemente-Juan, E. Coronado and B. S. Tsukerblat, *Inorg. Chem.*, 1999, **38**, 6081-6088.
[46] J. M. Clemente-Juan, E. Coronado, A. Gaita-Ariño, C. Giménez-Saiz, H. U. Güdel, A. Sieber, R. Bircher and H. Mutka, *Inorg. Chem.*, 2005, **44**, 3389-3395.
[47] J. M. Clemente-Juan, E. Coronado, A. Gaita-Ariño, C. Giménez-Saiz, G. Chaboussant, H. U. Güdel, R. Burriel and H. Mutka, *Chem. Eur. J.*, 2002, **8**, 5701-5708.
[48] N. Casanpastor, J. Basserra, E. Coronado, G. Pourroy and L. C. W. Baker, *J. Am. Chem. Soc.*, 1992, **114**, 10380-10383.
[49] J. M. Clemente, H. Andrés, M. Aebersold, J. J. Borrás-Almenar, E. Coronado, H. U. Güdel, H. Buttner and G. Kearly, *Inorg. Chem.*, 1997, **36**, 2244-2245.
[50] H. Andrés, J. M. Clemente-Juan, M. Aebersold, H. U. Güdel, E. Coronado, H. Buttner, G. Kearly, J. Melero and R. Burriel, *J. Am. Chem. Soc.*, 1999, **121**, 10028-10034.
[51] H. Andrés, J. M. Clemente-Juan, R. Basler, M. Aebersold, H. U. Güdel, J. J. Borrás-Almenar, A. Gaita-Ariño, E. Coronado, H. Buttner and S. Janssen, *Inorg. Chem.*, 2001, **40**, 1943-1950.
[52] J. M. Clemente-Juan, E. Coronado, A. Forment-Aliaga, J. R. Galán-Mascarós, C. Giménez-Saiz and C. J. Gómez-García, *Inorg. Chem.*, 2004, **43**, 2689-2694.
[53] H. Andrés, J. M. Clemente-Juan, M. Aebersold, H. U. Güdel, E. Coronado, H. Buttner, G. Kearly, J. Melero and R. Burriel, *J. Am. Chem. Soc.*, 1999, **121**, 10028-10034.
[54] G. Aromí, D. Águila, P. Gámez, F. Luis and O. Roubeau, *Chem. Soc. Rev.*, 2012, **41**, 537-546.
[55] M. Trif, F. Troiani, D. Stepanenko and D. Loss, *Phys. Rev. Lett.*, 2008, **101**, 217201.
[56] A. Palii, J. M. Clemente-Juan, B. Tsukerblat and E. Coronado, *Chem. Sci.*, 2014, **5**, 3598-3602.
[57] S. Cardona-Serra, J. M. Clemente-Juan, E. Coronado, A. Gaita-Ariño, N. Suaud, O. Svoboda, R. Bastardis, N. Guihery and J. J. Palacios, *Chem. Eu. J.*, 2015, **21**, 763-769.
[58] A. V. Palii, J. M. Clemente-Juan, E. Coronado and B. Tsukerblat, *J. Phys. Chem. C.*, 2015, **119**, 7911-7921.
[59] P. J. Domaille, in *Inorganic Syntheses*, ed. A. P. Ginsberg, John Wiley & Sons, New York, 1990, p. 96-104.
[60] Agilent Technologies UK Ltd, Oxford, UK, *CrysAlis PRO Software system*, 2013.
[61] G. M. Sheldrick, *Acta Cryst. A.*, 2008, **64**, 112-122.
[62] A. L. Spek, *Acta Crystallogr. D Biol. Crystallogr.*, 2009, **65**, 148-155.

[63] H. N. Miras, J. Yan, D. Long and L. Cronin, *Chem. Soc. Rev.*, 2012, **41**, 7403-7430.
[64] Y. Duan, J. M. Clemente-Juan, C. Giménez-Saiz and E. Coronado, *Inorg. Chem.*, 2016, **55**, 925-938.
[65] D. E. Katsoulis and M. T. Pope, *J. Am. Chem. Soc.*, 1984, **106**, 2737-2738.
[66] L. Lisnard, P. Mialane, A. Dolbecq, J. Marrot, J. M. Clemente-Juan, E. Coronado, B. Keita, P. De Oliveira, L. Nadjo and F. Sécheresse, *Chem. Eur. J.*, 2007, **13**, 3525-3536.
[67] J. R. Galán-Mascarós, C. Giménez-Saiz, S. Triki, C. J. Gómez-García, E. Coronado and L. Ouahab, *Angew. Chem. Int. Ed.*, 1995, **34**, 1460-1462.
[68] H. T. Evans, T. J. R. Weakley and G. B. Jameson, *J. Chem. Soc., Dalton Trans.*, 1996, **14**, 2537-2540.
[69] B. B. Yan, Y. Xu, X. H. Bu, N. K. Goh, L. S. Chia and G. D. Stucky, *J. Chem. Soc., Dalton Trans.*, 2001, , 2009-2014.
[70] J. Zhao, S. Zheng and G. Yang, *J. Solid State Chem.*, 2008, **181**, 2205-2216.
[71] Y. Duan, J. M. Clemente-Juan, J. L. G. Fierro, C. Giménez-Saiz and E. Coronado, *Chem. Commun.*, 2016, **52**, 13245-13248.
[72] R. Meng, B. Wang, H. Sui, B. Li, W. Song, L. Wu, B. Zhao and L. Bi, *Eur. J. Inorg. Chem.*, 2013, **10-11**, 1935-1942.
[73] M. D. Ritorto, T. M. Anderson, W. A. Neiwert and C. L. Hill, *Inorg. Chem.*, 2004, **43**, 44-49.
[74] L. Yang, J. Zhao, J. Zhao and J. Niu, *J. Coord. Chem.*, 2012, **65**, 3363-3371.
[75] H. Lv, J. Song, Y. V. Geletii, W. Guo, J. Bacsa and C. L. Hill, *Eur. J. Inorg. Chem.*, 2013, **10-11**, 1720-1725.
[76] K. Fukaya and T. Yamase, *Bull. Chem. Soc. Jpn.*, 2007, **80**, 178-182.
[77] J. Wang, J. Zhao, H. Zhao, B. Yang, H. He and G. Yang, *Crystengcomm*, 2014, **16**, 252-259.
[78] M. T. Pope, *Inorg. Chem.*, 1972, **11**, 1973.
[79] A. L. Nolan, C. C. Allen, R. C. Burns, G. A. Lawrance, E. N. Wilkes and T. W. Hambley, *Aust. J. Chem.*, 1999, **52**, 955-963.
[80] M. Ibrahim, A. Haider, Y. Lan, B. S. Bassil, A. M. Carey, R. Liu, G. Zhang, B. Keita, W. Li, G. E. Kostakis, A. K. Powell and U. Kortz, *Inorg. Chem.*, 2014, **53**, 5179-5188.
[81] J. M. Clemente-Juan, E. Coronado, A. Gaita-Ariño, C. Giménez-Saiz, G. Chaboussant, H. U. Güdel, R. Burriel and H. Mutka, *Chem. Eur. J.*, 2002, **8**, 5701-5708.
[82] B. S. Bassil, U. Kortz, A. S. Tigan, J. M. Clemente-Juan, B. Keita, P. de Oliveira and L. Nadjo, *Inorg. Chem.*, 2005, **44**, 9360-9368.
[83] J. M. Clemente-Juan, E. Coronado, A. Gaita-Ariño, C. Giménez-Saiz, H. U. Güdel, A. Sieber, R. Bircher and H. Mutka, *Inorg. Chem.*, 2005, **44**, 3389-3395.
[84] J. M. Clemente-Juan, E. Coronado, A. Forment-Aliaga, J. R. Galán-Mascarós, C. Giménez-Saiz and C. J. Gómez-García, *Inorg. Chem.*, 2004, **43**, 2689-2694.
[85] D. Long, E. Burkholder and L. Cronin, *Chem. Soc. Rev.*, 2007, **36**, 105-121.
[86] A. L. Nolan, C. C. Allen, R. C. Burns, D. C. Craig and G. A. Lawrance, *Aust. J. Chem.*, 2000, **53**, 59-66.
[87] S. Reinoso, J. R. Galán-Mascarós and L. Lezamat, *Inorg. Chem.*, 2011, **50**, 9587-9593.
[88] I. M. Mbomekalle, B. Keita, M. Nierlich, U. Kortz, P. Berthet and L. Nadjo, *Inorg. Chem.*, 2003, **42**, 5143-5152.
[89] U. Kortz, I. M. Mbomekalle, B. Keita, L. Nadjo and P. Berthet, *Inorg. Chem.*, 2002, **41**, 6412-6416.
[90] J. Zhao, Q. Han, D. Shi, L. Chen, P. Ma, J. Wang and J. Niu, *J. Solid State Chem.*, 2011, **184**, 2756-2761.
[91] C. A. Ohlin, S. J. Harley, J. G. McAlpin, R. K. Hocking, B. Q. Mercado, R. L. Johnson, E. M. Villa, M. K. Fidler, M. M. Olmstead, L. Spiccia, R. D. Britt and W. H. Casey, *Chem. Eur. J.*, 2011, **17**, 4408-4417.
[92] E. N. Glass, J. Fielden, A. L. Kaledin, D. G. Musaev, T. Lian and C. L. Hill, *Chem. Eur. J.*, 2014, **20**, 4297-4307.
[93] S. Gao, T. Li, X. Li and R. Cao, *Mater. Lett.*, 2006, **60**, 3622-3626.

[94] L. Lisnard, P. Mialane, A. Dolbecq, J. Marrot, J. M. Clemente-Juan, E. Coronado, B. Keita, P. de Oliveira, L. Nadjo and F. Sécheresse, *Chem. Eur. J.*, 2007, **13**, 3525-3536.
[95] Carlin, R. L. *Magnetochemistry*. Springer-Verlag: New York, 1986.
[96] K. Kojima, J. Matsuda, N. Kojima, T. Ban and I. Tsujikawa, *Bull. Chem. Soc. Jpn.*, 1987, **60**, 3213-3217.
[97] C. Giménez-Saiz, J. R. Galán-Mascarós, S. Triki, E. Coronado and L. Ouahab, *Inorg. Chem.*, 1995, **34**, 524-526.

Chapter 3. POM-Based SMMs

In this chapter, POM ligands have been chosen for the construction of single molecule magnets (SMMs). POM chemistry has recently offered excellent examples of SMMs and molecular spin qubits. Compared with conventional coordination compounds, POMs provide rigid and highly symmetric coordination sites. However, all POM-based SMMs reported to date exhibit a very limited range of possibilities for chemical processability. In this chapter, we present the synthesis and characterisation of a family of polyoxomolybdate-based single ion magnets (SIMs) {formulated as $[Ln(\beta\text{-}Mo_8O_{26})_2]^{5-}$, with Ln^{3+} = Tb (**3.1**), Dy (**3.2**), Ho (**3.3**), Er (**3.4**), Tm (**3.5**), and Yb (**3.6**)} that is soluble in organic solvents (such as acetone, acetonitrile, N,N-dimethylformamide, *etc.*).

These compounds were obtained by reacting $[(n\text{-}C_4H_9)_4N]_4[\beta\text{-}Mo_8O_{26}]$ with lanthanoid nitrate salts. They have been characterised by static and dynamic magnetic measurements. The magnetostructural analysis of this family is based on an effective crystal field model and compared with the results reported in the analogous lanthanoid SIMs based on polyoxotungstates.[34-40] Two different methods are presented to determine the crystal field (CF) parameters. Among this series of compounds, only **3.3** and **3.4** exhibit SMM-like behaviour above 2 K. For a deep understanding of the appearance of slow relaxation of the magnetization in this type of mononuclear complexes, the ligand-field parameters and the splitting of the *J* ground-state multiplet of the lanthanoid ions have been also estimated, which was modeled using an effective crystal field approach previously developed for this kind of ligands.

3. SIMs based on lanthanoid polyoxomolybdate complexes

3.1. Introduction

The main goal of spintronics is the active manipulation of the electron spin degrees of freedom in solid-state systems for carrying information.[1-2] Spintronic systems have experienced a rapid development and currently are used in a range of applications, including read-head devices and non-volatile magnetic memories (MRAM).[3-4] Extraordinary potential for these systems is expected for the fabrication of spin-transfer nano-oscillators (STNOs)[5] and quantum computers.[6-8] The progress of molecular electronics and molecular magnetism has led to the emergence of a new field known as molecular spintronics,[9-10] which combines the ideas and concepts of spintronics with the singular possibilities offered by molecular electronics and molecular magnetism to develop a second generation of spintronic devices.[11-14]

A particularly challenging area within this field is single-molecule spintronics, which intends to use individual molecules as main components of spintronic devices. In this context, single-molecule magnets (SMMs)[15] have been proposed as promising candidates.[16-18] These systems, which represent the limit of miniaturization of nanomagnets, are between the most complex magnetic entities, exhibiting slow relaxation of the magnetization[19] and magnetic hysteresis[20] at liquid-helium temperatures. Moreover, they may also present quantum phenomena from purely molecular origin.[21-24] In this context, SMMs based on mononuclear lanthanoid complexes deserve a special attention.[25-26] The first example of this class of molecular nanomagnets, also known as single-ion magnets (SIMs), was reported by Ishikawa and co-workers in the series with general formula $[LnPc_2]^-$, with lanthanoid ions sandwiched between two phthalocyaninato moieties displaying a square-antiprismatic D_{4d} symmetry.[27] Derivatives closely related to this family include the oxidised terbium phthalocyaninato complex $[TbPc_2]^0$. This system, besides its "double-decker" structure, which favours the adsorption on surfaces, is a neutral species. This feature facilitates its sublimation under UHV conditions. The processability of lanthanoid phthalocyaninato complexes has led to a series of breakthroughs including the realization of molecular/supramolecular spin valves[28-29] and the electrical control of nuclear spin qubits.[30-31] Indeed, sublimable lanthanoid complexes have demonstrated a great potential in molecular spintronics. Among the few sublimable lanthanoid-based systems reported so far, we can highlight the trinuclear Tb^{3+} complex $Tb_3(OQ)_9$ (OQ = quinolinato), where spin-polarised hopping

transport has been realised.[32] It has also been proposed as a model system for quantum error correction in quantum computing.[33]

A second series of SIMs is provided by POM chemistry.[34-36] In this case, mononuclear lanthanoid complexes encapsulated by POMs have produced various examples of SIMs exhibiting SMM behaviour. At the same time, these systems have also been of interest as spin qubits for quantum computing. Indeed, extended quantum coherence was recently achieved on concentrated samples of the holmium derivative of the series $[Ln(W_5O_{18})_2]^{9-}$ (in short LnW_{10}) through the use of atomic clock transitions.[37] Employing a different strategy, a large number of coherent manipulations was realised in the Gd^{3+} derivative[38] of the $[Ln(H_2O)P_5W_{30}O_{110}]^{12-}$ series (in short LnW_{30}).[39] This POM has also shown to be useful to design a 3-qubit quantum processor.[57] Within the same POM family, current rectification was achieved in a single molecule diode of DyW_{30}.[40] Except in the latter case, the incorporation of these molecular inorganic polyanions onto surfaces or its anchoring to electrodes have been limited by their poor solubility in organic solvents.

In this chapter, we will describe the preparation of a family of POM-based mononuclear lanthanoid complexes with a rigid square antiprism structure, analogous to one series of polyoxotungstate LnW_{10}, which overcomes these processing limitations. This family of complexes is formulated as $[Ln(\beta\text{-}Mo_8O_{26})_2]^{5-}$ (in short, $LnMo_{16}$), {Ln^{3+} = Tb (**3.1**), Dy (**3.2**), Ho (**3.3**), Er (**3.4**), Tm (**3.5**) and Yb (**3.6**)}, which consists of a lanthanoid ion trapped by two $[\beta\text{-}Mo_8O_{26}]^{4-}$ moieties. The experimental and magnetic characterisation is brought into the context for this series of polyoxomolybdates. For the magnetostructural analysis, two different methods have been presented to determine the crystal field (CF) parameters. The first assumes a linear dependence of the CF parameters with the number of *f*-electrons while the second estimates the ligand field parameters through an effective charge situated along the lanthanoid atom axis. These results are compared with the previously reported analogous lanthanoid SIMs based on polyoxotungstates. Compounds **3.3** and **3.4** exhibit SMM properties, which can be modeled using an effective crystal field approach previously developed for this kind of ligands. The key novelty consists in the use of polyoxomolybdates instead of polyoxotungstates to obtain SIMs. While the chemistry of polyoxomolybdates is more challenging, this result has opened the possibility of making these magnetic molecules soluble in organic solvents, thus facilitating their processing and incorporation into devices.

3.2. Results and Discussion

3.2.1. Synthetic approach

Reaction of $[(n\text{-}C_4H_9)_4N]_4[\beta\text{-}Mo_8O_{26}]$ with lanthanoid nitrate salts in stoichiometric ratio, using dry acetonitrile as solvent, gives rise to the formation of the polyoxomolybdates $[Ln(\beta\text{-}Mo_8O_{26})_2]^{5-}$ in solution. Crystals were obtained by layering the acetonitrile solution with diethyl ether. It is worth to note that these compounds are very unstable in solution in the presence of water, decomposing to the yellow Lindqvist species $[Mo_6O_{19}]^{2-}$. Therefore, all the preparation process was carried out using distilled solvents to avoid decomposition.

3.2.2. Crystal structures of 3.1-3.6

All salts contain $[Ln(\beta\text{-}Mo_8O_{26})_2]^{5-}$ anions, where Ln^{3+} = {Tb (**3.1**), Dy (**3.2**), Ho (**3.3**), Er (**3.4**), Tm (**3.5**) and Yb (**3.6**)}, and tetrabutylammonium (TBA^+) cations. The preparation of the Yb derivative and other isotypic lanthanoid POMs (with Ln^{3+} = Y, La, Ce, Pr, Nd, Gd and Yb) were previously reported, although the crystal structure was only solved for the La derivative,[41] and no magnetic characterisation was carried out.

The structure of this family of POMs consists of one Ln^{3+} ion sandwiched by two β-octamolybdate ($[\beta\text{-}Mo_8O_{26}]^{4-}$) units, in such a way that the Ln^{3+} ion exhibits an eight-fold square-antiprismatic coordination (D_{4d}, ideal symmetry around the Ln^{3+}). Such a coordination mode is also found in other lanthanoid-containing POMs based on the monovacant Lindqvist unit $[W_5O_{18}]^{6-}$, which have recently been reported to show SMMs behavior.[42-44] The octamolybdate $[\beta\text{-}Mo_8O_{26}]^{4-}$ moiety is composed of two subunits made of four coplanar, edge-shared octahedra (see **Fig. 3.1**). These two subunits are assembled in such a way that one octahedron of each subunit fits in the central position of the other subunit. This assembly implies that both subunits also share edges between them and, consequently, are not eclipsed but slightly displaced with respect to the other (**Fig. 3.1**). The topology of the octamolybdate anion is such that allows the possibility of coordinating up to two lanthanoid cations in opposite sides of the anion and, then, acting as a bis-tetradentate ligand. In the present work, the octamolybdate anion acts as a tetradentate ligand, coordinating only one lanthanoid cation in one of its sides. The coordination of the lanthanoid is completed by another octamolybdate ligand, which is

rotated 45º from the first, in order to give rise to the square-antiprismatic coordination of the lanthanoid cation (see **Fig. 3.12**). The structural parameters concerning the lanthanoid coordination sphere are listed in **Table 3.1**. This arrangement produces a sandwich polyoxomolybdate that is chiral as it is not superposable on its mirror image. Chirality appears as a result of the particular assembly of the octahedra of the octamolybdate anion and the square-antiprismatic coordination of the lanthanoid cation.

Table 3.1.- Structural parameters concerning the lanthanoid coordination sphere.

$LnMo_{16}$	d_{pp} [a] (Å)	d_{in} [b] (Å)	φ [c] (°)
3.1 ($TbMo_{16}$)	2.604(13)	2.853(15)	40.2(5)
3.2 ($DyMo_{16}$)	2.552(18)	2.844(18)	44.1(5)
3.3 ($HoMo_{16}$)	2.553(10)	2.825(10)	44.3(3)
3.4 ($ErMo_{16}$)	2.551(11)	2.819(11)	44.2(3)
3.5 ($TmMo_{16}$)	2.506(14)	2.818(14)	44.1(4)
3.6 ($YbMo_{16}$)	2.506(14)	2.796(14)	44.3(4)

[a] d_{pp} defines the average distance between two oxygen based square planes. [b] d_{in} is the average O–O distance within the oxygen-based square planes. [c] φ is defined as the relative orientation between the two squares defined by the coordinating oxygen atoms.

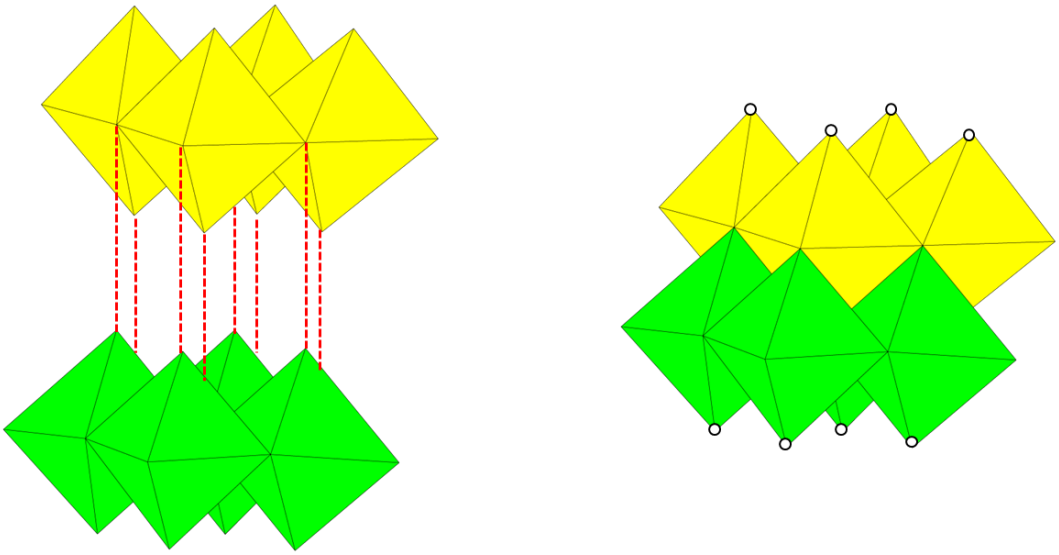

Fig. 3.1.- The assembling of the two subunits: four coplanar edge-shared octahedra. (left) The structure of the octamolybdate $[\beta\text{-}Mo_8O_{26}]^{4-}$ moiety. (right) Circles show the coordination sites of the polyoxoanion.

The crystal structure determination reveals that compounds **3.1**-**3.6** are true racemates and the two enantiomers (labelled as I and II in **Fig. 3.2**) are present in all

crystal structures. Enantiomers I and II can be generated from each other if one considers that only one of the β-octamolybdate units can be rotated by 90º (clockwise from I to II, in **Fig. 3.2**) through an ideal axis which passes through the lanthanoid ion and the two nearer μ_5 oxygen atoms of both β-octamolybdate units. Two diastereoisomers of I and II can be envisaged by effecting further clockwise 90º rotations of the same β-octamolybdate unit, giving rise to enantiomers III and IV (see **Fig. 3.2**). All these 90º rotations produce eight-fold square-antiprismatic coordination of the lanthanoid ion, while a 45º rotation would have produced an imaginary POM in which the lanthanoid ion would have a cubic coordination. Enantiomers III and IV are not present in compounds **3.1**-**3.6**. A possible reason for this lies in their shapes. I and II have sigmoid (or S) shapes in which the two opposite sides of the sigmoid are twisted forming a "dihedral" angle of 135º, while in III and IV this angle is 45º. From this difference in the "dihedral" angle, one can expect that III and IV would exhibit a higher dipolar moment than I and II. This fact could be the reason for which the tetrabutylammonium cation (a nonpolar cation) would crystallize preferentially with POMs I/II instead of crystallizing with III/IV. Following this idea, it would be necessary to use polar cations to crystallize enantiomers III and IV. This is going to be one of our future work.

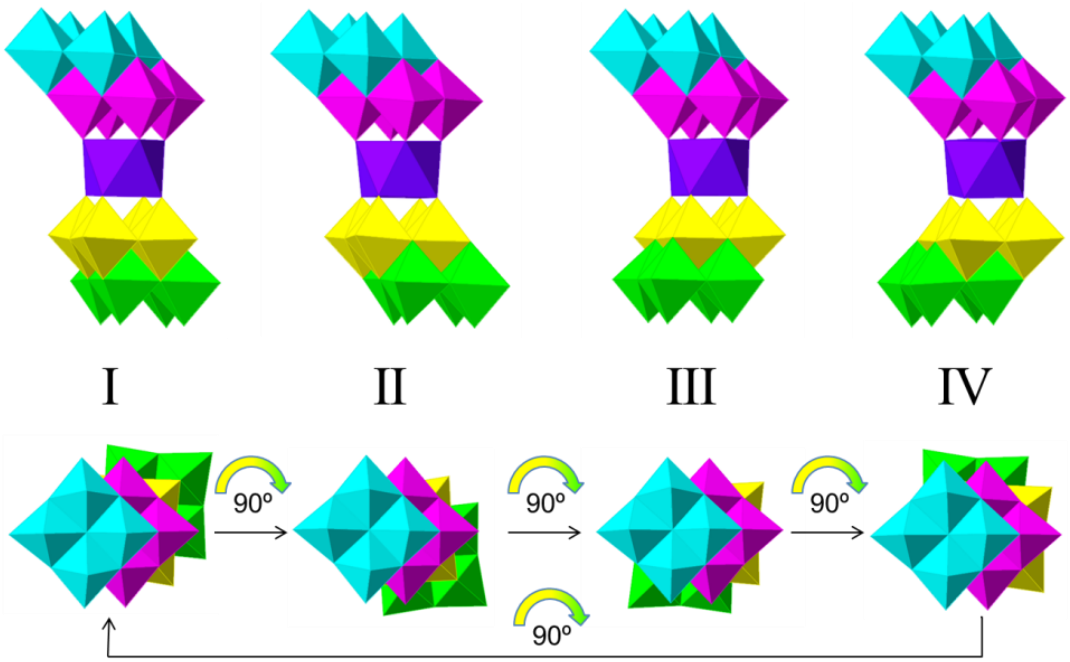

Fig. 3.2.- Polyhedral representations of the POMs $[Ln(\beta\text{-}Mo_8O_{26})_2]^{5-}$ showing the relation between the isomers I and II (present in compounds **3.1-3.6**) and the plausible isomers III and IV. The POMs have been coloured to make clearer the transformation between isomers affected by consecutive 90º rotations of only one β-octamolybdate unit (the yellow/green coloured one) while the other (the cyan/violet coloured one) remains unchanged.

Compound **3.1** ($TbMo_{16}$) crystallises in the monoclinic system while all other compounds **3.2-3.6** crystallise in the orthorhombic system (see **Table 3.5**), the packing of POMs being different in each system. The crystal structure of the Tb derivative **3.1** may be considered as formed by layers parallel to the *bc*-plane in which each POM is surrounded by 6 other polyanions in a pseudo-hexagonal arrangement. Each of these layers is formed by enantiomers, I and II, which self-organize separately in alternate rows parallel to the *b*-axis (**Fig. 3.3a** shows a projection of these layers along the *a*-axis). Adjacent layers pack in an eclipsed way by virtue of the inversion centres located between the layers, following a sequence of 2 consecutive layers that repeats along the *a* direction. This pattern gives rise to POM chains, parallel to the *a*-axis, in which the enantiomers I and II alternate.

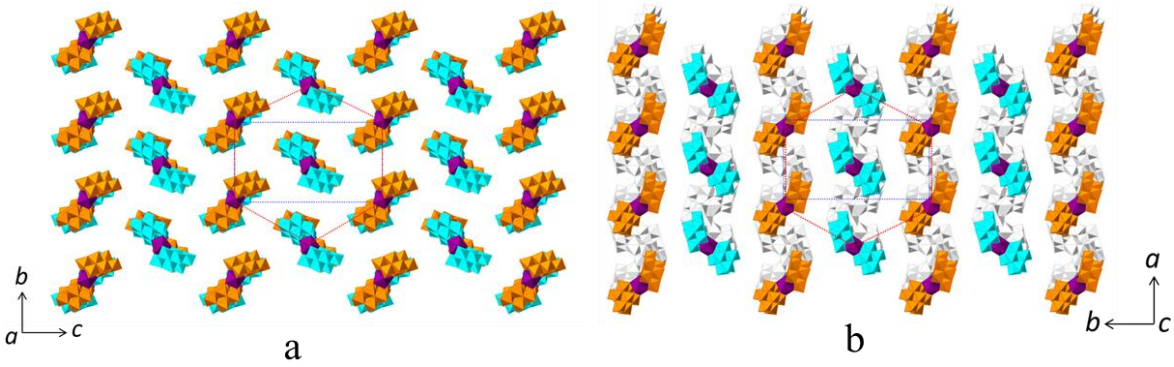

Fig. 3.3.- Projections of the crystal structures of monoclinic **3.1** (a) and orthorhombic **3.2-3.6** (b) along the *a*- and *c*- axis respectively, showing the layered pseudo-hexagonal arrangements of POMs.

Compounds **3.2-3.6** also form similar layers (parallel to the *ab* plane) that exhibit a pseudo-hexagonal arrangement of POMs (see **Fig. 3.3b**). These layers also contain the two enantiomers in separate, alternating rows (parallel to the *a*-axis). The adjacent layers, however, do not pack in an eclipsed way but they are slightly displaced from each other, following a sequence of four consecutive layers that repeats along the *c* direction. This layer displacement gives rise to zigzag chains of alternating POM enantiomers along the *c* direction.

The orthorhombic phase is obtained for Ln^{3+} cations having ionic radii equal or smaller than Dy^{3+}, while the monoclinic phase is obtained for Ln^{3+} ions having larger radii. To confirm this trend, the Gd^{3+} and Eu^{3+} derivatives have also been synthetized and their unit cells determined. Both of them exhibit the monoclinic phase, as well as the previously reported La^{3+} derivative.[41]

3.2.3. Solubility and stability

The use of tetraalkylammonium cations in combination with polyoxoanions allows the preparation of POM salts soluble in some organic solvents. By increasing the length of the alkyl chains the solubility in organic solvents can be enhanced. However, in general, the longer the chains, the less crystalline and more amorphous are the resulting salts. In this work, we have chosen the tetrabutylammonium cation because it produces crystalline salts that are soluble in a reasonable number of organic solvents. We have studied the solubility of this series of compounds in various anhydrous solvents (see **Table 3.2**). In addition, mass spectrometry was conducted for **3.4** to confirm its stability in acetonitrile solution (see **Fig. 3.4**). The major signals in the mass spectra (comparison with experimental values and simulated values) were detected at *m/z* range 998-1015 for $\{TBA_2[Ln(\beta\text{-}Mo_8O_{26})_2]\}^{3-}$ and *m/z* range 1160-1250 for $\{TBA_3[Ln(\beta\text{-}Mo_8O_{26})_2]\}^{2-}$, which shows that the compound is stable in acetonitrile solution.

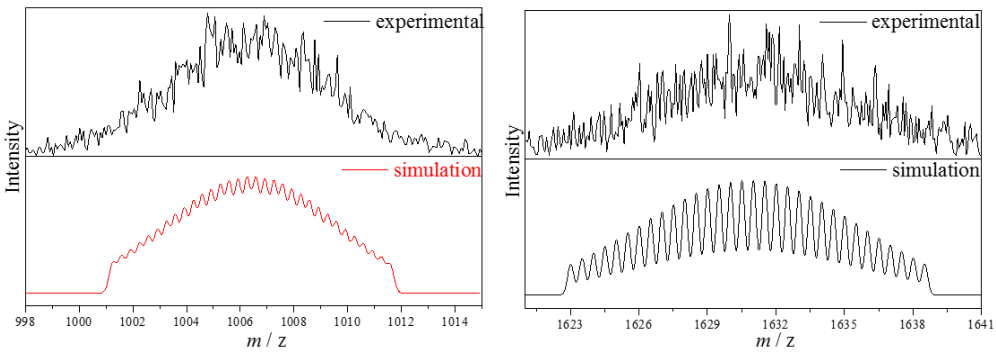

Fig. 3.4.- Mass spectrum (ESI-MS) of **3.4** in negative mode in dry acetonitrile solution (up: experimental; down: simulation). (left) Expanded view of the –3 charge state, $\{TBA_2[Er(\beta\text{-}Mo_8O_{26})_2]\}^{3-}$ (*m/z* range 998-1015). (right) Expanded view of the –2 charge state, $\{TBA_3[Er(\beta\text{-}Mo_8O_{26})_2]\}^{2-}$ (*m/z* range 1160-1250).

Table 3.2.- Solubilities of compounds **3.1-3.6** in several organic solvents.

Solvent	$LnMo_{16}$
Acetonitrile	soluble
Acetone	soluble
Benzonitrile	soluble
Formamide	soluble
N, N-Dimethylformamide	soluble
Ethanol	insoluble
Methanol	insoluble
Dichloromethane	insoluble
Chloroform	insoluble

3.2.4. Magnetic properties

Fresh samples of **3.1**-**3.6** were used for the static and dynamic magnetic measurements. The results of the *dc* measurements in the form of $\chi_m T$ *vs.* T are shown in **Fig. 3.5** and the experimental and calculated field dependence magnetization are shown in **Fig. 3.7** for all the members of the series. Those data were measured between 2 and 300 K with a commercial magnetometer equipped with a SQUID sensor. The diamagnetic contributions to the susceptibility were corrected using Pascal's constant tables. Direct current (*dc*) data were collected with an applied field of 1000 Oe.

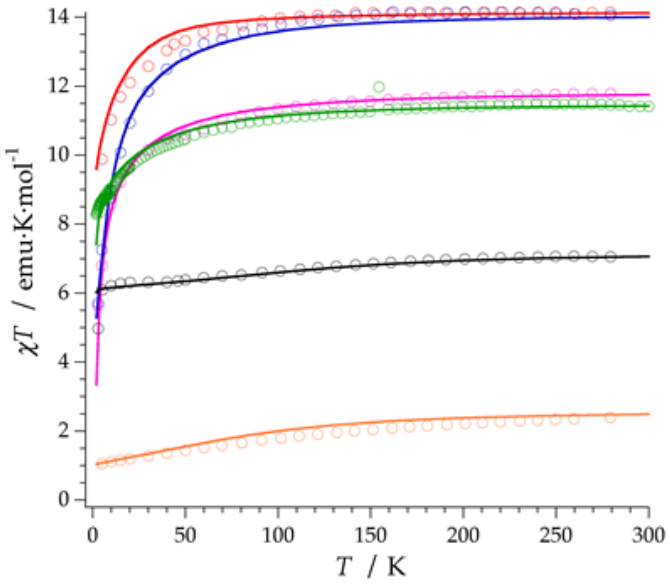

Fig. 3.5.- Temperature-dependent magnetic susceptibility of **3.1**-**3.6** using the REC model: Dy^{3+} (red), Ho^{3+} (blue), Tb^{3+} (pink), Er^{3+} (green), Tm^{3+} (black), Yb^{3+} (orange). Markers give experimental data, and solid lines theoretical results: fits for Tb^{3+}-Er^{3+} and predictions for Tm^{3+} and Yb^{3+}.

The room temperature $\chi_m T$ value of each sample is shown in **Table 3.3**, those values match closely with those expected for the free ion. As the temperature decreases, the $\chi_m T$ value gradually decreases because of depopulation of the highest $|M_J|$ sublevels. A simultaneous fit was performed on the four magnetic susceptibility curves of the Tb^{3+}, Dy^{3+}, Ho^{3+} and Er^{3+} derivatives of this series using an effective crystal field approach. The two determined parameters were tested by applying them to the real coordinates of the Tm^{3+} and Yb^{3+} derivatives. The predicted magnetic behaviour shows an excellent agreement with the experimental data (**Fig. 3.5**).

Table 3.3.- Total angular momentum of the lanthanoid cations, as given by Hund's rules, and $\chi_m T$ values for **3.1**-**3.6**.

Lanthanoid Ion	*J*	$\chi_m T$ of the free ion (emu·K/mol)	Experimental $\chi_m T$ of the Ln-POM complex at 280 K (emu·K/mol)
Tb^{3+}	6	11.75	11.79
Dy^{3+}	15/2	14.12	14.14
Ho^{3+}	8	14.00	14.06
Er^{3+}	15/2	11.43	11.45
Tm^{3+}	6	7.06	7.05
Yb^{3+}	7/2	2.48	2.39

The most satisfactory agreement was obtained when the radial displacement *(D_r)* equals 0.72 Å and the effective charge (Z_i) is 0.253 (see **Fig. 3.6**). In this effective crystal field model the Ln-O distance as well as the oxo charge are corrected by these two parameters to account for the covalency of the Ln-O bond. If we compare the obtained parameters with the ones extracted in the families LnW_{10} and $[Ln(\beta_2\text{-}SiW_{11}O_{39})_2]^{13-}$ (in short, LnW_{22}),[41] the radial displacement is smaller in this case. This means that the effective point charge needs a smaller covalent correction to produce an adequate relation between the crystal-field parameters that describe the experimental data. This difference can be related to the different Pauling electronegativity of the Mo and W atoms (2.16 and 2.36, respectively).[45] The larger difference in electronegativity between Mo (2.16) and O (3.44) enhances the ionic character of the Mo-O bonding and also the coordination bond Ln-O.

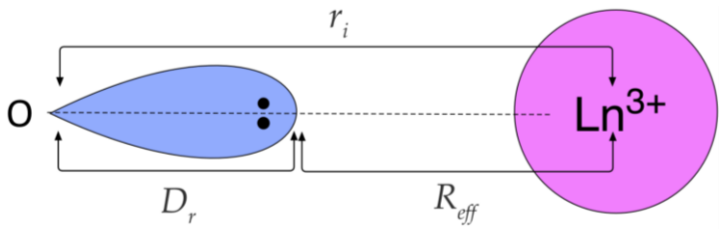

Fig. 3.6.- Electronic pair of oxo ligand oriented towards the nucleus of a trivalent lanthanoid cation. The effective charge Z_i is located between the lanthanoid and the donor atom at $R_{eff} = r_i - D_r$.

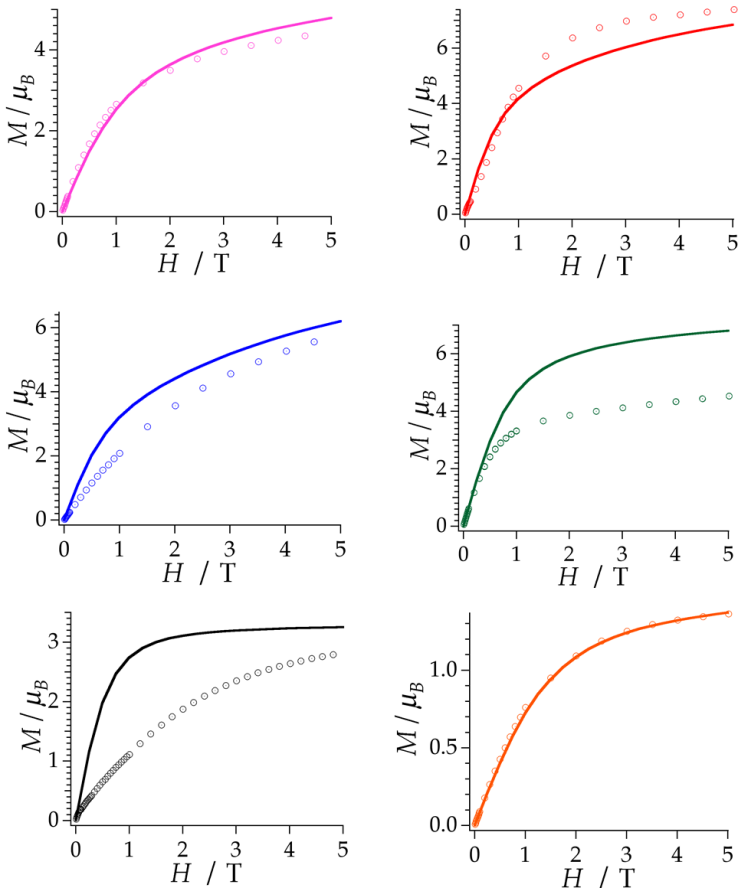

Fig. 3.7.- Experimental (circles) and calculated (solid lines) field dependence magnetization of **3.1**-**3.6** at 2 K measured from 0 to 5 T. Tb^{3+} (**3.1**) (pink), Dy^{3+} (**3.2**) (red), Ho^{3+} (**3.3**) (blue), Er^{3+} (**3.4**) (green), Tm^{3+} (**3.5**) (black) and Yb^{3+} (**3.6**) (orange).

The resulting energy levels for all the series are shown in **Fig. 3.8** and the main contributions to the ground state wave function in **3.1**-**3.6** are summarized in **Table 3.4**. A general trend for $LnMo_{16}$ compared with LnW_{10} and LnW_{22} is a slightly larger crystal field splitting. In average, the Ln-O distance is practically identical in both series, e.g. in ErW_{10} and $ErMo_{16}$ (2.367(7) Å and 2.367(3) Å). This would mean that polyoxomolybdates tend to produce a slightly stronger ligand field splitting compared with polyoxotungstates at a given metal-ligand distance.

The *ac* magnetic susceptibilities were collected in the range 2-12 K with an applied alternating field of 3.95 Oe at different frequencies in the range 1-10000 Hz. **3.3** and **3.4** show frequency dependent out-of-phase signals at very low temperatures, indicative a a SMM behaviour. However, no clear peak, indicative of a supermagnetic barrier, is observed even under an external applied field of 1000 Oe (see **Fig. 3.9** and **Fig. 3.10**). This feature is a characteristic of the fast relaxation process that takes place at low temperatures via a quantum tunnelling mechanism.

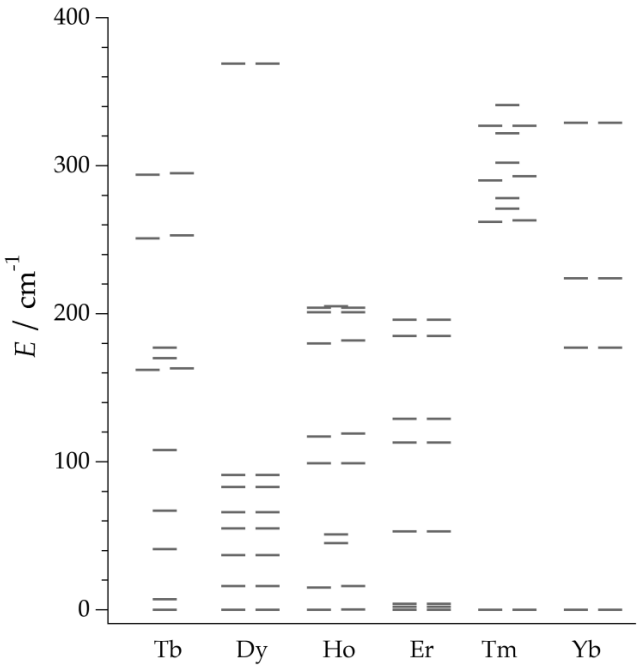

Fig. 3.8.- Energy level scheme caused by the crystal field splitting for **3.1**-**3.6**.

Table 3.4.- Main contributions to the ground state wave function in **3.1**-**3.6**.

POM	Lanthanoid Ion	*J*	Contribution of ground state
3.1	Tb	6	92 % |0>
3.2	Dy	15/2	79 % |±11/2> + 14 % |±9/2>
3.3	Ho	8	47 % |+4> + 47 % |–4>
3.4	Er	15/2	78 % |±1/2> + 12 % |±13/2> or 78 % |±15/2>, or 74 % |±13/2> + 15 % |±15/2>
3.5	Tm	6	50 % |+6> + 50 % |–6>
3.6	Yb	7/2	99 % |±5/2>

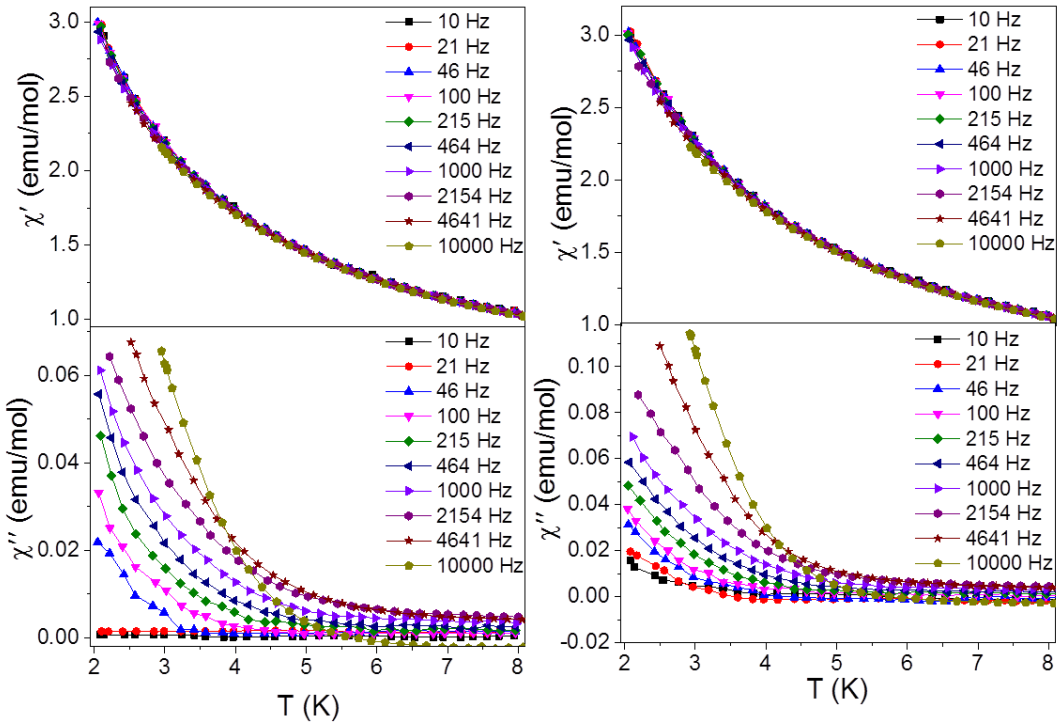

Fig. 3.9.- In-phase (up) and out-of-phase (down) dynamic susceptibility of **3.3** ($HoMo_{16}$): without an external field (left) and with an applied field of 1000 Oe (right). The frequencies are shown in the legend. Solid lines are eye-guides.

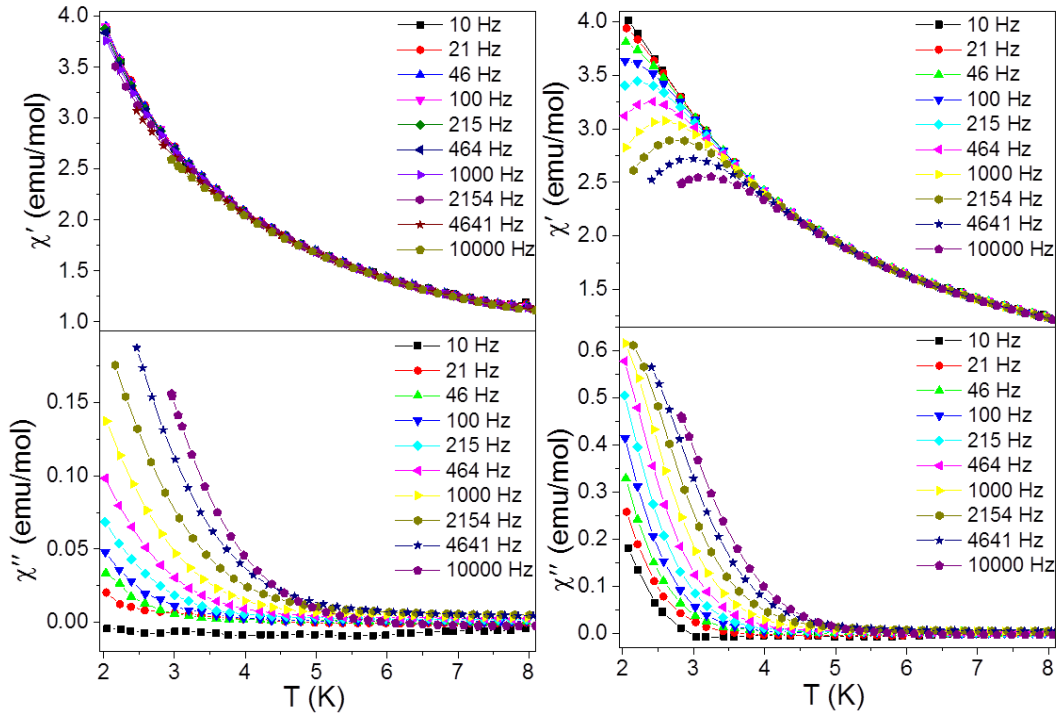

Fig. 3.10.- In-phase (up) and out-of-phase (down) dynamic susceptibility of **3.4** ($ErMo_{16}$): without an external field (left) and with an applied field of 1000 Oe (right). The frequencies are shown in the legend. Solid lines are eye-guides.

In order to explain why these two compounds exhibit a slow relaxation of the magnetization at low temperatures, we have concentrated on the wave functions of the lower-lying states. One can observe that in the case of Ho derivative (**3.3**) the ground state

is defined by a mixture of 47 % of |+4> and 47 % of |–4>. In this case, the extra-diagonal crystal field operators mix with the positive projection of the moment and its inverse. Thus, in absence of an external magnetic field, this wave function allows a fast change in the orientation of the magnetic moment and, thus, magnetic blocking cannot be observed at practical temperatures or frequencies. Nevertheless, when a longitudinal external field is applied, the Zeeman effect overcomes this mixture and the pure M_J = +4 and M_J = –4 character are recovered, slowing down the magnetic relaxation and allowing the observation of an out-of-phase magnetic susceptibility signal (with a levelling below 3 K for the higher frequencies). For the erbium derivative (**3.4**), the wave function of the calculated ground state appears to be M_J = 78 % |±1/2> + 12 % |±13/2> with two very near states above it (at about 1.6 cm^{-1} and 3.7 cm^{-1}). Those are described by M_J = 78 % |±15/2> and M_J = 74 % |±13/2> + 15 % |±15/2>, respectively. The low energy difference between the ground state and the first excited state (or even the second) is definitively below the precision of the theoretical method. In addition, thermal effects over the chemical structure can slightly affect the energy level description, becoming significant at this level of proximity of the energy levels. So, one can deduce, according to the experimental results, that one of the two Kramers doublets (either the one described by 78 % of |±15/2> or the one with M_J = 74 % |±13/2>) is the actual ground doublet. The proximity of a level with high M_J value (|±13/2>), very close to the ground state (dominated by M_J = |±1/2>), accounts in this case for the slow relaxation of the magnetization observed at low temperatures; still, since this high-M_J level is an excited state, that prevents the observation the superparamagnetic maximum in χ".

It is worth to compare the results of the particular lanthanoid ion placed in different POM ligands, which had been theoretically characterised previously with the same method used in the present system. For three Ho^{3+} POMs, the ground doublet is consistently characterised by a wave function with a high weight of M_J = ±4: with the calculated weights being 98 %, 86 % and 94 % for HoW_{10}, HoW_{22} and $HoMo_{16}$, respectively. From this, one would expect out-of-phase signal for all three cases, as indeed happens; moreover, one could expect that the SIM character is enhanced in the order HoW_{22} < $HoMo_{16}$ < HoW_{10}, whereas the actual experimental observation is $HoMo_{16}$ < HoW_{22} < HoW_{10} (no signal without applied field, signal but no maximum without applied field, maximum without applied field respectively). This unmatch points towards

limitations of the theory to make detailed dynamic predictions: there is probably a small uncertainty in the contributions of the calculated wave functions.

The Er^{3+} salt structure has been well determined for ErW_{10}, ErW_{22} and $ErMo_{16}$. Regarding to the lowest energy levels, we found a ground state characterised by $M_J = \pm 13/2$ in both heteroxopolytungstates and a first excited state dominated by $M_J = \pm 1/2$ (placed at ~16 cm^{-1} in ErW_{10} and 11 cm^{-1} in ErW_{22}). In contrast, the magnetic behavior is very different in the case of $ErMo_{16}$, where the ground doublet is dominated by $M_J = \pm 1/2$ (78 %) and the first excited state (located at about 18 cm^{-1}) presents 74 % of $M_J = \pm 15/2$. One could try to attribute the explanation of such a different behaviour to the slight differences in the first coordination sphere in these complexes. The interplanar distance, d_{pp}, was measured to be 2.46 Å in ErW_{10}, 2.48 Å in ErW_{22} and 2.55 Å in $ErMo_{16}$ (**3.4**). However, note that despite the different ground states, the low-energy magnetic energy level structures are essentially very similar: they are dominated by high-order crystal field parameters that result in the lowest and highest M_J doublets being close in energy ($M_J = \pm 1/2$ and $M_J = \pm 15/2$ or $M_J = \pm 13/2$ placed at less than 20 cm^{-1}) and very close to the ground state. In this situation, small changes in the coordination sphere can shift the relative positions of these doublets and have dramatic effects on the dynamic magnetic behavior at very low temperature, and this is precisely what happens here. This is a very different situation to that encountered in transition metal clusters, such as Mn_{12}, where the change from a low M_S ground state to a high M_S one requires a sign change in the second order parameter and, thus, important changes from the chemical point of view.

3.3. Conclusion

In the present work, we have used polyoxomolybdate ligands to prepare new SIMs exhibiting SMM properties, which can be modeled using an effective crystal field approach previously developed for this kind of ligands. The key novelty has been the unprecedented use of polyoxomolybdates instead of polyoxotungstates for obtaining SIMs. While the chemistry of polyoxomolybdates is more challenging, this result has opened the possibility of making these magnetic molecules soluble in organic solvents, thus facilitating their processing and incorporation into devices. This contrasts with the SIMs based on polyoxotungstate ligands, which are commonly only soluble in water. Last but not the least, the lower reduction potential of polyoxomolybdates may also be of

interest to incorporate delocalized electrons into the mixed-valence POM framework, thus increasing the interest of these magnetic molecules in spintronics.[46-49]

3.4. Experimental Section

3.4.1. General Methods and Materials

All reagents and solvents used are commercially available. Acetonitrile was freshly distilled before use. All lanthanoid salts were stored in a desiccator because they are hygroscopic. The precursor $[(n\text{-}C_4H_9)_4N]_4[\beta\text{-}Mo_8O_{26}]$ was prepared according to the procedure described in the literature[50] and identified by FT-IR spectroscopy and electron microscope analysis.

3.4.2. Synthesis

The synthesis of $[(n\text{-}C_4H_9)_4N]_5[Ln(\beta\text{-}Mo_8O_{26})_2]$, with Ln^{3+} = Tb (**3.1**), Dy (**3.2**), Ho (**3.3**), Er (**3.4**), Tm (**3.5**) and Yb (**3.6**) was carried out using a procedure previously used for the La derivative, but with some modifications:[41] a solution of $Ln(NO_3)_3{\cdot}6H_2O$ (0.186 mmol) in 5mL of acetonitrile was added dropwise to a solution of $[(n\text{-}C_4H_9)_4N]_4[\beta\text{-}Mo_8O_{26}]$ (0.809 g, 0.376 mmol) in 25 mL of acetonitrile under stirring. The resulting solution was stirred for 30 min and then 50 mL diethyl ether was added carefully to make a second layer and allowed to stand at room temperature in a closed container. After three days, colourless (for **3.1**, **3.2**, **3.5** and **3.6**) or pink (for **3.3** and **3.4**) block-shaped crystals formed which were collected by filtration and washed with a few drops of acetonitrile and dried under vacuum overnight to obtain analytically pure compounds. Yields (based on lanthanoid): 0.487 g, 65.7 % (for **3.1**); 0.453 g, 59.8 % (for **3.2**); 0.513 g, 67.7 % (for **3.3**); 0.492 g, 64.9 % (for **3.4**), 0.437 g, 57.6 % (for **3.5**) and 0.465 g, 61.2 % (for **3.6**).

Anal. Calcd for $C_{80}H_{180}N_5TbMo_{16}O_{52}$ (**3.1**): C, 25.70; H, 4.85; N, 1.87. Found: C, 25.05; H, 5.11; N, 1.82. The Tb : Mo ratio obtained by SEM-EDX is in agreement with the formula of **1** obtained from the structure refinement (Tb : Mo ratio found: 8.85:91.15, calcd: 9.21:90.79). Anal. Calcd for $C_{80}H_{180}N_5DyMo_{16}O_{52}$ (**3.2**): C, 25.68; H, 4.85; N, 1.87. Found: C, 25.14; H, 4.91; N, 2.00; Dy : Mo ratio found: 9.40:90.60, calcd: 9.47:90.53. Anal. Calcd for $C_{80}H_{180}N_5HoMo_{16}O_{52}$ (**3.3**): C, 25.66; H, 4.86; N, 1.87; Found: C, 24.95; H, 4.87; N, 1.90. Ho : Mo ratio found: 10.58:89.42, calcd: 9.53:90.47. Anal. Calcd for

$C_{80}H_{180}N_5ErMo_{16}O_{52}$ (**3.4**): C, 25.65; H, 4.84; N, 1.87. Found: C, 25.30; H, 4.98; N, 1.88. Er : Mo ratio found: 9.90:90.10, calcd: 9.58:90.42. Anal. Calcd for $C_{80}H_{180}N_5TmMo_{16}O_{52}$ (**3.5**): C, 25.64; H, 4.84; N, 1.87. Found: C, 25.96; H, 5.04; N, 1.85. Tm: Mo ratio found: 10.94:89.06, calcd: 9.73:90.27. Anal. Calcd for $C_{80}H_{180}N_5YbMo_{16}O_{52}$ (**3.6**): C, 25.61; H, 4.84; N, 1.87. Found: C, 24.72; H, 4.89; N, 1.85. Yb : Mo ratio found: 9.63:90.37, calcd: 9.99:90.01.

FT-IR data of compounds **3.1**-**3.6** are shown in **Fig. 3.11**. (**3.1**) in cm^{-1} (KBr pellet, 1700 - 400 cm^{-1}): 975(s), 954(s), 932(s), 920(s), 877(sh), 861(s), 798(s), 751(sh), 705(s), 672(sh), 638(s), 589(w), 553(s), 523(s), 481(s), 452(w), 420(s). (**3.2**): 975(s), 955(s), 932(s), 920(s), 877(sh), 861(s), 798(s), 752(sh), 706(s), 672(sh), 637(s), 589(w), 553(s), 523(s), 481(s), 452(w), 421(s). (**3.3**): 975(s), 955(s), 932(s), 920(s), 878(sh), 862(s), 798(s), 752(sh), 706(s), 672(sh), 637(s), 587(w), 553(s), 526(s), 483(s), 451(w), 421(s). (**3.4**): 975(s), 955(s), 932(s), 920(s), 878(sh), 862(s), 798(s), 752(sh), 705(s), 672(sh), 637(s), 587(w), 553(s), 526(s), 483(s), 452(w), 421(s). (**3.5**): 975(s), 955(s), 932(s), 920(s), 878(sh), 862(s), 798(s), 752(sh), 705(s), 672(sh), 637(s), 588(w), 553(s), 526(s), 483(s), 452(w), 420(s). (**3.6**): 975(s), 955(s), 932(s), 920(s), 878(sh), 862(s), 798(s), 752(sh), 705(s), 672(sh), 636(s), 589(w), 552(s), 527(s), 483(s), 451(w), 421(s).

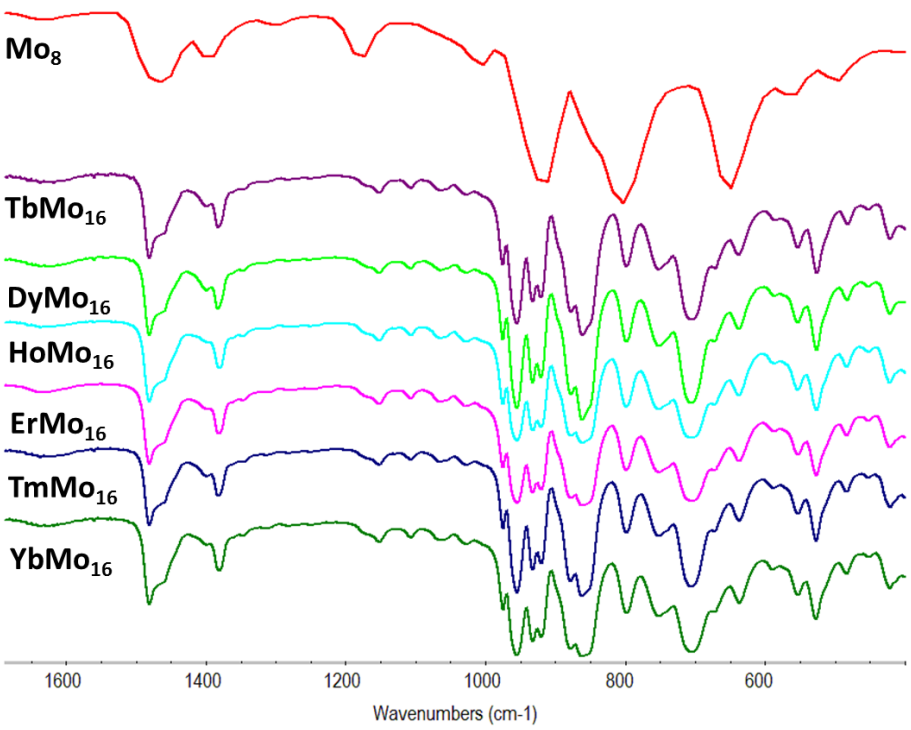

Fig. 3.11.- FT-IR spectra of the precursor $TBA_4[\beta\text{-}Mo_8O_{26}]$ (**Mo_8**) and the family $[Ln(\beta\text{-}Mo_8O_{26})_2]^{5-}$ (**$LnMo_{16}$**) where Ln^{III} = Tb, Dy, Ho, Er, Tm and Yb in the range of 1700-400 cm^{-1}.

3.4.3. X-ray Crystallography

Crystals of **3.1**-**3.6** are extremely efflorescent and solvent loss occurs immediately after they are separated from their mother solutions. Therefore, although the crystals were quickly covered with Paratone-N oil and placed in a stream of cooled nitrogen (120 K), some partial loss of solvent from the crystal could not be avoided. This fact causes the lowering in the quality of the single crystals as well as the large disorder in some of the organic cations present in the crystals (see below). A Nonius-Kappa CCD single-crystal diffractometer equipped with graphite-monochromated Mo Kα radiation (λ = 0.71073 Å) was used for data collection. The CrysAlis software package[51] was used for data collection routines, unit cell refinements, and data processing. Structure solution and refinement were carried out using SHELXS-97 and SHELXL-97.[52] The asymmetric units of **3.1**-**3.6** contain one complete POM anion (see **Fig. 3.12**) and five tetrabutylammonium (TBA^+) cations.

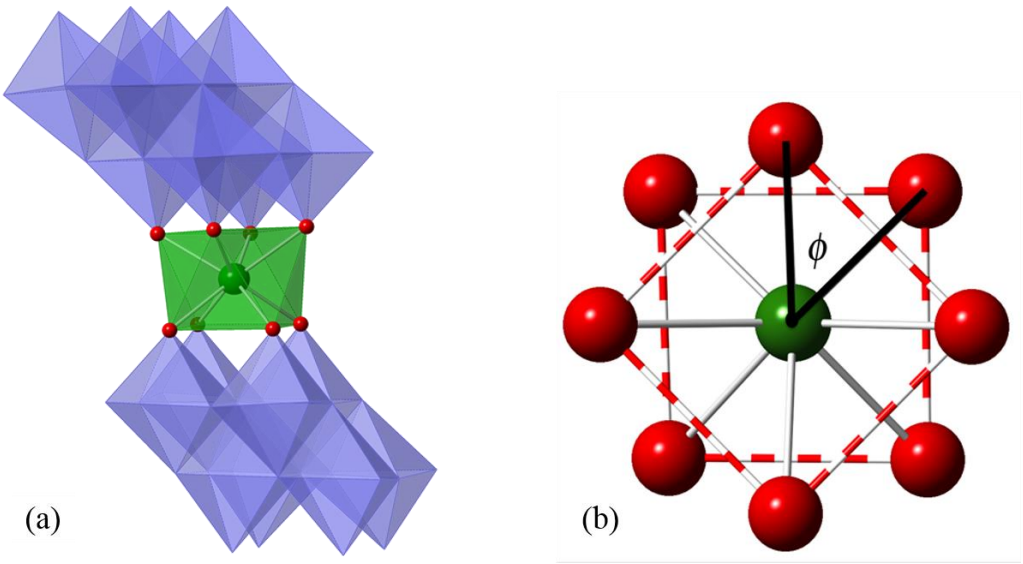

Fig. 3.12.- (a) Polyhedral and ball-and-stick representation of $LnMo_{16}$ series and (b) projection of the coordination sphere showing the square-antiprismatic coordination site. Green sphere, lanthanoid atom; red sphere, O atom; blue octahedra, {MoO_6}.

The structure solution reveals that some TBA^+ cations are extremely disordered, exhibiting unusually high isotropic thermal parameters. This fact was attributed to thermal libration caused by the loss of solvent molecules from the crystal, which creates voids in the surroundings of these TBA^+ cations. Attempts of modelling this disorder using the facilities included in SHELXL-97 (PART, DELU and SIMU instructions) did not result in lower thermal parameters and even gave rise to unstable refinements in some

cases. Therefore, only a small fraction of the disorder found in the butyl chains of the cations was modeled using the PART instructions. In particular, in all the crystal structures one of the five TBA^+ cations (labeled TBA5) was found to be so disordered that some of the isotropic thermal parameters of the carbon atoms could not be refined and had to be fixed to avoid their blowing up. In addition, in structure **3.4** some carbon atoms of this TBA^+ cation could be found in difference maps and, then, the whole cation was removed from the experimental structure factors and modeled using the SQUEEZE procedure.[53] Some acetonitrile molecules were also found in difference maps exhibiting large disorder and very high isotropic thermal factors. As they could not be modeled satisfactorily using atomic sites, they were removed from the atomic list and their diffuse contribution was also treated with the SQUEEZE program. This procedure gave void volumes and electron numbers per unit cell, which correspond quite reasonably to 8 acetonitrile molecules per formula in compounds **3.2**-**3.6**, and 6 acetonitrile molecules in compound **3.1**. All molybdenum and oxygen atoms were refined anisotropically in all six structures, while some TBA cations were left isotropic. Hydrogen atoms on carbon atoms were included at calculated positions and refined with a riding model. Multi-scan or analytical numeric absorption corrections were applied to the data of **3.1**-**3.6** using the software integrated in the program CrysAlis.[51] The cif files of all the structures have been deposited and the corresponding CCDC reference numbers for compounds **3.1**-**3.6** are 1446092–1446097. Crystallographic parameters for **3.1**-**3.6** are summarized in **Table 3.5**.

3.4.4. Magnetic measurements

Magnetic static and dynamic measurements of compounds **3.1**-**3.6** ($LnMo_{16}$) were performed by compacted powder molded from ground crystalline samples. Variable-temperature susceptibility measurements were carried out under a magnetic field of 1000 Oe in the temperature range 2–300 K on a magnetometer equipped with a SQUID sensor (Quantum Design MPMS-XL-5). The data were corrected for diamagnetic contribution from eicosane and for the diamagnetic contributions of the polyanions as deduced by using the Pascal's constant tables. Isothermal magnetization measurements at low temperature (2 K) were performed up to a field of 5 T in the same apparatus.

3.4.5. Ligand field calculations

The four magnetic susceptibility data of the polyanions **3.1**-**3.4** were used to carry out a simultaneous fit of an effective ligand field Hamiltonian. This was based on the Radial Effective Charge (REC) model, which uses effective point charges to model the ligand effects and thus estimate the crystal field parameters in mononuclear lanthanoid complexes.[54] For this purpose, the SIMPRE package was employed, which is a freely available fortran77 code.[55-56] This procedure provided the two parameters, namely the radial displacement and the effective charge, that can be used to describe the ligand field effects of the eight chemically equivalent oxygen atoms of the polyoxomolybdate ligands. As verification, the magnetic susceptibility of the two remaining members of the series (Tm^{3+} and Yb^{3+}) was predicted using the same parameters.

Table 3.5.- Crystallographic Data and Structure Refinement for compounds **$LnMo_{16}$**, where Ln^{3+} = Tb, Dy, Ho, Er, Tm and Yb.

Compound	**$TbMo_{16}$**	**$DyMo_{16}$**	**$HoMo_{16}$**	**$ErMo_{16}$**	**$TmMo_{16}$**	**$YbMo_{16}$**
empirical formula	$C_{92}H_{198}TbMo_{16}N_{11}O_{52}$	$C_{96}H_{204}DyMo_{16}N_{13}O_{52}$	$C_{96}H_{204}HoMo_{16}N_{13}O_{52}$	$C_{96}H_{204}ErMo_{16}N_{13}O_{52}$	$C_{96}H_{204}TmMo_{16}N_{13}O_{52}$	$C_{96}H_{204}YbMo_{16}N_{13}O_{52}$
formula weight	3984.57	4070.26	4072.69	4075.02	4076.69	4080.8
T/K	120(2)	120(2)	120(2)	120(2)	120(2)	120(2)
λ/Å	0.71073	0.71073	0.71073	0.71073	0.71073	0.71073
crystal system	monoclinic	orthorhombic	orthorhombic	orthorhombic	orthorhombic	orthorhombic
space group	$P2_1/c$	*Pcab*	*Pcab*	*Pcab*	*Pcab*	*Pcab*
a/Å	25.0421(7)	17.7626(4)	17.88390(15)	17.8110(3)	17.8375(2)	17.8722(3)
b/Å	17.1885(5)	32.9141(8)	32.8402(2)	33.1580(5)	32.8499(4)	32.7932(5)
c/Å	31.9702(9)	47.7196(12)	47.8961(4)	48.1554(8)	47.7986(8)	47.8651(7)
α/°	90	90	90	90	90	90
β/°	91.419(2)	90	90	90	90	90
γ/°	90	90	90	90	90	90
V/Å^3	13756.9(7)	27898.8(12)	28129.9(4)	28439.5(8)	28008.1(7)	28053.1(8)
Z	4	8	8	8	8	8
ρ_{calcd}/g cm^{-3}	1.924	1.938	1.923	1.903	1.934	1.932
μ/mm^{-1}	1.991	1.995	2.010	2.022	2.087	2.118
$R[F_o^2 > 2\sigma(F_o^2)]^a$	0.1205	0.1430	0.0904	0.0958	0.1116	0.1134
$R_w[F_o^2 > 2\sigma(F_o^2)]^b$	0.3127[c]	0.3186[d]	0.1803[e]	0.2688[f]	0.2275[g]	0.2363[h]

[a] $R = \Sigma(||F_o| - |F_c||)/\Sigma|F_o|$. [b] $R_w = \{\Sigma[w(F_o^2 - F_c^2)^2]/\Sigma[w(F_o^2)^2]\}^{1/2}$. $w = 1/[\sigma^2(F_o^2) + (AP)^2 + BP]$, where $P = (F_o^2 + 2F_c^2)/3$. [c] $A = 0.1438$, $B = 325.6534$. [d] $A = 0.0909$, $B = 1310.5703$. [e] A = 0.0001, B = 744.4572. [f] $A = 0.1720$, $B = 0.0000$. [g] $A = 0.0171$, $B = 1232.7322$. [h] $A = 0.0218$, $B = 1325.6974$.

3.5. References

[1] S. A. Wolf, D. D. Awschalom, R. A. Buhrman, J. M. Daughton, S. von Molnar, M. L. Roukes, A. Y. Chtchelkanova and D. M. Treger, *Science*, 2001, **294**, 1488-1495.

[2] M. E. Flatte, *Nature*, 2009, **462**, 419-420.

[3] J. Akerman, *Science*, 2005, **308**, 508-510.

[4] I. L. Prejbeanu, M. Kerekes, R. C. Sousa, H. Sibuet, O. Redon, B. Dieny and J. P. Nozieres, *J. Phys. Condens. Matter.*, 2007, **19**, 165218.

[5] J. D. Teufel, J. W. Harlow, C. A. Regal and K. W. Lehnert, *Phys. Rev. Lett.*, 2008, **101**, 197203.

[6] J. R. Petta, A. C. Johnson, J. M. Taylor, E. A. Laird, A. Yacoby, M. D. Lukin, C. M. Marcus, M. P. Hanson and A. C. Gossard, *Science*, 2005, **309**, 2180-2184.

[7] J. F. Gregg, *Nat. Mater.*, 2007, **6**, 798-799.

[8] K. L. Wang, I. Ovchinnikov, F. Xiu, A. Khitun and M. Bao, *J. Nanosci. Nanotechnol.*, 2011, **11**, 306-313.

[9] A. R. Rocha, V. M. García-Suárez, S. W. Bailey, C. J. Lambert, J. Ferrer and S. Sanvito, *Nat. Mater.*, 2005, **4**, 335-339.

[10] S. Sanvito, *Nat. Phys.*, 2010, **6**, 562-564.

[11] J. Camarero and E. Coronado, *J. Mater. Chem.*, 2009, **19**, 1678-1684.

[12] F. Prins, M. Monrabal-Capilla, E. A. Osorio, E. Coronado and H. S. J. van der Zant, *Adv Mater.*, 2011, **23**, 1545-1549.

[13] J. Dugay, M. Giménez-Marqués, T. Kozlova, H. W. Zandbergen, E. Coronado and H. S. J. van der Zant, *Adv Mater.*, 2015, **27**, 1288-1293.

[14] A. Holovchenko, J. Dugay, M. Giménez-Marqués, R. Torres-Cavanillas, E. Coronado and H. S. J. van der Zant, *Adv Mater.*, 2016, **28**, 7228-7233.

[15] R. Sessoli, H. L. Tsai, A. R. Schake, S. Wang, J. B. Vincent, K. Folting, D. Gatteschi, G. Christou and D. N. Hendrickson, *J. Am. Chem. Soc.*, 1993, **115**, 1804-1816.

[16] L. Bogani and W. Wernsdorfer, *Nat. Mater.*, 2008, **7**, 179-186.

[17] W. Wernsdorfer, *International Journal of Nanotechnology*, 2010, **7**, 497-522.

[18] E. Cremades, C. D. Pemmaraju, S. Sanvito and E. Ruiz, *Nanoscale*, 2013, **5**, 4751-4757.

[19] L. Thomas, F. Lionti, R. Ballou, D. Gatteschi, R. Sessoli and B. Barbara, *Nature*, 1996, **383**, 145-147.

[20] C. Paulsen, J. G. Park, B. Barbara, R. Sessoli and A. Caneschi, *J Magn Magn Mater.*, 1995, **140**, 1891-1892.

[21] A. Ardavan and S. J. Blundell, *J. Mater. Chem.*, 2009, **19**, 1754-1760.

[22] F. Troiani and M. Affronte, *Chem. Soc. Rev.*, 2011, **40**, 3119-3129.

[23] P. C. E. Stamp and A. Gaita-Ariño, *J. Mater. Chem.*, 2009, **19**, 1718-1730.

[24] J. Lehmann, A. Gaita-Ariño, E. Coronado and D. Loss, *Nat. Nanotechnol.*, 2007, **2**, 312-317.

[25] D. N. Woodruff, R. E. P. Winpenny and R. A. Layfield, *Chem. Rev.*, 2013, **113**, 5110-5148.

[26] S. T. Liddle and J. van Slageren, *Chem. Soc. Rev.*, 2015, **44**, 6655-6669.

[27] N. Ishikawa, M. Sugita, T. Ishikawa, S. Koshihara and Y. Kaizu, *J. Am. Chem. Soc.*, 2003, **125**, 8694-8695.

[28] M. Urdampilleta, S. Klyatskaya, J.-P. Cleuziou, M. Ruben and W. Wernsdorfer, *Nat. Mater.*, 2011, **10**, 502-506.

[29] M. Urdampilleta, S. Klayatskaya, M. Ruben and W. Wernsdorfer, *Acs Nano.*, 2015, **9**, 4458-4464.

[30] S. Thiele, F. Balestro, R. Ballou, S. Klyatskaya, M. Ruben and W. Wernsdorfer, *Science*, 2014, **344**, 1135-1138.

[31] C. Wackerlin, F. Donati, A. Singha, R. Baltic, S. Rusponi, K. Diller, F. Patthey, M. Pivetta, Y. Lan, S. Klyatskaya, M. Ruben, H. Brune and J. Dreiser, *Adv. Mater.*, 2016, **28**, 5195-5199.

[32] A. Bedoya-Pinto, H. Prima-García, F. Casanova, E. Coronado and L. E. Hueso, *Adv. Electron. Mater.*, 2015, **1**, 1500065.
[33] J. J. Baldoví, S. Cardona-Serra, J. M. Clemente-Juan, L. Escalera-Moreno, A. Gaita-Ariño and G. Mínguez Espallargas, *Epl.*, 2015, **110**, 33001.
[34] J. M. Clemente-Juan, E. Coronado and A. Gaita-Ariño, *Chem. Soc. Rev.*, 2012, **41**, 7464-7478.
[35] M. Vonci and C. Boskovic, *Aust. J. Chem.*, 2014, **67**, 1542-1552.
[36] N. V. Izarova and P. Kögerler, *N. V. Izarova and P. Kögerler, Polyoxometalate-based single-molecule magnets, Trends in Polyoxometalates Research*, 2015.
[37] M. Shiddiq, D. Komijani, Y. Duan, A. Gaita-Ariño, E. Coronado and S. Hill, *Nature*, 2016, **531**, 348-351.
[38] J. J. Baldoví, S. Cardona-Serra, J. M. Clemente-Juan, E. Coronado, A. Gaita-Ariño and H. Prima-García, *Chem. Commun.*, 2013, **49**, 8922-8924.
[39] S. Cardona-Serra, J. M. Clemente-Juan, E. Coronado, A. Gaita-Ariño, A. Camón, M. Evangelisti, F. Luis, M. J. Martínez-Pérez and J. Sese, *J. Am. Chem. Soc.*, 2012, **134**, 14982-14990.
[40] S. Sherif, G. Rubio-Bollinger, E. Pinilla-Cienfuegos, E. Coronado, J. Carlos Cuevas and N. Agrait, *Nanotechnology*, 2015, **26**, 291001.
[41] A. Kitamura, T. Ozeki and A. Yagasaki, *Inorg. Chem.*, 1997, **36**, 4275-4279.
[42] M. A. AlDamen, J. M. Clemente-Juan, E. Coronado, C. Martí-Gastaldo and A. Gaita-Ariño, *J. Am. Chem. Soc.*, 2008, **130**, 8874-8875.
[43] M. A. AlDamen, S. Cardona-Serra, J. M. Clemente-Juan, E. Coronado, A. Gaita-Ariño, C. Martí-Gastaldo, F. Luis and O. Montero, *Inorg. Chem.*, 2009, **48**, 3467-347.
[44] J. J. Baldoví, J. M. Clemente-Juan, E. Coronado, Y. Duan, A. Gaita-Ariño and C. Giménez-Saiz, *Inorg. Chem.*, 2014, **53**, 9976-9980.
[45] C. Bustos, D. M. Carey, K. Boubekeur, R. Thouvenot, A. Proust and P. Gouzerh, *Inorg. Chim. Acta*, 2010, **363**, 4262-4268.
[46] S. Cardona-Serra, J. M. Clemente-Juan, A. Gaita-Ariño, N. Suaud, O. Svoboda and E. Coronado, *Chem. Commun.*, 2013, **49**, 9621-9623.
[47] S. Cardona-Serra, J. M. Clemente-Juan, E. Coronado, A. Gaita-Ariño, N. Suaud, O. Svoboda, R. Bastardis, N. Guihery and J. J. Palacios, *Chem. Eur. J.*, 2015, **21**, 763-769.
[48] C. Bosch-Serrano, J. M. Clemente-Juan, E. Coronado, A. Gaita-Ariño, A. Palii and B. Tsukerblat, *Chemphyschem*, 2012, **13**, 2662-2665.
[49] A. Palii, J. M. Clemente-Juan, B. Tsukerblat and E. Coronado, *Chem. Sci.*, 2014, **5**, 3598-3602.
[50] Alvin P. Ginsberg, *Inorganic Syntheses*, 1990, **27**, 80.
[51] Agilent Technologies UK Ltd, Oxford, UK, *CrysAlis PRO Software system*, 2013.
[52] G. M. Sheldrick, *Acta Cryst. A.*, 2008, **64**, 112-122.
[53] A. L. Spek, *Acta Crystallogr D Struct Biol.*, 2009, **65**, 148-155.
[54] J. J. Baldoví, J. J. Borrás-Almenar, J. M. Clemente-Juan, E. Coronado and A. Gaita-Ariño, *Dalton Trans.*, 2012, **41**, 13705-13710.
[55] J. J. Baldoví, S. Cardona-Serra, J. M. Clemente-Juan, E. Coronado, A. Gaita-Ariño and A. Palii, *J. Comput. Chem.*, 2013, **34**, 1961-1967.
[56] J. J. Baldoví, J. M. Clemente-Juan, E. Coronado, A. Gaita-Ariño and A. Palii, *J. Comput. Chem.*, 2014, **35**, 1930-1934.
[57] M. D. Jenkins, Y. Duan, B. Diosdado, J. J. García-Ripoll, A. Gaita-Ariño, C. Giménez-Saiz, P. J. Alonso, E. Coronado, and F. Luis, *Phys. Rev.*, 2017, **B 95**, 064423.

Chapter 4. A Photo-Responsive Fe-POM

In this chapter, we will describe the synthesis and characterisation of a new photo-responsive molecular polyanion with the formula $\{K\subset[(A\text{-}\alpha\text{-}PW_9O_{34})_2Fe_2(C_2O_4)_2]\}^{15-}$ (**4.1**) in which two Fe(III) ions are simultaneously coordinated by two A-α-$[PW_9O_{34}]^{9-}$ POM units and two oxalato ligands. When irradiated with UV light, its potassium salt, $K_{15}\{K\subset[(A\text{-}\alpha\text{-}PW_9O_{34})_2Fe_2(C_2O_4)_2]\}\cdot 29H_2O$ (**Q-4.1**), exhibits a remarkable photocolouration effect, attributable to the partial reduction of the POM to give rise to a mixed-valence species. The photo-induced process is intramolecular and involves an electron transfer from the oxalato ligands, which partially decompose releasing CO_2, towards the Fe(III) and the POM. This mechanism has been confirmed by DRS, IR, XPS, Mössbauer spectroscopies, magnetism and elemental analysis. An analogous derivative of **Q-4.1** with formula $K_{15}\{K\subset[(A\text{-}\alpha\text{-}PW_9O_{34})_2Fe_2(C_3H_2O_4)_2]\}\cdot 27H_2O$ (**Q-4.2**) containing malonato ligands does not exhibit such a photoactive behaviour, evidencing that the oxalate ligand is essential for the photoactivity of **4.1**. To our knowledge, **4.1** represents the first POM-based compound in which the photocolouration effect does not require the presence of intermolecular short interactions.

4. Light-induced decarboxylation in a photo-responsive iron-containing complex based on polyoxometalate and oxalato ligands

4.1. Introduction

The study of molecule-based materials whose physical or chemical properties can be tuned by applying external stimuli is attracting considerable interest in chemistry owing to the wide variety of functional materials one can design.[1] As external stimulus, light has been extensively used in this context. Thus, many examples of photo-magnetic materials,[2] photo-chromic materials,[3] and electro-chromic materials[4] have been reported.

As we know, POMs have the ability to accept, step by step, one or more electrons giving rise to mixed-valence coloured species (heteropolyblues or heteropolybrowns).[5] POMs are being increasingly used as building blocks for the construction of systems with stimuli-responsive behaviour (in particular photo-responsive).[6] The common strategy consists in the combination of POMs with photo-sensitive groups in order to integrate the smart response in hybrid systems by means of electrostatic interactions, H-bonding or other intermolecular interactions. Recent examples include photo-responsive systems obtained by combining POM anions with azobenzene-modified cationic surfactants, which can reversibly assemble and disassemble in solution with light irradiation[6c] or supramolecular systems, obtained by using ionic liquids H-bonded to the surface of fluorescent POMs, which exhibit tunable photoluminescence properties by adjusting the pH of the solution.[6g]

Regarding the solid-state, photochromic materials with strong UV-induced colour changes and remarkable colouration contrast can be obtained associating POM anions with organic cations (mainly organoammonium cations (OACs)).[6a,6b,7] For example, in 2007, Jobic *et al.*[6b] reported an organic-inorganic hybrid molybdenum(VI)-containing compound with the formula $(H_2DABCO)_2(NH_4)_2[Mo_8O_{27}]\cdot 4H_2O$ (DABCO = 1,4-diazabicyclo[2.2.2]octane) (see **Fig. 4.1a**), which shows colour change from pale yellow to purple under UV illumination.

The photoactivity in such systems has been described in terms of a UV-induced photoreduction of the POM, concomitant with an intermolecular electron transfer assisted by proton transfer from the OAC towards the POM (**Scheme 4.1**). The effect is reversible in contact with air due to oxidation:

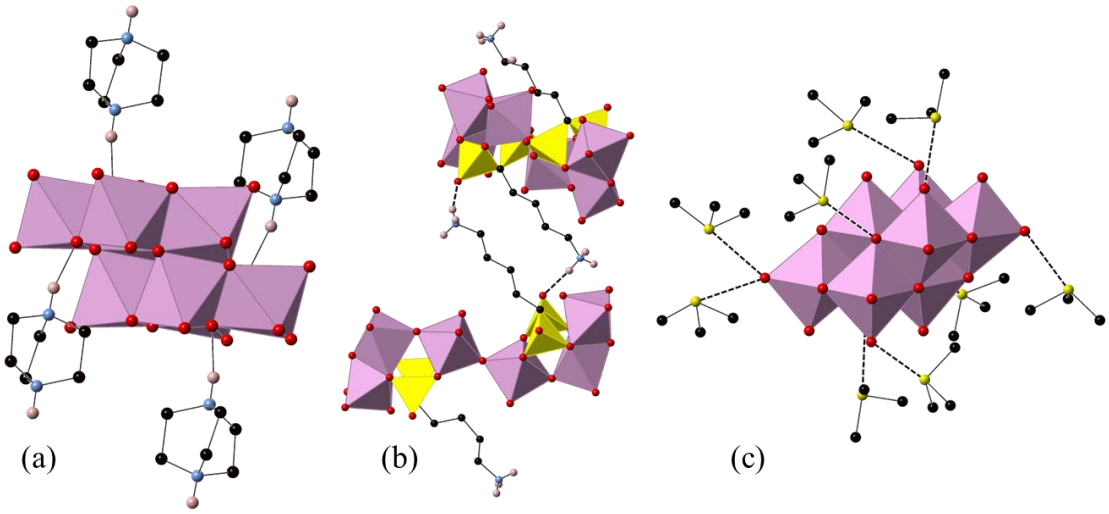

Fig. 4.1.- Combined polyhedral and ball-and-stick representations of organic-inorganic hybrid photo-responsive POM systems: (a) $(H_2DABCO)_2(NH_4)_2[Mo_8O_{27}]\cdot 4H_2O$; (b) $Na_2Rb_6[(Mo_3O_8)_4(O_3PC(C_4H_8NH_3)(O)PO_3)_4]\cdot 23H_2O$ and (c) $(Me_3S)_4[Mo_8O_{26}]$. Water molecules, counter ions and all C-bound H atoms have been omitted for clarity. Pink octahedra, $[MoO_6]$; yellow tetrahedra, $[PO_4]$; yellow sphere, S; blue sphere, N; black spheres, C; red spheres, O; pink sphere, H.

According to this mechanism, the photoactivity in these systems requires the formation of direct H-bonds between POMs and OACs, something that cannot be systematically achieved.[8] A way to improve the possibility of H-bond formation has been developed by P. Mialane, R. Dessapt *et al.*, consisting in directly grafting OAC-functionalized bisphosphonate ligands to the inorganic core of POMs.[6d] One example of such compounds with the formula $Na_2Rb_6[(Mo_3O_8)_4(O_3PC(C_4H_8NH_3)(O)PO_3)_4]\cdot 23H_2O$ is shown in **Fig. 4.1b**.

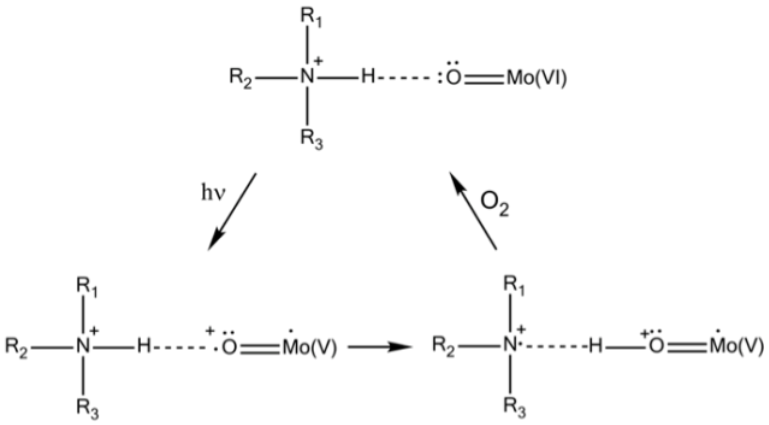

Scheme 4.1

The same researchers have also proposed a new class of solid-state photochromic hybrids combining sulfonium cations with POMs and, so, circumventing the dependence

on an H-bonding network.[6e] One example of sulfonium-POM assemblies with the formula $(Me_3S)_4[Mo_8O_{26}]$ which shown efficient solid-state photochromism in ambient conditions is shown in **Fig. 4.1c**. In this case, the mechanism of the photochromic effect requires the establishment of short S···O contacts to allow the UV-induced electron transfer from the sulfonium cations to the adjacent POM (**Scheme 4.2**). As before, slow bleaching happens in contact with air:

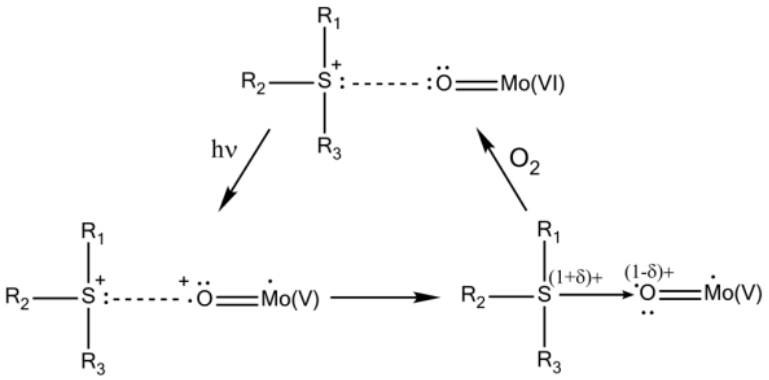

Scheme 4.2

On the other hand, some Fe(III) carboxylate complexes exhibit sensitivity to visible and UV light, which makes them photo-reactive through ligand to metal charge transfer (LMCT) reactions and, therefore, valuable in chemistry of environmental systems[9] and for laboratory photochemical applications in general (e.g. in actinometry).[10] A prototypical example of such complexes is the tris(oxalato)ferrate(III) complex whose photo-induced LMCT reaction (reaction **1**) gives rise to the (photo)generation of Fe(II) ions (both, in solution and in the solid-state), and to a subsequent reductive reaction via $CO_2^{\bullet-}$ radical anions (reaction **3**).[11]

$$[Fe^{III}(C_2O_4)_3]^{3-} + h\nu \rightarrow Fe^{2+} + C_2O_4^{\bullet-} + 2(C_2O_4)^{2-} \quad (\mathbf{1})$$

$$C_2O_4^{\bullet-} \rightarrow CO_2 + CO_2^{\bullet-} \quad (\mathbf{2})$$

$$[Fe^{III}(C_2O_4)_3]^{3-} + CO_2^{\bullet-} \rightarrow Fe^{2+} + 3(C_2O_4)^{2-} + CO_2 \quad (\mathbf{3})$$

In this context, we are going to explore the possibility of combining Fe(III) carboxylate complexes with POMs in the same molecular unit with the aim of obtaining a new type of photoactive solid-state systems which would be independent of the establishment of any kind of inter- or intramolecular short interactions (*i.e.*, H-bonds or S···O contacts). Therefore, our objective is to obtain a heteroleptic Fe(III) complex in which both, carboxylate and POM, act as ligands.

However, the only reported examples of Fe(III) complexes containing both, oxalato and POM ligands are represented by the family $[Fe_4(C_2O_4)_4(H_2O)_2(B\text{-}\beta\text{-}XW_9O_{33})_2]^{14-}$ (X = As^{III}, Sb^{III}, Bi^{III}), in which no photoactivity has been reported.[12] Here, we will describe the synthesis and characterisation (X-ray crystal structure, diffuse reflectance, IR evolution upon irradiation, UV in aqueous solution, XPS, Mössbauer spectroscopy, and magnetic properties) of a novel mixed ferrioxalate-POM compound formulated as $K_{15}\{K\subset[(A\text{-}\alpha\text{-}PW_9O_{34})_2Fe_2(C_2O_4)_2]\}\cdot 29H_2O$ (**Q-4.1**) exhibiting fast and evident photocolouration when exposed to direct sunlight or UV irradiation in the solid state. For comparison, we also report the analogous malonate derivative, $K_{15}\{K\subset[(A\text{-}\alpha\text{-}PW_9O_{34})_2Fe_2(C_3H_2O_4)_2]\}\cdot 27H_2O$ (**Q-4.2**), which does not exhibit such a photoactive behaviour, evidencing that the oxalate ligand is essential for the photoactivity of **4.1**. We will demonstrate that the photocolouration process involves a simultaneous intramolecular electron transfer from the oxalato ligand to the Fe(III) (leading to Fe(II)) and to the POM framework (leading to a reduced mixed-valence species containing W(V)). Such a process is accompanied by a release of CO_2.

4.2. Results and discussion

4.2.1. Synthetic approach

Reaction of the potassium salts of $[Fe(C_2O_4)_3]^{3-}$ or $[Fe(C_3H_2O_4)_3]^{3-}$ with the trivacant ligand A-α-$[PW_9O_{34}]^{9-}$ in aqueous solution at 60 °C results in the crystallization of the sandwich-type molecular complexes **4.1** and **4.2** which contain two iron atoms, each one coordinated by one oxalato ligand in **4.1** (or malonato for **4.2**) and two A-α-$[PW_9O_{34}]^{9-}$ moieties. The formation of **4.1** and **4.2** takes place owing to the lability of the tris(oxalato) and tris(malonato)ferrate(III) complexes, which quickly and readily exchange two dicarboxylate ligands by two A-α-$[PW_9O_{34}]^{9-}$ moieties (substitution of the three dicarboxylate ligands is not possible due to the steric effect imposed by the bulky A-α-$[PW_9O_{34}]^{9-}$ anion). The reaction can be represented as follows {L = $(C_2O_4)^{2-}$ for **4.1** and $(C_3H_2O_4)^{2-}$ for **4.2**}:

$$K^+(aq) + 2\ A\text{-}\alpha\text{-}[PW_9O_{34}]^{9-} + 2\ [Fe(L)_3]^{3-} \rightarrow$$
$$\{K\subset[(A\text{-}\alpha\text{-}PW_9O_{34})_2Fe_2(L)_2]\}^{15-} + 4\ (L)^{2-}(aq)$$

This is consistent with the impossibility to obtain analogous POMs containing Cr or Ru using the same reaction conditions as for **4.1**, *i.e.* using the more kinetically inert tris(oxalato)chromate(III) or tris(oxalato)ruthenate(III) complexes. On the other hand, reaction of A-α-$[PW_9O_{34}]^{9-}$ with the kinetically labile $[Co(C_2O_4)_3]^{3-}$ or $[Mn(C_2O_4)_3]^{3-}$ do not give the analogous POMs of **4.1** containing Co(III) or Mn(III) due to their strong oxidizing character in aqueous solution.

The crystal structures of **4.1** and **4.2** (see below) have revealed that both POMs enclose a potassium ion in their internal cavity. It seems that K^+ ions act as templates for the assembly of two A-α-$[PW_9O_{34}]^{9-}$ and two $Fe(C_2O_4)^+$ (or $Fe(C_3H_2O_4)^+$) moieties to form **4.1** and **4.2**. We have attempted unsuccessfully to enclose other alkaline ions (Na^+, for example) in the central cavity of these POMs. Hence, the presence of K^+ ions in the reaction medium seems to be essential for the formation of **4.1** and **4.2**. This is attributed to the rigidity of the POM, which has a cavity size only suitable to accommodate potassium.

4.2.2. Crystal Structures

The X-ray structures of **4.1** and **4.2** reveal that both POMs contain two A-α-$[PW_9O_{34}]^{9-}$ moieties, two iron ions, two oxalato (for **4.1**) or malonato (for **4.2**) ligands and one potassium cation encapsulated in the central cavity of each POM (**Fig. 4.2** and **Fig. 4.3**). The two iron ions are sandwiched between the trivacant A-α-$[PW_9O_{34}]^{9-}$ anions in such a way that each iron atom is coordinated by two oxygen atoms from two-edge sharing tungsten atoms of each trivacant unit, while the two remaining coordination sites are occupied by one chelating oxalato or malonato ligand (**Fig. 4.2** and **Fig. 4.3**). The packing arrangements of **4.1** along *a*-, *b*- and *c*- axis are shown in **Fig. 4.4**.

There are many reported examples of sandwich POMs trapping two or more metal ions between two A-α-$[PW_9O_{34}]^{9-}$ ligands.[24] However, regarding first row 3*d*-transition metals, the most representative series is $[(A\text{-}\alpha\text{-}PW_9O_{34})_2(M(H_2O)_2)_3]^{n-}$ (M^{II} = Mn, Fe, Co, Ni, Cu, Zn, and M^{III} = Fe).[24a-c] The reason why **4.1** and **4.2** enclose only two iron atoms and not more lies in the presence of the chelating oxalato or malonato ligands, which occupy two *cis* positions in the octahedral coordination sphere of the metal ions. This fact forces the two A-α-$[PW_9O_{34}]^{9-}$ units to be slightly side-slipped in order to occupy the

other four positions of the octahedral coordination spheres of the iron ions (**Fig. 4.5**), giving as a result the impossibility to sandwich a third iron ion. In the previously reported POM compounds enclosing three octahedrally-coordinated 3*d* transition metal ions, the absence of a chelating ligand (other than A-α-$[PW_9O_{34}]^{9-}$) allowed the two trivacant units to be placed directly over each other, leaving the remaining *trans* coordination positions to be occupied by non-chelating ligands.

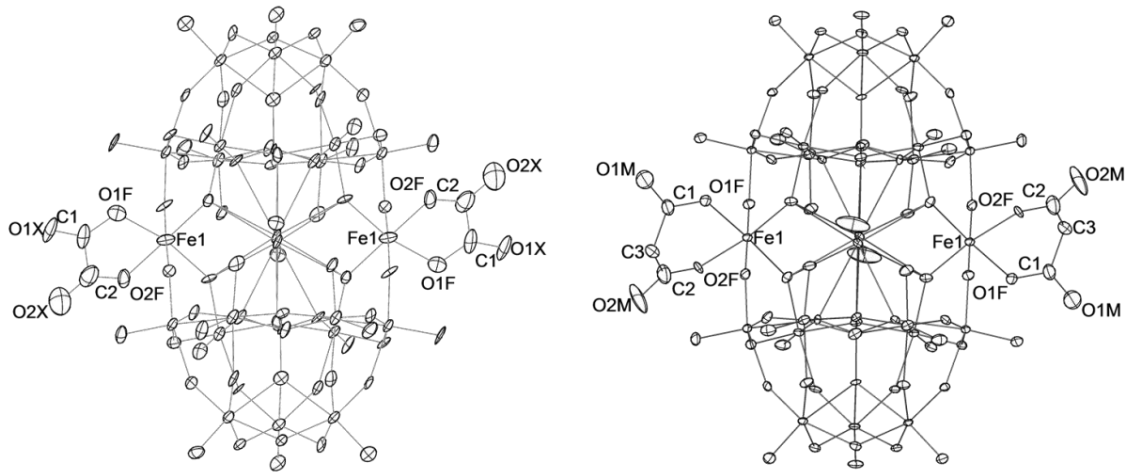

Fig. 4.2.- Anisotropic ellipsoid representations of **4.1** (left) and **4.2** (right) together with some of the atom labelling scheme, showing the disorder of the encapsulated potassium ion in the central cavity of the POMs. The ellipsoids are drawn at 50 % probability level, and hydrogen atoms have been omitted for clarity.

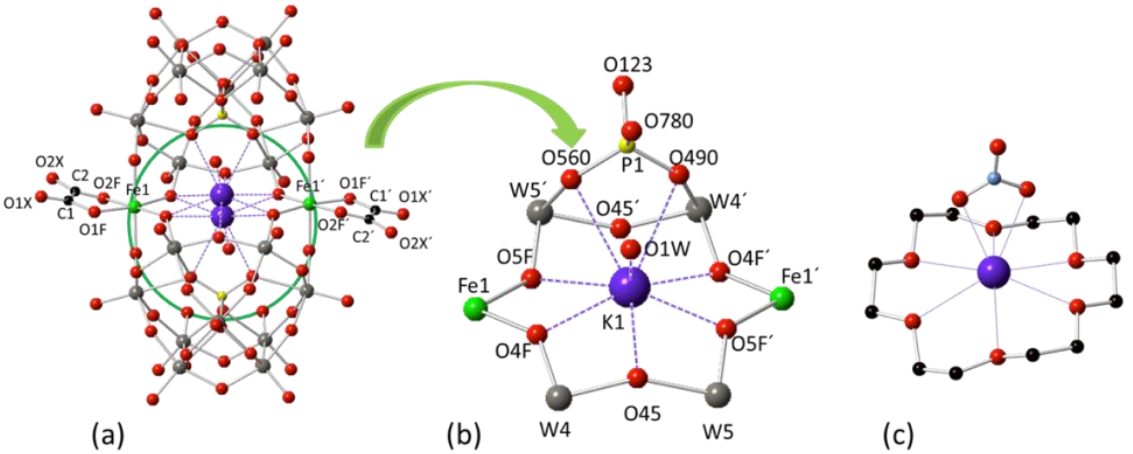

Fig. 4.3.- (a) Ball and stick representation of **4.1**, showing the disorder of the encapsulated potassium ion in the central cavity of the POM. (b) Detailed view of the coordination of the encapsulated potassium ion (the disorder is not shown). (c) Ball and stick representation showing the coordination of potassium by 18-crown-6 and nitrate in $[K\subset(18\text{-crown-6})](NO_3)(HNO_3)$.[23] The colour code of the spheres is as follows: W (grey), Fe (green), K (violet), P (yellow), O (red) and C (black). K···O coordination contacts are shown as dotted lines.

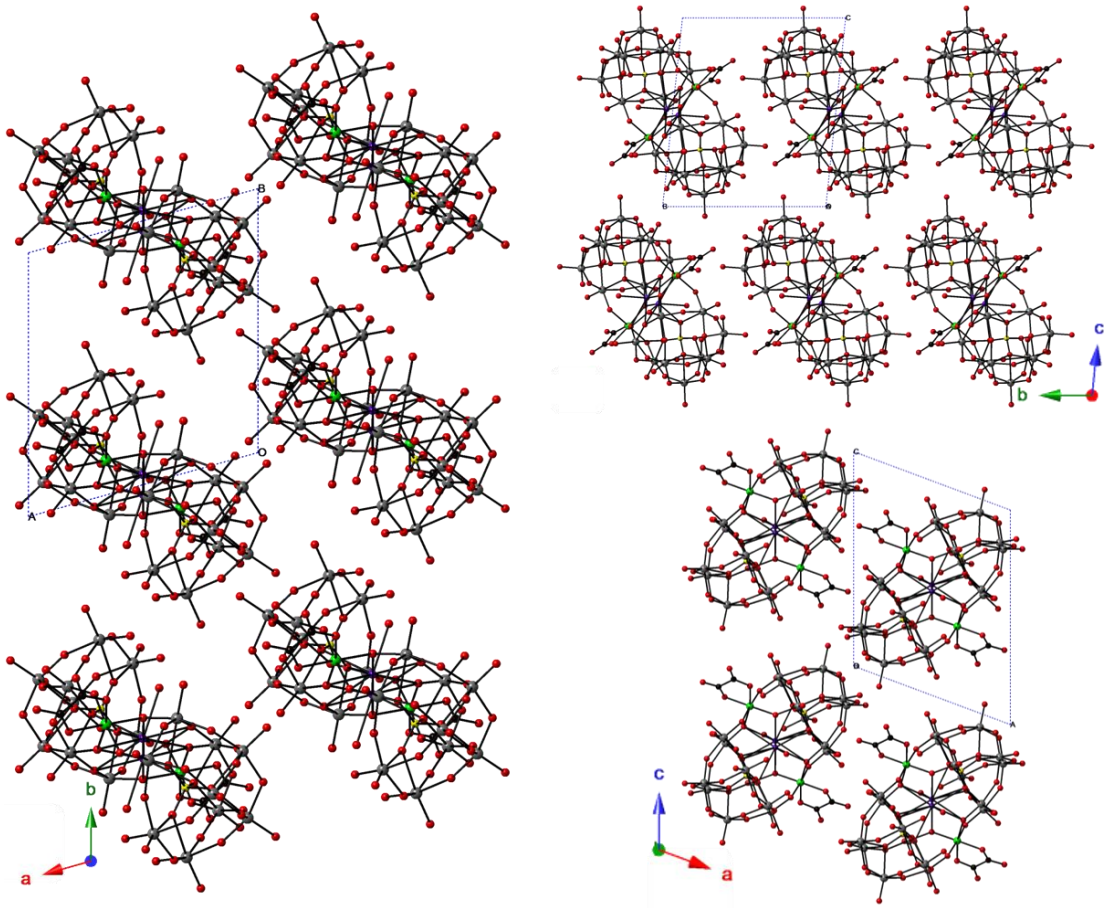

Fig. 4.4.- Ball and stick representations of the packing structure of POM **4.1**, showing the disorder of the encapsulated potassium ion in the central cavity of the POMs. The colour code of the spheres is as follows: W (grey), Fe (green), K (violet), P (yellow), O (red) and C (black).

Therefore, the described arrangement of ligands and metal ions in **4.1** and **4.2** would give rise to an overall, idealized C_{2h} symmetry (in which the binary axis passes through the two iron atoms). However, the mean planes of the dicarboxylate ligands are tilted in opposite directions with respect to the mean plane formed by the Fe atom and the equatorial O ligands by 18.7(9)° and 22.9(5)° for **4.1** and **4.2**, respectively (see **Fig. 4.5**),‡ reducing the overall symmetry of the POM from C_{2h} to C_i. Bond valence sum calculations[25] suggest an oxidation state of 3+ for the iron ions in **4.1** and **4.2** (this is confirmed by Mössbauer and magnetic measurements, see below) and that all O atoms in the POMs are non-protonated.§

‡ All six atoms of the oxalato ligand are used to calculate the mean plane, while only the coordinated oxygen atoms and the sp^2 carbon atoms of the malonato ligand are used to calculate the mean plane.

§ For the determination of the oxidation states of metal centers, bond valence sum (BVS) calculations were carried out using the method of I. D. Brown.[27] R_0 values were taken from the literature[28] for calculations performed on Fe and O sites [R_0 (Fe – O) = 1.745].

The side-slipped arrangement of the two A-α-$[PW_9O_{34}]^{9-}$ moieties creates an internal cavity in the centre of **4.1** and **4.2** which is occupied by a nine-coordinated potassium cation. This internal cavity can be considered as an oxygen pocket formed by an equatorial ring of six μ_2-O atoms of the POM (O4F, O5F, O45, O4F', O5F' and O45') having a chair-like arrangement about the potassium ion and four other μ_3-O atoms of the POM (O490, O560, O490', O560'), two at each opposite side of the equatorial ring (see **Fig. 4.3**). The six μ_2-O atoms either bridge two W atoms (O45 and O45') or W and Fe atoms (O4F, O5F, O4F' and O5F'), while the four μ_3-O atoms bridge one P and two W atoms. The potassium ion is enclosed in the centre of this oxygen pocket although it is disordered over two equivalent and close positions separated by 1.11 Å (or 1.02 Å) in **4.1** (or **4.2**). This disorder enables K^+ to be coordinated by two of the μ_3-O atoms located in one side of the equatorial ring made of the six μ_2-O atoms. K$\cdots\mu_2$-O distances range from 2.595(19) to 2.868(19) Å for **4.1** (2.559(6) to 2.834(6) Å for **4.2**) and K$\cdots\mu_3$-O distances are 2.917(19) and 2.943(16) Å in **4.1** (2.924(6) and 2.957(6) Å in **4.2**). A water molecule completes the ninth coordination of the K^+ ion with a K$\cdots O_w$ distance of 2.72(3) Å for **4.1** (2.783(10) Å for **4.2**). This situation is strongly reminiscent of the typical potassium complexes of the 18-crown-6 polyether ligand.[26] The rigidity of the internal cavity created by the POM, however, makes it much more selective to K^+ coordination than the flexible organic 18-crown-6 polyether, which can also coordinate other smaller or larger alkaline cations.[26]

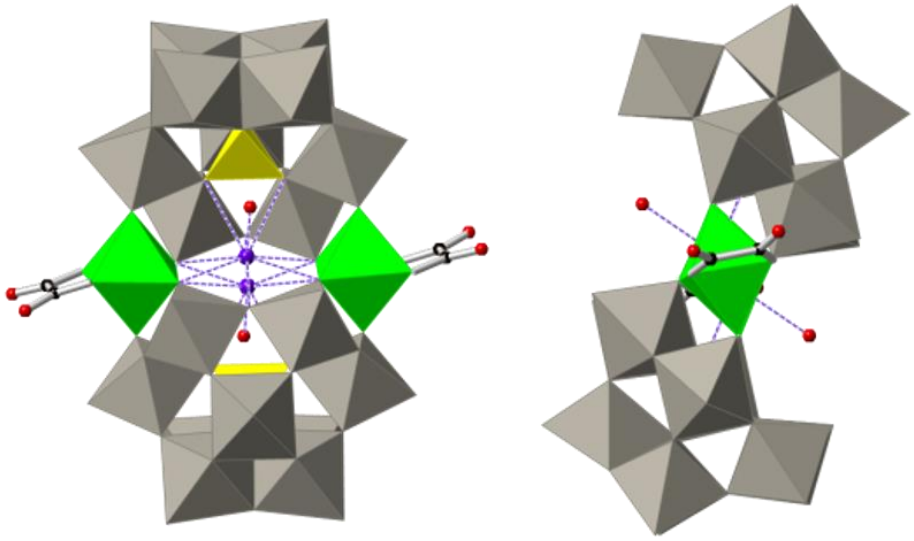

Fig. 4.5.- Combined polyhedral/ball-and-stick representations of the POM in **4.1**. Gray octahedra, [WO_6]; yellow tetrahedra, [PO_4]; green octahedra, [FeO_6]; black spheres, C; red spheres, O.

4.2.3. Thermogravimetric analysis

For the thermogravimetric analysis, samples were heated until 500 °C under nitrogen atmosphere. For **4.1**, the TG curve (see the experimental section **Fig. 4.22**) shows two distinct weight loss steps with a total weight loss of 10.57 % (the first one from 25 to ca. 203 °C and the second one from 203 to ca. 450 °C). For **4.2** (see the experimental section **Fig. 4.24**), it shows three distinct weight loss steps with a total weight loss of 10.44 %, which are 25 to ca. 203 °C, 203 to ca. 350 °C and 350 to ca. 450 °C.

The interpretation of the thermogravimetric analysis curves of **4.1** and **4.2** are based on previously reported thermal decomposition reactions of the salts $K_3[Fe(C_2O_4)_3]\cdot 3H_2O$[21] and $K_3[Fe(C_3H_2O_4)_3]\cdot H_2O$.[22] According to them, the thermal decomposition reactions of **4.1** and **4.2** can be established as:

$$K_{16}[(PW_9O_{34})_2Fe_2(C_2O_4)_2]\cdot 29H_2O \rightarrow K_{12}P_2W_{18}O_{68}Fe_2 + K_2O + K_2CO_3 + CO_2 + 2CO + 29H_2O$$

$$K_{16}[(PW_9O_{34})_2Fe_2(C_3H_2O_4)_2]\cdot 27H_2O \rightarrow K_{12}P_2W_{18}O_{68}Fe_2 + K_2O + K_2CO_3 + CO_2 + 2CO + C_2H_4 + 27H_2O$$

which allow to calculate the theoretical percentage values for the total weight loss of **4.1** and **4.2** (10.56 % and 10.44 %, respectively).

4.2.4. UV-vis spectra in aqueous solution

The stabilities in aqueous solution of **4.1** and **4.2** have been studied by UV spectroscopy (**Fig. 4.6**). Both compounds display similar absorption bands in the range 190 - 400 nm: **4.1** exhibits a shoulder at 201 nm (204 nm for **4.2**) and a band centred at 257 nm (258 nm for **4.2**). The absorption at higher energy is due to the *pπ-dπ* charge-transfer transitions of the $O_t \rightarrow W$ in the polyoxoanion (O_t: terminal oxygen), while the lower energy band can be assigned to the *pπ-dπ* charge-transfer transitions of the $O_{b,c} \rightarrow W$ in the polyoxoanion[29] ($O_{b,c}$: bridging oxygen). The evolution of the UV spectra during 24 h reveals that the position of the absorption bands does not change with time, but they become less intense, pointing to a slow decomposition of both compounds in aqueous solution at room

temperature. The compounds, however, can be recrystallised from aqueous solution if the process is carried out within a short time using concentrated solutions of **4.1** or **4.2** (~ 30 min).

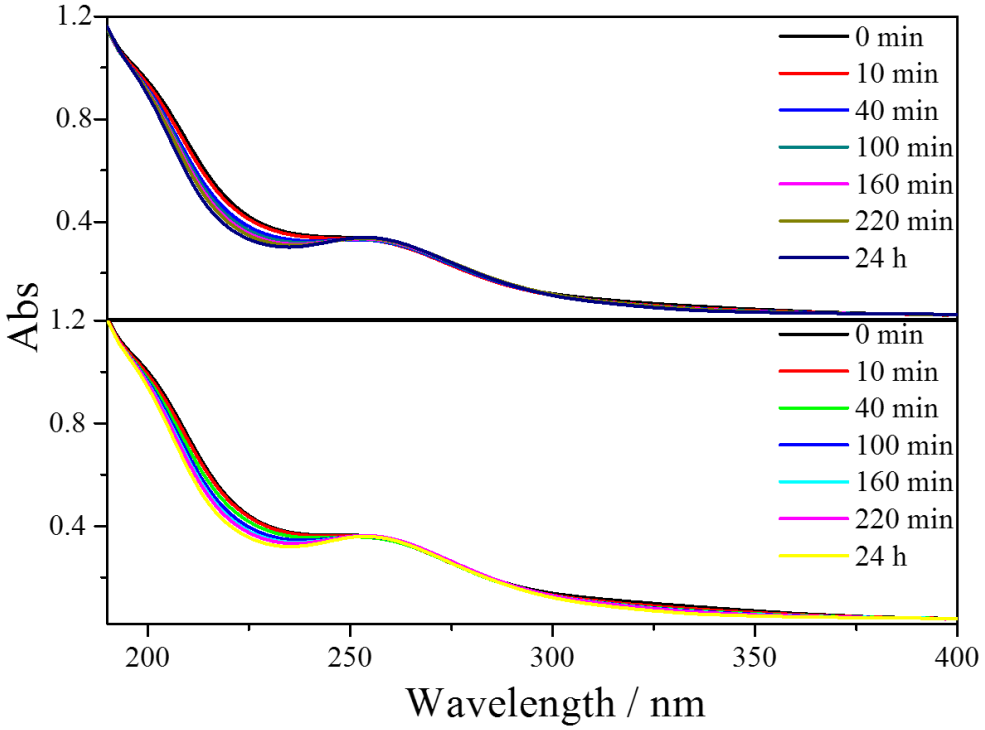

Fig. 4.6.- Time evolution of UV-Vis spectra of **4.1** (up) and **4.2** (down) in aqueous solution.

4.2.5. Photocolouration effect in solid-state

When a solid sample of **4.1** is exposed to direct sunlight or UV irradiation, a colour change from light yellowish-green to black, evident by the naked eye, starts in a question of seconds (**Fig. 4.7**). If this black solid is stored in the dark in the presence of air, the solid reverts to its original colour after about 7 days (no colour reversion takes place under O_2-free atmosphere).

UV-vis/diffuse absorbance spectra of **4.1**, before and after irradiation with UV light (351 nm) during different irradiation times are shown in **Fig. 4.8**. Before UV irradiation, the sample exhibits two absorption bands in the visible: a weak, broad absorption band centred at 630 nm and a narrower and stronger band at 460 nm. In addition, there are two broad and significant bands at lower wavelengths (ranging between 210-270 and 320-370 nm) attributed to O → W ligand-to-metal charge transfer (LMCT) bands of the POM (**Fig. 4.8**, inset).

Fig. 4.7.- (I). (a-h) Photogenerated colour change of **4.1** after different times of UV irradiation at 351 nm (0 - 20 min). After being irradiated, the compound was stored in the dark during 7 days (i) and then reirradiated again (j-l). (II) Crystals of **4.1** before irradiation (left) and after 5 min of UV irradiation at 351 nm (right). (III) (m) Crystals of **4.1** after 5 min UV irradiation at 351 nm. (n) The same crystals as in (m) cut to observe the colour of the interior. (o-p) Different views of the cut crystals in (n). These photographs show that the interior of transparent crystals exhibit the same colour as their surface, suggesting that the photocolouration process happens in the bulk crystals. For powder samples, with less transparency, the photocolouration effect mostly happens on the surface.

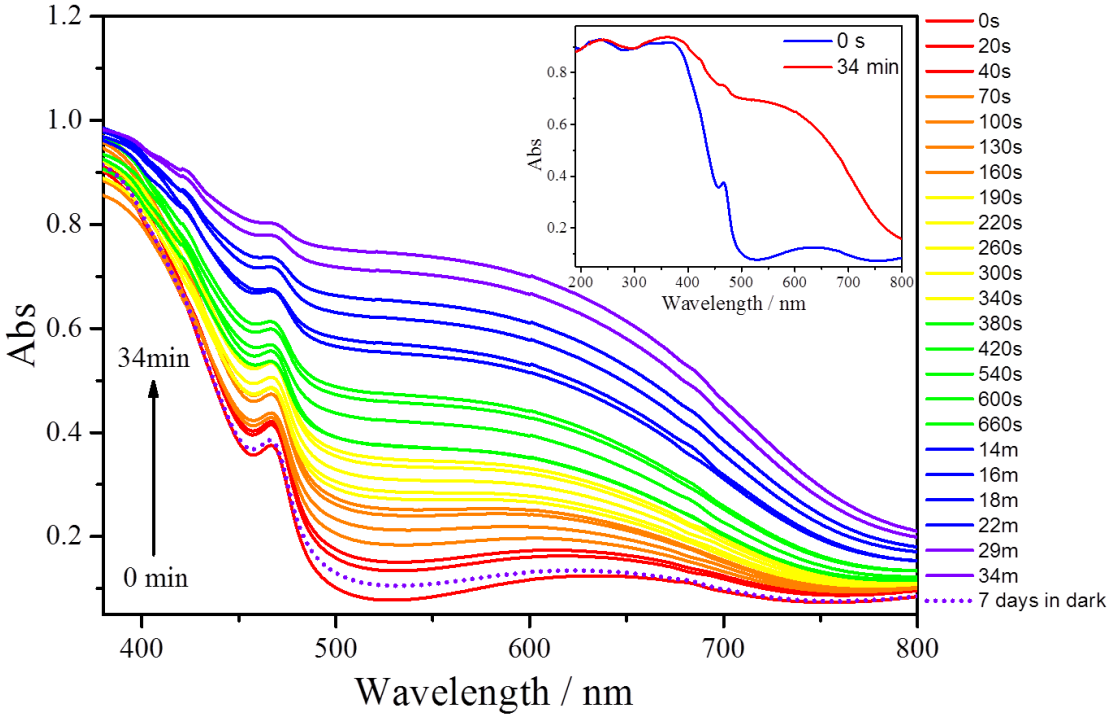

Fig. 4.8.- Evolution of the photogenerated absorption of **4.1** after 0, 0.17, 0.67, 1.17, 1.67, 2.17, 2.67, 3.17, 3.67, 4.33, 5, 5.67, 6.33, 9, 10, 11, 14, 16, 18, 22, 29 and 34 min of UV irradiation (351 nm). After being irradiated for 34 min, the compound was stored in the dark during 7 days and its absorption spectrum recorded (dotted line). Inset: UV-vis/diffuse absorbance spectra of **4.1** (before UV irradiation and after 34 min UV irradiation) in the 190-800 nm range.

After irradiation, the colour of the sample turns black, in agreement with the growth of the two absorption bands in the visible range. The broader band in this region is quite comparable with those of other irradiated photochromic POMs,[6d,6e,30] suggesting that the photo-induced colouration is mainly due to the POM core. This should imply that in **4.1** the two POM moieties have been reduced as a result of the UV irradiation and contain W(V) species. Therefore, the absorptions in the visible range can be attributed to *d-d* transitions (if the electron is trapped onto a specific W centre) or intervalence charge transfer (IVCT) of W(V) → W(VI) (if it can be delocalized onto several adjacent $\{WO_6\}$). In addition, the position of the maximum absorption of the broader band undergoes a blue shift with irradiation time from 630 nm to about 550 nm, suggesting that the degree of reduction in the POMs increases with irradiation time. After the UV irradiation was stopped, the sample was stored in the dark at room temperature in the presence of air. In these conditions, the sample slowly reverts to its original colour. After 7 days, the absorption spectrum is very similar to the original one (dotted line in **Fig. 4.8**) meaning that W(V) is reoxidised to W(VI) in the presence of air. The colouration and bleaching

process can be repeated at least 6 times if the sample is exposed again to UV light, although the intensity of the black colour decreases after each cycle. In contrast, the solid samples of **4.2** do not exhibit any light-induced colour change under similar conditions, as shown by its UV-vis/diffuse absorbance spectra (**Fig. 4.9**).

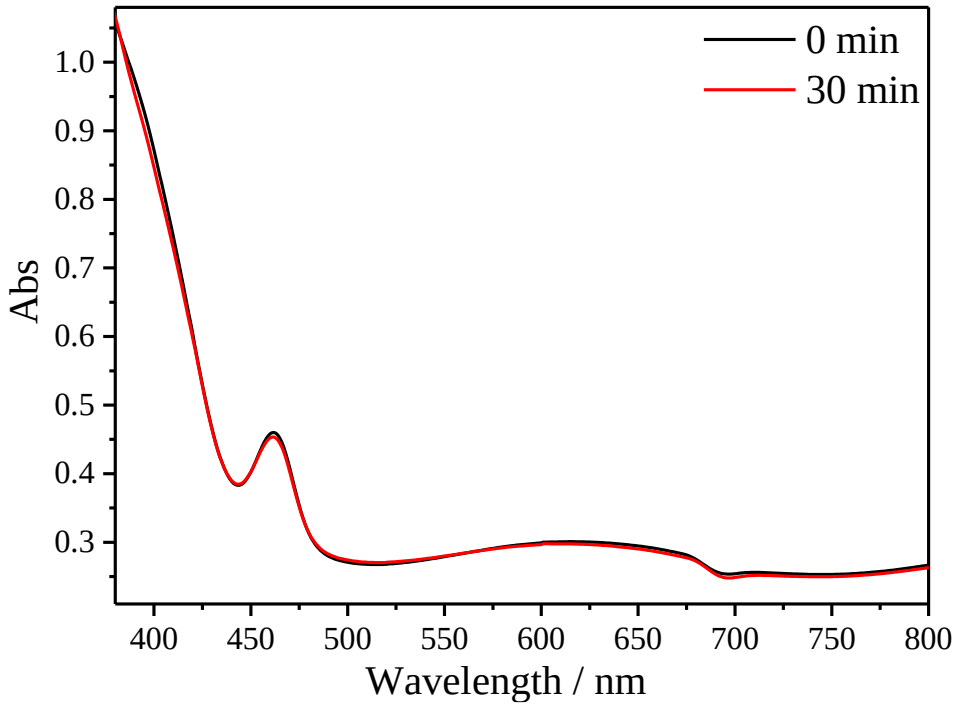

Fig. 4.9.- Comparison of the photogenerated absorption of **4.2** at 0 min (black line) and after 30 min (red line) of UV irradiation (351 nm).

The colouration kinetics of **4.1** have been quantified by analysing its reflectivity values, *R(t)*, in the range of 380 - 800 nm as a function of the irradiation time, *t* (**Fig. 4.10**). Details of the parameters related to the colouration kinetics are given in **Fig. 4.11**. In summary, it has been found that the $R^{525}(t)$ *vs. t* curves of **4.1** can be fitted using the pseudo-second-order law below(see **Fig. 4.11**):

$$R^{525}(t) = \frac{\mathrm{a}}{[\mathrm{b}t + 1]} + [R^{525}(0) - \mathrm{a}]$$

The $t_{1/2}$ value obtained for the photocolouration process (4.25 min) corresponds to a relatively fast photo-response, when compared with other POM-based photochromic materials.[30c,32]

The *R(t) vs. t* relationship for **4.1** is perfectly fitted by the pseudo-second-order law. (See reference[31] for details of the kinetics model used here). $R^{525}(0)$ is the reflectivity

value at t = 0, i.e., at the time just before UV illumination. The a parameter is the difference between the reflectivity values at t = 0 and at $t = \infty$, *i.e.*, at the end of the photocolouration process. The half-life $t_{1/2}$ is defined as the time required for $R(t)$ to reach the $[R(0)+R(\infty)]/2$ value. $t_{1/2}$ is given by $t_{1/2} = b^{-1}$.

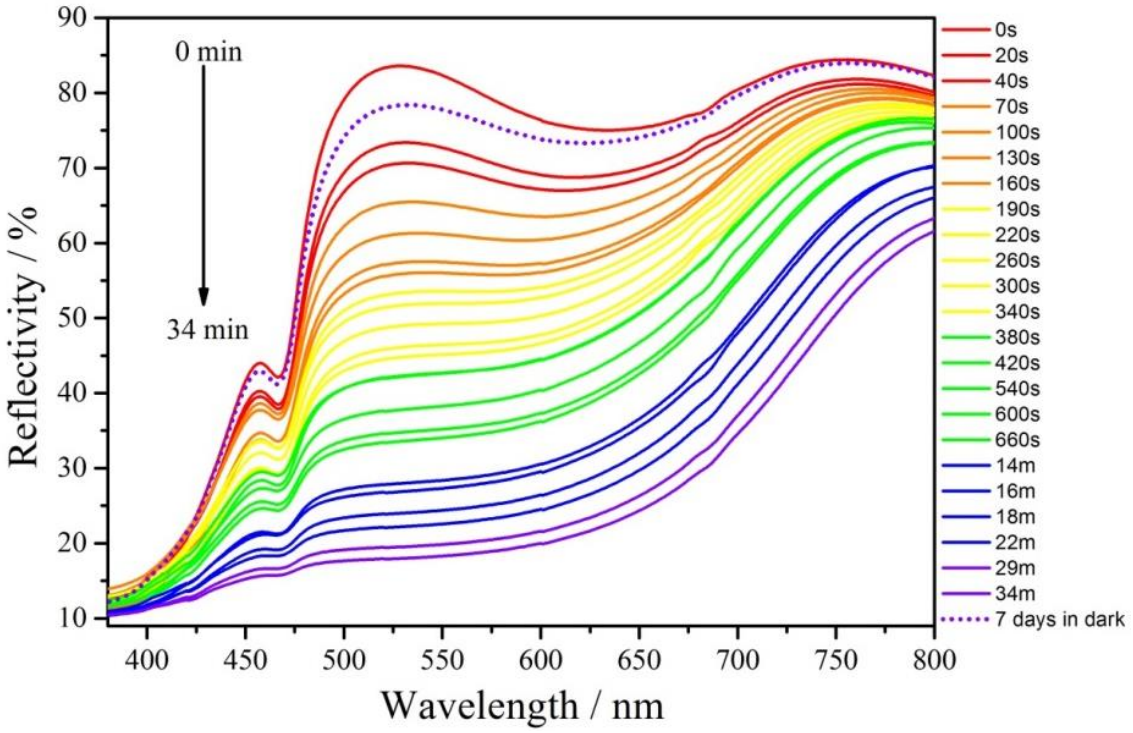

Fig. 4.10.- Time evolution of the photogenerated reflectivity $R(t)$ of **4.1** in the 380 – 800 nm range of UV irradiation (351 nm). After being irradiated for 34 min, the compound was stored in the dark during 7 days and its absorption spectrum recorded (dotted line).

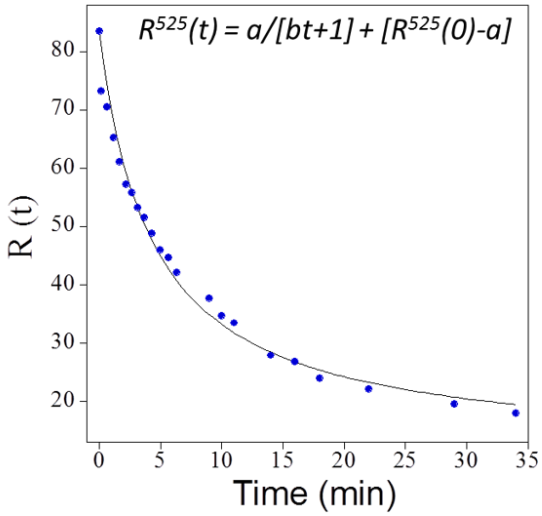

$R^{525}(0)$	0.835
a	0.722
b	0.230
R^2	0.99174
$t_{1/2}$ (min)	4.35

Fig. 4.11.- (Left). Reflectivity $R(t)$ *vs.* t plot for **4.1** measured at 525 nm of UV irradiation (351 nm) with different irradiation time. (Right). Regression coefficient values of the fitting parameters describing the $R(t)$ *vs.* t relationship for **4.1**.

4.2.6. Photocolouration effect in solution

The photocolouration effect is exhibited also by irradiated solutions of **4.1**, although it is not as remarkable as in the solid state, as shown by the UV-vis spectra of an irradiated $2.5 \cdot 10^{-3}$ M aqueous solution of **4.1** (**Fig. 4.12**). The UV-vis spectra show absorption peaks located around 462 nm that gradually increase with irradiation time, until 25 min of irradiation. For longer times, the peak intensities decrease until a constant value is reached for more than 45 min of irradiation.

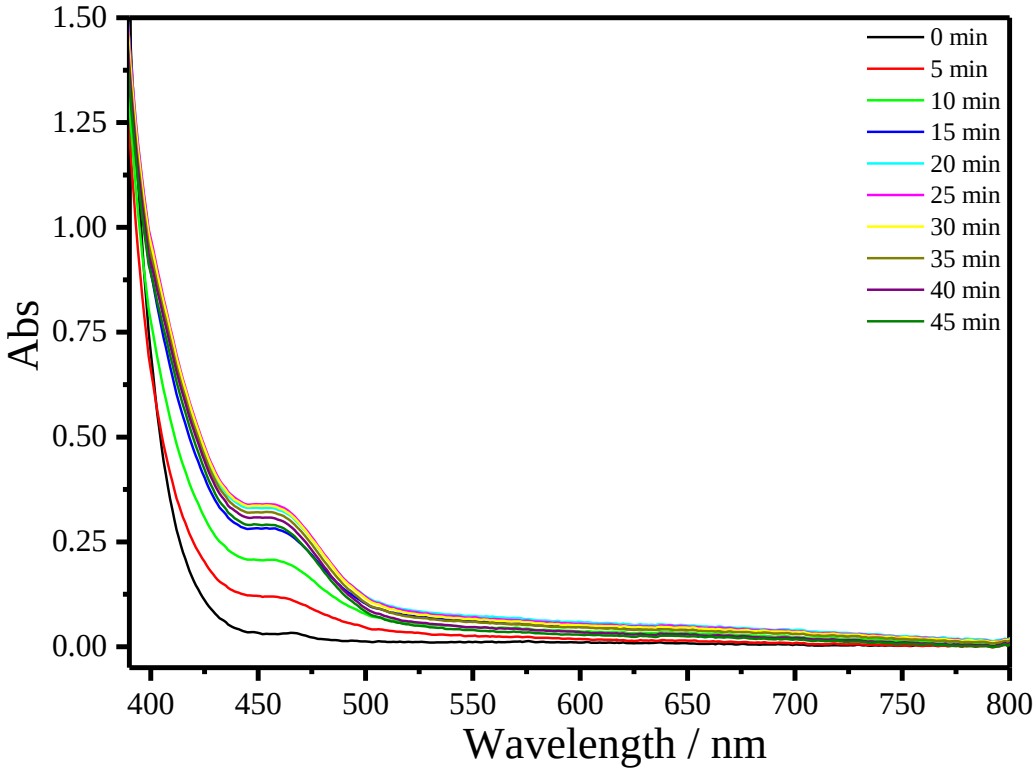

Fig. 4.12.- UV-vis spectra evolution of sample **4.1** in aqueous solution $2.5 \cdot 10^{-3}$ M after 0, 5, 10, 15, 20, 25, 30, 35, 40 and 45 min of UV irradiation (351 nm).

4.2.7. Infrared spectroscopy

The IR spectra of **4.1** (as a KBr pressed pellet) before and after UV photoirradiation have been investigated (**Fig. 4.13**). Before irradiation it exhibits the typical bands of the chelating oxalato ligand[33] at 1714 cm^{-1} (ν_a(C=O), very weak), 1668 cm^{-1} (ν_a(C=O), strong), 1384 and 1401 cm^{-1} ((ν_s(CO) + ν(CC), strong) and 1285 cm^{-1} (ν_s(CO) + δ(O–C=O), medium) and bands corresponding to the POM framework at 1076

and 1018 cm^{-1} (ν_a(P–O), strong), 940 cm^{-1} (ν_a(W–O_t), strong), 852 and 800 cm^{-1} (ν_a(W–O_a–W), strong) and 742 cm^{-1} (ν_a(W–O_b–W), strong). Bands at 659 and 519 cm^{-1} can be assigned to Fe–O–W and Fe–O–C vibrations. Upon irradiation, the intensity of all oxalato bands decreases gradually as the irradiation time increases, while there are two new bands that appear and increase in intensity with the irradiation time at 2341 and 2364 cm^{-1}. These bands can be attributed to carbon dioxide (R- and P- branches of the $\nu_a(CO_2)$ band, respectively) trapped in the KBr pellet.[34]

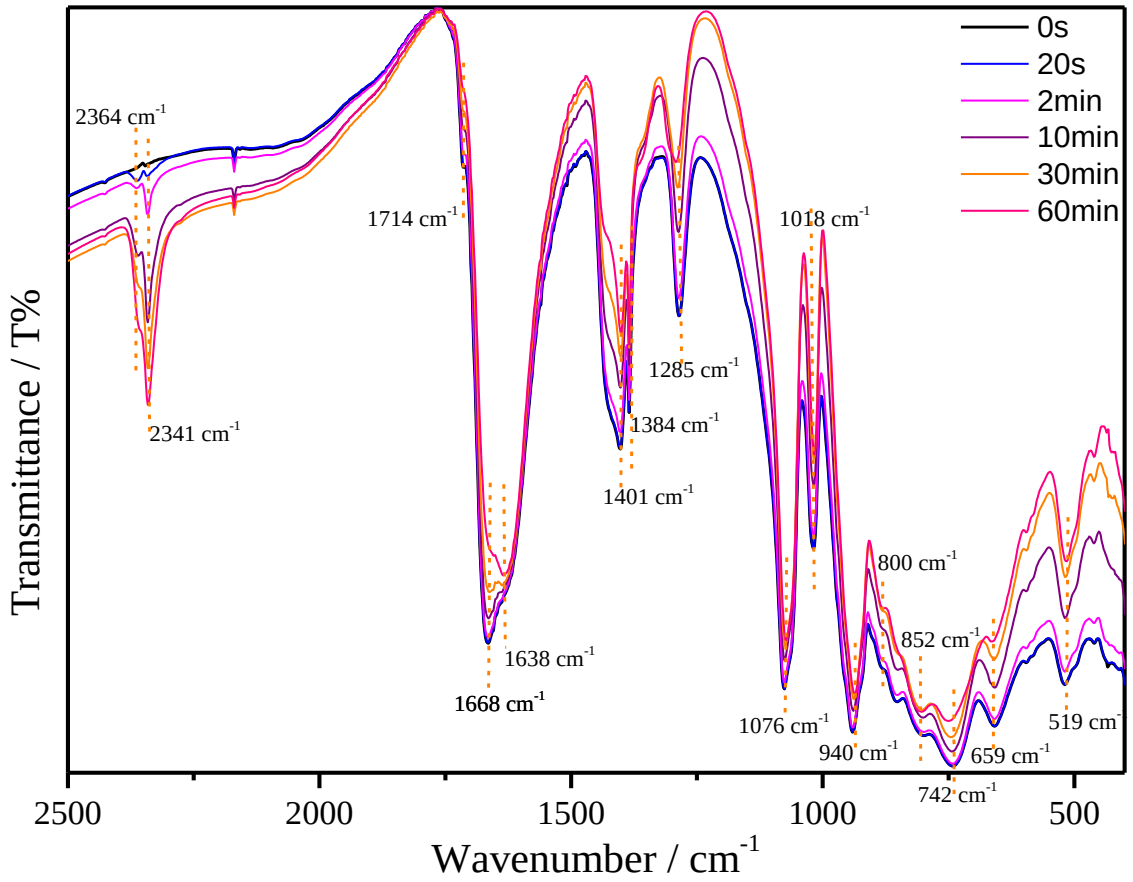

Fig. 4.13.- Evolution of the IR spectra of **4.1** upon different irradiation times of UV light (351 nm).

These results confirm a photo-induced decomposition of the oxalato ligand into carbon dioxide, akin to the photo-decomposition of the oxalato ligands in the tris(oxalato)ferrate(III) complex anion.[35] During this process, two electrons must be released from each oxalato ligand that decomposes, which may be accepted by the POM framework and/or the iron atoms. The decrease in the intensity of all the POM bands upon irradiation is consistent with a reduction of the POM.[30a]

4.2.8. XPS Spectra

The XPS W4f spectra measured for **4.1** before irradiation, after UV irradiation and after being stored in the dark during 7 days are shown in **Fig. 4.14**. All three XPS W4f spectra can be resolved into $4f_{7/2}$ and $4f_{5/2}$ doublets (caused by spin-orbit coupling) and deconvoluted into two couples of peaks (**Fig. 4.14a-c**), corresponding to the typical binding energies of W(VI) (centred at 37.9 and 35.7 eV) and W(V) oxidation states (centred at 37.0 and 34.9 eV). As shown in **Table 4.1**, W(V) species appear even in the non-irradiated sample (**Fig. 4.14a**), suggesting that the photoreduction of the POM occurred in part when the sample was exposed to the X-ray source, as observed in other previously published works.[30d,36] The analysis of data indicates that after photoirradiation with 351 nm UV light for 3 days under vacuum, the amount of W(V) increases and that of the W(VI) decreases (**Fig. 4.14b**). The concentration of W(V) is 11.0 % (**Table 4.1**), as determined from the peak area ratio of W(V) to W(VI) (much higher than that observed before irradiation), indicating the reduction of more W(VI) to W(V) under UV irradiation.

Table 4.1.- XPS data of **4.1** before irradiation, 3 days UV irradiation (351 nm) under vacuum and 7 days in the dark in air.

Species		Before irradiation		After irradiation		7 days in the dark	
		Peak BE/eV	W(V) %	Peak BE/eV	W(V) %	Peak BE/eV	W(V) %
W4f	W(VI) $4f_{5/2}$	35.7	3.0 %	35.4	11.0 %	35.7	4.0 %
	W(VI) $4f_{7/2}$	37.9		37.5		37.9	
	W(V) $4f_{5/2}$	34.9		34.9		34.9	
	W(V) $4f_{7/2}$	37.0		37.0		37.0	

The XPS spectrum of the photo-irradiated sample stored in dark (**Fig. 4.14c**) exhibits very similar binding energies of the W4f peaks to those of the non-irradiated sample, and can be deconvoluted into one pair of peaks that corresponds to the typical binding energies of W(VI) (centred at 37.9 and 35.7 eV). The concentration of W(V) in these two samples is also very similar (4.0 % compared to 3.0 % for the irradiated and the initial samples, respectively).

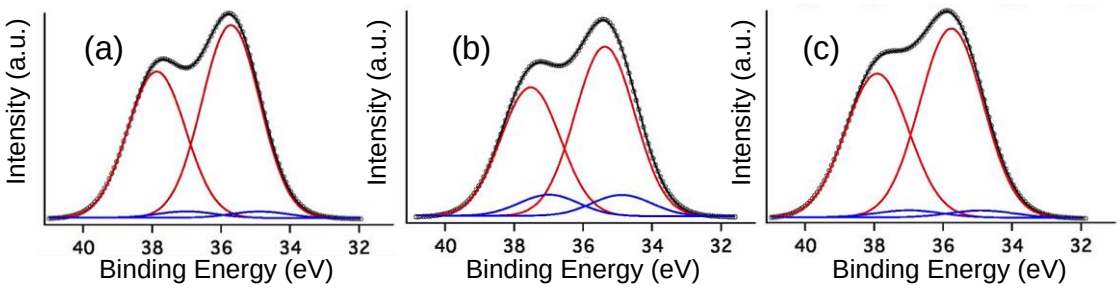

Fig. 4.14.- XPS W4f spectra collected for **4.1** before irradiation (a), after 3 days of UV irradiation (351 nm) (b), and 7 days more in the dark (c). Dotted lines correspond to the experimental data that can be deconvoluted into two pairs of peaks corresponding to W(VI) (red curves) and W(V) (blue curves). The fitting of the experimental data (black curves) has been obtained by summation of the deconvoluted peaks.

4.2.9. Mössbauer spectroscopy

The Mössbauer spectra of **4.1-^{57}Fe** and **4.2-^{57}Fe** consist of a broad absorption peak (**Fig. 4.15a** (left) and **Fig. 4.15** (right)), which may be fitted by a quadrupole doublet. Only a broad peak is observed in both spectra because the widths of each line of the doublets are higher than the corresponding quadrupole splittings, QS (**Table 4.2**). The isomer shifts relative to α-Fe at 295 K, IS, are within the range of high spin, S = 5/2, Fe(III) values[37] and similar to those of Fe(III) coordinated to oxalato or malonato ligands in other compounds.[20,38]

After irradiation by UV light (365 nm) the **4.1-^{57}Fe** sample changes colour from light yellowish-green to almost black. After 6 h irradiation time the sample was moved to the Mössbauer spectrometer. At least 45 minutes of data collection were necessary for a reliable analysis (**Fig. 4.15b**). The spectrum obtained can only be analysed by two quadrupole doublets. One of the doublets has an IS (**Table 4.2**) typical of high-spin Fe(II), (S = 2),[20,37,39] far above the range of the Fe(III) IS values. The second doublet is similar to the Fe(III) signal in the pristine sample but with higher QS most likely due to a more distorted environment of Fe(III) in the UV-irradiated sample.

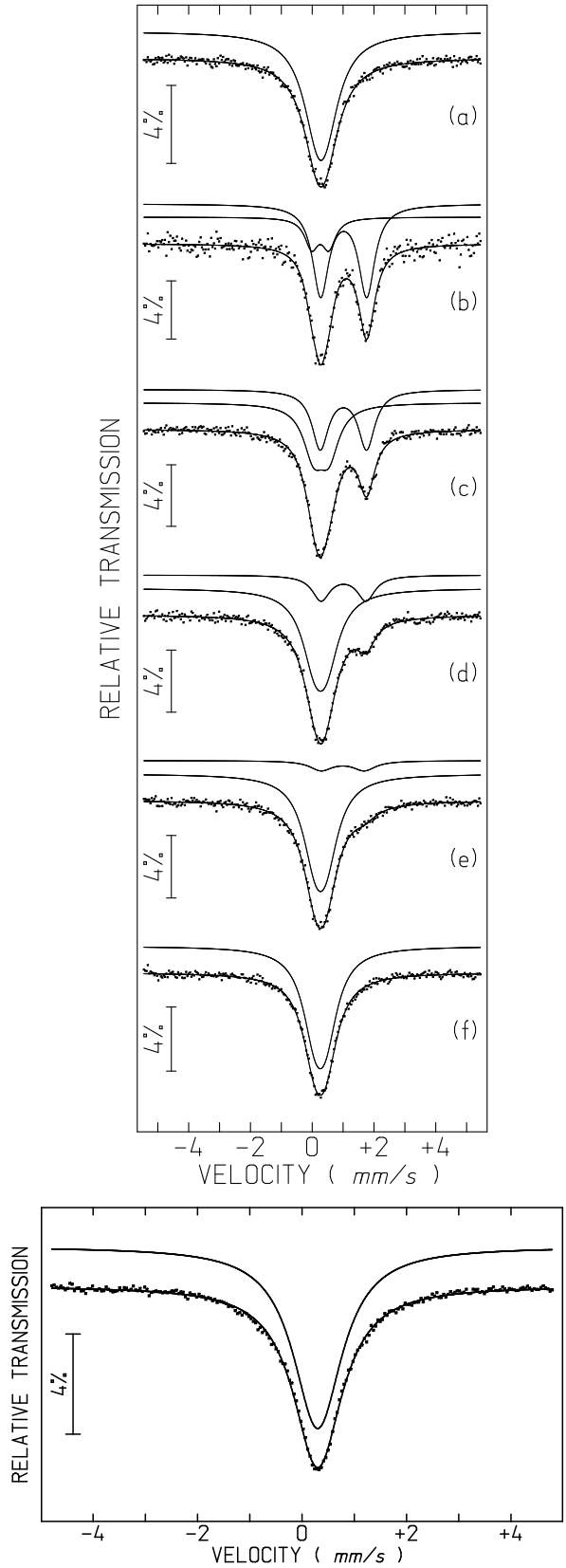

Fig. 4.15.- (Up) Mössbauer spectra of **4.1-^{57}Fe** sample taken before (a) and after 6 h UV irradiation for t_{UV} ~ 0.75 h (b), 18 h (c), 42 h (d), 66 h (e), 12 days (f). t_{UV}, time after irradiation was switched off, is defined in the text. The lines over the experimental points are the sum of two quadrupole doublets shown slightly shifted for clarity (estimated parameters in **Table 4.2**). (Down) Mössbauer spectrum of **4.2-^{57}Fe** sample.

Table 4.2.- Estimated parameters from the Mössbauer spectra taken at room temperature of sample **4.1-^{57}Fe** and **4.2-^{57}Fe**.

	t_{UV}	IS (mm/s)	QS (mm/s)	I	Fe state
4.2-^{57}Fe	-	0.41	0.10	100 %	Fe(III)
4.1-^{57}Fe	-	0.40	0.35	100 %	Fe(III)
4.1-^{57}Fe after 1st UV	irradiation				
	0.75 hours	0.37	0.56	21 %	Fe(III)
		1.13	1.49	79 %	Fe(II)
	8 hours	0.36	0.54	33 %	Fe(III)
		1.13	1.50	67 %	Fe(II)
	18 hours	0.40	0.50	50 %	Fe(III)
		1.12	1.50	50 %	Fe(II)
	30 hours	0.39	0.50	60 %	Fe(III)
		1.12	1.51	40 %	Fe(II)
	42 hours	0.38	0.38	77 %	Fe(III)
		1.13	1.46	23 %	Fe(II)
	54 hours	0.38	0.39	87 %	Fe(III)
		1.09	1.44	13 %	Fe(II)
	66 hours	0.38	0.35	89 %	Fe(III)
		1.10	1.40	11 %	Fe(II)
	10 days	0.37	0.35	96 %	Fe(III)
		1.05	1.38	4 %	Fe(II)
	12 days	0.37	0.28	100 %	Fe(III)
4.1-^{57}Fe after 2nd UV	irradiation				
	0.75 hours	0.38	0.35	80 %	Fe(III)
		1.07	1.70	20 %	Fe(II)
	4 hours	0.38	0.33	84 %	Fe(III)
		1.08	1.69	16 %	Fe(II)
	24 hours	0.38	0.30	86 %	Fe(III)
		1.07	1.67	14 %	Fe(II)
	7days	0.37	0.28	97 %	Fe(III)
		1.03	1.68	3 %	Fe(II)
	12 days	0.38	0.26	100 %	Fe(III)

IS isomer shift relative to metallic α-Fe at 295 K; QS quadrupole splitting; I relative areas. Estimated errors are ≤ 0.02 mm/s for IS, QS, ≤ 2 % for I, t_{UV}, elapsed time between mid-spectrum collection and the moment when UV irradiation was switched off, is defined in the text.

Both high-spin Fe(III) and Fe(II) doublets are present in the spectra taken at different times after the UV-irradiation (up to 10 days). The relative area of Fe(II), I(Fe^{II}), decreases with increasing time after irradiation (**Fig. 4.15** and **Fig. 4.17**). In order to evidence the time dependence of I(Fe^{II}), all spectra, except the first one after irradiation, were collected during approximately the same time and t_{UV} was defined as the elapsed time between mid-spectrum collection and the moment when UV irradiation was switched off (which corresponds to t_{UV} = 0). The relative areas estimated for t_{UV} = 0.75 hours suggest that approximately 79 % of all the Fe is in the 2+ oxidation state, i.e. I(Fe^{II})

~79 %. The steep decrease of I(Fe^{II}) with increasing t_{UV} during the first hours (**Table 4.2** and **Fig. 4.17**) suggests that the I(Fe^{II}) deduced from the spectra are actually an average of the I(Fe^{II}) range of values occurring during the spectrum collection time. This means that immediately after UV irradiation I(Fe^{II}) is most likely higher than 79 %.

When t_{UV} ~ 66 hours, I(Fe^{II}) reaches 11 % ± 2 %, but at this stage it is decreasing very slowly with increasing time. After approximately 10 days the colour of the sample has become light yellowish-green again but a small shoulder on the Fe(III) absorption peak evidences the presence of an Fe(II) doublet with an estimated I(Fe^{II}) ~4 %. Only after 12 days all traces of Fe(II) disappear from the spectrum (**Table 4.2**, **Fig. 4.15f** and **Fig. 4.17**).

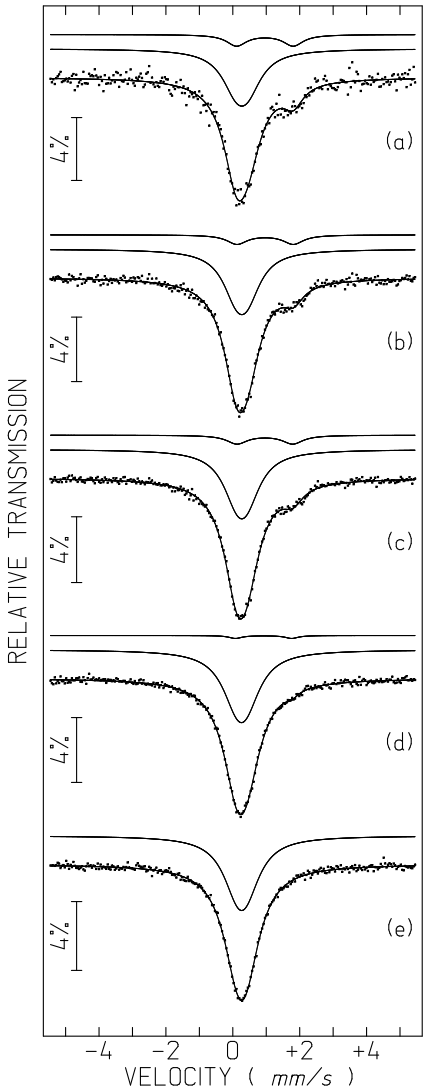

Fig. 4.16.- Mössbauer spectra of **4.1-^{57}Fe** sample taken after a second 6 h UV irradiation for t_{UV} ~ 0.37 h (a), 4 h (b), 24 h (c), 7 days (d), and 12 days (e). t_{UV}, time after irradiation was switched off, is defined in the text. The lines over the experimental points are the sum of two quadrupole doublets shown slightly shifted for clarity (estimated parameters in **Table 4.2**).

IS of Fe(III) is consistent with octahedral coordination in agreement with the structure determined by single-crystal XRD for the pristine compound. IS of Fe(II) is also consistent with octahedral coordination but the presence of a fraction of Fe(II) in lower coordination, such as penta-coordination, may not be excluded.[37,40]

The effect of a second UV irradiation of the sample after all Fe is back in the 3+ oxidation state, is not the same as the effect of the 1st irradiation. The sample colour resulting from this second irradiation is not so dark and the Mössbauer spectra (**Fig. 4.16**) taken for similar t_{UV} reveal that I(Fe^{II}) is significantly lower in the first days after irradiation (**Table 4.2**, **Fig. 4.16** and **Fig. 4.17**). The estimated I(Fe^{II}) for the spectrum taken during 45 minutes immediately after turning off UV light is only ~ 20 %. After 12 days all the Fe is back in the 3+ oxidation state.

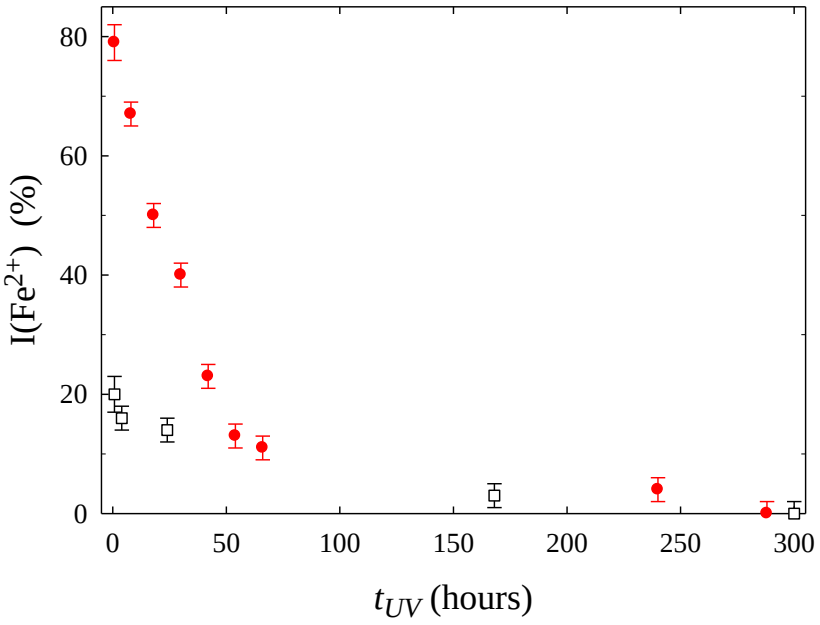

Fig. 4.17.- Relative areas of Fe(II), I(Fe^{II}), estimated from Mössbauer spectra of **4.1-^{57}Fe** *vs.* average time after first (closed circles) and second (open squares) UV-irradiation.

The IS and the QS of Fe(II) obtained after the 2nd irradiation are significantly different (IS smaller and QS higher) from those obtained after the 1st irradiation. The lower IS may be explained if we assume that after the 2nd irradiation Fe(II) is mainly pentacoordinated.[37,40] This coordination of Fe(II) would also lead to a more distorted electronic charge distribution around the Fe(II) in agreement with higher QS.

As referred above, QS of Fe(III) increases significantly after the 1st UV-irradiation, suggesting a more distorted environment for this cation. However, as I(Fe^{II}) decreases, QS of Fe(III) also decreases, until it becomes slightly lower than in the pristine sample where I(Fe^{II}) is zero. This may suggest that by the end of the 1st "UV-irradiation-Fe(II) decay" cycle the structure of the sample is no longer identical to the pristine one although all the Fe is in the same oxidation state, 3+, and apparently with the same coordination number, 6. Only the ligands of Fe(III) and/or their geometrical arrangement seem to be different. Such a structural modification would be related to the distinct behaviour during the second UV-irradiation, rendering the sample more reluctant to Fe(III) reduction. In summary, Mössbauer spectroscopy clearly shows that the UV-irradiation induces a Fe(III) reduction to Fe(II). The variation of hyperfine parameters also suggests structural modifications after the 1st cycle of UV irradiation and Fe(II) decay back to Fe(III).

4.2.10. Magnetic properties

The χ_mT product of **4.1** has a constant value around 8.4 cm^3 mol^{-1} K above 40 K (see **Fig. 4.18**) which is consistent with the presence of two Fe(III) ions with spins S = 5/2 (8.75 cm^3 mol^{-1} K). Below this temperature, a sharp drop occurs which suggests the presence of antiferromagnetic exchange coupling between the two metal ions and/or the effect of the local anisotropy of Fe(III). Below 1 T, magnetization data at 2 K show a small increase with the magnetic field, in agreement with a nonmagnetic ground spin state. Above 1 T, the magnetization increases more rapidly due to a level crossing to a state having higher spin multiplicities.

The appropriate spin Hamiltonian for this type of dinuclear compound is written as:

$$\widehat{H} = -2J\hat{S}_1\hat{S}_2 + D\left(\hat{S}_{z1}^2 + \hat{S}_{z2}^2\right)$$

In this equation, $\hat{S}_1$ and $\hat{S}_2$ are the spin operators associated with the Fe(III) ions and *J* and *D* are the exchange and ZFS parameters, respectively. Taking into account both effects and using a simultaneous fit of susceptibility and magnetization curves, we have obtained an excellent fit of the experimental data from the following parameters $D = -1.5$ cm^{-1}, $J = -0.24$ cm^{-1} and $g = 2.05$ (solid line in **Fig. 4.18**). The dependence of the fit with respect to the parameters is shown in a two-dimensional plot of the error factor R on the values *J* and *D* (see inset **Fig. 4.18**). A minimum error region can be observed for each sign of *D*, negative and positive. However, the minimum of the region with

negative *D* has an error two orders of magnitude lower. This difference in quality between the two minimum shows that only a solution with both negative parameters can reproduce the crossing of the magnetization curves.

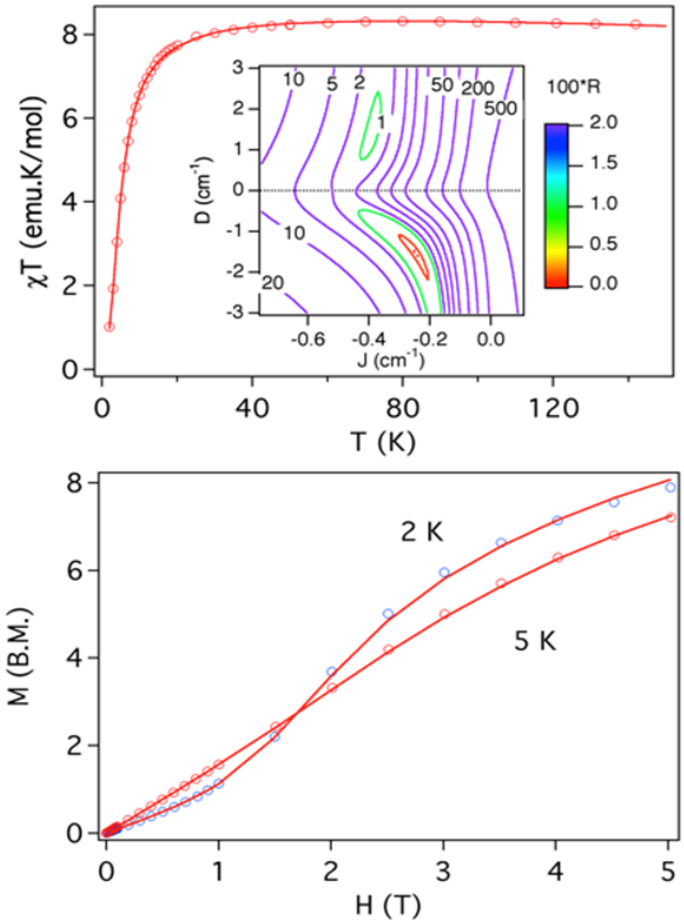

Fig. 4.18.- Magnetic properties of **4.1**. (Up) thermal dependence of the χ_mT product (inset: surface error plot of χ_m *vs*. T as a function of *J* and *D* revealing two banana minima); (Down) magnetization curves at 2 and 5 K. Solid lines represent the calculated curve from the best simultaneous fit of susceptibility and magnetization curves.

Other combinations of parameters do not lead to a crossing between the M curves at 2 and 5 K, regardless of the field value. Similar results were obtained for **4.2**. The minimum errorless set of parameters is $D = -2.4$ cm^{-1}, $J = -0.10$ cm^{-1}, and $g = 2.01$ (see **Fig. 4.19**). This negative value of *D* is very unusual for Fe^{III}. There is similar magnitude and sign of *D* in Fe(III) peroxides.[41-42] Negative sign can be attributed to low symmetry and spin-orbit coupling of the $^6A_1$ ground-state with excited quartet-LF and sextet-CT states.[43] Another model that considers a positive value for the ZFS and replaces the isotropic exchange by anisotropic dipolar interaction has not given satisfactory solutions.

Magnetic dipolar interactions between cations of different molecules were not considered because, in general, distances greater than 10 Å separate them.

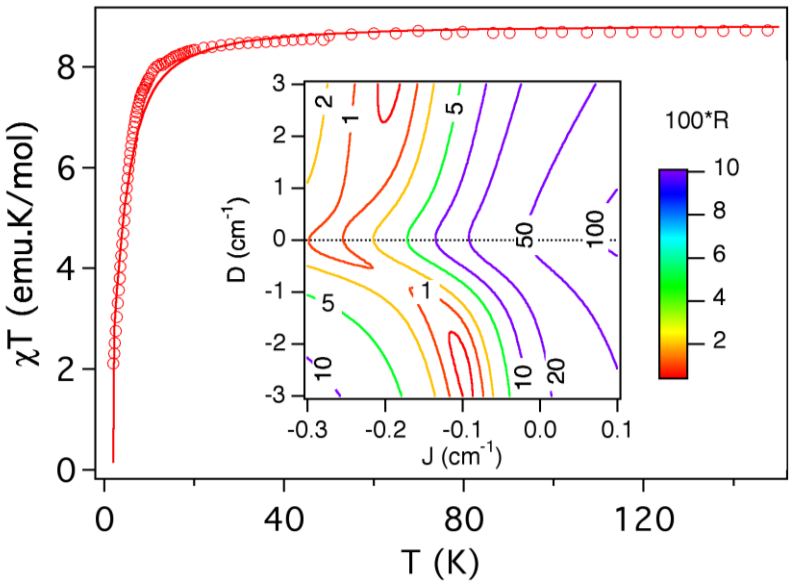

Fig. 4.19.- Magnetic properties of **4.2**: thermal dependence of the χ_mT product (inset: surface error plot of χ_m *vs*. T as a function of *J* and *D*). Solid line represents the calculated curve from the best simultaneous fit of susceptibility curve.

Magnetic measurements on an irradiated sample have also been performed in order to understand more details about the photocolouration process. Thermal dependence of the χ_mT product for this sample shows no significant changes with respect to **4.1**. Still, important differences appear in the isothermal magnetization performed at low temperatures (see **Fig. 4.20**). For example, the crossing of the magnetization curves at 2 and 5 K is not observed. This is not surprising since, according with the scenario depicted by DRS, IR, XPS and Mössbauer measurements, only a part of the oxalato ligands have been oxidised and, therefore, there is a mixture of different coordination spheres and possible oxidation states for iron ions. Thus, a quantitative data fitting is not possible. Assuming an average effect with only one *J* and *D* parameter in the sample and using the same model used before, a positive *D* of about 7 cm^{-1} has been obtained and negligible exchange. This large *D* value may reflect the presence of Fe(II), which is more anisotropic than Fe(III). Still, what is important to notice is that the irradiation leads to a small but detectable modification in the magnetic properties of the solid, which is in agreement with the fact that the decarboxylation process caused by the irradiation takes place mainly in the surface of the sample.

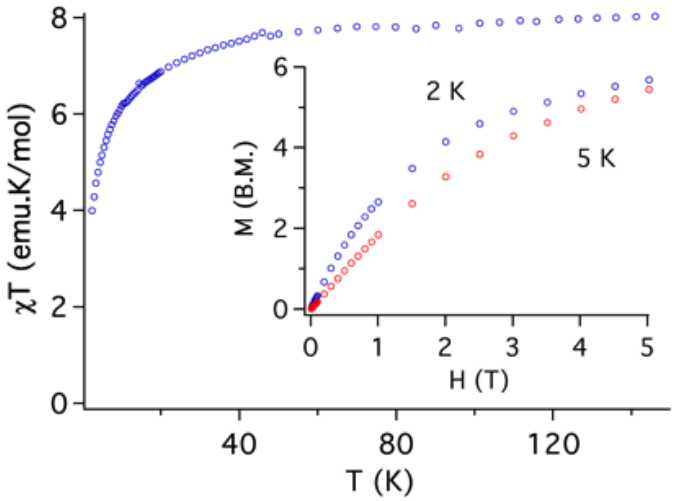

Fig. 4.20.- Magnetic properties of irradiated sample **4.1**: thermal dependence of the χ_mT product (inset: magnetization curves at 2 and 5 K).

4.2.11. Mechanism of the photo-induced colouration

In this section, we gather the experimental results described in the previous sections with the objective of proposing a mechanism for the photo-induced colouration of **4.1**. When exposed to UV irradiation, the light yellowish-green solid samples of **4.1** become black in a fast photocolouration process having a $t_{1/2}$ value of 4.25 min (as indicated by UV-vis/DRS measurements), while **4.2** does not exhibit any photo-induced colour change. IR spectroscopy indicates that the UV irradiation initiates a photodecomposition of the oxalato ligands of **4.1** into CO_2. This is confirmed by carbon analysis results, which indicate that there is less amount of carbon in the irradiated compound than in the initial one (0.49 % *vs.* 0.81 %). Each oxalato ligand that decomposes into CO_2 releases two electrons that are transferred to the iron and/or tungsten atoms of the POM. The DRS measurements suggest that the photocolouration is due to the photoreduction of W(VI) ($5d^0$) to W(V) ($5d^1$) and occurs via *d-d* transitions and/or W(VI)/W(V) intervalence charge transfer in the POM core; XPS measurements confirm the presence of up to 11.0 % of W(V) in the irradiated compound. On the other hand, Mössbauer measurements confirm the presence of Fe(II) (79 %) in the irradiated samples of **4.1-^{57}Fe** and discard it in non-irradiated samples. The magnetic properties of non-irradiated and irradiated samples of **4.1** are compatible with this scenario.

In view of all these experimental evidences, the photocolouration effect in **4.1** could arise according to the mechanism proposed in **Scheme 4.3**. The UV irradiation induces

the photo-dissociation of the coordinated bond between Fe(III) and the oxalato ligand, resulting in a ligand-to-metal charge transfer that yields Fe(II) and carbon dioxide radical ion ($CO_2^{\bullet-}$). Concomitantly, the radical ion most likely reacts with the POM yielding reduced W(V) ions, responsible for the intense photo-induced colouration of **4.1**.

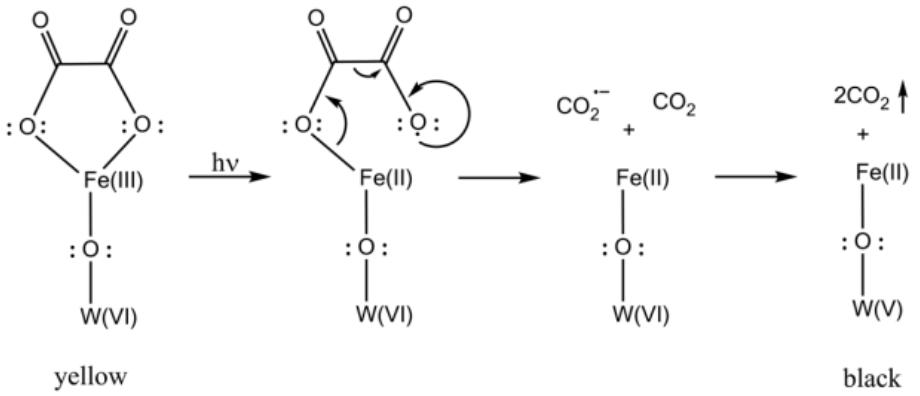

Scheme 4.3.- The mechanism depicted here implies a W atom directly connected (through an oxo bridge) to a Fe atom, but can be transposable to other W atoms.

According to the carbon analysis results and the TGA curve of an irradiated sample of **4.1** (see **Fig. 4.26**), it is possible to deduce the formula $K_{16}[(PW_9O_{34})_2Fe_2(C_2O_4)_x]\cdot nH_2O$ (x = 1.16 and n = 20.6), which reflects the partial loss of oxalato ligands under these conditions of UV irradiation (the decrease in the number of water molecules of crystallization is due to the vacuum conditions employed during the irradiation process). This formula must be regarded in compositional terms only, as it does not reflect the possible structural modifications of the trivacant A-α-$[PW_9O_{34}]^{9-}$ moieties, neither the change in coordination environment of the Fe atoms that almost certainly happen after the photo-decomposition of the oxalato ligands and concomitant reduction of Fe atoms and POM core (powder diffraction indicates that solid samples of **4.1** tend to amorphise upon irradiation, see **Fig. 4.27**).

If this irradiated black solid is stored in the dark in the presence of air, it reverts to its original light yellowish-green colour after about 7 days (DRS measurements show that the absorbance of a reversed sample is almost the same than before irradiation). As no colour reversion takes place under O_2-free atmosphere, it must be assumed that O_2 is able to oxidize the W(V) back to W(VI). This is confirmed by the XPS measurements of a reversed sample, which indicates that the concentration of W(V) is similar to the value found in the initial, non-irradiated sample. Moreover, Mössbauer measurements indicate

that also the Fe(II) ions are oxidized back to Fe(III) after keeping the irradiated samples during 12 days in dark in the presence of air.

Finally, the process of photo-induced colouration and colour reversion in the presence of air can be repeated at least 6 times for the same sample, although the photo-induced colouration is less intense after every cycle (the fading time keeps approximately constant after each cycle (~7 days)). This could have been anticipated because fewer amounts of oxalato ligands are left in the sample after each cycle of UV irradiation. Although the decrease of oxalato ligand after the second irradiation could not be confirmed by carbon analysis (the low percentage of C in the re-irradiated samples gave non-reproducible values), it is consistent with the Mössbauer results, which show that much less concentration of Fe(II) is attained after the irradiation of a reversed sample with UV light, in the same conditions as the irradiation of the pristine sample (20 % after the second irradiation *vs.* 79 % after the first irradiation).

4.3. Conclusions

In conclusion, **4.1** represents a new photo-responsive POM-based system that exhibits a remarkable photocolouration effect (from light yellowish-green to black) in the solid state when irradiated with UV light due to the partial photodecomposition of oxalato ligands and release of CO_2, concomitant with a partial reduction of W(VI) and Fe(III) to W(V) and Fe(II). As the photo-induced colouration effect can be repeated several times, this result opens the possibility to obtain new POM-based materials incorporating other photoactive Fe(III) carboxylate moieties which would give rise to different photo-responsive systems with tuneable properties. The interesting future work consists in studying the deposition of **4.1** on different substrates to test its use as chemical actinometer in solid state. The most widely accepted actinometer is the tris(oxalato)ferrate(III) complex (also called ferrioxalate), due to its wide wavelength range of absorption and high quantum yield.[10] Thanks to the POM, **4.1** exhibits a high-contrast photocolouration effect, which is advantageous for its use in solid state actinometry without the need of a postirradiation analytical procedure. Notice that in the standard ferrioxalate actinometry, phenanthroline is needed as a complexation reagent for Fe(II) and the subsequent colour development. In our case, this may enable the in-situ quantification of the light intensity in a simpler way by monitoring the absorbance of the irradiated solid sample of **4.1**.

4.4. Experimental section

4.4.1. General methods and materials

All reagents were of high purity grade, obtained from commercial sources, and used without any further purification. ^{57}Fe was obtained from CHEMGAS as iron powder with an isotope purity of 96.28 % in ^{57}Fe. The trivacant ligand $K_9[A\text{-}\alpha\text{-}PW_9O_{34}]\cdot 16H_2O$ was prepared according to the literature procedures[13] and confirmed by IR spectra. The potassium salts of the tris(oxalato)ferrate(III) and tris(malonato)ferrate(III) anions, $K_3[Fe(C_2O_4)_3]\cdot 3H_2O$ and $K_3[Fe(C_3H_2O_4)_3]\cdot H_2O$, were synthesized according to published procedures.[14] All the preparation and characterisation processes of POM **4.1** were carried out in dark to avoid photo-decomposition. Pure water ($\rho > 18$ MΩ·cm) was used throughout. It was obtained using an Elix-3/Millipore-Q Academic water purification system. IR spectra were recorded with KBr pellets on a Thermo NICOLET-5700 FT-IR spectrophotometer. Microanalysis was carried out with a Philips XL-30 scanning electron microscope coupled with a Philips EDAX Microanalysis system and the carbon content was determined by micro-analytical procedures using an EA 1110 CHNS-O elemental analyser from CE Instruments. Thermogravimetric analysis was performed on a Mettler Toledo TGA/SDTA851e analyzer. X-ray Powder Diffraction Measurements were carried out using ground samples of **4.1**, **4.2** and an irradiated sample of **4.1**, which were packed into 0.7 mm borosilicate capillaries prior to being mounted and aligned on an Empyrean PANalytical powder diffractometer, using Cu Kα radiation (λ = 1.54056 Å). For each sample, three repeated measurements were collected at room temperature ($2\theta = 4 - 40°$) and merged in a single diffractogram.

Diffuse Reflectance Spectroscopy (DRS) of solid samples was performed at room temperature and data converted to obtain absorption spectra. DRS was carried out on a Jasco V-670 spectrophotometer equipped with an integrated sphere coated with $BaSO_4$ and an internal diameter of 60 mm, where the baseline was recorded using a poly(tetrafluoroethylene) reference. Time evolution of UV-visible spectra of the aqueous solution with irradiation (with six Luzchem LZC-UVA lamps (λ_{exc} = 351 nm, P = 8 W)) were recorded on an Agilent 8453 UV-vis spectrophotometer from 380 to 800 nm using 10-mm-optical-path quartz cuvettes in milli-Q water. X-ray Photoelectron Spectroscopy (XPS) was performed at the X-ray Spectroscopy Service at the Universidad de Alicante using a K-Alpha X-ray photoelectron spectrometer system (Thermo Scientific). All

spectra were collected using Al Kα radiation (1486.6 eV), monochromatized by a twin crystal monochromator, yielding a focused X-ray spot (elliptical in shape with a major axis length of 400 μm) at 3 mA·C and 12 kV. The alpha hemispherical analyser was operated in the constant energy mode with survey scan pass energies of 200 eV to measure the whole energy band and 50 eV in a narrow scan to selectively measure the particular elements. XPS data were analysed using the Avantage software. A smart background function was used to approximate the experimental backgrounds. Charge compensation was achieved with the system flood gun that provides low energy electrons and low energy argon ions from a single source.

4.4.2. Synthesis of $K_{15}\{K\subset[(A\text{-}\alpha\text{-}PW_9O_{34})_2Fe_2(C_2O_4)_2]\}\cdot 29H_2O$ (Q-4.1)

$K_3[Fe(C_2O_4)_3]\cdot 3H_2O$ (0.178 g, 0.363 mmol) was dissolved in 3 mL of milli-Q water at 60 °C under stirring. To this emerald green solution, solid $K_9[A\text{-}\alpha\text{-}PW_9O_{34}]\cdot 16H_2O$ (0.387 g, 0.135 mmol) was added in small portions. By the end of the addition, the colour of the solution changed from emerald green to olive green. The solution was filtered while hot and the filtrate kept in the dark at room temperature in an open vial. After two hours, needle-shaped, light yellowish-green crystals were formed which were filtered and washed with milli-Q water to afford 0.251 g of the pure product (63.0 % based on A-α-$[PW_9O_{34}]^{9-}$).

Selected IR bands (2 % KBr pellet 2500-400 cm^{-1}) (**Fig. 4.21**): 1664.6(m), 1654.8(m), 1637.4(m), 1618.5(m), 1401.0(s), 1284.9(s), 1076.4(m), 1019.8(s), 940.9(m, sh), 885.2(w), 854.5(w), 741.5(m, sh), 658.8(s), 595.3(w), 518.4(m). Anal. Calcd (Found) for $K_{15}\{K\subset[(A\text{-}\alpha\text{-}PW_9O_{34})_2Fe_2(C_2O_4)_2]\}\cdot 29H_2O$: C 0.82 (0.81), Fe 1.90 (1.90), P 1.05 (0.90), W 56.35 (56.85), and K 10.61 (10.24). The TGA curve of **4.1** (**Fig. 4.22**) shows two distinct weight loss steps (the first one from 25 to ca. 203 °C and the second one from 203 to ca. 450 °C, with a total weight loss of 10.57 %), which correspond mainly to the loss of crystal waters and to the decomposition of the oxalato ligands, respectively (calcd 10.56 %). Powder X-ray diffraction pattern of this compound (**Fig. 4.23**) has been collected to confirm the phase purity of the bulk compound.

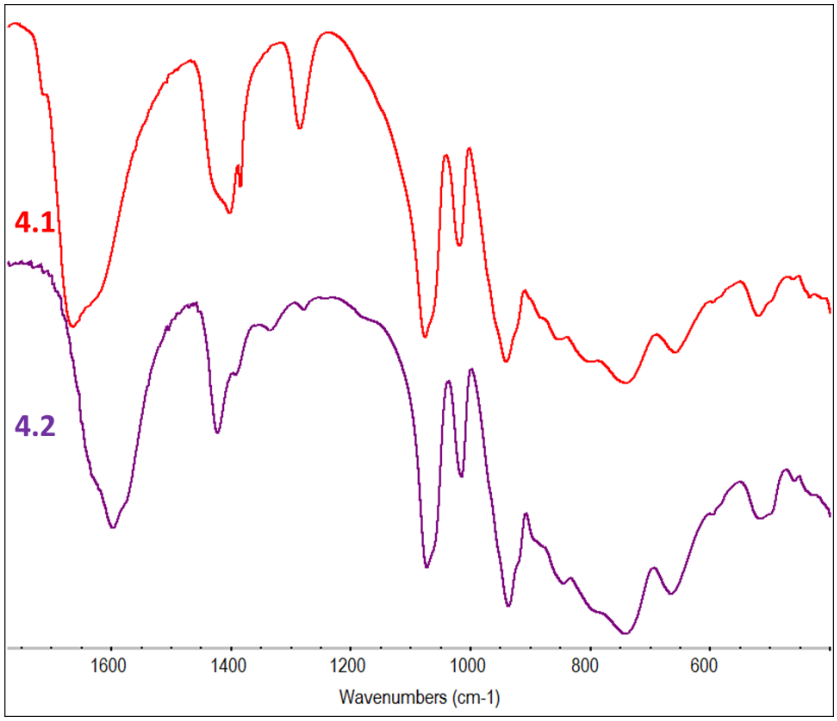

Fig. 4.21.- FT-IR spectra of **4.1** (red) and **4.2** (violet).

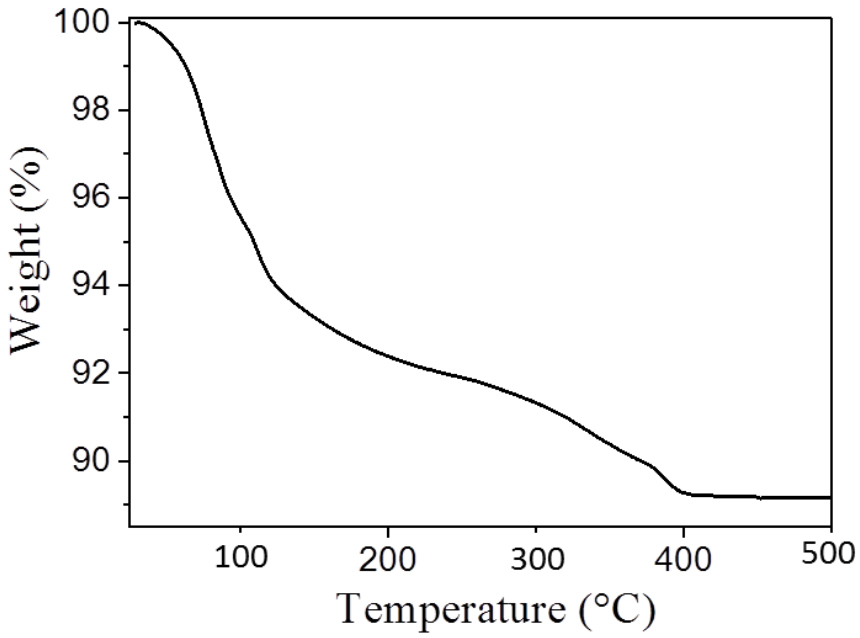

Fig. 4.22.- Thermogram curve of **4.1** from room temperature to 500 °C (experimental total weight loss: 10.57 %).

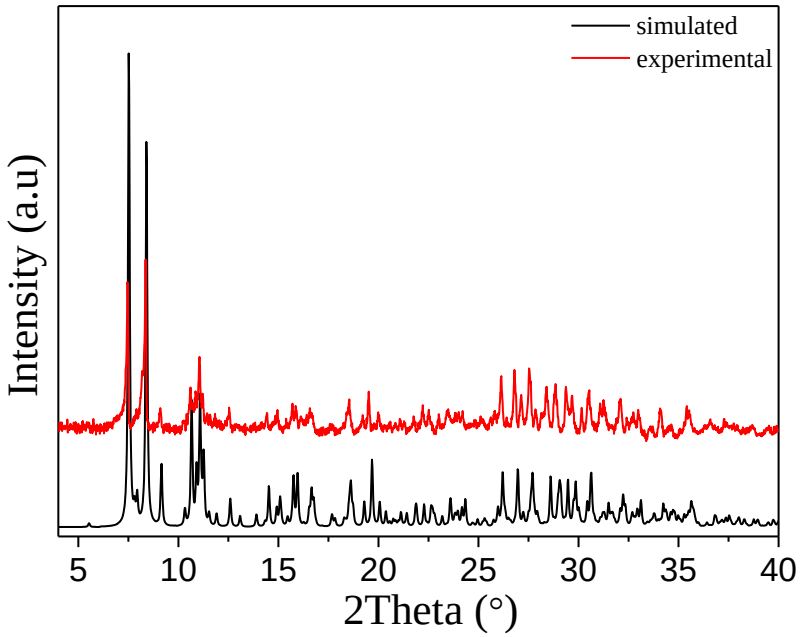

Fig. 4.23.- Comparison of simulated and experimental powder X-ray diffraction patterns for **4.1**.

4.4.3. Synthesis of $K_{15}\{K\subset[(A\text{-}\alpha\text{-}PW_9O_{34})_2Fe_2(C_3H_2O_4)_2]\}\cdot 27H_2O$ (Q-4.2)

The synthesis of **4.2** was carried out following the same procedure as for **4.1**, except that different amounts of the starting materials were used: 0.970 g (1.95 mmol) of $K_3[Fe(C_3H_2O_4)_3]\cdot H_2O$ (dissolved in 15 mL water) and 1.935 g (0.67 mmol) of $K_9[A\text{-}\alpha\text{-}PW_9O_{34}]\cdot 16H_2O$. Light green crystals (1.670 g in the first crop) were collected after one night, washed with a small amount of cold water and dried in air (Yield: 85.0 % based on A-α-$[PW_9O_{34}]^{9-}$).

Selected IR bands (2 % KBr pellet 2500-400 cm^{-1}) (**Fig. 4.21**): 2361.8(m), 1598.2(m), 1424.6(s), 1384.4(s), 1074.6(s), 1016.2(s), 937.0(s), 846.3(s), 742.4(m, sh), 666.5(s), 515.2(w). Anal. Calcd (Found) for $K_{15}\{K\subset[(A\text{-}\alpha\text{-}PW_9O_{34})_2Fe_2(C_3H_2O_4)_2]\}\cdot 27H_2O$: C 1.22 (1.18), Fe 1.90 (1.91), P 1.05 (0.98), W 56.25 (57.80), and K 10.60 (10.03). The TGA curve of **4.2** (**Fig. 4.24**) shows three distinct weight loss steps. The first step (25-203 °C) is attributed to the loss of water molecules. The second (203-350 °C) and third steps (350-450 °C) correspond to the decomposition of the malonato ligands. After that, no significant weight loss is detected. The total weight loss observed is 10.66 % (calcd 10.44 %). Powder X-ray diffraction pattern (**Fig. 4.25**) of this compound has been collected to confirm the phase purity of the bulk compound.

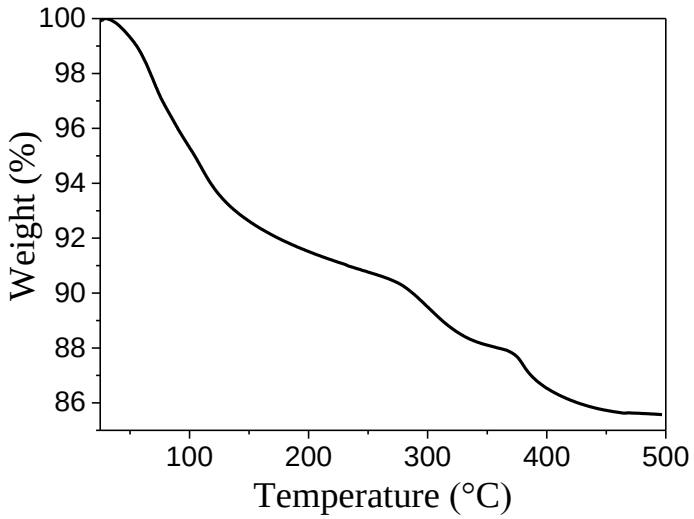

Fig. 4.24.- Thermogram curve of **4.2** from room temperature to 500 °C (experimental total weight loss: 10.66 %).

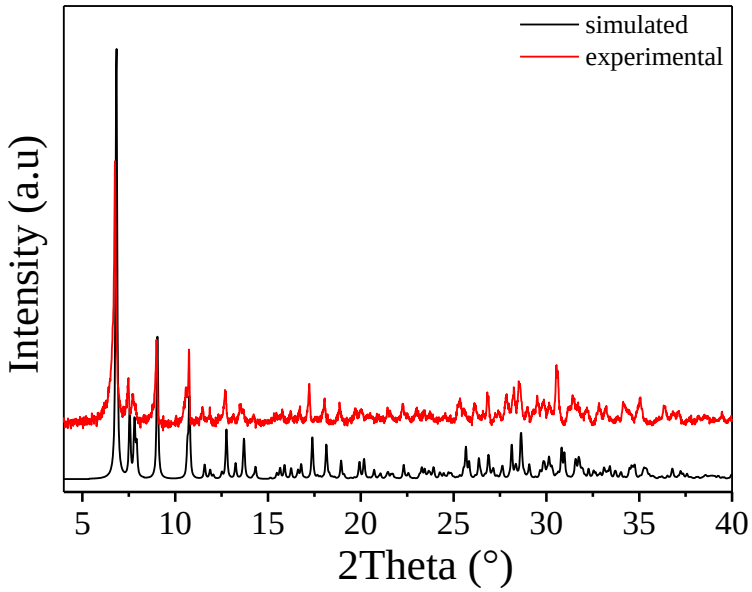

Fig. 4.25.- Comparison of simulated and experimental powder X-ray diffraction patterns for **4.2**.

4.4.4. Synthesis of $K_{15}\{K\subset[(A\text{-}\alpha\text{-}PW_9O_{34})_2{}^{57}Fe_2(C_2O_4)_2]\}\cdot 29H_2O$ (**4.1**-^{57}**Fe**) and $K_{15}\{K\subset[(A\text{-}\alpha\text{-}PW_9O_{34})_2{}^{57}Fe_2(C_3H_2O_4)_2]\}\cdot 27H_2O$ (**4.2**-^{57}**Fe**)

4.1-^{57}**Fe** and **4.2**-^{57}**Fe** were obtained following the same procedures as for **4.1** and **4.2**, but using $K_3[^{57}Fe(C_2O_4)_3]\cdot 3H_2O$ and $K_3[^{57}Fe(C_3H_2O_4)_3]\cdot H_2O$ as starting materials, respectively. These ^{57}Fe enriched tris(carboxylate)ferrate(III) salts were obtained as follows: solid ^{57}Fe (0.10 g, 1.79 mmol) and 5 mL of concentrated hydrochloric acid (12.1 mol/L)

were mixed and heated to 60 °C with stirring during one hour. Then, 5 mL of 30 % H_2O_2 were added and the resulting clear, yellowish-green solution was rotavaporated several times with water to remove residual H_2O_2, until yellow crystals were obtained ($^{57}FeCl_3{\cdot}6H_2O$). The crystals were dissolved in 2 mL of water and a solution containing KOH (0.451 g, 8.05 mmol) and oxalic acid (0.506 g, 5.62 mmol) in 5 mL of water was added. The mixture was allowed to evaporate slowly at room temperature and, after several days, 0.72 g of green crystals of $K_3[^{57}Fe(C_2O_4)_3]{\cdot}3H_2O$ were obtained (yield: 82.1 % based on ^{57}Fe). $K_3[^{57}Fe(C_3H_2O_4)_3]{\cdot}H_2O$ was obtained using the same procedure but replacing oxalic acid by malonic acid (yield: 94.0 % based on ^{57}Fe).

4.4.5. Preparation of irradiated samples of 4.1

Depending on the experiments, the grinded polycrystalline samples were irradiated with different number of lamps: two (for the DRS and IR measurements) and ten (for elemental analysis, TGA and XPS measurements) with Luzchem LZC-UVA lamps (λ_{exc} = 351 nm, P = 8 W) and, for Mössbauer spectroscopy, with one Spectroline (Model ENF-260c/FE, UV lamp, λ_{exc} = 365 nm). Anal. Calcd for a 3-day irradiated sample of **4.1** under vacuum: C (0.49). The TGA curve (see **Fig. 4.26**) shows two distinct weight loss steps (the first one from 25 to ca. 203 °C and the second one from 203 to ca. 450 °C, with a total weight loss of 7.57 %), which correspond mainly to the loss of crystal waters and to the decomposition of the oxalato ligands, respectively. From the elemental analysis and TGA results, a formula of the irradiated compound can be written as $K_{16}[(PW_9O_{34})_2Fe_2(C_2O_4)_{1.16}]{\cdot}20.6H_2O$. Powder X-ray diffraction pattern (see **Fig. 4.27**) of this compound has been collected which suggests that the bulk sample tends to amorphise upon irradiation under UV light.

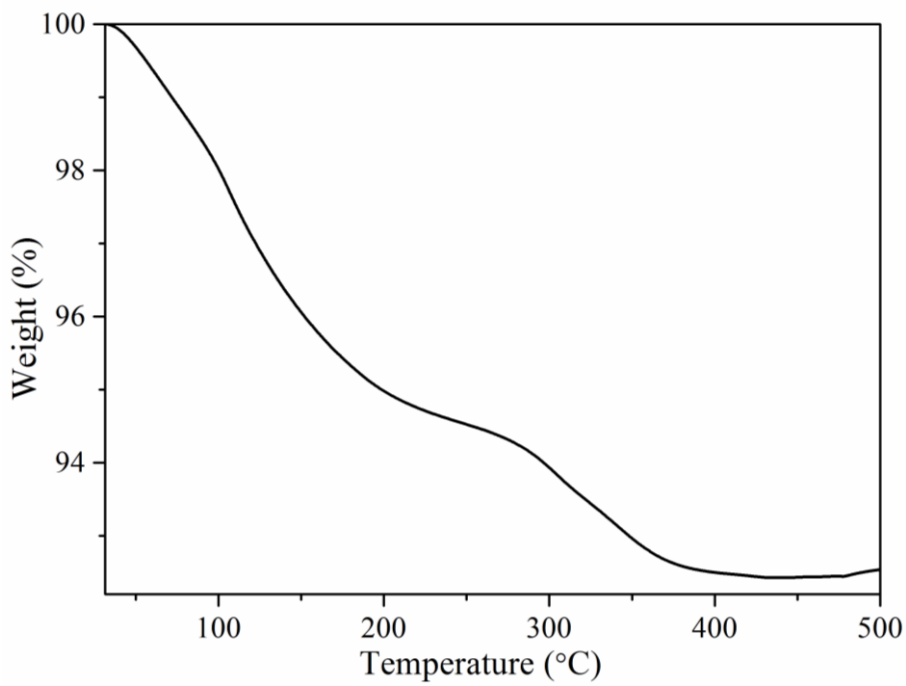

Fig. 4.26.- Thermogram curve of an irradiated sample of **4.1** from room temperature to 500 °C (experimental total weight loss: 7.57 %).

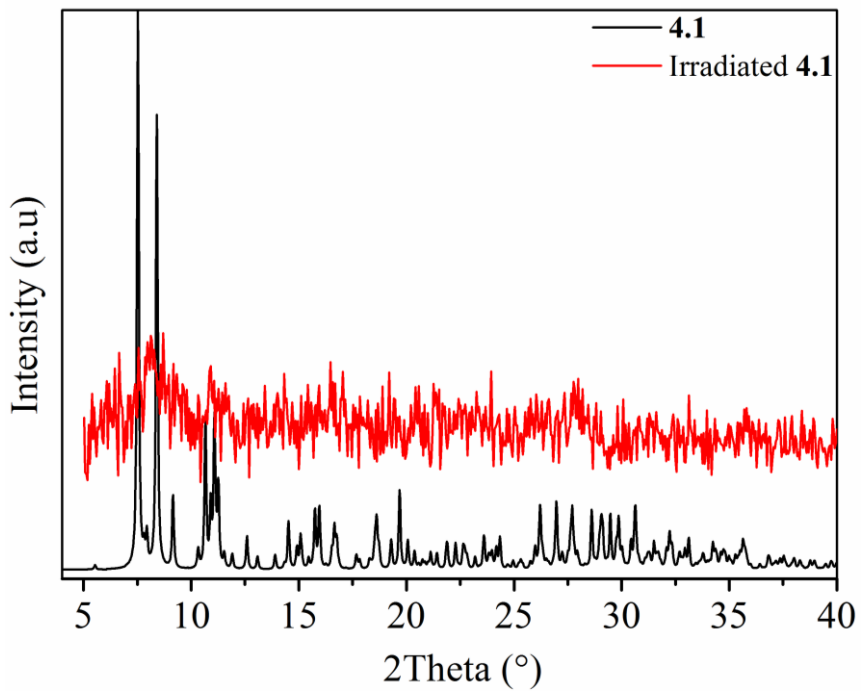

Fig. 4.27.- Comparison of the powder X-ray diffraction patterns of sample **4.1** before and after irradiation.

4.4.6. X-ray Crystallography

Suitable crystals of **4.1** and **4.2** were coated with Paratone N oil, suspended on small fiber loops, and placed in a stream of cooled nitrogen (120 K) on an Oxford Diffraction Supernova diffractometer equipped with a graphite-monochromated Enhance (Mo) X-ray Source (λ = 0.71073 Å). The data collection routines, unit cell refinements and data processing were carried out using the CrysAlis software package,[15] structure solution and refinement were carried out using SHELXS-97 and SHELXL-2014.[16] All atoms were refined anisotropically in both crystal structures except some water molecules of solvation having partial occupancies. An analytical numeric absorption correction was applied to the data of **4.1** using a multifaceted crystal model[17] integrated in the program CrysAlis, while for **4.2** a multi-scan absorption correction based on equivalent reflections was applied to the data using the program SORTAV.[18] In case of **4.1**, many residual densities were found in the final Fourier maps near the heavy W or Fe atoms. These residuals are attributed to relatively small twin components, which account for less than 10 % of the main component and, therefore, were left unmodeled. In **4.2** residual densities are found near the water molecules of crystallization located in the regions between the large POMs. These regions are usually occupied by disordered water molecules and metal cations. Hydrogen atoms of the malonato ligand were included at calculated positions and refined with a riding model. Hydrogen atoms of water molecules were not located. The cif files of both structures have been deposited in the inorganic crystal structure database (ICSD) with the deposition number CSD-430800. Crystallographic data for the two structures are summarized in **Table 4.3** and Fe-O bond distances and O-Fe-O angles are shown in **Table 4.4**.

Table 4.3.- Crystallographic data for $K_{15}\{K\subset[(A\text{-}\alpha\text{-}PW_9O_{34})_2Fe_2(C_2O_4)_2]\}\cdot 29H_2O$ (**Q-4.1**) and $K_{15}\{K\subset[(A\text{-}\alpha\text{-}PW_9O_{34})_2Fe_2(C_3H_2O_4)_2]\}\cdot 27H_2O$ (**Q-4.2**).

Compound	**Q-4.1**	**Q-4.2**
Empirical formula	$C_4H_{56}Fe_2K_{16}O_{104}P_2W_{18}$	$C_6H_{58}Fe_2K_{16}O_{103}P_2W_{18}$
Formula weight	5877.02	5887.06
Temperature (K)	120.05(10) K	120.00(10) K
Wavelength [Å]	0.71073 Å	0.71073 Å
Crystal system	Triclinic	Monoclinic
Space group	*P–1*	*C2/c*
a/Å	12.7825(4)	16.7363(2)
b/Å	13.3179(4)	26.2852(4)
c/Å	15.8979(3)	23.9398(4)
α/°	90.6680(18)	90
β/°	109.604(2)	101.127(2)
γ/°	104.435(3)	90
V/Å^3	2455.52(12)	10333.6(3)
Z	1	4
ρ_{calcd}/g cm^{-3}	3.974	3.784
μ/mm^{-1}	22.108	21.013
$R[F_o^2 > 2\sigma(F_o^2)]$ [a]	0.0770	0.0327
$R_w[F_o^2 > 2\sigma(F_o^2)]$ [b]	0.1800 [c]	0.0766 [d]

[a] $R = \Sigma(||F_o| - |F_c||)/\Sigma|F_o|$. [b] $R_w = \{\Sigma[w(F_o^2 - F_c^2)^2]/\Sigma[w(F_o^2)^2]\}^{1/2}$. $w = 1/[\sigma^2(F_o^2) + (AP)^2 + BP]$, where $P = (F_o^2 + 2F_c^2)/3$. [c] $A = 0.0659$, $B = 247.7103$. [d] $A = 0.0292$, $B = 277.8406$.

Table 4.4.- Fe-O bond distances (Å) and O-Fe-O angles (º) in **4.1** and **4.2**.

	4.1	**4.2**
Fe(1)-O(1F)	1.947(19)	2.028(6)
Fe(1)-O(9F)^{i}	1.957(13)	1.976(6)
Fe(1)-O(6F)	1.990(14)	1.992(6)
Fe(1)-O(2F)	2.011(18)	2.022(6)
Fe(1)-O(4F)^{i}	2.025(15)	1.977(6)
Fe(1)-O(5F)	2.037(14)	1.982(5)
O(1F)-Fe(1)-O(9F)^{i}	91.3(7)	94.4(2)
O(1F)-Fe(1)-O(6F)	87.6(7)	87.7(2)
O(9F)^{i}-Fe(1)-O(6F)	175.3(7)	176.6(2)
O(1F)-Fe(1)-O(2F)	82.1(8)	86.4(2)
O(9F)^{i}-Fe(1)-O(2F)	91.1(7)	87.1(2)
O(6F)-Fe(1)-O(2F)	93.2(7)	90.3(2)
O(1F)-Fe(1)-O(4F)^{i}	97.9(7)	87.5(2)
O(9F)^{i}-Fe(1)-O(4F)^{i}	87.8(6)	89.0(2)
O(6F)-Fe(1)-O(4F)^{i}	87.9(6)	93.8(2)
O(2F)-Fe(1)-O(4F)^{i}	178.9(6)	172.5(2)
O(1F)-Fe(1)-O(5F)	167.8(7)	175.3(2)
O(9F)^{i}-Fe(1)-O(5F)	93.1(6)	90.0(2)
O(6F)-Fe(1)-O(5F)	88.9(6)	87.9(2)
O(2F)-Fe(1)-O(5F)	86.5(7)	92.1(2)
O(4F)^{i}-Fe(1)-O(5F)	93.6(6)	94.2(2)

Symmetry transformations: (*i*) –x+1, –y, –z+1 (for **4.1**); –x, –y, –z+1 (for **4.2**).

4.4.7. Mössbauer spectroscopy

Mössbauer spectroscopy was carried out in collaboration with Prof. João C. Waerenborg from the Chemistry Department at IST/ITN, Instituto Superior Técnico (Universidade Técnica de Lisboa, Portugal).

Due to the low Fe content of **4.1** and **4.2** and the presence of W, which strongly absorbs the 14.4 keV Mössbauer gamma rays, the samples for Mössbauer spectroscopy were prepared using ^{57}Fe enriched starting material. The spectra were collected at room temperature in transmission mode using a conventional constant-acceleration spectrometer and a 25 mCi ^{57}Co source in a Rh matrix. The velocity scale was calibrated using α-Fe foil. Isomer shifts, IS, are given relative to this standard at room temperature. The absorbers were obtained by packing the powdered samples into perspex holders. Absorber thicknesses were calculated on the basis of the corresponding electronic mass-absorption coefficients for the 14.4 keV radiation, according to G. J. Long *et al.*[19] The spectra were fitted to lorentzian lines.[20] The relative areas and widths of both peaks in a quadrupole doublet were kept equal during refinement.

4.4.8. Magnetic measurements

Variable-temperature susceptibility measurements were carried out in the temperature range 2-300 K on compacted powder moulded from ground crystalline samples of **4.1** and **4.2** on a magnetometer equipped with a SQUID sensor (Quantum Design MPMS-XL-5). The data were corrected for the diamagnetic contributions of the polyanions as deduced by using the Pascal's constant tables. Isothermal magnetization measurements at low temperature (2 K and 5 K) were performed up to a field of 5 T in the same apparatus.

4.5. References

[1] (a) E. Coronado and G. Mínguez Espallargas, *Chem. Soc. Rev.*, 2013, **42**, 1525-1539; (b) S. Biswas, P. Kumari, P. M. Lakhani and B. Ghosh, *Eur. J. Pharm. Sci*, 2016, **83**, 184-202; (c) E. Cariati, E. Lucenti, C. Botta, U. Giovanella, D. Marinotto and S. Righetto, *Coord. Chem. Rev.*, 2016, **306**, 566-614; (d) H. Chen, D. Liu and Z. Guo, *Chem. Lett.*, 2016, **45**, 242-249; (e) M. Karimi, A. Ghasemi, P. Sahandi Zangabad, R. Rahighi, S. M. Moosavi Basri, H. Mirshekari, M. Amiri, Z. Shafaei Pishabad, A. Aslani, M. Bozorgomid, D. Ghosh, A. Beyzavi, A. Vaseghi, A. R. Aref, L. Haghani, S. Bahrami and M. R. Hamblin, *Chem. Soc. Rev.*, 2016, **45**, 1457-501; (f) M. Lemanowicz, A. Gierczycki and W. Kuźnik, *Polimery*, 2016, **61**, 92-97; (g) Z. Liu, W. Wang, R. Xie, X. Ju and L. Chu, *Chem. Soc. Rev.*, 2016, **45**, 460-474; (h) T. Lu, W. Peng, S. Zhu and D. Zhang, *Nanotechnology*, 2016, **27**, 122001; (i) C. G. Palivan, R. Goers, A. Najer, X. Zhang, A. Car and W. Meier, *Chem. Soc. Rev.*, 2016, **45**, 377-411; (j) H. Wang, Q. Huang, H. Chang, J. Xiao and Y. Cheng, *Biomater Sci.*, 2016, **4**, 375-390.

[2] (a) P. Gütlich, Y. García and T. Woike, *Coord. Chem. Rev.*, 2001, **219**, 839-879; (b) S. Ohkoshi, H. Tokoro, T. Hozumi, Y. Zhang, K. Hashimoto, C. Mathonière, I. Bord, G. Rombaut, M. Verelst, C. C. D. Moulin and F. Villain, *J. Am. Chem. Soc.*, 2006, **128**, 270-277; (c) S. Ohkoshi and H. Tokoro, *Acc. Chem. Res.*, 2012, **45**, 1749-1758; (d) G. Abellán, E. Coronado, C. Martí-Gastaldo, A. Ribera, J. L. Jordá and H. García, *Adv Mater.*, 2014, **26**, 4156-4162; (e) G. Abellán, C. Martí-Gastaldo, A. Ribera and E. Coronado, *Acc. Chem. Res.*, 2015, **48**, 1601-1611; (f) H. Tokoro and S. Ohkoshi, *Bull. Chem. Soc. Jpn.*, 2015, **88**, 227-239.

[3] (a) D. Bléger and S. Hecht, *Angew. Chem. Int. Ed.*, 2015, **54**, 11338-11349; (b) M. Fredersdorf, R. Göstl, A. Kolmer, V. Schmidts, P. Monecke, S. Hecht and C. M. Thiele, *Chem. Eur. J.*, 2015, **21**, 14545-14554; (c) W. Wang, J. Hu, M. Zheng, L. Zheng, H. Wang and Y. Zhang, *Org Biomol Chem.*, 2015, **13**, 11492-11498; (d) M. Han, Y. Luo, B. Damaschke, L. Gómez, X. Ribas, A. Jose, P. Peretzki, M. Seibt and G. H. Clever, *Angew. Chem. Int. Ed.*, 2016, **55**, 445-449.

[4] (a) E. J. Harbron, C. M. Davis, J. K. Campbell, R. M. Allred, M. T. Kovary and N. J. Economou, *J Phys Chem C.*, 2009, **113**, 13707-13714; (b) S. Köytepe, M. H. Demirel, A. Gültek and T. Seçkin, *Polym. Int.*, 2014, **63**, 778-787.

[5] (a) M. T. Pope, *Heteropoly and Isopoly Oxometalates*, Springer-Verlag Berlin, Heidelberg, 1983; (b) M. T. Pope and A. Muller, *Angew. Chem. Int. Ed. Engl.*, 1991, **30**, 34-48; (c) W. He, S. Li, H. Zang, G. Yang, S. Zhang, Z. Su and Y. Lan, *Coord. Chem. Rev.*, 2014, **279**, 141-160; (d) M. Mirzaei, H. Eshtiagh-Hosseini, M. Alipour and A. Frontera, *Coord. Chem. Rev.*, 2014, **275**, 1-18; (e) J. J. Walsh, A. M. Bond, R. J. Forster and T. E. Keyes, *Coord. Chem. Rev.*, 2016, **306**, 217-234.

[6] (a) T. He and J. Yao, *Prog Mater Sci.*, 2006, **51**, 810-879; (b) V. Coué, R. Dessapt, M. Bujoli-Doeuff, M. Evain and S. Jobic, *Inorg. Chem.*, 2007, **46**, 2824-2835; (c) Y. Yang, L. Yue, H. Li, E. Maher, Y. Li, Y. Wang, L. Wu and V. W. Yam, *Small*, 2012, **8**, 3105-3110; (d) H. El Moll, A. Dolbecq, I. M. Mbomekalle, J. Marrot, P. Deniard, R. Dessapt and P. Mialane, *Inorg. Chem.*, 2012, **51**, 2291-2302; (e) K. Hakouk, O. Oms, A. Dolbecq, H. El Moll, J. Marrot, M. Evain, F. Molton, C. Duboc, P. Deniard, S. Jobic, P. Mialane and R. Dessapt, *Inorg. Chem.*, 2013, **52**, 555-557; (f) Q. Zheng, L. Vilà-Nadal, C. Busche, J. S. Mathieson, D. Long and L. Cronin, *Angew. Chem. Int. Ed.*, 2015, **54**, 7895-7899; (g) Y. Gong, Q. Hu, C. Wang, L. Zang and L. Yu, *Langmuir*, 2016, **32**, 421-427; (h) W. Chen, U. Tong, T. Zeng, C. Streb and Y. Song, *J. Mater. Chem.* C, 2015, **3**, 4388-4393; (i) C. Streb, *Dalton Trans.*, 2012, **41**, 1651-1659; (j) B. Matt, J. Fize, J. Moussa, H. Amouri, A. Pereira, V. Artero, G. Izzet and A. Proust, *Energy Environ. Sci.*, 2013, **6**, 1504-1508; (k) A. Proust, R. Thouvenot and P. Gouzerh, *Chem. Comm.*, 2008, 1837-1852; (l) C. Zhao, C. S. Kambara, Y.

Yang, A. L. Kaledin, D. G. Musaev, T. Lian and C. L. Hill, *Inorg. Chem.*, 2013, **52**, 671-678.
[7] T. Yamase, *Chem. Rev.*, 1998, **98**, 307-325.
[8] R. Q. Fang, X. M. Zhang, H. S. Wu and S. W. Ng, *Acta Crystallogr. Sect E Struct Rep Online*, 2004, **60**, M359-M361.
[9] L. Deguillaume, M. Leriche, K. Desboeufs, G. Mailhot, C. George and N. Chaumerliac, *Chem. Rev.*, 2005, **105**, 3388-3431.
[10] H. J. Kuhn, S. E. Braslavsky and R. Schmidt, *Pure Appl Chem*, 2004, **76**, 2105-2146.
[11] (a) E. L. Simmons and W. W. Wendlandt, *Coord. Chem. Rev.*, 1971, **7**, 11-27; (b) Y. G. Zuo and J. Hoigne, *Environ. Sci. Technol.*, 1992, 26, 1014-1022; (c) B. C. Faust and R. G. Zepp, *Environ. Sci. Technol.*, 1993, **27**, 2517-2522.
[12] (a) A. Dolbecq, J. Compain, P. Mialane, J. Marrot, E. Rivière and F. Sécheresse, *Inorg. Chem.*, 2008, **47**, 3371-3378; (b) A. Sartorel, M. Carraro, G. Scorrano, B. S. Bassil, M. H. Dickman, B. Keita, L. Nadjo, U. Kortz and M. Bonchio, *Chem.-Eur. J.*, 2009, **15**, 7854-7858.
[13] (a) R. Contant, *Can. J. Chem.*, 1987, **65**, 568-573; (b) P. J. Domaille, *Inorg. Synth.*, A. P. Ginsberg, John Wiley & Sons, New York, 1990, 96-104.
[14] D. Collison and A. K. Powell, *Inorg. Chem.*, 1990, **29**, 4735-4746.
[15] Agilent Technologies UK Ltd, Oxford, UK, *CrysAlis PRO Software system*, 2013.
[16] Sheldrick, G. M. *SHELXTL* Version 2014/7. *http://shelx.uni-ac.gwdg.de/SHELX/index.php*.
[17] R. C. Clark and J. S. Reid, *Acta Crystallogr. A*, 1995, **51**, 887-897.
[18] R. H. Blessing, *J. Appl. Crystallogr.*, 1997, **30**, 421-426.
[19] G. J. Long, T. E.Cranshaw and G. Longworth, *Mossb. Effect. Ref. Data J.*, 1983, **6**, 42-49.
[20] E. Coronado, J. R. Galán-Mascarós, C. Martí-Gastaldo, J. C. Waerenborgh and P. Gaczyński, *Inorg. Chem.*, 2008, **47**, 6829-6839.
[21] G. M. Bancroft, Dharmawa.kg and A. G. Maddock, *Inorg. Chem.*, 1970, **9**, 223-226.
[22] A. Abras, M. F. D. Filho and M. M. Braga, *Thermochim Acta*, 1986, **101**, 35-44.
[23] A. N. Chekhlov, *Russ. J. Inorg. Chem.*, 2008, **53**, 928-932.
[24] (a) W. H. Knoth, P. J. Domaille and R. D. Farlee, *Organometallics*, 1985, **4**, 62-68; (b) W. H. Knoth, P. J. Domaille and R. L. Harlow, *Inorg. Chem.*, 1986, **25**, 1577-1584; (c) N. M. Okun, T. M. Anderson and C. L. Hill, *J. Am. Chem. Soc.*, 2003, **125**, 3194-3195; (d) V. Artero, A. Proust, P. Herson, F. Villain, C. C. D. Moulin and P. Gouzerh, *J. Am. Chem. Soc.*, 2003, **125**, 11156-11157; (e) N. Belai and M. T. Pope, *Chem. Comm.*, 2005, 5760-5762; (f) T. M. Anderson, R. Cao, E. Slonkina, B. Hedman, K. O. Hodgson, K. I. Hardcastle, W. A. Neiwert, S. X. Wu, M. L. Kirk, S. Knottenbelt, E. C. Depperman, B. Keita, L. Nadjo, D. G. Musaev, K. Morokuma and C. L. Hill, *J. Am. Chem. Soc.*, 2005, **127**, 11948-11949; (g) R. Villanneau, S. Renaudineau, P. Herson, K. Boubekeur, R. Thouvenot and A. Proust, *Eur. J. Inorg. Chem.*, 2009, 479-488; (h) L. F. Piedra-Garza, M. H. Dickman, O. Moldovan, H. J. Breunig and U. Kortz, *Inorg. Chem.*, 2009, **48**, 411-413; (i) Y. Saku, Y. Sakai, A. Shinohara, K. Hayashi, S. Yoshida, C. N. Kato, K. Yozac and K. Nomiya, *Dalton Trans.*, 2009, 805-813; (j) R. Cao, K. P. O'Halloran, D. A. Hillesheim, K. I. Hardcastle and C. L. Hill, *CrystEngComm*, 2010, **12**, 1518-1525; (k) C. N. Kato, Y. Katayama, M. Nagami, M. Kato and M. Yamasaki, *Dalton Trans.*, 2010, **39**, 11469-11474; (l) G. Wang, C. Pan, K. Li, X. Cui, H. Wang, Y. Wang, S. Shi and J. Xu, *Inorg. Chem. Comm.*, 2010, **13**, 116-118; (m) R. Villanneau, D. Racimor, E. Messner-Henning, H. Rousseliere, S. Picart, R. Thouvenot and A. Proust, *Inorg. Chem.*, 2011, **50**, 1164-1166; (n) D. Zhao and R. Ye, *J. Cluster Sci.*, 2011, **22**, 563-571; (o) R. Cao, K. P. O'Halloran, D. A. Hillesheim, S. Lense, K. I. Hardcastle and C. L. Hill, *CrystEngComm.*, 2011, **13**, 738-740; (p) M. Barsukova-Stuckart, L. F. Piedra-Garza, B. Gautam, G. Alfaro-Espinoza, N. V. Izarova, A. Banerjee, B. S. Bassil, M. S. Ullrich, H. J. Breunig, C. Silvestru and U. Kortz, *Inorg. Chem.*, 2012, **51**, 12015-12022; (q) H. Yang, L. Zhang, L. Yang, X. Zhang, W. You and Z. Zhu,

Inorg. Chem. Comm., 2013, **29**, 33-36; (r) R. Villanneau, A. Ben Djamaa, L. Chamoreau, G. Gontard and A. Proust, *Eur. J. Inorg. Chem.*, 2013, 1815-1820; (s) R. Al-Oweini, B. S. Bassil, T. Palden, B. Keita, Y. Lan, A. K. Powell and U. Kortz, *Polyhedron*, 2013, **52**, 461-466; (t) J. M. Berg, A. J. Gaunt, I. May, A. L. Pugmire, S. D. Reilly, B. L. Scott and M. P. Wilkerson, *Inorg. Chem.*, 2015, **54**, 4192-4199.

[25] I. D. Brown and D. Altermatt, *Acta Crystallogr., B*, 1985, **41**, 244-247.

[26] J. W. Steed, *Coord. Chem. Rev.*, 2001, **215**, 171-221.

[27] I. D. Brown and D. Altermatt, *Acta Crystallogr., B*, 1985, **41**, 244-247.

[28] S. M. Kanowitz and G. J. Palenik, *Inorg. Chem.*, 1998, **37**, 2086-2088.

[29] Y. Wang, X. Sun, S. Li, P. Ma, J. Niu and J. Wang, *Cryst. Growth Des.*, 2015, **15**, 2057-2063.

[30] (a) X. A. Zhang, W. J. Wu, Y. H. Man, T. Tian, X. Z Tian and J. F. Wang, *Sci. China B*, 2007, **50**, 318-326; (b) L. Zhang, W. Gu, X. Liu, Z. Dong and B. Li, *CrystEngComm*, 2008, **10**, 652-654; (c) J. Compain, P. Deniard, R. Dessapt, A. Dolbecq, O. Oms, F. Sécheresse, J. Marrot and P. Mialane, *Chem. Commun.*, 2010, **46**, 7733-7735; (d) X. Luo and C. Yang, *Phys. Chem. Chem. Phys.*, 2011, **13**, 7892-7902.

[31] R. Dessapt, M. Collet, V. Coué, M. Bujoli-Doeuff, S. Jobic, C. Lee and M. Whangbo, *Inorg. Chem.*, 2009, **48**, 574-580.

[32] R. Dessapt, M. Collet, V. Coué, M. Bujoli-Doeuff, S. Jobic, C. Lee and M. Whangbo, *Inorg. Chem.*, 2009, **48**, 574-580.

[33] K. Nakamoto, *Infrared and Raman Spectra of Inorganic and Coordination Compounds. Part B: Applications in Coordination, Organometallic and Bioinorganic Chemistry*, John Wiley & Sons, 2009.

[34] G. Keresztury, M. Incze, F. Sóti and L. Imre, *Spectrochim. Acta A Mol. Biomol. Spectrosc.*, 1980, **36**, 1007-1008.

[35] (a) A. S. Brar and B. S. Randhawa, *Bull. Chem. Soc. Jpn.*, 1981, 54, 3166-3169; (b) B. S. Randhawa, *J. Radioanal. Nucl.*, 1998, **230**, 295-298.

[36] W. Feng, Y. S. Ding, Y. Liu and R. Lu, *Mater. Chem. Phys.*, 2006, **98**, 347-352.

[37] N. N. Greenwood and T. C. Gibb, *Mössbauer Spectroscopy*, Chapman and Hall, London, 1971.

[38] P. S. Bassi, B. S. Randhawa and S. Kaur, *Hyperfine Interactions*, 1986, **28**, 745-748.

[39] E. Coronado, J. R. Galán-Mascarós, C. J. Gómez-García, J. M. Martínez-Agudo, E. Martínez-Ferrero, J. C. Waerenborgh and M. Almeida, *J. Solid State Chem.*, 2001, **159**, 391-402.

[40] F. Menil, *J. Phys. Chem. Solids*, 1985, **46**, 763-789.

[41] F. Neese and E. I. Solomon, *J. Am. Chem. Soc.*, 1998, 120, 12829-12848.

[42] A. J. Simaan, F. Banse, J. J. Girerd, K. Wieghardt and E. Bill, *Inorg. Chem.*, 2001, 40, 6538-6540.

[43] Y. Zhang, M. S. Gebhard and E. I. Solomon, *J. Am. Chem. Soc.*, 1991, 113, 5162-5175.

Chapter 5. General Conclusions

This thesis has been focused on the chemistry of new POMs. This includes the preparation of POMs with new topologies, the encapsulation of magnetic cations from the 3*d* and 4*f* blocks, the study of their stability in solid state and in solution and the study of their magnetic properties and photocolouration behaviour. Several new systems of POMs with interesting magnetic or photo-responsive properties were successively obtained and well characterised.

Although specific conclusions have been included at the end of each chapter, the most relevant overall conclusions will be summarized hereafter:

(1) In order to obtain high nuclearity cobalt-containing POM clusters with new topologies, two main synthetic strategies have been followed: (i) reacting preformed lacunary POM species with transition metal ions and/or additional oxoanions (step-by-step approach) and (ii) direct self-assembly of tungstate (or molybdate, vanadate, *etc.*) anions, transition metal ions and/or additional oxoanions (one-pot approach). Both strategies require strict control of the key synthetic parameters, such as pH, temperature, concentration of reagents, *etc*. While the first approach is a more directed synthetic strategy towards the preparation of a specific POM species, the second one is prone to generate multiple POM products in solution, which usually need to be separated in the workup or by crystallization/recrystallization steps.

Ten new cobalt-substituted POMs have been synthesized following these two different synthetic strategies. These are displayed in **Fig. 5.1**. **2.1**, **2.2** and **2.4** were prepared following the step-by-step approach while **2.2**, **2.3**, **2.5**, **2.6**, **2.7**, **2.8** and **2.9** were obtained by the one-pot approach. The preparation of some of these POMs has been achieved thanks to the implementation of two novel synthetic strategies in POM chemistry: (i) a partial reductive hydrolysis of a Co(III)-containing POM using hydrazine, and (ii) the substitution of a variable number of terminal water ligands in **2.1** by other polyoxoanion fragments to construct larger POMs. The future application of these novel strategies will allow the preparation of new POMs containing *d*-transition metal ions having new topologies, high-nuclearities, and interesting magnetic and/or catalytic properties.

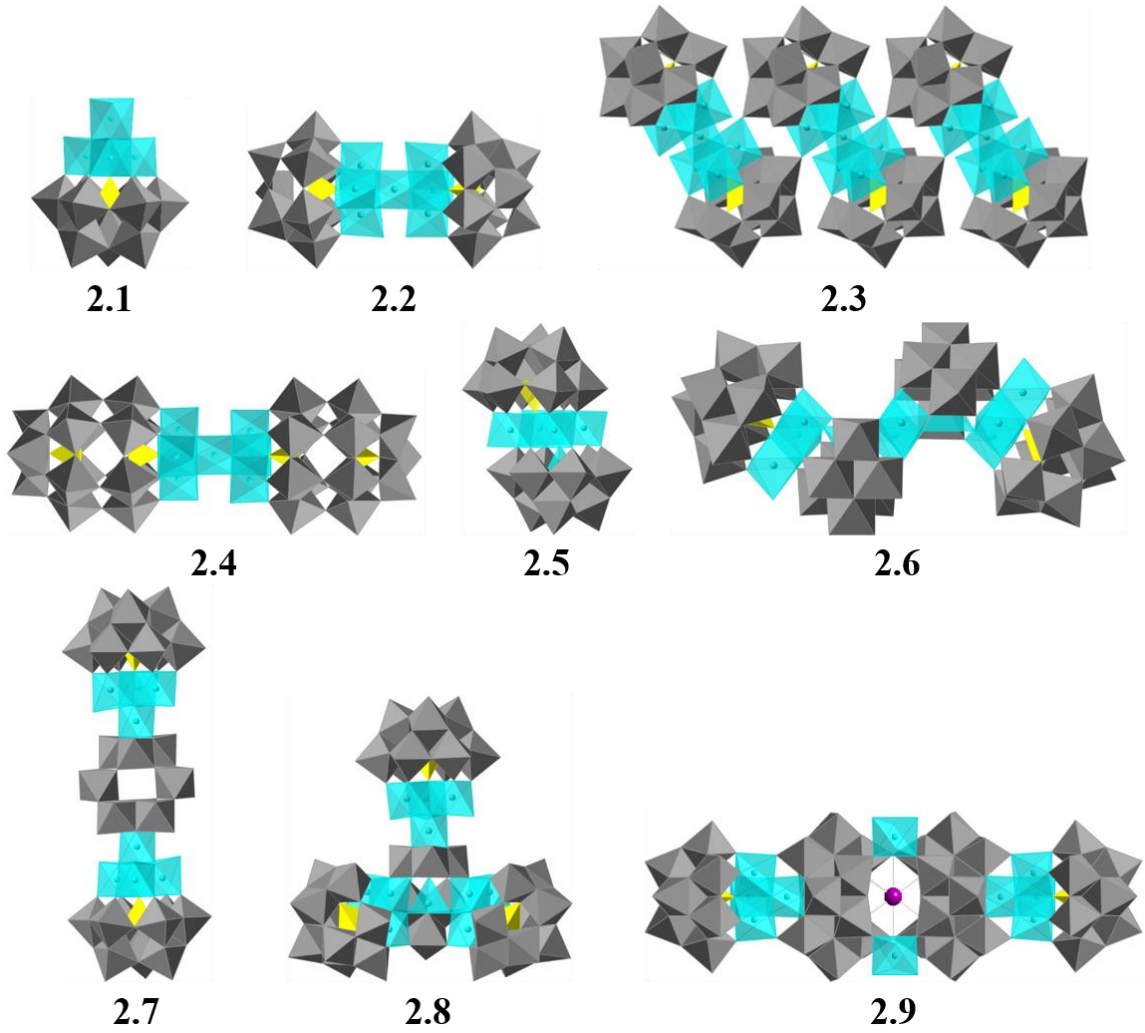

Fig. 5.1.- Polyhedral representations of all cobalt-containing POMs in chapter 2. Gray octahedra, [WO_6]; yellow tetrahedra, [PO_4]; cyan octahedra, [CoO_6]; cyan tetrahedra, [CoO_4]; purple sphere, K.

(2) The chemistry of polyoxomolybdates (more challenging than that of polyoxotungstates) was used to obtain SIMs. A family of organic soluble lanthanoid-containing polyoxomolybdates has been obtained, which is based on two [β-Mo_8O_{26}]$^{4-}$ encapsulating a lanthanoid ion (see **Fig. 5.2**). This result has opened the possibility of making these magnetic molecules soluble in organic solvents, thus facilitating their processing and incorporation into devices. This is in contrast with the SIMs based on polyoxotungstate ligands, which commonly are only soluble in water. Finally yet importantly, the enhanced reduction potential of polyoxomolybdates may also be of interest to incorporate delocalized electrons into the mixed-valence POM framework, thus increasing the interest of these magnetic molecules in spintronics.

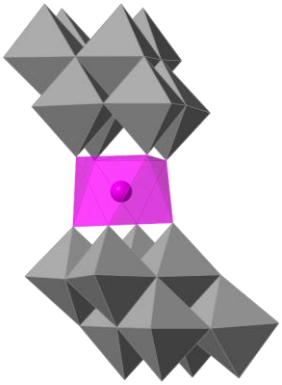

Fig. 5.2.- Polyhedral representations of the Ln^{3+}-containing POMs in chapter 3. Gray octahedra, [WO_6]; pink polyhedra, [LnO_8].

(3) A new photo-responsive POM-based system was obtained following the one-pot synthetic approach, which is formed by a Fe(III) complex containing both oxalato and POM ligands (see **Fig. 5.3**). This compound exhibits remarkable photo-induced colouration effect in the solid state when irradiated with UV light due to the partial photodecomposition of oxalato ligands and release of CO_2, concomitant with a partial reduction of W(VI) and Fe(III) to W(V) and Fe(II). As the photocolouration effect can be repeated several times, this result opens the possibility to obtain new POM-based materials incorporating other photoactive Fe(III) carboxylate moieties which would give rise to different photo-responsive systems with tunable properties. The potential and interesting future work consists in studying the deposition on different substrates to test its use as chemical actinometer in solid state.

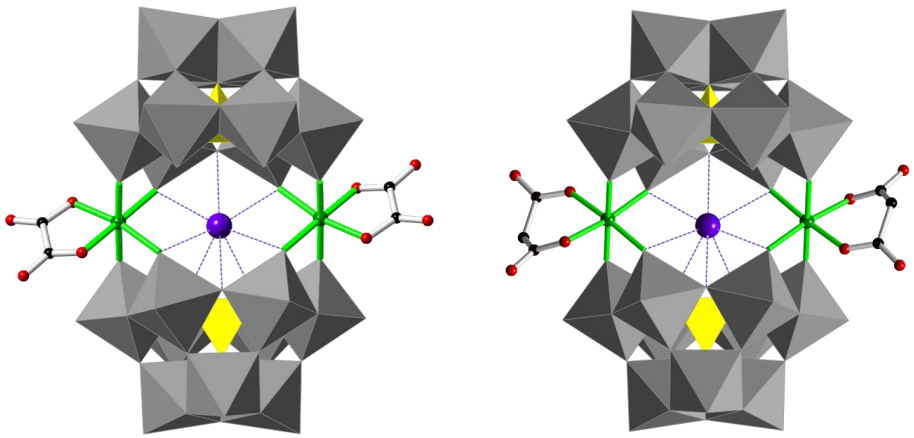

Fig. 5.3.- Combined polyhedral and ball-and-stick representations of the two Fe(III)-containing POMs in chapter 4. Gray octahedra, [WO_6]; yellow tetrahedra, [PO_4]; green spheres, Fe; black spheres, C; red spheres, O; purple spheres, K.

Chapter 6. Resumen de la Tesis Doctoral

Título:

El uso de polioxometalatos para el diseño de clústeres magnéticos con alta nuclearidad, moléculas imán con un solo centro magnético y materiales fotosensibles

Antecedentes científicos, Motivación y Objetivos

Los polioxometalatos (POM) son clústeres inorgánicos formados por oxígeno y átomos metálicos de los grupos 5 y 6 (llamados metales constituyentes, generalmente Mo, W, V y Nb) en sus estados de oxidación maximos (es decir, iones d^0 y/o d^1) que, además, suelen contener otros heteroátomos, como fósforo o silicio. Los POMs muestran una amplísima variedad estructural, tanto en su forma como en su tamaño (que se encuentra típicamente entre 1 y 5 nm, es decir tamaño nanoscópico) y altas cargas aniónicas (usualmente, entre –3 y –16). Aunque desde su descubrimiento, a mediados del siglo XIX, miles de POMs han sido descritos, el interés por estos compuestos (síntesis, estructuras, propiedades y aplicaciones) no para de crecer. En las últimas dos décadas, nuestro grupo ha estado investigando el uso de los POMs como moléculas modelo para estudiar fenómenos electronicos fundamentales de los sólidos como son el canje magnético y la transferencia electrónica.[1-11] Recientemente, la investigación en POMs ha evolucionado, y se ha descubierto que son candidatos ideales para ser utilizados en campos tan diversos como el nanomagnetismo molecular, la espintrónica,[8,10,12] la computación cuántica[13-14] y el fotocromismo molecular.[15] Este interés se debe a los siguientes motivos:

(i) Los POMs son muy estables, robustos y resistentes a la oxidación ya que mantienen su integridad estructural en estado sólido, en disolución e incluso cuando se depositan sobre superficies.

(ii) Los POMs pueden actuar como ligandos polidentados (mediante sus grupos oxo y/o hidroxo) y acomodar uno o varios iones magnéticos en localizaciones específicas, formando clústeres magnéticos con una gran variedad de topologías y tamaños.

(iii) Los POMs pueden aceptar fácilmente uno o más electrones que, generalmente, están deslocalizados en los metales constituyentes (W, Mo, *etc*.), dando lugar a clústeres de valencia mixta con interesantes propiedades magnéticas y efectos fotocrómicos y electrocrómicos.

Los dos primeros motivos abren la puerta a multitud de posibilidades para el estudio de la interacción de espines localizados en clústeres de distintas nuclearidades magnéticas encapsulados en POMs. Además, el tercer argumento hace de los POMs una clase única de materiales inorgánicos, ya que pueden actuar como aceptores electrónicos en procesos de transferencia electrónica fotoinducida, a menudo con un comportamiento reversible y una excelente estabilidad. Finalmente, la combinación de la transferencia electrónica junto con el canje magnético hace de la química de POMs una herramienta fundamental y excitante para el estudio de diversas propuestas teóricas que pueden permitir avanzar en el conocimiento de sistemas moleculares en el área de la espintrónica.[16]

El tema central de esta tesis doctoral es el diseño, síntesis y caracterización estructural de nuevos POMs, así como la determinación de su estabilidad en estado sólido y en disolución y el estudio de sus propiedades magnéticas y fotocrómicas. En cuanto a las propiedades magnéticas, se pretende obtener POMs que presenten nuevas topologías de clústeres magnéticos y también polioxometalatos con comportamiento de molécula imán basada en un solo centro magnético (*Single Ion Magnet* o *SIM*) que sean solubles tanto en agua como en disolventes orgánicos, para favorecer su futura procesabilidad. En cuanto a la fotosensibilidad, se pretende obtener POMs que muestren cambios de colour en estado sólido mediante un mecanismo intramolecular, diferente a los que se han descrito hasta ahora en la literatura (que son de tipo intermolecular). En todos los casos será primordial relacionar las propiedades observadas con las estructuras de los compuestos.

Resumen en español

A continuación, se describe la estructura de la tesis y se detallan los aspectos más relevantes tratados en cada uno de los capítulos de la presente disertación.

En el **Capítulo 1** se presenta una breve introducción histórica sobre los POMs y una descripción detallada de los aspectos más relevantes de la síntesis, estructuras, propiedades y aplicaciones de los POMs.

Los resultados se han estructurado en tres capítulos (**Capítulo 2**, **Capítulo 3** y **Capítulo 4**).

En el **Capítulo 2** se discute la síntesis y caracterización de diez nuevos polioxometalatos sustituidos con cobalto. Este capítulo ofrece una visión profunda de los detalles experimentales de la síntesis y caracterización de POMs que contienen cobalto y que se obtuvieron durante la elaboración de este trabajo doctoral. Este capítulo se divide en tres partes:

1) Síntesis y caracterización completa de cuatro nuevos POMs que encapsulan clústeres constituidos por cuatro o siete iones de cobalto (tetracobalto(II) o heptacobalto(II,III)) con topologías de tipo cubano o di-cubano. La naturaleza química y las propiedades físicas de estos compuestos se describen en este primer apartado. Finalmente, se explica el interés que estas singulares estructuras de espín, surgidas de las topologías de tipo cubano y dicubano, tienen en espintrónica molecular y en computación cuántica.

2) Se presenta un procedimiento que permite sintetizar nuevos POMs que contienen una o dos subunidades, formuladas como '$[Co_4(OH)_3(H_2O)_{6-n}(PW_9O_{34})]^{3-}$' (n = 3 o 5), además de otros fragmentos de polyoxoaniones. La sustitución de las moléculas de agua que coordinan a los átomos de cobalto en esas subunidades por ligandos oxo o hidroxo pertenecientes a otros fragmentos de POMs, da lugar a cuatro nuevos compuestos de mayor tamaño. La estructura cristalina y la caracterización física de estos compuestos (espectroscopia IR y UV-vis, análisis elemental, ciclovoltametría y estudios magnéticos) se presentan en esta parte.

3) Se describen dos estructuras de POMs sustituidos con cobalto cuyas fórmulas son:

$[Co^{II}_4(H_2O)_2(Co^{III}W_9O_{34})(PW_9O_{34})]^{12-}$ (**2.8**) y $[Co_2\{Co_3(H_2O)(Co(OH)_2W_7O_{26})(PW_9O_{34})\}_2]^{22-}$ (**2.9**). El POM **2.8** está formado por dos unidades trivacantes diferentes (B-α-$[PW_9O_{34}]^{9-}$ y B-α-$[Co^{III}W_9O_{34}]^{11-}$) que encapsulan a cuatro iones Co(II), dando lugar a la formación de un clúster de cinco cobaltos $[Co^{II}_4Co^{III}]$. Este POM representa el primer ejemplo de un sándwich asimétrico con la topología de *Weakley*. En cambio, el compuesto **2.9** es un POM con una forma más alargada, terminado en ambos extremos por dos ligandos trivacantes B-α-$[PW_9O_{34}]^{9-}$ que, junto a dos unidades puente $[W_7O_{26}]^{10-}$, encapsulan un nuevo clúster con diez iones Co(II) con coordinación octaédrica y tetraédrica. Este compuesto representa uno de los pocos ejemplos de sándwich triple en la química de los polioxometalatos. Por otra parte, la síntesis de **2.9** se ha realizado utilizando un método original consistente en la hidrólisis reductiva parcial de **2.8**.

En el **Capítulo 3** se describe la síntesis y caracterización de nuevos SIMs basados en POMs. En concreto, se ha desarrollado una serie de polioxomolibdatos que contienen iones lantanoides y que son solubles en disolventes orgánicos. Esta característica es necesaria para la preparación de materiales híbridos que combinen el comportamiento de molécula imán (o *single molecular magnet*, SMM) con otras propiedades de interés como la conductividad, la actividad óptica o la transición de espín (*spin-crossover*). Esta serie de complejos se ha caracterizado mediante medidas magnéticas estáticas y dinámicas. Para los derivados de Ho y Er, se ha observado una lenta relajación de la magnetización. Los parámetros del campo de ligandos y el desdoblamiento del multiplete en el estado fundamental del ion lantánoide se han estimado a partir del análisis de las medidas magnéticas.

Finalmente, el **Capítulo 4** describe la síntesis y caracterización de un nuevo polianion molecular fotosensible con fórmula $\{K\subset[(A\text{-}\alpha\text{-}PW_9O_{34})_2Fe_2(C_2O_4)_2]\}^{15-}$ (**4.1**) en la que dos iones Fe(III) están coordinados simultáneamente por dos unidades de polioxometalato A-α-$[PW_9O_{34}]^{9-}$ y dos ligandos oxalato. Cuando la sal de potasio del POM **4.1**, $K_{15}\{K\subset[(A\text{-}\alpha\text{-}PW_9O_{34})_2Fe_2(C_2O_4)_2]\}\cdot 29H_2O$, se irradia con luz ultravioleta (UV) se produce un efecto de fotocoloración destacable, atribuido a la reducción parcial del POM para dar lugar a especies de valencia mixta. El proceso fotoinducido es intramolecular e implica una transferencia electrónica del ligando oxalato, que se descompone parcialmente liberando CO_2, hacia el Fe(III) y el POM. Este mecanismo ha sido confirmado mediante espectroscopias DRS, IR, XPS y Mössbauer, así como por

medidas magnéticas y de análisis elemental. Además, se ha obtenido un derivado análogo de **4.1**, con fórmula $K_{15}\{K\subset[(A\text{-}\alpha\text{-}PW_9O_{34})_2Fe_2(C_3H_2O_4)_2]\}\cdot 27H_2O$ (**Q-4.2**), que contiene ligandos malonato y no muestra comportamiento fotoactivo lo que evidencia que el ligando oxalato es esencial para la fotoactividad de **4.1**. Hasta donde sabemos, **4.1** es el primer compuesto basado en POMs en el que el efecto de fotocoloración no requiere la presencia de interacciones intermoleculares de corto alcance.

Metodologia General

La síntesis de nuevos POMs se ha basado en dos estrategias generales: (i) la utilización de POMs vacantes que puedan incorporar en su estructura un número variable de cationes de transición de los bloques *d* y *f* (método de síntesis en varias etapas) y (ii) el auto-ensamblado en disolución de iones tungstato o molibdato en presencia de fosfato y cationes metálicos de transición (reacción directa). En ambos casos, se han buscado nuevas condiciones de síntesis que den lugar a compuestos no descritos con anterioridad, por ejemplo, reacciones de hidrólisis reductiva. Para obtener nuevos clústeres magnéticos con diferentes nuclearidades y topologías se ha utilizado, principalmente, el catión Co(II), mientras que para obtener moléculas imán con un solo centro magnético (SIMs) se han empleado cationes lantanoides, Ln^{3+}, como Tb, Dy, Ho, Er, Tm e Yb. Para conseguir la solubilidad de los POMs en agua se han obtenido sales de cationes alcalinos mientras que, para conseguir la solubilidad en disolventes orgánicos, se obtuvieron sales de tetraalquilamonio. La estrategia a seguir para obtener nuevos POMs fotosensibles ha consistido en obtener complejos heterolépticos de Fe(III) utilizando POMs y dicarboxilatos como ligandos.

La caracterización de las muestras en estado sólido ha incluido el uso de espectroscopia infrarroja (IR), análisis elemental (utilizando microscopia electrónica de barrido y microanálisis por dispersión de energía, SEM-EDX, o espectroscopia de plasma de acoplamiento inductivo, ICP-OES), análisis termogravimétrico (TGA), espectroscopia de reflectancia difusa (DRS) UV/vis, espectroscopia fotoelectrónica de rayos X (XPS) y espectroscopia Mössbauer. Para la determinación de las estabilidades en disolución se ha utilizado espectroscopia UV/vis, voltametría cíclica en disolución, resonancia magnética nuclear (NMR) de ^{31}P y espectrometría de masas para producir iones por electroespray (ESI-MS). La caracterización estructural ha requerido la obtención de los nuevos POMs

en forma de monocristales y se ha realizado mediante difracción de rayos X de monocristal. La difracción de rayos X en polvo se ha utilizado para determinar o excluir la presencia de una o más fases en los sólidos. La caracterización magnética se ha realizado mediante la medida de la susceptibilidad magnética *dc* en función de la temperatura, así como medidas de susceptibilidad magnética *ac* en presencia de campo. La determinación del mecanismo de fotocromismo se ha apoyado en algunas de las técnicas antes mencionadas (IR, DRS, XPS, Mössbauer), que se realizaron tras irradiar las muestras con luz de determinadas longitudes de onda.

Capítulo 1. Introducción General

En este capítulo se hace una descripción detallada sobre los polioxometalatos. El capítulo incluye, en primer lugar, una breve descripción histórica y, posteriormente, una introducción detallada sobre los aspectos más relevantes de las síntesis, estructuras, propiedades y aplicaciones de los POMs.

Capítulo 2. POMs de alta nuclearidad basados en cobalto

La familia de POMs que contiene cobalto es una de las más extendidas y ampliamente estudiadas desde que Baker describió los primeros ejemplos en 1956.[17] Una búsqueda en la bibliografía de los polioxotungstatos que incorporan clústeres de cobalto muestra que han sido descritas casi todas las nuclearidades comprendidas entre 2 y 16 átomos de cobalto. Todos estos clústeres de Co(II) constituyen unos excelentes candidatos para realizar estudios en detalle sobre el canje magnético entre estos iones. En el pasado, nuestro grupo ha estudiado en detalle la naturaleza anisotrópica de las interacciones de canje en clústeres de Co(II) con distintas topologías y nuclearidades encapsuladas en POMs.[1-7] Cabe remarcar que los clústeres de Co con topología cubano/dicubano no habían sido descritos (**Fig. 2.1**) todavía en la química de polioxotungstatos, pese a que existían algunos ejemplos con esa topología para otros metales.[18-21]

Desde el punto de vista sintético, las especies de POM que contienen estructuras cubanas o di-cubanas, se pueden emplear como unidades básicas para la construcción de POMs con cobaltos de mayores nuclearidades, mediante el ensamblaje de los clústeres de

cubano o di-cubano con unidades fosfato, acetato, carbonato u otros ligandos. Desde el punto de vista magnético, los POMs cubanos o di-cubanos son sistemas modelo para el estudio de la naturaleza del canje anisótropo entre los iones Co(II) con esas topologías. El interés de estos sistemas también se puede expandir a áreas como la catálisis. Por ejemplo, se ha prestado especial atención en los últimos años a los clústeres metálicos tetra-nucleares tipo cubano debido a su interés potencial como catalizadores en la oxidación del agua (*water oxidation catalysts*, WOCs).[22-25]

Resultados y Discusión

PARTE 1: Clústeres de cobalto con topologías tipo cubano basados en ligandos polioxometalato trivacantes

En esta parte se muestra que, usando el ligando heptadentado trivacante B-α-$[PW_9O_{34}]^{9-}$, se puede obtener el POM formulado como $[Co_4(OH)_3(H_2O)_6(PW_9O_{34})]^{4-}$ (**2.1**), que contiene un cubano con cuatro iones Co(II): $[Co_4O_4]$. Con respecto a la topología de dicubano, se pueden obtener tres tipos de POMs diferentes que incorporan el clúster $[Co_7O_8]$: $[Co_7(OH)_6(H_2O)_6(PW_9O_{34})_2]^{9-}$ (**2.2**) y $[Co_7(OH)_6(H_2O)_4(PW_9O_{34})_2]_n^{9n-}$ (**2.3**) (ambos contienen el ligando trivacante derivado del polyoxoanión de Keggin B-α-$[PW_9O_{34}]^{9-}$) y $[Co_7(OH)_6(H_2O)_6(P_2W_{15}O_{56})_2]^{15-}$ (**2.4**) (que contiene el ligando trivacante derivado del polioxoanión de Dawson α-$[P_2W_{15}O_{56}]^{12-}$). La diferencia principal entre los POMs **2.2** y **2.3** es que el primero es un polioxoanión aislado mientras que el segundo tiene naturaleza polimérica debido a que las unidades individuales vecinas están unidas mediante dos enlaces W–O–Co(II). Los POMs **2.2** y **2.4** contienen Co(III) en la posición central del clúster de dicubano y Co(II) en las seis posiciones metálicas restantes del clúster. Debido a esta característica, se puede considerar que este clúster de cobalto heptanuclear está formado por dos grupos triangulares de Co(II) (**Fig. 1.11c**) unidos mediante un ion Co(III) diamagnético. Los POMs que encapsulan clústeres Co(II)/Co(III) no son habituales. Por lo que sabemos, tan solo existen tres ejemplos previos descritos: el polianión $[Co^{II}(H_2O)(Co^{III}W_{11}O_{39})]^{7-}$, que contiene un clúster de cobalto dinuclear similar al mostrado en la **Fig. 1.11a**,[17] el POM $[Co^{II}_2Co^{III}_4(OH)_5(H_2O)_2(CH_3CO_2)(Si_2W_{18}O_{66})]^{6-}$, que contiene un clúster de cobalto hexanuclear (**Fig. 1.11k**) con cuatro iones Co(III) y dos iones Co(II) aparentemente desordenados entre las seis posiciones de los cobaltos,[26] y el polioxoniobato

$[H_2Co_8O_4(Nb_6O_{19})_4]^{18-}$, que encapsula un clúster de cobalto octanuclear formado por un cubano central $[Co^{III}_4O_4]$ rodeado por cuatro iones Co(II).[27]

En lo que respecta a la síntesis, los POMs **2.1**, **2.2**, **2.3** y **2.4** se obtienen siempre con unos rendimientos muy bajos (entre el 1 y el 8 %) debido a que aparecen como subproductos en la síntesis de otros polioxoaniones que ya eran conocidos previamente. En concreto, los POMs de tipo sándwich que encapsulan clústeres de tetracobalto con las topologías de Weakley ($[Co_4(H_2O)_2(PW_9O_{34})_2]^{10-}$) y Finke ($[Co_4(H_2O)_2(P_2W_{15}O_{56})_2]^{16-}$). Para aislar los POMs deseados es necesario eliminar del medio de reacción los polianiones de Weakley y Finke, cosa que se consigue produciendo su precipitación mediante la adición de cationes Cs^+ a la disolución. La obtención de los POMs que encapsulan los clústeres heptanucleares con topología de dicubano (**2.2**, **2.3** y **2.4**) se consigue mediante la oxidación parcial de los iones Co(II) empleados en la síntesis. Los iones Co(III) generados encuentran un mejor acomodo en la posición central del clúster de dicubano debido a que se encuentran coordinados por seis ligandos hidroxo. La oxidación puede producirse mediante la adición de un oxidante (persulfato o agua oxigenada) o mediante la acción del oxígeno del aire cuando las disoluciones se dejan expuestas a la atmósfera durante periodos de tiempo suficientemente largos. En cuanto al clúster con topología de cubano, solo ha podido obtenerse cuando se utiliza el ligando trivacante derivado del polioxoanión de Keggin (B-α-$[PW_9O_{34}]^{9-}$), resultando infructuosos los intentos de obtenerlo con el ligando trivacante derivado del polioxoanión de Dawson (α-$[P_2W_{15}O_{56}]^{12-}$).

Se ha realizado un estudio de la estabilidad en disolución acuosa a diferentes valores de pH de los POMs **2.1**, **2.2** y **2.4** (se ha excluído de este estudio el POM **2.3** por su naturaleza polimérica) concluyéndose que todos ellos se descomponen lentamente en un amplio intervalo de pH, dando lugar a la formación de un POM de Keggin monosustituido: $[PCo(H_2O)W_{11}O_{39}]^{5-}$. El estudio electroquímico (voltametrías cíclicas) de los mismos compuestos corrobora la conclusión alcanzada con el estudio espectroscópico.

En cuanto a las propiedades magnéticas, se ha encontrado que el POM **2.1** muestra interacciones ferromagnéticas entre los tres iones Co(II) magnéticamente equivalentes (situados en posición basal), así como entre cada uno de ellos y el ion Co(II) situado en posición apical. El comportamiento magnético se ha modelizado asumiendo que dentro del trímero existe una interacción de canje anisotrópico dominante, mientras que la interacción del trímero con el ion Co(II) apical es mucho más débil. Por lo tanto, el estado fundamental del clúster tetranuclear de Co en **2.1** puede considerarse resultante de una

interacción débil entre dos dobletes de espín diferentes: un doblete, $|S, M\rangle = |3/2, \pm 1/2\rangle$, que surge de una interacción anisotrópica y ferromagnética entre los tres átomos de cobalto basales y el doblete fundamental de Kramers que surge del átomo de cobalto apical. A diferencia de otros clústeres de Co(II) con otras topologías, la interacción entre los dos dobletes de espín no equivalentes da lugar a que **2.1** presente un esquema de energía con cuatro niveles que comprenden más de 5 cm^{-1}. Esta situación podría ser útil para producir una puerta cuántica que opere en espacios de dos qubits.

Por otra parte, los POMs **2.2**, **2.3** y **2.4**, que contienen clústeres heptanucleares, muestran un comportamiento antiferromagnético a muy bajas temperaturas debido a la interacción antiferromagnética entre los dos trímeros idénticos acoplados ferromagnéticamente. Al igual que antes, cada unidad trinuclear tiene un esquema de energía formado por niveles doblemente degenerados. La interacción antiferromagnética entre estas dos unidades da lugar a un esquema de niveles más complejo, con un estado fundamental diamagnético (S = 0) cuasidegenerado con una combinación antisimétrica de funciones ±M. Este resultado implica que estos POMs podrían actuar como moléculas magnéticas sensibles eléctricamente, en las cuales su estado de espín fundamental podría variarse mediante la aplicación de un campo eléctrico externo.

PARTE 2: Construcción de POMs extendidos que contienen '$[Co_4(OH)_3(H_2O)_{6-n}(PW_9O_{34})]^{3-}$' (n = 3 ó 5) como una subunidad común

En esta sección se describe una estrategia sintética directa (*one-pot*) que da lugar a cuatro POMs que contienen cobalto (**2.2**, **2.3**, **2.5**, **2.6** y **2.7**). Cada POM se obtiene a partir de una disolución inicial común que contiene WO_4^{2-}, PO_4^{3-} y Co^{2+} a la que se aplican pequeñas variaciones en las condiciones de reacción (**2.2** y **2.3** se pudieron obtener también empleando un método de síntesis por etapas, tal y como se explicó en la primera parte de este capítulo, aunque con contracationes diferentes). Cada uno de esos POMs contiene un fragmento (o subunidad) que se puede formular como '$[Co_4(OH)_3(H_2O)_{6-n}(PW_9O_{34})]^{3-}$' (n = 3 o 5), y que incorpora un clúster de tipo cubano $[Co^{II}_3Co^{III}O_4]$. Esta subunidad es topológicamente similar al POM previamente descrito $[Co_4(OH)_3(H_2O)_3(PW_9O_{34})]^{4-}$ (**2.1**) que existe como unidad independiente y que incorpora el cubano $\{Co^{II}_4O_4\}$.[28] El uso de persulfato como oxidante es el responsable del estado de oxidación 3+ del átomo de cobalto en la posición apical del clúster cubano. Este

ion Co(III) es estabilizado por la sustitución de las tres moléculas de agua que coordinan al cobalto apical en **2.1** por grupos oxo e hidroxo de otros fragmentos de POM presentes en la disolución, dando lugar a POMs con tamaños mayores.

Las estructuras de los POMs **2.2** ($[Co_7(OH)_6(H_2O)_6(PW_9O_{34})_2]^{9-}$) y **2.3** ($[Co_7(OH)_6(H_2O)_4(PW_9O_{34})_2]_n^{9n-}$) se describen en la primera parte de este capítulo. Ambos POMs se pueden considerar como el resultado de sustituir las tres moléculas de agua apicales del POM **2.1** por ligandos hidroxo del hipotético fragmento '$[Co^{II}_3(OH)_3(H_2O)_3(PW_9O_{34})]^{6-}$' y, en el caso del POM **2.3**, una molécula de agua basal es también sustituida por un ligando oxo terminal de un POM vecino, dando lugar a una cadena polimérica.

El POM **2.5** ($[Co_8(OH)_6(H_2O)_6\{W_8O_{28}(OH)_2\}(PW_9O_{34})_2]^{16-}$) consiste en dos unidas por subnidades de **2.1** un fragmento puente, formulado como '$[W_8O_{28}(OH)_2]^{10-}$', que reemplaza a las tres moléculas de agua apicales de ambas subunidades **2.1**. Así pues, **2.5** contiene dos clústeres de cobalto de tipo cubano bien separados por el fragmento puente.

El POM **2.6** ($[Co_{11}(OH)_5(H_2O)_5(W_6O_{24})(PW_9O_{34})_3]^{22-}$) consiste en una subunidad de **2.1** en la que las tres moléculas de agua apicales de **2.1** son remplazadas por el fragmento '$\{[Co_3(H_2O)]_2[Co(OH)_2W_6O_{24}](PW_9O_{34})_2\}^{18-}$', dando lugar a un único POM que encapsula dos clústeres de cobalto aislados con nuclearidades de 4 y 7.

El POM **2.7** está formado por dos subunidades de **2.1** en las que las tres moléculas de agua apicales y dos moléculas de agua basales son sustituidas por un fragmento central de diparatungstato formulado como '$[\{K\subset(H_2W_{12}O_{41})_2\}\{Co(H_2O)_4\}_2]^{11-}$'. El resultado es la formación de un POM con forma alargada que contiene dos cubanos de cobalto separados.

El compuesto **2.7** es estable en disolución acuosa, al menos, durante 48 horas, tal y como indican las medidas de espectroscopia UV-vis, mientras que **2.2**, **2.5** y **2.6** se descomponen lentamente formando el polianión Keggin monosubstituido $[PCo(H_2O)W_{11}O_{39}]^{5-}$ como producto mayoritario. La voltamperometría cíclica del POM **2.7** muestra una reducción irreversible de la estructura oxo-tungsteno y una oxidación electroquímica cuasi-reversible de los centros de cobalto. Las propiedades magnéticas de **2.6** y **2.7** han sido estudiadas, pese a que la presencia de varios iones aislados Co(II) con coordinación octaédrica fuera del POM hace imposible el ajuste numérico de las medidas. A pesar de ello, las propiedades magnéticas de **2.6** y **2.7** pueden entenderse cualitativamente a partir de las interacciones magnéticas ya conocidas que existen en los

clústeres de cobalto encapsulados en POMs anteriormente descritos. La estrategia sintética que se emplea en este trabajo puede extenderse para obtener nuevos POMs de tamaños mayores formados por la unión de subunidades de **2.1** con otros fragmentos de polioxoaniones mediante la sustitución de las moléculas de agua coordinadas a los átomos de cobalto delcubano incorporado en el POM **2.1**.

PARTE 3: Un clúster de decacobalto(II) con estructura de triple sándwich obtenido mediante la hidrólisis reductora de un POM de pentacobalto (II/III) tipo Weakley

Se han obtenido y caracterizado dos nuevos POMs que contienen clústeres de cinco iones Co(II/III) (**2.8**) y diez iones Co(II) (**2.9**). El polioxoanión **2.8** ($[Co^{II}_4(H_2O)_2(Co^{III}W_9O_{34})(PW_9O_{34})]^{12-}$) tiene la misma topología que el al POM con estructura de tipo sándwich $[Co^{II}_4(H_2O)_2(PW_9O_{34})_2]^{10-}$, descrito por primera vez por Weakley. Se trata del primer ejemplo de POM con esta topología que tiene dos heteroátomos diferentes en los ligandos trivacantes $[XW_9O_{34}]^{n-}$ (X = P^V and Co^{III}). El POM **2.9** ($[Co^{II}_2\{Co^{II}_3(H_2O)(Co^{II}(OH)_2W_7O_{26})(PW_9O_{34})\}_2]^{22-}$) fue sintetizado mediante hidrólisis reductora parcial de **2.8** usando hidracina. El polioxoanión contiene un dímero Co_2 central unido a dos trímeros Co_3 mediante dos fragmentos $[Co(OH)_2W_7O_{26}]^{10-}$. El conjunto termina con dos ligandos trivacantes B-α-$[PW_9O_{34}]^{9-}$ en los extremos. El clúster de Co(II) encapsulado en **2.8** es decanuclear y consta de ocho iones cobalto con coordinación octaédrica y dos con coordinación tetraédrica.

Al comparar las estructuras de **2.8** y **2.9**, se puede concluir que la reacción con hidracina tiene tres efectos principales: (i) la reducción del ion Co(III) tetraédrico en **2.8** a Co(II) en **2.9**, (ii) la hidrólisis parcial del ligando trivacante $[Co^{III}W_9O_{34}]^{11-}$, que se transforma en los fragmentos puente $[Co(OH)_2W_7O_{26}]^{10-}$ (el ligando $[PW_9O_{34}]^{9-}$ no sufre hidrólisis en las condiciones utilizadas) y (iii) la pérdida de un ion Co(II) del clúster tetranuclear de **2.8**, dando lugar a dos tríadas de cobalto en **2.9**. Además, se produce una isomerización en las uniones de los trímeros de cobalto con los ligandos trivacantes $[PW_9O_{34}]^{9-}$ debida a una rotación de 60° de estos ligandos al formarse el POM **2.8**. Los átomos de tungsteno que se pierden durante el proceso de hidrólisis de **2.8** condensan para formar el ya conocido anión paratungstato, que aparece como subproducto. Estos resultados abren la puerta a sintetizar nuevos POMs que contengan clústers de iones de metales de la primera serie de transición a partir de POMs más pequeños utilizando la

reacción con hidracina. De este modo, una futura línea de investigación que se deriva de este trabajo consiste en explorar si la aproximación de hidrólisis reductora parcial empleada en este trabajo puede ser un método general para obtener nuevos POMs con mayores nuclearidades y con propiedades magnéticas y/o catalíticas de interés.

Capítulo 3. SMM basados en POMs

Un área especialmente desafiante es el de la espintrónica basada en moléculas, que pretende emplear moléculas individuales como principal componente de dispositivos espintrónicos. En este contexto, las moléculas aisladas con comportamiento de imán (*single-molecule magnets*, SMMs)[29] se han propuesto como potenciales candidatas.[30-32] Estos sistemas, que representan el límite de miniaturización de los nanoimanes, están entre las entidades más complejas que exhiben una relajación lenta de la magnetización a bajas temperaturas[33] acompañadas por histéresis magnética.[34] Además, también pueden presentar fenómenos cuánticos de origen puramente molecular.[35-38] En este contexto, los SMMs basados en complejos mononucleares de iones lantanoides merecen especial atención.[39-40] El primer ejemplo de esta clase de nanoimanes moleculares o SIMs, fue descrito por el grupo de Ishikawa en la serie con fórmula general $[LnPc_2]^-$, donde los iones lantanoides son coordinados con simétrica cuadrada-antiprismática (D_{4d}) por dos ftalocianinatos.[41] Se han obtenido otros derivados relacionados a partir del complejo de ftalocianinato de terbio oxidado $[TbPc_2]^0$. La estructura *'double-decker'* de este sistema favorece su adsorción en superficies y, además, es neutro, lo que facilita su sublimación en condiciones de ultra-alto vacío. La procesabilidad de estos complejos ha permitido alcanzar una serie de hitos, entre los que incluye la preparación de válvulas de espín moleculares/supramoleculares[42-43] y el control eléctrico de qubits de espines nucleares.[44-45] Entre los pocos sistemas sublimables basados en lantanoides descritos hasta la fecha, cabe destacar el complejo trinuclear Tb^{3+}, $Tb_3(OQ)_9$ (OQ = quinolinato), en el que se ha observado transporte mediado por *hopping* con polarización de espín.[46] Esta molécula también ha sido propuesta como un sistema modelo para correcciones de error cuántico en computación cuántica.[47]

En el contexto de los SIMs basados en lantanoides, los POMs han proporcionado ejemplos excelentes. Cabe destacar la familia LnW_{10} formada por dos unidades de $[W_5O_{18}]^{6-}$ encapsulando al ion lantanoide.[48-52]

Resultados y Discusión

En esta parte se describe la preparación de una familia de complejos mononucleares de iones lantanoides basados en POMs análoga a la de LnW_{10}, pero que supera las limitaciones de procesabilidad de esa familia. Esta familia de complejos se formula como $[Ln(\beta\text{-}Mo_8O_{26})_2]^{5-}$ (abreviado como $LnMo_{16}$), {Ln^{III} = Tb (**3.1**), Dy (**3.2**), Ho (**3.3**), Er (**3.4**), Tm (**3.5**) y Yb (**3.6**)} y consiste en un ion lantanoide coordinado por dos unidades del polioxomolibdato $[\beta\text{-}Mo_8O_{26}]^{4-}$ para formar una geometría de antiprisma cuadrada (simetría ideal D_{4d}) alrededor del lantanoide. Además de la síntesis, se realiza la caracterización estructural y magnética de esta serie de polioxomolibdatos. Para el análisis magnetoestructural, se presentan dos métodos diferentes para determinar los parámetros del campo cristalino (CC). El primero asume una dependencia lineal de los parámetros de CC con el número de electrones *f*, mientras que el segundo asume distancias Ln-O y cargas puntuales efectivas para determinar los parámetros de CC. Estos resultados se comparan con los descritos previamente para SIMs de lantánoides análogos basados en polioxotungstatos. Los compuestos **3.3** y **3.4** exhiben propiedades de SMM, que se pueden racionalizar a la vista del estado fundamental de los iones Ho^{3+} y Er^{3+} en este campo cristalino. La novedad clave consiste en el uso de polioxomolibdatos en vez de polioxotungstatos para obtener SIMs. Pese a que la química de polioxomolibdatos representa un desafío, este resultado demuestra que se pueden preparar moléculas magnéticas que sean solubles en disolventes orgánicos, lo cual abre la posibilidad de obtener materiales híbridos mediante su combinación con los contraiones correspondientes y de procesar estos POMs para incorporarlos en dispositivos espín-electrónicos.

Capítulo 4. Un POM foto-reactivo que contiene Fe

Como es conocido, algunos complejos carboxílicos de Fe(III) son sensibles a la luz visible y UV, lo que les hace foto-reactivos a través de reacciones de transferencia de carga del ligando al metal (*ligand to metal charge transfer*, LMCT) y, por tanto, son importantes en la química de sistemas del medio ambiente[53] y para aplicaciones fotoquímicas de laboratorio en general (por ejemplo, en actinometría).[54] Un ejemplo paradigmático de estos complejos es el complejo tris(oxalato)ferrato(III) cuya reacción

fotoinducida de LMCT (reacción **1**) da lugar a la (foto)generación de iones Fe(II) (tanto en disolución como en estado sólido) y a la subsecuente reacción reductiva vía aniones radicales $CO_2^{\bullet-}$ (reacción **3**).[55-57]

$$[Fe^{III}(C_2O_4)_3]^{3-} + h\nu \rightarrow Fe^{2+} + C_2O_4^{\bullet-} + 2(C_2O_4)^{2-} \quad (\mathbf{1})$$

$$C_2O_4^{\bullet-} \rightarrow CO_2 + CO_2^{\bullet-} \quad (\mathbf{2})$$

$$[Fe^{III}(C_2O_4)_3]^{3-} + CO_2^{\bullet-} \rightarrow Fe^{2+} + 3(C_2O_4)^{2-} + CO_2 \quad (\mathbf{3})$$

En este contexto, se ha explorado la posibilidad de combinar complejos carboxilato de Fe(III) con POMs en la misma unidad molecular con el objetivo de obtener un nuevo tipo de sistema fotoactivo en el cual la fotoreacción ocurre a través de una transferencia de carga fotoinducida a nivel intramolecular. Esta aproximación contrasta con la habitual, que consiste en establecer interacciones intermoleculares entre el POM (aceptor de electrones) y una molécula dadora de electrones (*i.e.*, enlaces de H o contactos S···O). Sin embargo, el único ejemplo descrito de complejos de Fe(III) que contienen ligandos tanto oxalatos como POM, representado por la familia $[Fe_4(C_2O_4)_4(H_2O)_2(B\text{-}\beta\text{-}XW_9O_{33})_2]^{14-}$ (X = As^{III}, Sb^{III}, Bi^{III}), no presenta fotoactividad.[58-59]

Resultados y Discusión

En este trabajo, se presenta la síntesis y caracterización (estructura cristalina de rayos X, reflectancia difusa, evolución según la irradiación de IR, UV en disolución acuosa, espectroscopía Mössbauer y propiedades magnéticas) de un nuevo compuesto mixto ferrioxalato-POM formulado como $K_{15}\{K\subset[(A\text{-}\alpha\text{-}PW_9O_{34})_2Fe_2(C_2O_4)_2]\}\cdot 29H_2O$ (**Q-4.1**). Este POM exhibe un proceso de fotocoloración rápido y evidente (consistente en un cambio de color, desde amarillo verdoso suave a negro) cuando es expuesto en estado sólido a la luz del sol directa o a la irradiación UV. También se ha obtenido el derivado análogo de malonato, $K_{15}\{K\subset[(A\text{-}\alpha\text{-}PW_9O_{34})_2Fe_2(C_3H_2O_4)_2]\}\cdot 27H_2O$ (**Q-4.2**), que no muestra fotoactividad. Los resultados demuestran que el proceso de fotocoloración implica una transferencia electrónica intramolecular simultáneamente desde el ligando oxalato al Fe(III) (obteniéndose Fe(II)) y a la estructura del polioxotungstato (formándose una especie reducida de valencia mixta que contiene W(V)). Este proceso está acompañado por la descomposición del ligando oxalato y la liberación de CO_2.

A la vista de las evidencias experimentales, el efecto de fotocoloración en **4.1** se puede producir según el proceso propuesto en el **esquema 4.3**. La irradiación UV induce la fotodisociación del enlace coordinado entre el Fe(III) y el ligando oxalato, dando lugar a una transferencia de carga ligando-a-metal que forma Fe(II) y el ion radical de dióxido de carbono ($CO_2^{\bullet -}$). Simultáneamente, el ion radical puede reaccionar con el POM dando lugar a iones W(V), que son los responsables de la intensa fotocoloración de **4.1**.

Por lo tanto, el POM **4.1** es un nuevo sistema fotoactivo que muestra un cambio de color en estado sólido cuando se irradia con luz UV. La muestra resultante (de color negro) recupera su color inicial (amarillo verdoso) si se almacena en la oscuridad en presencia de aire durante aproximadamente 7 días (cabe remarcar que no se produce la recuperación del color en una atmósfera exenta de oxígeno). Una vez la muestra ha recuperado su color incial, el efecto de fotocoloración puede ser repetido varias veces (irradiando de nuevo con luz UV y volviendo a almacenar el producto en oscuridad con presencia de oxígeno). Este resultado abre la puerta a la posibilidad de obtener nuevos materiales fotoactivos basados en POMs que incorporen otros carboxilatos de Fe(III) que permitan la modulación de la fotorespuesta. En el futuro se pretende depositar el POM **4.1** en distintas superficies para comprobar su uso como actinómetro químico en estado sólido. El actinómetro químico más utilizado actualmente (sobre todo en disolución) es el complejo tris(oxalato)ferrato(III) (también conocido como ferrioxalato), debido su amplio espectro de absorción y a su alta eficiencia cuántica.[54] Debido a que el POM **4.1** muestra un gran contraste en el efecto de fotocoloración, su uso como actinómetro en estado sólido no requeriría la necesidad de un proceso analítico de postirradiación. Nótese que en los actinómetros basados en ferrioxalatos, tras la irradiación, se necesita realizar un tratamiento con fenantrolina para complejar el Fe(II) fotogenerado (la medición de la absorbancia del complejo Fe(II)-fenantrolina permite el cálculo del número de fotones que ha incidido sobre la muestra). En nuestro caso, se podría realizar la cuantificación *in-situ* de la intensidad de la luz de un modo más sencillo mediante la monitorización de la absorbancia de la muestra sólida irradiada de **4.1**.

Referencias

[1] C. J. Gómez-García, E. Coronado, J. J. Borrás-Almenar, M. Aebersold, H. U. Güdel and H. Mutka, *Physica B.*, 1992, **180**, 238-240.

[2] J. R. Galán-Mascarós, C. J. Gómez-García, J. J. Borrás-Almenar and E. Coronado, *Adv Mater.*, 1994, **6**, 221-223.

[3] J. M. Clemente, H. Andrés, M. Aebersold, J. J. Borrás-Almenar, E. Coronado, H. U. Güdel, H. Buttner and G. Kearly, *Inorg. Chem.*, 1997, **36**, 2244-2245.

[4] J. M. Clemente-Juan, E. Coronado, A. Gaita-Ariño, C. Giménez-Saiz, G. Chaboussant, H. U. Güdel, R. Burriel and H. Mutka, *Chem. Eur. J.*, 2002, **8**, 5701-5708.

[5] J. M. Clemente-Juan, E. Coronado, A. Forment-Aliaga, J. R. Galán-Mascarós, C. Giménez-Saiz and C. J. Gómez-García, *Inorg. Chem.*, 2004, **43**, 2689-2694.

[6] J. M. Clemente-Juan, E. Coronado, A. Gaita-Ariño, C. Giménez-Saiz, H. U. Güdel, A. Sieber, R. Bircher and H. Mutka, *Inorg. Chem.*, 2005, **44**, 3389-3395.

[7] A. Palii, B. Tsukerblat, S. Klokishner, K. R. Dunbar, J. M. Clemente-Juan and E. Coronado, *Chem. Soc. Rev.*, 2011, **40**, 3130-3156.

[8] J. M. Clemente-Juan, E. Coronado and A. Gaita-Ariño, *Chem. Soc. Rev.*, 2012, **41**, 7464-7478.

[9] S. Cardona-Serra, J. M. Clemente-Juan, E. Coronado, A. Gaita-Ariño, A. Camón, M. Evangelisti, F. Luis, M. J. Martínez-Pérez and J. Sesé, *J. Am. Chem. Soc.*, 2012, **134**, 14982-14990.

[10] J. J. Baldoví, S. Cardona-Serra, J. M. Clemente-Juan, E. Coronado, A. Gaita-Ariño and H. Prima-García, *Chem. Commun.*, 2013, **49**, 8922-8924.

[11] S. Cardona-Serra, J. M. Clemente-Juan, E. Coronado, C. Martí-Gastaldo and E. Navarro-Moratalla, *Eur. J. Inorg. Chem.*, 2013, **10-11**, 1903-1909.

[12] A. Giusti, G. Charron, S. Mazerat, J. Compain, P. Mialane, A. Dolbecq, E. Riviere, W. Wernsdorfer, R. N. Bibouni, B. Keita, L. Nadjo, A. Filoramo, J. Bourgoin and T. Mallah, *Angew. Chem. Int. Ed.*, 2009, **48**, 4949-4952.

[13] R. E. P. Winpenny, *Angew. Chem. Int. Ed.*, 2008, **47**, 7992-7994.

[14] D. Stepanenko, M. Trif and D. Loss, *Inorg. Chim. Acta.*, 2008, **361**, 3740-3745.

[15] (a) T. He and J. Yao, *Prog Mater Sci.*, 2006, **51**, 810-879; (b) V. Coué, R. Dessapt, M. Bujoli-Doeuff, M. Evain and S. Jobic, *Inorg. Chem.*, 2007, **46**, 2824-2835; (c) Y. Yang, L. Yue, H. Li, E. Maher, Y. Li, Y. Wang, L. Wu and V. W. Yam, *Small*, 2012, **8**, 3105-3110; (d) H. El Moll, A. Dolbecq, I. M. Mbomekalle, J. Marrot, P. Deniard, R. Dessapt and P. Mialane, *Inorg. Chem.*, 2012, **51**, 2291-2302; (e) K. Hakouk, O. Oms, A. Dolbecq, H. El Moll, J. Marrot, M. Evain, F. Molton, C. Duboc, P. Deniard, S. Jobic, P. Mialane and R. Dessapt, *Inorg. Chem.*, 2013, **52**, 555-557; (f) Q. Zheng, L. Vilà-Nadal, C. Busche, J. S. Mathieson, D. Long and L. Cronin, *Angew. Chem. Int. Ed.*, 2015, **54**, 7895-7899; (g) Y. Gong, Q. Hu, C. Wang, L. Zang and L. Yu, *Langmuir*, 2016, **32**, 421-427; (h) W. Chen, U. Tong, T. Zeng, C. Streb and Y. Song, *J. Mater. Chem. C*, 2015, **3**, 4388-4393; (i) C. Streb, Dalton Trans., 2012, **41**, 1651-1659; (j) B. Matt, J. Fize, J. Moussa, H. Amouri, A. Pereira, V. Artero, G. Izzet and A. Proust, *Energy Environ. Sci.*, 2013, **6**, 1504-1508; (k) A. Proust, R. Thouvenot and P. Gouzerh, *Chem. Comm.*, 2008, 1837-1852; (l) C. Zhao, C. S. Kambara, Y. Yang, A. L. Kaledin, D. G. Musaev, T. Lian and C. L. Hill, *Inorg. Chem.*, 2013, **52**, 671-678.

[16] J.J. Baldoví, S. Cardona-Serra, A. Gaita-Ariño, E. Coronado. *Chapter 8 - Design of Magnetic Polyoxometalates for Molecular Spintronics and as Spin Qubits*. In: Rudi van Eldik and Leroy Cronin, Editor(s), *Advances in Inorganic Chemistry, Academic Press*, 2017, **69**, 213-249.

[17] L. C. W. Baker and T. P. Mccutcheon, *J. Am. Chem. Soc.*, 1956, **78**, 4503-4510.

[18] U. Kortz, A. Tézé and G. Hervé, *Inorg. Chem.*, 1999, **38**, 2038-2042.

[19] X. Fang, M. Speldrich, H. Schilder, R. Cao, K. P. O'Halloran, C. L. Hill and P. Kögerler, *Chem. Commun.*, 2010, **46**, 2760-2762.

[20] X. Fang, K. McCallum, H. D. Pratt III, T. M. Anderson, K. Dennis and M. Luban, *Dalton Trans.*, 2012, **41**, 9867-9870.
[21] X. Fang, P. Kögerler, M. Speldrich, H. Schilder and M. Luban, *Chem. Commun.*, 2012, **48**, 1218-1220.
[22] H. Lv, Y. V. Geletii, C. Zhao, J. W. Vickers, G. Zhu, Z. Luo, J. Song, T. Lian, D. G. Musaev and C. L. Hill, *Chem. Soc. Rev.*, 2012, **41**, 7572-7589.
[23] F. Evangelisti, R. More, F. Hodel, S. Luber and G. R. Patzke, *J. Am. Chem. Soc.*, 2015, **137**, 11076-11084.
[24] X. Han, Y. Li, Z. Zhang, H. Tan, Y. Lu and E. Wang, *J. Am. Chem. Soc.*, 2015, **137**, 5486-5493.
[25] B. Schwarz, J. Forster, M. K. Goetz, D. Yuecel, C. Berger, T. Jacob and C. Streb, *Angew. Chem. Int. Ed.*, 2016, **55**, 6329-6333.
[26] J. Guo, D. Zhang, L. Chen, Y. Song, D. Zhua and Y. Xu, *Dalton Trans.*, 2013, **42**, 8454-8459.
[27] Z. Liang, D. Zhang, P. Ma, J. Niu and J. Wang, *Chem. Eur. J.*, 2015, **21**, 8380-8383.
[28] Y. Duan, J. M. Clemente-Juan, C. Giménez-Saiz and E. Coronado, *Inorg. Chem.*, 2016, **55**, 925-938.
[29] R. Sessoli, H. L. Tsai, A. R. Schake, S. Wang, J. B. Vincent, K. Folting, D. Gatteschi, G. Christou and D. N. Hendrickson, *J. Am. Chem. Soc.*, 1993, **115**, 1804-1816.
[30] L. Bogani and W. Wernsdorfer, *Nat. Mater.*, 2008, **7**, 179-186.
[31] W. Wernsdorfer, *International Journal of Nanotechnology*, 2010, **7**, 497-522.
[32] E. Cremades, C. D. Pemmaraju, S. Sanvito and E. Ruiz, *Nanoscale*, 2013, **5**, 4751-4757.
[33] L. Thomas, F. Lionti, R. Ballou, D. Gatteschi, R. Sessoli and B. Barbara, *Nature*, 1996, **383**, 145-147.
[34] C. Paulsen, J. G. Park, B. Barbara, R. Sessoli and A. Caneschi, *J Magn Magn Mater.*, 1995, **140**, 1891-1892.
[35] A. Ardavan and S. J. Blundell, *J.* Mater. *Chem.*, 2009, **19**, 1754-1760.
[36] F. Troiani and M. Affronte, *Chem. Soc. Rev.*, 2011, **40**, 3119-3129.
[37] P. C. E. Stamp and A. Gaita-Ariño, *J. Mater. Chem.*, 2009, **19**, 1718-1730.
[38] J. Lehmann, A. Gaita-Ariño, E. Coronado and D. Loss, *Nat. Nanotechnol.*, 2007, **2**, 312-317.
[39] D. N. Woodruff, R. E. P. Winpenny and R. A. Layfield, *Chem. Rev.*, 2013, **113**, 5110-5148.
[40] S. T. Liddle and J. van Slageren, *Chem. Soc. Rev.*, 2015, **44**, 6655-6669.
[41] N. Ishikawa, M. Sugita, T. Ishikawa, S. Koshihara and Y. Kaizu, *J. Am. Chem. Soc.*, 2003, **125**, 8694-8695.
[42] M. Urdampilleta, S. Klyatskaya, J.P. Cleuziou, M. Ruben and W. Wernsdorfer, *Nat. Mater.*, 2011, **10**, 502-506.
[43] M. Urdampilleta, S. Klayatskaya, M. Ruben and W. Wernsdorfer, *Acs Nano.*, 2015, **9**, 4458-4464.
[44] S. Thiele, F. Balestro, R. Ballou, S. Klyatskaya, M. Ruben and W. Wernsdorfer, *Sci.*, 2014, **344**, 1135-1138.
[45] C. Wackerlin, F. Donati, A. Singha, R. Baltic, S. Rusponi, K. Diller, F. Patthey, M. Pivetta, Y. Lan, S. Klyatskaya, M. Ruben, H. Brune and J. Dreiser, *Adv Mater.*, 2016, **28**, 5195-5199.
[46] A. Bedoya-Pinto, H. Prima-García, F. Casanova, E. Coronado and L. E. Hueso, *Adv. Electron. Mater.*, 2015, **1**, 1500065.
[47] J. J. Baldoví, S. Cardona-Serra, J. M. Clemente-Juan, L. Escalera-Moreno, A. Gaita-Ariño and G. Mínguez Espallargas, *Epl*, 2015, **110**, 33001.
[48] M. Vonci and C. Boskovic, *Aust. J. Chem.*, 2014, **67**, 1542-1552.
[49] M. A. AlDamen, J. M. Clemente-Juan, E. Coronado, C. Martí-Gastaldo and A. Gaita-Ariño, *J. Am. Chem. Soc.*, 2008, **130**, 8874-8875.
[50] M. A. AlDamen, S. Cardona-Serra, J. M. Clemente-Juan, E. Coronado, A. Gaita-Ariño, C. Martí-Gastaldo, F. Luis and O. Montero, *Inorg. Chem.*, 2009, **48**, 3467-3479.

[51] S. Ghosh, S. Datta, L. Friend, S. Cardona-Serra, A. Gaita-Ariño, E. Coronado and S. Hill, *Dalton Trans.*, 2012, **41**, 13697-13704.
[52] M. Shiddiq, D. Komijani, Y. Duan, A. Gaita-Ariño, E. Coronado and S. Hill, *Nature*, 2016, **531**, 348-351.
[53] L. Deguillaume, M. Leriche, K. Desboeufs, G. Mailhot, C. George and N. Chaumerliac, *Chem. Rev.*, 2005, **105**, 3388-3431.
[54] H. J. Kuhn, S. E. Braslavsky and R. Schmidt, *Pure Appl. Chem.*, 2004, **76**, 2105-2146.
[55] E. L. Simmons and Wendland.Ww, *Coord. Chem. Rev.*, 1971, **7**, 11-27.
[56] Y. G. Zuo and J. Hoigne, *Environ. Sci. Technol.*, 1992, **26**, 1014-1022.
[57] B. C. Faust and R. G. Zepp, *Environ. Sci. Technol.*, 1993, **27**, 2517-2522.
[58] A. Dolbecq, J. Compain, P. Mialane, J. Marrot, E. Rivière and F. Sécheresse, *Inorg. Chem.*, 2008, **47**, 3371-3378.
[59] A. Sartorel, M. Carraro, G. Scorrano, B. S. Bassil, M. H. Dickman, B. Keita, L. Nadjo, U. Kortz and M. Bonchio, *Chem. Eur. J.*, 2009, **15**, 7854-7858.

Appendix. Experimental techniques

A.1. X-ray photoelectron spectroscopy (XPS)

Note: XPS of chapter 2 was carried out by **Prof. José Luis García Fierro** from CSIC - Instituto de Catálisis y Petroleoquímica (ICP), Madrid, Spain. XPS of chapter 4 was carried out by the Research Technical Services of Universidad de Alicante, Spain.

XPS is a semi-quantitative non-destructive spectroscopic technique that measures the elemental composition and electronic states of the elements that exist within a material. Typically, a sample is irradiated with a source of X-rays, so the energy of the incident photon is transferred to a bound electron. If the energy of the photon is greater than the binding energy (BE) of the electron and the electron has enough energy to overcome the work function of the solid, it can leave the solid and been measured.

A typical XPS spectrum is represented by the number of electrons detected versus the BE of those electrons. Each element possess characteristic XPS peaks at characteristic BE that serve to identify the elements present on the surface of the analysed materials. These characteristic peaks correspond to the electron configuration of the electrons within the atoms (1s, 2s, 2p,…). As the number of detected electrons in each peak is related to the amount of element within the area irradiated, the surface composition can be quantified.

The basic components of a monochromatic XPS set-up (as shown in **Fig. A.1**) are:

- *Source of X-rays.*
- *Ultra-high vacuum (UHV) chamber,* in which the sample will be introduced.
- *Electron focusing system* composed of lens that conduce the photoelectrons to the spectrometer.
- *Spectrometer*, which possess an analyser capable of selecting the energy of the photoelectrons.
- *Electron detector.*
- *Computer program* that analyse the collected data.

In a typical experiment, the sample is fitted inside a UHV chamber and irradiated with the X-ray source which produces photons capable of de-bound electrons for the surface of sample (top 1-10 nm of the sample). Those photoelectrons pass through the electron focusing system and arrive to the spectrometer, in which a hemispherical capacitor –composed by two metallic hemispheres– defines the path energy of the

electrons and measures the kinetic energy of the photoelectron. This kinetic energy is finally detected in the detector and transduced by a computer software.

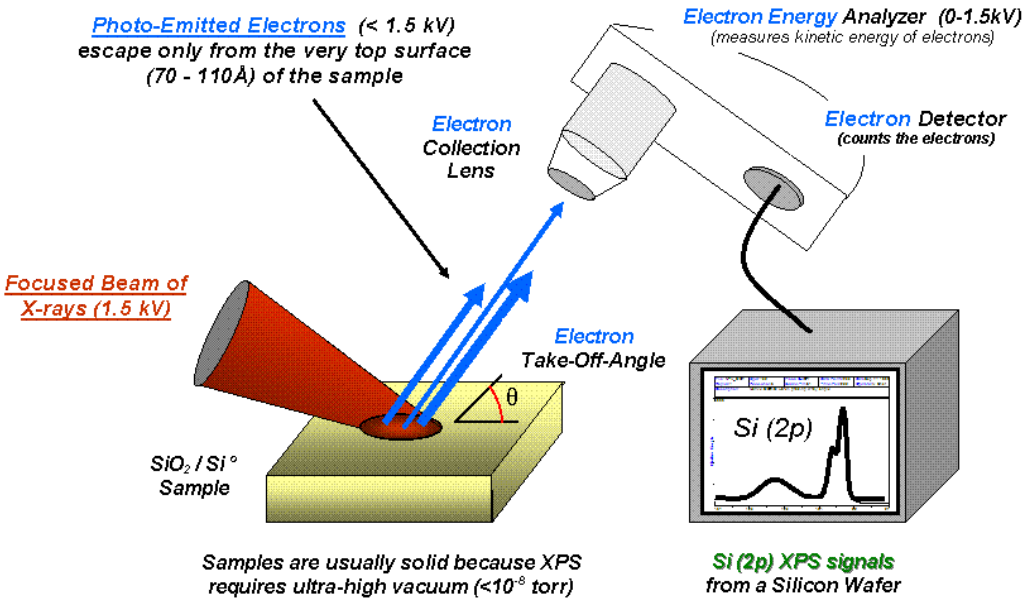

Fig. A.1. Representation of the basic components of a monochromatic XPS set-up (adapted from: *Handbooks of Monochromatic XPS Spectra - Fully Annotated, PDF of Volumes 1 and 2*, B.V.Crist, published by XPS International LLC, 2005, Mountain View, CA, USA).

The vast majority of XPS measurements done in the present thesis have been done by using a Thermo Scientific K-Alpha ESCA instrument equipped with aluminium $K\alpha_{1,2}$ monochromatized radiation at 1486.6 eV X-ray source. In non-conductive samples, it was necessary to use an electron flood gun to minimize surface charging. Neutralization of the surface charge was performed by using a low energy flood gun (electrons in the range 0 to 14 eV) and a low Argon ions gun. The XPS measurements were carried out using monochromatic Al-K radiation (hν = 1486.6 eV). Photoelectrons were collected from a take-off angle of 90° relative to the sample surface. The measurement was done in a Constant Analyser Energy mode (CAE) with a 100 eV pass energy for survey spectra and 20 eV pass energy for high resolution spectra. Charge referencing was done by setting the lower BE C 1s photo peak at 285.0 eV C1s hydrocarbon peak. Surface elemental composition was determined using the standard Scofield photoemission cross sections.

A.2. Mössbauer spectroscopy

Note: Mössbauer spectroscopy in this thesis was carried out by **Prof. João C. Waerenborg** from the Chemistry Department at IST/ITN, Instituto Superior Técnico (Universidade Técnica de Lisboa, Portugal).

Mössbauer spectroscopy is a spectroscopic technique, which allows investigating with high accuracy the changes in the energy levels of an atomic nucleus due to the surrounding environment. The technique consists in measuring the energy dependence of the resonant absorption of Mössbauer gamma rays by nuclei. To obtain these gamma rays a radioactive source is needed. In the laboratory, the isotope ^{57}Co is used, which spontaneously captures an electron to reach a metastable state of ^{57}Fe, which in turns decays in a more stable state (ground state) by a gamma ray cascade that includes the 14.4 keV Mössbauer gamma ray. To work just in this energy range, the spectrometer has an energy window, which should be centered at 14.4 keV.

A Mössbauer spectrometer is a device that performs Mössbauer spectroscopy or a device that uses the Mössbauer effect to determine the chemical environment of Mössbauer nuclei present in the sample. It is formed by the following three main parts (as shown in **Fig. A.2**):

- A source that moves back and forth to generate a Doppler effect.
- A collimator that filters out non-parallel gamma rays.
- A detector.

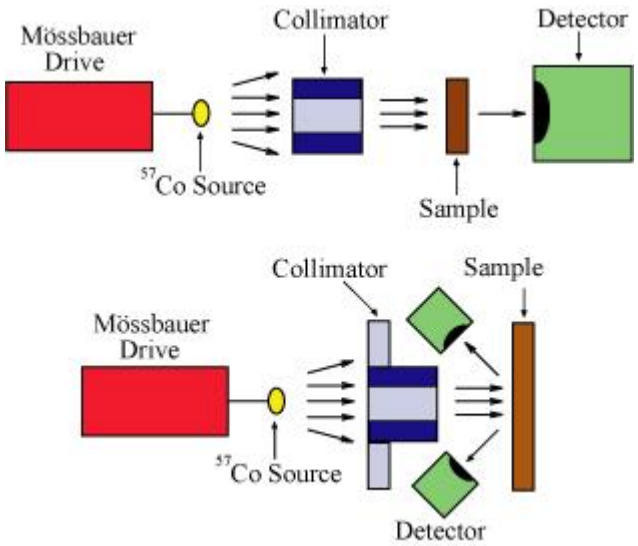

Fig. A.2. The schematic representation of Mössbauer spectrometer (adapted from *http://serc.carleton.edu/research_education/geochemsheets/techniques/mossbauer.html*).

Typically, there are three types of nuclear interactions, which are observed in Mössbauer spectroscopy:

- Isomer shift (or chemical shift).
- Quadrupole splitting.
- Hyperfine splitting (or Zeeman splitting).

Isomer shift (δ) is a relative measure describing a shift in the resonance energy of a nucleus due to the transition of electrons within its *s* orbital. The whole spectrum is shifted in either a positive or negative direction depending upon the *s* electron charge density. The *s* electron density can also be affected by the oxidation state and the chemical environment of the atom. The isomer shift is useful for determining oxidation state, valency states, electron shielding and the electron-drawing power of electronegative groups.

Quadrupole splitting reflects the interaction between the nuclear energy levels and surrounding electric field gradient (EFG). Nuclei in states with non-spherical charge distributions, *i.e.* all those with angular quantum number (*I*) greater than 1/2, produce an asymmetrical electric field (produced by an asymmetric electronic charge distribution or ligand arrangement) which splits the nuclear energy levels. This produces a nuclear quadrupole moment. The Quadrupole splitting can be used for determining oxidation state, spin state, site symmetry and the arrangement of ligands.

Magnetic splitting (hyperfine splitting) is a result of the interaction between the nucleus and any surrounding magnetic field. A nucleus with spin, I, splits into 2I + 1 sub-energy levels in the presence of magnetic field. For example, a nucleus with spin state I = 3/2 will split into 4 non-degenerate sub-states with m_I values of +3/2, +1/2, -1/2 and −3/2. Each split is hyperfine, being in the order of 10^{-7} eV. The selection rule of magnetic dipoles means that transitions between the excited state and ground state can only occur where m_I changes by 0 or 1. This gives six possible transitions for a 3/2 to 1/2 transition. Generally speaking, in the majority of cases only six peaks can be monitored in a spectrum produced by a hyperfine splitting nucleus.

The three Mössbauer parameters: isomer shift, quadrupole splitting and hyperfine splitting can often be used to identify a particular compound by comparison to spectra for standards.

Combination of all. Many times all effects are observed: isomer shift, quadrupole splitting, and magnetic Zeeman Effect. In those cases, the isomer shift is given by the average of all lines. The quadrupole splitting when all the four excited substates are

equally shifted (two substates are lifted and other two are lowered) is given the shift of the outer two lines relative to the inner two lines (generally innermost two lines are not considered). If the shifting of four substates is not equal then the quadrupole splitting is often extracted using fitting software where all the six lines are taken into account. In addition, the relative intensities of the various peaks reflect the relative concentrations of compounds in a sample and can be used for semi-quantitative analysis.

A.3. Single-crystal X-ray Diffraction

Single-crystal X-ray Diffraction is a non-destructive analytical technique which provides detailed information about the internal lattice of crystalline substances, including unit cell dimensions, bond-lengths, bond-angles and details of site-ordering. Directly related is single-crystal refinement, where the data generated from the X-ray analysis is interpreted and refined to obtain the crystal structure.

X-ray diffraction is now a common technique for the study of crystal structures and atomic spacing. X-ray diffraction is based on constructive interference of monochromatic X-rays and a crystalline sample. These X-rays are generated by a cathode ray tube, filtered to produce monochromatic radiation, collimated to concentrate and directed toward the sample. The interaction of the incident rays with the sample produces constructive interference (and a diffracted ray) when conditions satisfy Bragg's Law ($n\lambda = 2d \sin\theta$). This law relates the wavelength of electromagnetic radiation to the diffraction angle and the lattice spacing in a crystalline sample. These diffracted X-rays are then detected, processed and counted. By changing the geometry of the incident rays, the orientation of the centered crystal and the detector, all possible diffraction directions of the lattice should be attained. All diffraction methods are based on generation of X-rays in an X-ray tube. These X-rays are directed at the sample, and the diffracted rays are collected. A key component of all diffraction is the angle between the incident and diffracted rays.

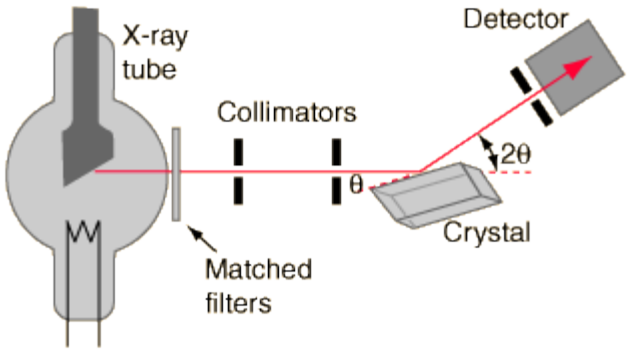

Fig. A.3. Representation of the single-crystal X-ray diffractometers (adapted from *http://hyperphysics.phy-astr.gsu.edu/hbase/quantum/bragg.html*).

An X-ray diffractometer consists of three basic elements (as shown in **Fig. A.3**): an X-ray tube, a sample holder and an X-ray detector. X-rays are generated in a cathode ray tube by heating a filament to produce electrons, accelerating the electrons toward a target

by applying a voltage and impact of the electrons with the target material. When electrons have sufficient energy to dislodge inner shell electrons of the target material, characteristic X-ray spectra are produced. Filtering, by foils or crystal monochrometers, is required to produce monochromatic X-rays needed for diffraction. Molybdenum is the most common target material for single-crystal diffraction, with MoKα radiation at 0.7107 Å. These X-rays are collimated and directed onto the sample. When the geometry of the incident X-rays impinging the sample satisfies the Bragg Equation, constructive interference occurs. A detector records and processes this X-ray signal and converts the signal to a count rate which is then output to a device such as a printer or computer monitor.

- **Sample Selection and Preparation.**

Samples for single-crystal diffraction should be selected from unfractured, optically clear crystals. This can be determined by viewing the samples under crossed polars on a petrographic microscope. Crystals can be broken off a larger sample and the best fragment selected. To minimize absorption affects, equant crystals are preferred. If the sample is inequant, this must be corrected for during absorption corrections to the data.

- **Sample Mounting.**

Samples are suspended on small fiber loops. This fiber is attached to a brass mounting pin, usually by the use of modeling clay, and the pin is then inserted into the goniometer head.

- **Sample Centering.**

The goniometer head and sample are then affixed to the diffractometer. Samples are centered by viewing the sample under the video camera and adjusting the X, Y and Z directions until the sample is centered under the cross-hairs for all crystal orientations.

- **Data Collection.**

Once the crystal is centered, a preliminary rotational image is often collected to screen the sample quality and to select parameters for later steps. An automatic collection routine can be used to collect a preliminary set of frames for determination of the unit cell. Reflections from these frames are auto-indexed to select the reduced primitive cell and calculate the orientation matrix (which relates the unit cell to the actual crystal position within the beam). The primitive unit cell is refined using least-squares and then converted to the appropriate crystal system and Bravias lattice. This new cell is also refined using least-squares to determine the final orientation matrix for the sample.

After the refined cell and orientation matrix have been determined, intensity data is collected. Generally this is done by collecting a sphere or hemisphere of data using an incremental scan method, collecting frames in 0.1° to 0.3° increments (over certain angles while others are held constant). For highly symmetric materials, collection can be constrained symmetrically to reduce the collection time. A complete data collection may require between hours to days, depending on the specimen and the diffractometer.

- **Corrections for Background, Absorption, *etc.***

After the data have been collected, corrections for instrumental factors, polarization effects, X-ray absorption correction must be applied to the entire data set. This integration process also reduces the raw frame data to a smaller set of individual integrated intensities.

- **Phase Problem and Fourier Transformation.**

Once the data have been collected, the phase problem must be solved to find the unique set of phases that can be combined with the structure factors to determine the electron density and, therefore, the crystal structure. A number of different procedures exist for solution of the phase problem, but the most common method currently is using direct methods and least squares, initially assigning phases to strong reflections and iterating to produce a refined fit.

- **Structure solution.**

Solution of the phase problem leads to the initial electron density map. Elements can be assigned to intensity centers, with heavier elements associated with higher intensities. Distances and angles between intensity centers can also be used for atom assignment based on likely coordination. If the sample is of a known material, a template may be used for the initial solution.

- **Structure Refinement.**

Once the initial crystal structure is solved, various steps can be done to attain the best possible fit between the observed and calculated crystal structure. The final structure solution will be presented with an *R* value, which gives the percent variation between the calculated and observed structures.

A.4. Inductively Coupled Plasma/Optical Emission Spectrometry (ICP-OES)

Inductively coupled plasma/optical emission spectrometry (ICP/OES) is a powerful tool for the trace analysis of metal elements (0.0002-1000ppm) and a limited number of non-metallic elements (e.g. S, P) in a variety of different sample matrices. It's based on Atomic Emission Spectroscopy, where the sample at high temperature plasma up to 8000 Kelvin converted to free, excited or ionized ions. The excited atom emits a radiation(s) when it goes back to ground state. The emitted characteristic radiations and intensities are measure optically by detectors.

The block diagram of ICP-OES set-up includes the following five parts (as shown in **Fig. A.4**):

- Sample introduction and Aerosol Generation.
- ICP Torch: Radio frequency (RF) powered torch as a source.
- Polychromators as a wavelength selector.
- Photomultiplier (PMT) or charge capacitive discharged arrays (CCD) as detector.
- Signal Processor.

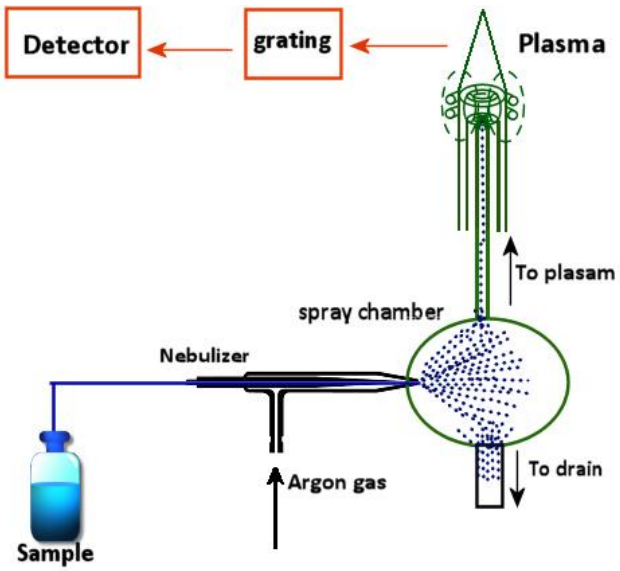

Fig. A.4. Diagram of ICP-OES (adapted from *Chemical Analysis, Modern Instrumentation Methods and Techniques*. second edition, Francis Rouessac and Annick Rouessac).

Commonly, samples are introduced into the ICP as liquid form. Liquid sample goes through different steps when injected to the ICP. The first process called nebulization

where sample is converted to a mist of finely divided droplet called aerosol. In the **nebulizer,** the sample is sucked into capillary tube by a high-pressure stream of Argon gas flowing around the tip of the tube. This pressure breaks the liquid into fine droplets in various sizes in the **spray chamber**.

In the spray chamber, separation of aerosol occurred where the large droplets go to drain the fine droplet carried to the plasma. More than 99 % of the injected sample goes to drain and less than 1 % carried out to the plasma. The Plasma is a highly energized 'cloud' of gaseous ions and their electrons.

Ionization of the flowing argon is initiated by a spark from a Tesla coil. The resulting ions, and their associated electrons, then interact with the fluctuating magnetic field produced by the induction coil. This interaction causes the ions and electrons within the coil to flow in the closed annular paths depicted ohmic heating is consequence of the resistance of the ions and electrons to this movements. Adding mechanical energy to the electrons/ions by the use of the induced field within the heart of the plasma in this manner is called "Inductively Coupling". Where the argon ions inside the magnetic field are accelerated base on the right hand rule.

The temperature of the plasma is varying in different sections ranging from 2000 to 9000 K but it is considered relatively uniform. The plasma excites atoms, which leads to photon emission and ionization. It has a high stability and considered as inert environment and low interference and this makes the ICP-OES produce better qualitative and quantitative analytical data. The emitted radiation from the plasma is used for analysis.

The following features of ICP-OES distinguish it from atomic absorption spectrophotometers used for similar purposes:

- Simultaneous, sequential analysis of multiple elements possible.
- Wide linear region of analytical curve.
- Few chemical interference or ionization interference, making analysis of high-matrix samples possible.
- High sensitivity (low limit of detection for majority of elements is 10ppb or lower).
- High number of measurable elements (elements that are difficult to analyze in atomic absorption spectrometry such as Zr, Ta, rare earth, P and B can be easily analysed).
- Stability.

A.5. Superconducting Quantum Interference Device (SQUID)

Superconducting Quantum Interference Device (SQUID) is one of the most sensitive detectors of magnetic flux and field known, which can detect a change of energy as much as 100 billion times weaker than the electromagnetic energy that moves a compass needle. Due to their unique properties, SQUID devices are widely used in several applications, such as bio-magnetism, magnetic microscopy, quantum information or nanoscience. A SQUID sensor is basically a magnetic flux-voltage converter having an extremely low magnetic flux noise. The physical quantities (magnetic field, current, voltage, displacements, *etc.*) to be detected are converted in a magnetic flux by using suitable flux transformer circuits.

The main part of the SQUID magnetometer contains essentially the following details:

- Pick-up coils.
- Magnet coil.
- Heat switch.
- Magnetic shielding.

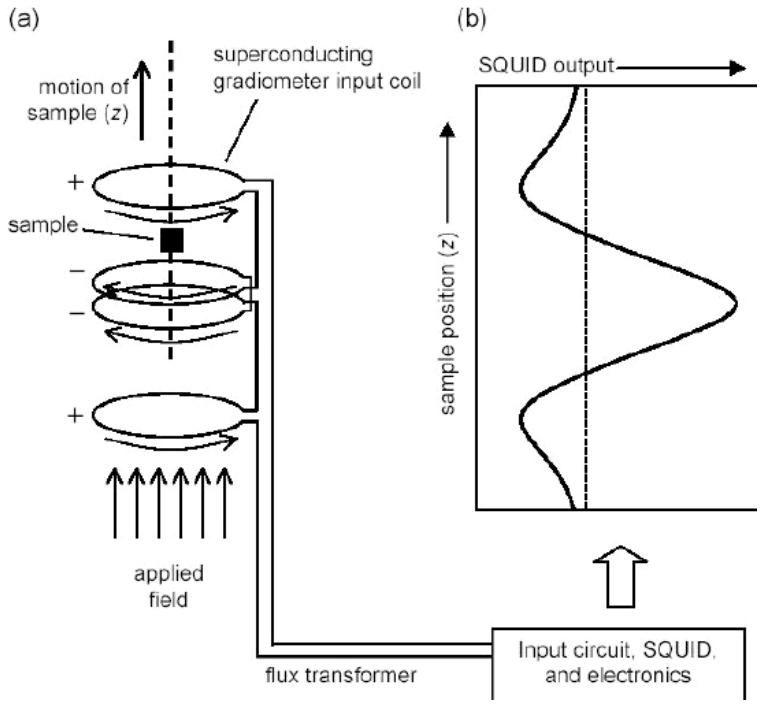

Fig. A.5. (a) Schematic of SQUID magnetometer–susceptometer. (b) Calibrated output from SQUID electronics, recorded as a function of position (adapted from *The SQUID Handbook: Applications of SQUIDs and SQUID Systems*. Volume II, pp.391 – 440).

A radio frequency (RF) SQUID is made up of one Josephson junction, which is mounted on a superconducting ring. An oscillating current is applied to an external circuit, whose voltage changes as an effect of the interaction between it and the ring. The magnetic flux is then measured.

DC Magnetometry.

DC magnetic measurements determine the equilibrium value of the magnetization in a sample. The sample is magnetized by a constant magnetic field and the magnetic moment of the sample is measured, producing a DC magnetization curve M(*H*).

AC Magnetometry.

In AC magnetic measurements, a small AC drive magnetic field is superimposed on the DC field, causing a time-dependent moment in the sample. The field of the time-dependent moment induces a current in the pickup coils, allowing measurement without sample motion. The detection circuitry is configured to detect only in a narrow frequency band, normally at the fundamental frequency (that of the AC drive field). In order to understand what is measured in AC magnetometry, first consider very low frequencies, where the measurement is most similar to DC magnetometry. In this case, the magnetic moment of the sample follows the M(*H*) curve that would be measured in a DC experiment. As long as the AC field is small, the induced *AC* moment is $M_{AC} = (dM/dH) \cdot H_{AC}\, sin(\omega t)$ where H_{AC} is the amplitude of the driving field, ω is the driving frequency, and $\chi = dM/dH$ is the slope of the M(*H*) curve, called the susceptibility. The susceptibility is the quantity of interest in AC magnetometry.

Curriculum Vitae

Yan Duan

University of Valencia

Instituto de Ciencia Molecular (ICMol)

C/ José Beltrán 2

Burjassot, Valencia 46100

Spain

Sex: Female

Email: yan.duan@uv.es

Mobile phone: +34 6222 89 812

Phone: + 34 96 354 44 50

Date of Birth: 1986.06.29

Education Background:

2004-2008	Undergraduate
	School of Chemistry & Materials Science
	Shaanxi Normal University
	Major: Inorganic Chemistry
2008-2010	Master degree
	State Key Laboratory of Coordination Chemistry
	School of Chemistry and Chemical Engineering
	Nanjing University
	Major: Inorganic Chemistry
2010-2012	Master degree
	Instituto de Ciencia Molecular
	Universidad de Valencia
	Major: Organic Chemistry
2012-Present	Ph.D. Student
	Instituto de Ciencia Molecular
	Universidad de Valencia
	Major: Organic Chemistry
Jun 2014 - Jul 2014	Short term exchange student
	School of Chemistry
	Newcastle University
	Major: Organic Functionalize of Polyoxometalates

Skills:

- Experienced in synthesizing of coordination complexes under hydrothermal conditions on the basis of the principle of supramolecular self-assembly.
- Experienced in design and synthesis of organophosphonate ligands in order to acquire novel metal organophosphonate clusters.
- Experienced in design and synthesis of organic/inorganic hybrid materials of polyoxometalates.
- Experienced in handling sensitive reactions/reagents. Glove box, Schlenk line and other related techniques.
- Proficiency in growing single crystals and isolation and separation and mounting of Single Crystals for single crystal X-ray diffraction, as well, the refinement of single crystal data.
- Handling powder X-ray diffraction experiments.
- Ability to interpret the magnetic properties of the low-dimensional metal-organic coordination complexes.
- Characterising the related properties of the compounds by EDXA, FT-IR spectroscopy, elemental analysis, Thermo gravimetric Analysis (TGA) and UV-Visible Spectrophotometer.

Languages: Chinese, English, Spanish

Publication Highlights:

Book Chapter

Li-Min Zheng, **Yan Duan**:

Book name: *Structural and Magnetic Studies of Cobalt Phosphonates*. *Metal Phosphonate Chemistry: From Synthesis to Applications*.

Edited by Abraham Clearfield and Konstantinos Demadis, 01/2012: **Chapter 8**: pages 235-278; Royal Society of Chemistry., ISBN: Print ISBN: 978-1-84973-356-4 PDF e-ISBN: 978-1-84973-357-1

Journal Publications

[1] **Yan Duan**, Juan M. Clemente-Juan, Eugenio Coronado, Carlos Giménez-Saiz: *Construction of larger polyoxometalates containing '$[Co_4(OH)_3(H_2O)_{6-n}(PW_9O_{34})]^{3-}$' (n = 3 or 5) as a common subunit.* Crystal Growth & Design, Submitted.

[2] M. D. Jenkins, **Y. Duan**, B. Diosdado, J. J. García-Ripoll, A. Gaita-Ariño, C. Giménez-Saiz, P. J. Alonso, E. Coronado, F. Luis: *Coherent manipulation of three-qubit states in a molecular single-ion magnet.* **Physical Review B 00**, 004400 (2017); DOI: 10.1103/PhysRevB.00.004400.

[3] Verónica Jornet Mollá, **Yan Duan**, Carlos Giménez-Saiz, João C. Waerenborgh and Francisco M. Romero: *Hydrogen-bonded Networks of $[Fe(bpp)_2]^{2+}$ Spin Crossover Complexes and dicarboxylate anions: structural and photomagnetic properties*. **Dalton Transactions** 2016, 45, 17918 – 17928; DOI: 10.1039/C6DT02934E.

[4] **Yan Duan**, Juan Modesto Clemente Juan, J L G Fierro, Carlos Giménez-Saiz and Eugenio Coronado: *A decacobalt(II) cluster with triple-sandwich structure obtained by partial reductive hydrolysis of a pentacobalt(II/III), Weakley-type, polyoxometalate*. **Chemical Communications** 2016, 52, 13245 – 13248; DOI: 10.1039/C6CC05485D.

[5] **Yan Duan**, José J. Baldoví, Carlos Bustos, Salvador Cardona-Serra, Pierre Gouzerh, Richard Villanneau, Geoffrey Gontard, Juan Modesto Clemente Juan, Alejandro Gaita-Ariño, Carlos Giménez-Saiz, Anna Proust, Eugenio Coronado: *Single ion magnets based on lanthanoid polyoxomolybdate complexes*. **Dalton Transactions** 2016, 45, 16653 – 16660; DOI: 10.1039/C6DT02258H.

[6] **Yan Duan**, João Carlos Waerenborgh, Juan Modesto Clemente Juan, Carlos Giménez-Saiz, Eugenio Coronado: *Light-induced decarboxylation in a photo-responsive iron-containing complex based on polyoxometalate and oxalato ligands*. **Chemical Science** 2017, 8, 305 – 315; DOI: 10.1039/C6SC01919F.

[7] José J Baldoví, **Yan Duan**, Roser Morales, Alejandro Gaita-Ariño, Eliseo Ruiz, Eugenio Coronado: *Rational Design of Lanthanoid Single-Ion Magnets: Predictive Power of the*

Theoretical Models. **Chemistry-A European Journal** 2016, 22, 13532 – 13539; DOI: 10.1002/chem.201601741.

[8] Muhandis Shiddiq, Dorsa Komijani, **Yan Duan**, Alejandro Gaita-Ariño, Eugenio Coronado, Stephen Hill: *Enhancing coherence in molecular spin qubits via atomic clock transitions.* **Nature** 2016, 531, 348 – 351; DOI: 10.1038/nature16984.

[9] **Yan Duan**, Juan M. Clemente-Juan, Carlos Giménez-Saiz, Eugenio Coronado: *Cobalt clusters with cubane-type topologies based on trivacant polyoxometalate ligands.* **Inorganic Chemistry** 2016, 55, 925 – 938; DOI: 10.1021/acs.inorgchem.5b02532.

[10] José J Baldoví, Juan M Clemente-Juan, Eugenio Coronado, **Yan Duan**, Alejandro Gaita-Ariño, Carlos Giménez-Saiz: *Construction of a General Library for the Rational Design of Nanomagnets and Spin Qubits Based on Mononuclear f-Block Complexes. The Polyoxometalate Case.* **Inorganic Chemistry** 2014, 53, 9976 − 9980; DOI: 10.1021/ic501867d.

[11] Carlos Martí-Gastaldo, Concha Bosch-Navarro, Filipo Bussolo, Eugenio Coronado, **Yan Duan** and Helena Prima-García*: Influence of the covalent grafting of organic radicals to graphene on its magnetoresistance.* **Journal of Materials Chemistry C** 2013, 1, 4590 – 4598; DOI: 10.1039/c3tc30799a.

[12] Peng-Fei Wang, **Yan Duan**, Juan Modesto Clemente-Juan, You Song, Kang Qian, Song Gao, Li-Min Zheng: *Magnetization relaxation in a three-dimensional ligated cobalt phosphonate containing ferrimagnetic chains.* **Chemistry-A European Journal** 02/2011; 17(13):3579 – *35*83; DOI: 10.1002/chem.201002348.

[13] Peng-Fei Wang, **Yan Duan**, Li-Min Zheng: *One-dimensional metal phosphonates based on 6-phosphononicotinic acid: A structural and magnetic study*. **Science China-Chemistry** 10/2010; 53(10):2112 – 2117; DOI: 10.1007/s11426-010-4097-6.

[14] Peng-Fei Wang, **Yan Duan**, Tian-Wei Wang, Yi-Zhi Li, Li-Min Zheng: *Three-dimensional metal phosphonodicarboxylates with GIS-zeolite topology: syntheses, structures and magnetic studies.* **Dalton Transactions** 10/2010; 39(44):10631 – *10636*; DOI: 10.1039/c0dt00601g.

[15] Yan-Hui Su, Deng-Ke Cao, **Yan Duan**, Yi-Zhi Li, Li-Min Zheng: *Metal diphosphonates with double-layer and pillared layered structures based on N-cyclohexylaminomethanediphosphonate*. **Journal of Solid State Chemistry** 07/2010; 183(7):1588 – 1594; DOI: 10.1016/j.jssc.2010.05.008.

[16] Peng-Fei Wang, **Yan Duan**, Deng-Ke Cao, Yi-Zhi Li, Li-Min Zheng: *Metal carboxylate-phosphonates containing flexible N-donor co-ligands.* **Dalton Transactions** 04/2010; 39(19):4559 – *45*65; DOI: 10.1039/b927100g.

Conference Proceedings:

1.
Title: Synthesis and magnetic properties of two Mixed-Valence Polyoxometalates of interest in molecular magnetism: $[PMo_{12}O_{40}]Ni_2(Phen)_4(H_2O)_2$ and $[PMo_{12}O_{40}]Ni_3(Phen)_4(H_2O)$
Conference name: 1st European Conference on Polyoxometalate Chemistry for Molecular Nanoscience
Type of event: Conference
Participation type: Oral talk
Conference city: Puerto Santiago (Tenerife), España
Date: 2013
Author: **Yan DUAN**; Salvador Cardona-Serra; Juan Modesto Clemente-Juan; Eugenio Coronado; Carlos Giménez-Saiz.

2.
Title: Single-Ion Magnets based on Lanthanoid Polyoxometalate Complexes Soluble in Organic Solvents. The series $[Ln(Mo_8O_{26})_2]^{5-}$ (Ln^{III} = Tb, Dy, Ho, Er, Tm, and Yb)
Conference name: 40 International Conference on Coordination Chemistry
Type of event: Conference
Participation type: Poster
Conference city: Valencia, España
Date: 2012
Author: **Yan Duan**; Salvador Cardona-Serra; Juan Modesto Clemente-Juan; Eugenio Coronado; Carlos Giménez-Saiz.

3.
Title: surface deposition of a new polyoxometalate-[60] fullerene hybrid
Conference name: European School on Molecular Nanoscience
Type of event: Conference
Participation type: Oral talk
Conference city: Peniscola, Castellon, España
Date: 2011
Author: **Yan Duan**; Elena Pinilla-Cienfuegos; Benjamin Matt; Filippo Busolo; Carlos Giménez-Saiz; Eugenio Coronado.

4.
Title: A decacobalt(II) cluster with triple-sandwich structure obtained by reductive hydrolysis of a pentacobalt(II/III), Weakley-type, polyoxometalate
Conference name: FMOCS IV @ PoCheMoN 2016
Type of event: Conference
Participation type: Oral talk
Conference city: Newcastle University, Newcastle upon Tyne, UK
Date: 2016-07
Author: **Yan Duan**; Juan Modesto Clemente-Juan; Carlos Giménez-Saiz; Eugenio Coronado.